Large Amplitude Driving of a Persistent Current Qubit

by

David Marc Berns

Submitted to the Department of Physics
in partial fulfillment of the requirements for the degree of

Doctor of Philosophy

at the

MASSACHUSETTS INSTITUTE OF TECHNOLOGY

June 2008

Author . . . .
Department of Physics
May 16, 2008

Certified by . . . .
Terry P. Orlando
Professor of Electrical Engineering
Thesis Supervisor

Certified by . . . .
Mildred S. Dresselhaus
Institute Professor
Thesis Co-Supervisor

Accepted by . . . .
Thomas J. Greytak
Associate Department Head for Education

Large Amplitude Driving of a Persistent Current Qubit

by

David Marc Berns

Submitted to the Department of Physics
on May 16, 2008, in partial fulfillment of the
requirements for the degree of
Doctor of Philosophy

Abstract

In this thesis, the persistent current qubit in the presence of large amplitude microwave radiation is studied. Three main results are presented in this work. A new coherent quasiclassical regime has been observed, where coherent quantum dynamics persist even while transitions between energy levels are caused by many photon modes simultaneously. A new theoretical treatment of this regime has been developed, and remarkable agreement between theory and experiment is observed. Also presented is a novel application of strong driving, where unwanted excited state population is cooled to the ground state by utilizing a second avoided crossing. This method of cooling, via a third, ancillary qubit level, is analogous to atomic sideband cooling. Cooling from 400mK to 3mK has been achieved. Finally, a new type of spectroscopy is presented, where an entire manifold of quantum levels is characterized with a single driving frequency, by studying the amplitude dependence of the qubit's behavior. Characterization of energy level spacings reaching 120GHz is achieved with radiation on the order of 0.1GHz.

Thesis Supervisor: Terry P. Orlando
Title: Professor of Electrical Engineering

Thesis Co-Supervisor: Mildred S. Dresselhaus
Title: Institute Professor

For my parents

Acknowledgments

I would like to begin by acknowledging the institute, which is defined by its professors and research staff. I came to MIT in love with physics, hoping to learn "real" physics, beyond what they taught us as undergraduates, and ended up leaving with something very different than that. It turns out that MIT is not in the business of teaching physics, but instead it is about teaching its students how to be scientists. MIT cares about creating people who can think and work quickly, constructively, creatively, and precisely. MIT is about showing you what good work truly is and letting you either fail to understand or achieve its notion of good work, or let you become a person you never knew could exist before you came here. There are no exact criteria that tells you if you ever truly lived up to the standards of the institute, nor is there ever any praise to think that you may have. And with this intense training comes sacrifice...in confidence and comfort, and in the kindness of many. And though I don't agree with all the methods or values of MIT, I would still like to say thank you to the institute for teaching me how to be a better thinker and professional. Though the years were difficult, it was an educational experience I wouldn't trade for anything.

The most influential person during my time at MIT was my research advisor, Terry Orlando. Terry had the rarest gift of all at MIT, which was to put his students first. The way most advisors at MIT teach is through selfishness, demanding their (your) work be excellent. Terry on the other hand was concerned about his students' professional development, not his own. Terry's insight and passion for physics kept my interest in the subject strong through difficult times, and his gift in teaching his students how to find the inner scientist in themselves, through everything, is something I will always be thankful for. Terry is also in a league of his own at MIT because he has always cared so much about the personal happiness of his students, and with graduate school typically not being a time for this, I will always be grateful. Both professionally and personally, Terry was a beacon for me to navigate through the rough world that is MIT, and I thank him for that. More than anything though, Terry has become one of my best friends and favorite people in the world, and for that I would like to say thank you.

Will Oliver was a secondary research mentor for me at MIT. Will more than anyone showed me what it meant to do good science. He was completely unforgiving of any effort less than 100 percent, both in passion and in quality of work. Will always set the bar for the research in this thesis, and though at times it seemed too high, his insistence on a high bar, that slowly went up during my time at MIT, taught me what "real" science was, and for that I am eternally grateful. Will also showed me what it really meant to love doing something...he showed me what it meant to have a real "fire" inside for something, which I never could have imagined or understood without seeing it firsthand, and I thank him for that.

Sergio Valenzuela was another mentor to me, and even more so an amazing person. Sergio's view of science was an invaluable balance to the perspective held by many at MIT, and one that gave me a lot of peace while I was discovering how I best did science. Even more important to me though, Sergio showed me what it meant to be a good man, and he will forever be a role model to me on how to be both wise and kind.

I also had the opportunity to work closely with a fantastic theoretical team, which included Mark Rudner, Andrey Shytov, and Leonid Levitov. Being able to work with such world-class theorists was both an honor and a privilege. Their interest and involvement in our research spurred excitement about our work both within our group and in the community as a whole, and their contributions helped make the work in this thesis much more profound. I will always be indebted for their fantastic work and enthusiasm.

Some of my best friends have come from MIT, and their friendships during and after MIT have made my life a pleasure. Bill Kaminsky, Mark Rudner, Ed Barkley, Joe Rumpler, Brian Mullins, and Ali Motamedi have become some of my best friends, and I am so thankful for our relationships. This group of people is one of the smartest, funniest, and most kind set of people I know.

A few other amazing friends kept me sane and happy during my time at MIT, including Gilad Jacobs, Lyman Fox, Tom Kotwal, and Brendon Lewis. Thank you for all the fun times and all the support throughout my time at MIT.

Finally, I would like to thank my family. It is my family that made this thesis possible, and it is my family that made this thesis worth doing. Thank you also for all your love and support during my time at MIT.

Contents

List of Figures

Chapter 1

Introduction

1.1 Motivation

In the last ten years, quantum information science [1, 2] has blossomed into a popular and well-respected discipline within the physical sciences. Besides the promise of great advances in computational abilities and other technological applications, the study of quantum information also presents an opportunity to study the fundamental nature of quantum mechanics.

1.1.1 Simulation, Computation, and Other Applications

Classical information science studies the storage, manipulation, and communication of information, where the fundamental component of data is the bit. It was not until 1980 that it was first suggested that computation could in principle be performed with a quantum computer, made of quantum bits (qubits) [3].

Strong theoretical interest in quantum computing did not arise though until 1982, when Richard Feynman suggested that quantum computers might be more useful in the simulation of quantum systems than a classical computer [4]. This notion was not verified until 1996, when it was shown that a quantum computer could indeed efficiently simulate other quantum systems, where no efficient quantum simulation algorithms were known for a classical computer [5]. The first quantum simulation performed with another quantum system was done in 1999 with nuclear spins [6].

The more general problem of whether a quantum computer could outperform classical computers was first considered by Deutsch [7]. He asked whether a quantum computer could challenge the strongest form of the Church-Turing thesis, which says that any algorithmic process can be simulated efficiently using a probabilistic Turing machine. The answer to this question is still not known [8], but there are now many examples of problems with efficient solutions on quantum computers, where no known efficient solutions on classical computers exist [2]. The most famous of these efficient quantum solutions is Peter Shor's algorithm that finds the prime factors of an integer [9]. Besides addressing Deutsch's original question, the algorithm also has important consequences for public key cryptography, due to the widespread use of the RSA cryptosystem, whose security rests solely on the intractability of factoring large numbers into their prime factors [10]. The first implementation of Shor's factoring algorithm was achieved in 2001 using nuclear spins [11].

Another important application of quantum information science is in private key cryptography, the basic notion of which was first put forth in 1983 [12]. The basic idea behind classical private key cryptosystems is that only the parties in communication have access to the keys. However, this is obviously difficult to do without an eavesdropper compromising the key when the two parties originally exchange it. The quantum solution lies in the fact that quantum information is always disturbed when it is measured. This way, it is possible to develop a means of communicating a key by which the private parties can always know whether their key has been intercepted along the way. Private key cryptography was first demonstrated in 1992 with photons traveling in free space [13].

There are many other applications of quantum information science, and I would like to mention just one more such application. Probably the most popular quantum technology to have been studied, other than cryptology and computation, is teleportation [14]. There one transmits the state of a quantum system, over arbitrary distances, to another quantum system. The popularity of quantum teleportation is certainly attributable to the dream of traveling to a distant place by just reappearing there. Though still not possible for humans, teleportation with photons was indeed demonstrated in 1997 [15].

1.1.2 Fundamental Physics

The study of quantum systems that can be used for quantum information applications is also of great interest from a fundamental physics standpoint. For instance, macroscopic quantum physics is still largely unexplored territory [16]. Since the birth of quantum mechanics there have been questions about when macroscopic realism becomes reality out of our fundamentally quantum mechanical world, embodied no better than in Schrödinger's famous cat paradox [17]. Temporal Bell inequalities under the assumptions of macroscopic realism have indeed recently been found [18], and experiments using devices much like the one studied in this thesis have been proposed to test those inequalities [19, 20]. Though the assumptions used in deriving the inequalities and the exact nature of what one can learn by studying the inequalities are still under debate [21, 22], the study of the transition from quantum mechanics to macroscopic realism is of great importance for understanding nature.

Another fundamental issue that can be explored with qubits is quantum measurement [16]. During an ideal projective quantum measurement, the states of the system being measured become entangled with the measurement apparatus states [23]. However, quantum theory has seemed to leave ambiguous which system states will entangle with the measurement apparatus states [24]. As any experimentalist of quantum mechanics knows though, measurement apparatuses measure one unique set of system states. The reason why one system basis is realized over another during measurement has been unresolved since the birth of quantum measurement theory. The most popular theory on how the measured basis is chosen is given by Zurek and Paz [24, 25], who argue that decoherence effectively chooses the measured system basis based on the interaction between the measurement apparatus and the environment. The basic idea is that the realized measurement basis is that set of states which is able to persist despite constant environmental monitoring. Work has already begun on designing the apparatus-environment Hamiltonian in order to create quantum measurement apparatuses with specified measurement bases [26].

Another issue within quantum measurement theory that can potentially be studied with qubits is the collapse of the wavefunction [16]. If the quantum state being measured is in a superposition of states, why is only one state realized in an ideal projective measurement? The collapse of the wavefunction is the ad hoc assumption that superposition states will be projected onto a single state during measurement. There are many theories as to what really happens during the collapse, including those based on gravity [27], those based on missing non-linear terms in Schrödinger's equation [28], and those based on decoherence [29]. In fact, these are the same theories that try to explain why quantum phenomenon aren't typically seen on the macroscopic scale. Qubits like the one studied in this thesis should provide the ability to design the Hamiltonian of a quantum system specifically for testing collapse theories.

Finally, many of the quantum phenomena seen in textbooks, e.g., Rabi oscillations between quantum states, have been studied mostly in atomic systems. Qubits developed in the solid state will allow for a comparison of the results seen in atomic and molecular physics, enhancing our understanding of these quantum processes. Besides the difference in environment, qubits developed in the solid state can also be engineered with a variety of Hamiltonians, providing a greater breadth of physics than that which is provided to us naturally in atomic and molecular systems.

1.2 Outline

This doctoral thesis presents experiments done on the persistent current qubit, with a major focus on the qubit's behavior in the presence of large amplitude driving fields.

Chapter 2 will introduce the reader to the persistent current qubit. The Hamiltonian for the qubit will be derived and an intuitive discussion of its properties and behavior will be presented. I will then discuss how the qubit is measured in the experiments. As a necessary prerequisite for all of the above, the Josephson junction will also be introduced. Chapter 2 will conclude with a brief description of the process used to fabricate the device, as well as a brief overview of the experimental setup used in the work presented.

In Chapter 3 I will present a new quasiclassical regime of coherent quantum dynamics of a qubit, realized at low driving frequencies in the strong driving limit. A two-level system approximation, consisting of the lowest two levels of the qubit's energy spectrum, with a single avoided crossing between them, is considered. Background theory will be covered, including a very helpful analogy to Mach-Zehnder interferometry that will be used throughout the thesis. A new theoretical model that is valid in the quasiclassical regime will be described, and remarkable agreement between theory and observation will be shown.

Chapter 4 then moves on to strong driving experiments with an additional energy level and side avoided crossing. I will present a novel way of cooling qubits, where thermally excited population in the two-level model is forced to the ground state via radio frequency driving. The technique is analogous to atomic sideband cooling, where a third, ancillary level is utilized to cool an effective two-level system. The added energy level and avoided crossing accessed in this chapter will act as the ancillary level for qubit cooling. Effective temperatures as low as $T_{\text{eff}} \approx 3$ millikelvin are achieved for bath temperatures $T_{\text{bath}} = 30 - 400$ millikelvin.

In chapter 5 I will then consider more than 2 avoided crossings, and discuss a novel way of characterizing the full energy spectrum of the qubit by studying the population changes as a function of driving amplitude. Only a single driving frequency is utilized, which may be orders of magnitude smaller than the energy scales being probed. The main feature of amplitude spectroscopy will be "spectroscopy diamonds", which contain interference patterns and population inversion that serve as a fingerprint of the qubit's energy spectrum. By analyzing these features, the energy spectrum of a manifold of states with energies from 0.01 to 120 GHz$\times h$ (where h is Planck's constant) was determined, using a single driving frequency near 0.1 GHz.

Finally, Chapter 6 will conclude with a summary of the major results of the thesis, along with a summary of unfinished and future work.

Appendix A contains a discussion of the rotating wave approximation, a technique which allows for the analytic solution of the driven, two-level atom. The appendix will provide a review of the approximation, along with a derivation of its assumptions that I have not seen performed anywhere else in the literature. A similar approximation will be used when driving the persistent current qubit, and a full understanding of the rotating wave approximation will provide insight into the analysis performed in this thesis.

Appendix B is a self-contained review paper discussing the implementation of the factorized quantum lattice-gas algorithm for the one dimensional diffusion equation, using the persistent current qubit. The algorithm is the quantum extension of classical lattice-gases, whose goal is to simulate fluid dynamics without reference to specific microscopic interactions. The quantum version allows for improvements in memory usage and viscosity constraints over its classical counterpart. The class of all factorized quantum lattice-gas algorithms was very popular at the beginning of experimental quantum computing efforts because they require coherence over only individual lattice sites (a few qubits), rather than over the entire lattice (hundreds of qubits), which is a daunting experimental challenge.

Two contrasting implementation schemes are presented, one unique to the PC qubit, the other analogous to what would be done in nuclear magnetic resonance quantum computing. The work originally served as a feasibility study of quantum computing with persistent current qubits, with very positive conclusions. The work now also serves as a review of the differences between the PC Qubit and NMR systems, as well as a review of Bloch sphere rotations. Finally, the paper provides an introduction to some of the fundamental concepts one confronts when trying to implement an algorithm with the persistent current qubit, and qubits in general.

Appendix C contains four more reprints, on the work presented in Chapter 3, Chapter 4, and Chapter 5.

Chapter 2

The Persistent Current Qubit

There are many physical systems that can be utilized as qubits [2]. These range from systems provided to us by nature, like nuclear spins [30], to man-made systems, like quantum dots [31]. One of the most popular classes of qubits is known as superconducting qubits [32]. These are fabricated superconducting circuits that use Josephson junctions [33] as the elements that allow for qubit-like behavior [34, 35, 36]. There are many superconducting circuits that can be used as a qubit [37, 38, 39, 40], and here I will only consider one, the persistent current qubit [41]. In this chapter I will review the persistent current qubit and how it is measured. I will also briefly discuss how the device was made and the experimental setup used to study the qubit.

2.1 Theory of the Persistent Current Qubit

How does one make a quantum mechanical system from a circuit? And what exactly is the quantum object in a persistent current (PC) qubit that is suitable for quantum computation? Is it an electron inside the superconductor, or maybe a Cooper pair? Ch. 2.1 will address these issues by deriving the eigenstates of the PC qubit from first principles. I will begin with a discussion of Josephson junctions, the main component of any superconducting qubit. From there I will find the Hamiltonian of the PC qubit, and proceed via a tight-binding approach to a two-level model for the qubit. Though the qubit dynamics of more than two levels is the focus of Ch. 4 and Ch. 5,

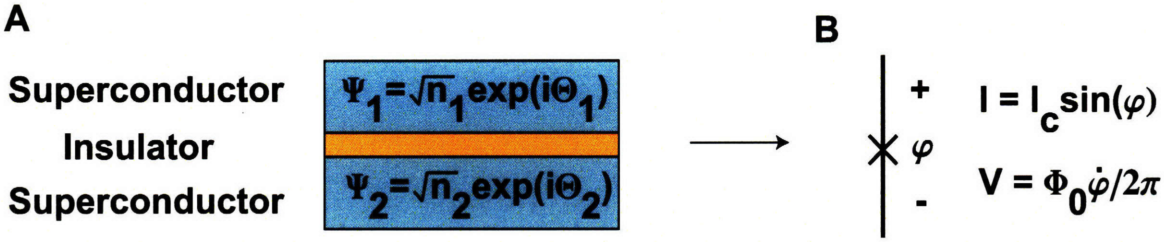

Figure 2-1: Josephson junction schematic and circuit symbol. (**A**) A Josephson junction is physically just a thin insulator sandwiched between two superconductors. The wavefunction for all the Cooper pairs in a superconductor can be described by $\Psi = \sqrt{\mathrm{n}}\exp(i\Theta)$, where n is the density of Cooper pairs and Θ is a phase. (**B**) The circuit symbol for a Josepshon junction. The current I and voltage V across a JJ are related to the gauge invariant phase difference φ across the sandwiching superconductors (see text).

a thorough understanding of the two-level PC qubit is very important for this thesis, and will be the focus of Ch. 2.1. Ch. 3 will focus purely on two-level dynamics, and will provide the necessary background for the multi-level studies discussed later on.

2.1.1 Josephson Junctions

The fundamental building block for all superconducting qubits is the Josephson junction. Physically, a Josephson junction (JJ) is simply an insulator sandwiched between two superconductors. A schematic of this sandwich is seen in Fig. 2-1A. The current-voltage properties of the JJ can be derived by solving the quantum mechanical boundary-value problem the metal-insulator-metal sandwich presents [42]. By assuming that all the Cooper pairs in a superconductor can be described by a wavefunction of the form $\Psi = \sqrt{\mathrm{n}}\exp(i\Theta)$, where n is the density of Cooper pairs and Θ is a phase, one can find the current-phase and voltage-phase relationships for the Josephson junction circuit element. One finds that the current I through the junction is

$$\mathrm{I} = \mathrm{I_c}\sin(\varphi) \tag{2.1}$$

where $\varphi = \Theta_1 - \Theta_2 - \frac{2\pi}{\Phi_0}\int_1^2 \mathbf{A}(\mathbf{r},\mathrm{t}) \cdot \mathrm{d}\mathbf{l}$ is the gauge invariant phase difference across the sandwiching superconductors, where the line integral over the magnetic vector potential $\mathbf{A}(\mathbf{r},t)$ is from superconductor 1 to superconductor 2, and I_c is known as the critical current of the junctions, and is a function of the materials used to create the junction and the width of the junction. One can also show that the voltage V across the junction is

$$V = \frac{\Phi_0}{2\pi}\dot{\varphi}, \tag{2.2}$$

where Φ_0 is a single flux quantum. The standard way of drawing a JJ as a circuit element, along with its current-phase and voltage-phase relationships, is summarized in Fig. 2-1B.

The energy associated with a single JJ can be broken up into two terms. The first is the capacitive energy, where the capacitance of the JJ is denoted by C. The second contribution to the JJ energy is the integrated power found from the current-voltage relations (Eq. 2.1 and Eq. 2.2), giving the total energy E stored by the JJ

$$E = \frac{1}{2}CV^2 + E_j(1 - \cos(\varphi)) \tag{2.3}$$

where $E_j = \frac{\Phi_0 I_c}{2\pi}$ is the Josephson energy.

2.1.2 The Persistent Current Qubit Hamiltonian

Armed with the energy for a single junction, one can now find the Hamiltonian of the PC Qubit [43]. A schematic of the qubit is seen in Fig. 2-2. The qubit is simply a loop of superconducting wire interrupted by three Josephson junctions, where the third junction's cross-sectional area is smaller than the area of the other two junctions by a factor α. Taking the capacitive energy terms as the kinetic part, the Lagrangian is

$$\mathcal{L} = \sum_{i=1}^{3}\frac{1}{2}C_iV_i^2 - \sum_{i=1}^{3}E_{ji}(1 - \cos(\varphi_i)). \tag{2.4}$$

By analyzing the total phase around the qubit loop, one can show [42] that the JJ phases are constrained by the magnetic flux threading the loop such that

$$\varphi_1 - \varphi_2 + \varphi_3 = 2\pi f, \tag{2.5}$$

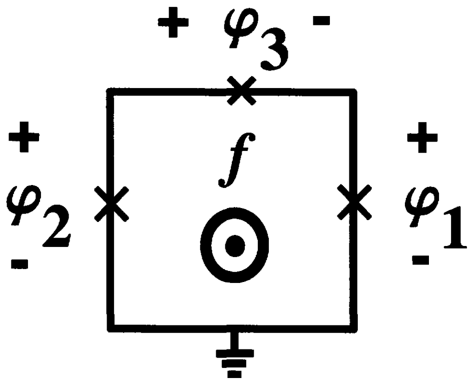

Figure 2-2: Schematic of the PC qubit. The PC qubit is a loop of superconducting wire interrupted by three Josephson junctions, where the third junction's cross-sectional area is smaller than the area of the other two junctions by a factor α. f is the applied magnetic flux piercing the qubit loop, in units of a flux quantum Φ_0.

where f is the applied magnetic flux piercing the qubit loop in units of Φ_0. With this flux/phase constraint, and the voltage relation for a JJ, the Lagrangian for the qubit can be rewritten as

$$\mathcal{L} = (\frac{\Phi_0}{2\pi})^2 \mathrm{C}\,\dot{\varphi}_\mathrm{p}^2 + (1+\alpha)(\frac{\Phi_0}{2\pi})^2 \mathrm{C}\,\dot{\varphi}_\mathrm{m}^2 - \mathrm{E_j}[2+\alpha-2\cos(\varphi_\mathrm{p})\cos(\varphi_\mathrm{m}) - \alpha\cos(2\pi f + 2\varphi_\mathrm{m})] \tag{2.6}$$

where $\varphi_\mathrm{p} = (\varphi_1 + \varphi_2)/2$ and $\varphi_\mathrm{m} = (\varphi_1 - \varphi_2)/2$, and C is the capacitance of the larger junctions.

Taking one variable to be the phase $\varphi_\mathrm{p,m}$, the conjugate momenta are $\partial\mathcal{L}/\partial\dot{\varphi}_\mathrm{p,m}$. In analogy to a 2D simple harmonic oscillator (SHO) in real space, one can view $\varphi_\mathrm{p,m}$ as a 2D "position" space, and call the conjugate momentum $\mathrm{P_{p,m}}$, a 2D "momentum" space. From here one can write down the Hamiltonian as

$$H = \frac{1}{2}\frac{\mathrm{P_p^2}}{\mathrm{M_p}} + \frac{1}{2}\frac{\mathrm{P_m^2}}{\mathrm{M_m}} + \mathrm{E_j}[2+\alpha-2\cos(\varphi_\mathrm{p})\cos(\varphi_\mathrm{m}) - \alpha\cos(2\pi f + 2\varphi_\mathrm{m})] \tag{2.7}$$

where $\mathrm{M_p} = 2\mathrm{C}(\frac{\Phi_0}{2\pi})^2$ and $\mathrm{M_m} = 2\mathrm{C}(1+\alpha)(\frac{\Phi_0}{2\pi})^2$. The quantum version of this Hamiltonian is obtained by simply replacing $P_\mathrm{p,m}$ with the operators $\frac{\hbar}{i}\frac{\partial}{\partial\varphi_\mathrm{p,m}}$, and having $\varphi_\mathrm{p,m}$ become operators as well. Fig. 2-3 shows the energy levels calculated by finding the eigenvalues of the quantum mechanical, matrix form of Eq. 2.7 [44]. The

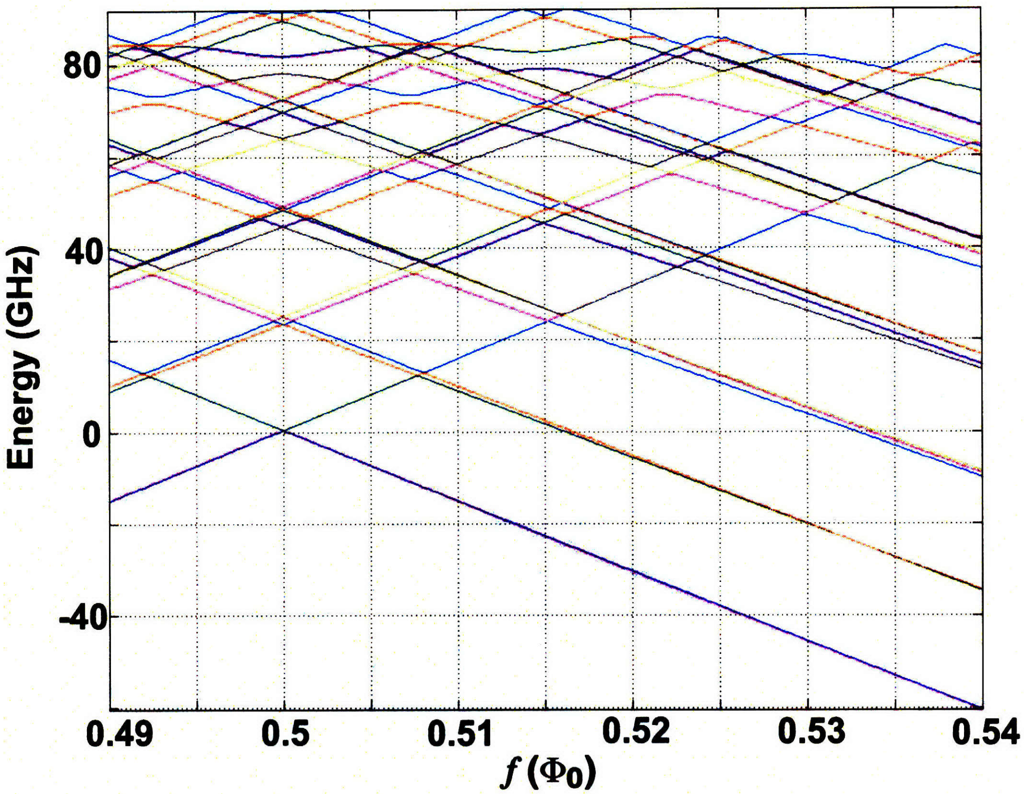

Figure 2-3: 25 lowest energy levels of the PC qubit found numerically. Energy eigenvalues are plotted as a function of the magnetic flux f applied to the qubit. The energy levels are symmetric about f=1/2.

2D phase space was discretized and δ-function basis states were used, with periodic boundary conditions imposed on a single lattice site.

2.1.3 Tight-Binding Solution

The Hamiltonian derived for the PC qubit (Eq. 2.7) is the same as for a particle in an anisotropic 2D periodic potential, except here, the phases $\varphi_{\mathrm{p,m}}$ play the role of position coordinates. Each individual lattice site is a 2D double-well, as seen in a plot of the potential energy in Fig. 2-4. The qubit parameters are chosen such that inter-well tunneling is negligible compared to intra-well tunneling, and so a tight-binding solution is extremely accurate for the problem at hand.

The fundamental concept behind tight-binding is the use of a linear combination of

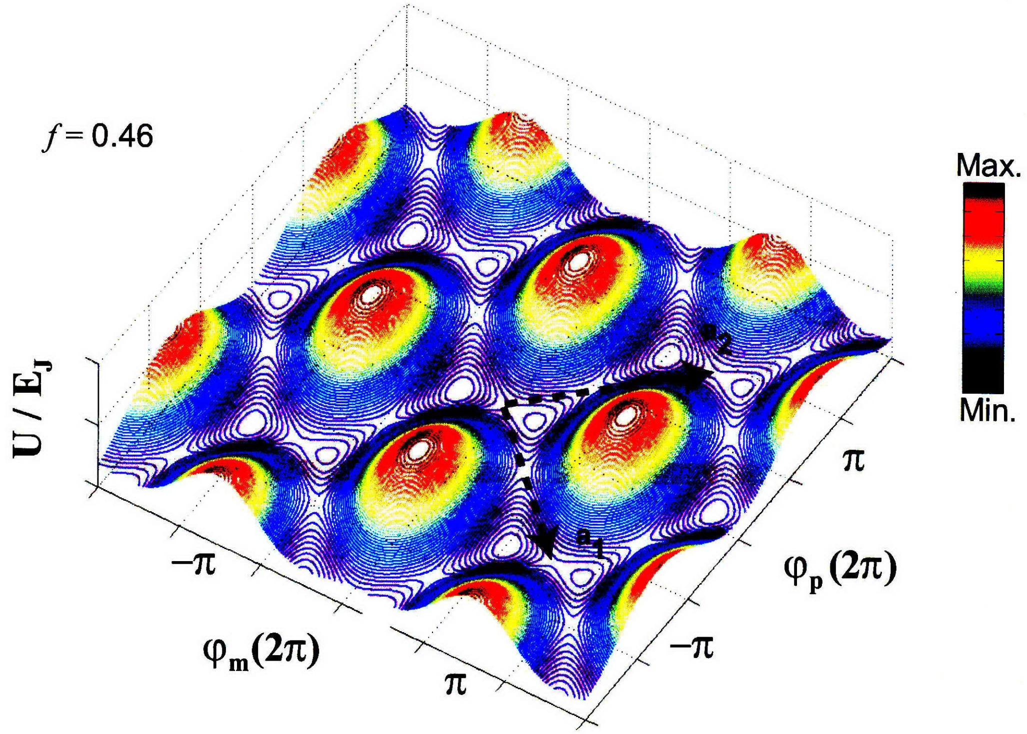

Figure 2-4: Contour plot of the 2D potential energy for the PC qubit at $f = 0.46$, far detuned from the symmetry point $f = 1/2$. The qubit sees an anisotropic 2D periodic potential, with lattice vectors $\mathbf{a_1}$ and $\mathbf{a_2}$. By designing for negligible inter-well tunneling, the potential can be viewed as a single double-well. When the transverse (φ_p direction) quantum modes of the 2D double-well can be ignored, the potential energy can be treated as a 1D double-well along the $\varphi_{\rm m}$ direction.

localized wavefunctions to create the entire system's wavefunction. The wavefunction over the entire 2D plane can be written as

$$\Psi = \begin{pmatrix} c_{\alpha_1}[\mathbf{R}_{00}] \\ c_{\alpha_2}[\mathbf{R}_{00}] \\ \dots \\ c_{\alpha_N}[\mathbf{R}_{00}] \\ c_{\alpha_1}[\mathbf{R}_{01}] \\ c_{\alpha_2}[\mathbf{R}_{01}] \\ \dots \end{pmatrix} \tag{2.8}$$

where α_1, α_2, etc., denote different localized wavefunctions, and $\mathbf{R}_{n_1 n_2}$, denotes different lattice sites written in terms of the basis $\mathbf{a}_1$ and $\mathbf{a}_2$ pictured in Fig. 2-4. Bloch's equation, $c_{\alpha_1}[\mathbf{R}_{n_1 n_2}] = \exp(i\mathbf{k} \cdot \mathbf{R}_{n_1 n_2}) c_{\alpha_1}[\mathbf{R}_{00}]$, allows one to solve the problem at just one lattice site, with the wavefunction

$$\Psi = \begin{pmatrix} c_{\alpha_1}[\mathbf{R}_{00}] \\ c_{\alpha_2}[\mathbf{R}_{00}] \\ \dots \\ c_{\alpha_N}[\mathbf{R}_{00}] \end{pmatrix} \tag{2.9}$$

The Schrödinger equation can then be written as

$$H_{ij}\Psi = E\Psi, \tag{2.10}$$

where

$$H_{\mathrm{ij}} = \sum_{\mathrm{n_1, n_2}} \langle \Psi_{\mathrm{i}}(\mathbf{R}_{00}) | \hat{H} | \Psi_{\mathrm{j}}(\mathbf{R}_{\mathrm{n_1 n_2}}) \rangle \exp(i\mathbf{k} \cdot \mathbf{R}_{\mathrm{n_1 n_2}}), \tag{2.11}$$

where $\hat{H}$ is the quantum Hamiltonian of the system, and the i,j labels denote different localized states. Note that in arriving to Eq. 2.10, it has been assumed that the localized states at adjacent lattice sites have negligible overlap.

For illustrative purposes, I will now consider for the localized basis only the ground

SHO states of each individual well of the double-well, call them $|0,\mathrm{L}\rangle$ and $|0,\mathrm{R}\rangle$. These uncoupled left and right well states, respectively, along with higher energy uncoupled well levels, are referred to as diabatic states. I will also take as the zero of energy the configuration when the two wells are aligned; i.e., when $f{=}1/2$. Finally, by considering only nearest neighbor interactions, Eq. 2.10 becomes

$$-\frac{1}{2}\begin{pmatrix} \varepsilon & -\Delta_{0,0}-\Delta_{\mathrm{out}}\exp^{i\mathbf{k}\cdot\mathbf{a_1}}-\Delta_{\mathrm{out}}\exp^{i\mathbf{k}\cdot\mathbf{a_2}} \\ -\Delta_{0,0}-\Delta_{\mathrm{out}}\exp^{-i\mathbf{k}\cdot\mathbf{a_1}}-\Delta_{\mathrm{out}}\exp^{-i\mathbf{k}\cdot\mathbf{a_2}} & -\varepsilon \end{pmatrix}\begin{pmatrix} c_{|0,\mathrm{L}\rangle} \\ c_{|0,\mathrm{R}\rangle} \end{pmatrix} = E\begin{pmatrix} c_{|0,\mathrm{L}\rangle} \\ c_{|0,\mathrm{R}\rangle} \end{pmatrix}, \quad (2.12)$$

where $\Delta_{0,0} \propto \exp^{-E_\mathrm{j}/E_\mathrm{c}}$ is related to the tunneling rate between the two sides of the double-well, Δ_{out} is related to the tunneling rate between adjacent lattice sites, where $\Delta_0/\Delta_{\mathrm{out}} \propto \exp^{\mathrm{E_j/E_c}}$, $\mathrm{E_c} = e^2/2\mathrm{C}$, $\varepsilon \simeq 2(\partial U/\partial f)(f-1/2) = \Phi_0 I_3(f-1/2)$, and I_3 is the current through the third junction, which is also the circulating current in the qubit [43]. In general, avoided crossings will be denoted as $\Delta_{q,q'}$, where q and q' are the energy levels, in the left and right well respectively, coupled by the specified avoided crossing. The quantity $f-1/2$ is known as the **flux detuning** and will be denoted as δf. As noted earlier, the qubit was designed to have a negligible inter-well tunneling rate Δ_{out}, via a large $\mathrm{E_j/E_c}$, approximately 400 here. In fact, this ratio is large enough so that the inter-well tunneling can be completely ignored. The Hamiltonian then reduces to

$$\mathrm{H} = -\frac{1}{2}\begin{pmatrix} \varepsilon & \Delta_{0,0} \\ \Delta_{0,0} & -\varepsilon \end{pmatrix} = -\frac{1}{2}(\varepsilon\sigma_z + \Delta_{0,0}\sigma_x), \quad (2.13)$$

where σ_z and σ_x are Pauli matrices defined in App. A.1. Eq. 2.13 represents a 2D problem, since the localized basis states are two-dimensional. The 2D nature of the PC qubit's Hamiltonian will become important in Ch. 5, but for now one can consider just a simple 1D double-well, by assuming complete symmetry with respect to the long axis of the double-well (the φ_m axis).

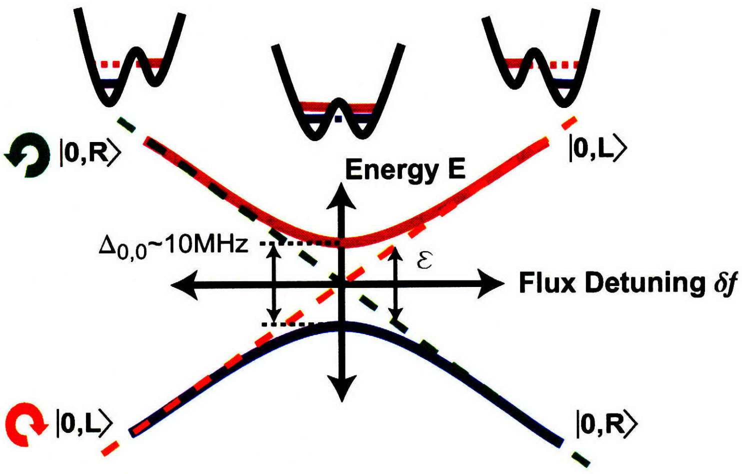

Figure 2-5: 1D, two-level representation of the PC qubit. The ground state energy of the double-well follows the solid blue curve, while the excited state energy follows the upper red curve. At $\delta f=0$, the double-well is symmetric and the eigenstates are symmetric and anti-symmetric combinations of the diabatic states $|0,\mathrm{L}\rangle$ and $|0,\mathrm{R}\rangle$. As flux is tuned away from $\delta f=0$, the double-well tilts and the eigenstates are just $|0,\mathrm{L}\rangle$ and $|0,\mathrm{R}\rangle$. The energies of the diabatic states are represented by dashed lines. If there were no coupling between wells, the eigenstates would always be the diabatic states. $|0,\mathrm{L}\rangle$ and $|0,\mathrm{R}\rangle$ correspond to opposite circulating currents in the qubit loop.

Fig. 2-5 diagrams the simplified two-level, 1D double-well system, and how it changes with flux detuning δf. At $\delta f=0$, the double-well is symmetric and the eigenstates are symmetric and anti-symmetric combinations of the two diabatic states $|0,\mathrm{L}\rangle$ and $|0,\mathrm{R}\rangle$. As one increases the flux from the degeneracy point, the double-well tilts and the eigenstates are now just the two diabatic states. The same thing happens as you tilt the wells the other direction, except the ordering of energy eigenstates flips.

The two-level system described in Eq. 2.13 has eigenvalues

$$E_{\pm} = \pm\frac{1}{2}\sqrt{\varepsilon^2 + \Delta_{0,0}^2} \tag{2.14}$$

with eigenstates given by

$$|\Psi_-\rangle = \cos\frac{\chi}{2}|0,\mathrm{R}\rangle + \sin\frac{\chi}{2}|0,\mathrm{L}\rangle \text{ and } |\Psi_+\rangle = -\sin\frac{\chi}{2}|0,\mathrm{R}\rangle + \cos\frac{\chi}{2}|0,\mathrm{L}\rangle \tag{2.15}$$

where $\chi \equiv \tan^{-1}(\frac{\Delta_{0,0}}{\varepsilon})$.

The diabatic states $|0, \mathrm{R}\rangle$ and $|0, \mathrm{L}\rangle$ (along with the higher energy diabatic states), correspond to counter-clockwise and clockwise circulating currents, respectively. This is easily seen by calculating the circulating current I_3 from the energy levels, and seeing that it is of opposite sign for the ground and excited states away from δf=0. The circulating current generated by the qubit eigenstates is the means by which the state of the PC qubit will be measured, via a magnetometer.

The main difference between this Hamiltonian and the one commonly seen in atomic physics or NMR, is that the σ_x coupling element is a constant that is always there, whereas in the other cases the coupling element typically arises when a microwave field is applied. With an adjustable σ_z term and a constant σ_x term, one can tune the eigenstates of the system, whereas without the constant σ_x term one would only be able to change the energy level spacing. Also note that applied magnetic fields, both DC and AC, enter the Hamiltonian solely along the z-axis, whereas in atomic physics and NMR, magnetic fields can couple into the system along any axis, though typically the AC field is along σ_x and the DC field is along the σ_z direction. This makes arbitrary quantum gate operations a bit more difficult to accomplish in the PC qubit (see attached paper [45] in App. B for a discussion of the challenges involved in implementing gate operations with the PC qubit). It is exactly this distinction however that will provide for some extremely interesting new physics in this thesis.

2.2 Theory of Measuring the Persistent Current Qubit

So the superconducting qubit has eigenstates with different magnetic fluxes. The most natural way to measure these states is with a DC Superconducting Quantum Interference Device (DC SQUID). This section will introduce the DC SQUID, and how it is used to measure the qubit state. I will begin by deriving the energy of the SQUID, and show how this allows one to use it as a magnetometer. I will consider

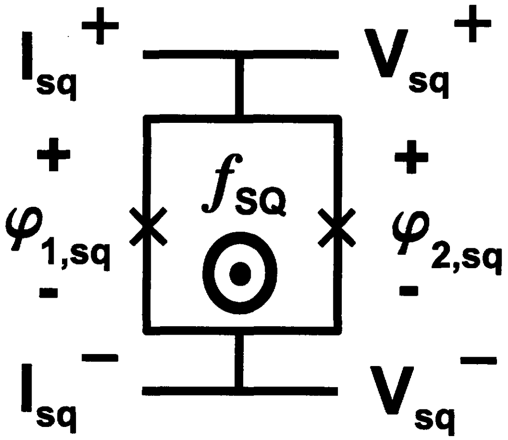

Figure 2-6: Schematic of the DC SQUID. The DC SQUID is a loop of superconducting wire interrupted by two Josephson junctions, with four leads attached, two used to pulse the SQUID and two for measuring the SQUID voltage after pulsing. f_{sq} is the applied magnetic flux piercing the SQUID loop, in units of a flux quantum Φ_0.

the most common way to use the DC SQUID to measure magnetic flux, and then describe a faster readout that will allow the study of quantum coherent phenomena. The effect of thermal noise on the SQUID will also be considered.

2.2.1 The DC SQUID as a magnetometer

A DC SQUID is simply a superconducting loop with two JJ's [42]. However, unlike the qubit, there will be four wires connected to the loop, two to apply a current I_{sq} to the SQUID, and two to measure the voltage V_{sq} across the SQUID. The DC SQUID is pictured in Fig. 2-6. Throughout this work it will be assumed that both junctions of the SQUID have the same $I_{c,sq}$ (and hence the same $E_{j,sq}$) and capacitance C_{sq}, with negligible self-inductance. The phase variables of junctions 1 and 2 will be denoted $\varphi_{1,sq}$ and $\varphi_{2,sq}$, respectively. From Kirchoff's current law, one knows that the current through the SQUID is just the sum of the currents due to each junction (Eq. 2.1)

$$I_{sq} = I_{c,sq}\sin(\varphi_{1,sq}) + I_{c,sq}\sin(\varphi_{2,sq}) \tag{2.16}$$

Just as was done for the qubit loop, one can show that the JJ phases are con-

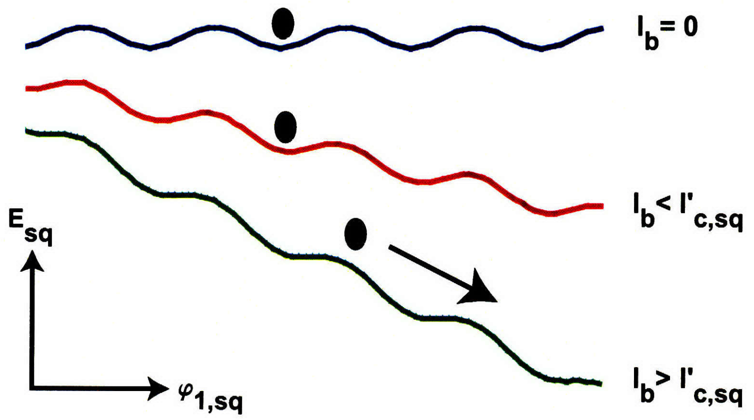

Figure 2-7: Switching measurement overview. The phase particle associated with the SQUID sits in a local minimum of the SQUID potential energy. As the bias current I_b is ramped, the SQUID potential energy tilts until the phase particle falls out of the local minimum, when I_b reaches $|I'_{c,sq}|$. More realistically, thermal activation and quantum tunneling cause escape from the local minima to occur at a distribution of currents about $|I'_{c,sq}|$.

strained by the magnetic flux threading the loop such that

$$\varphi_{2,sq} - \varphi_{1,sq} = 2\pi f_{sq} \tag{2.17}$$

where f_{sq} is the applied flux piercing the SQUID loop in units of Φ_0. Combining Eqs. 2.16 and 2.17, one finds that the current through the SQUID is

$$I_{sq} = 2I_{c,sq}\cos(\pi f_{sq})\sin(\varphi_{1,sq} + \pi f_{sq}) \tag{2.18}$$

This equation has the same form as the single junction case (Eq. 2.1), so one can immediately write down the energy of the SQUID E_{sq} from Eq. 2.3

$$E_{sq} = \frac{1}{2}C'_{sq}V_{sq}^2 + E'_{j,sq}(1 - \cos(\varphi'_{1,sq})) \tag{2.19}$$

where $C'_{sq} = 2C_{sq}$, $V_{sq} = \frac{\Phi_0\dot{\varphi}'_{1,sq}}{2\pi}$, $E'_{j,sq} = \frac{\Phi_0 I'_{c,sq}}{2\pi}$, $I'_{c,sq} = 2I_{c,sq}\cos(\pi f_{sq})$, and $\varphi'_{1,sq} = \varphi_{1,sq} + \pi f_{sq}$.

One now adds a current source I_b to the SQUID to make it a working magnetometer. The current source will act as a force on the phase particle [51], giving an extra term in the potential energy of the form $I_b(\varphi_{1,sq} + \pi f_{sq})$. Dropping the constant phase offset due to the flux penetrating the loop, and the constant energy term, the SQUID energy then becomes

$$E_{sq} = \frac{1}{2} M_{sq} \dot{\varphi}_{1,sq}^2 - \frac{\Phi_0 I_b}{2\pi} \varphi_{1,sq} - \frac{\Phi_0 I'_{c,sq}}{2\pi} \cos \varphi_{1,sq}, \tag{2.20}$$

where $M_{sq} = C'_{sq}(\frac{\Phi_0}{2\pi})^2$. This is just the energy of a particle in a cosine potential that is tilted by the bias current. When I_b reaches $|I'_{c,sq}|$, the particle will escape from a local minimum and start to "roll" down the tilted cosine potential, generating a voltage due to its changing phase. A schematic of the switching process is seen in Fig. 2-7. The way this is used as a magnetometer is that the current $I'_{c,sq}$ at which escape, and a non-zero voltage occur, depends on the magnetic flux f_{sq} seen by the SQUID. Mapping out $I'_{c,sq}$ as a function of flux allows one to then apply an unknown magnetic flux, and then go back to the original $I'_{c,sq}$ vs. f_{sq} scan and deduce the unknown magnetic flux from $I'_{c,sq}$.

The way the SQUID switching measurement is most commonly implemented is by using a triangle current waveform for ramping the current, with a peak value above the maximal critical current $2I_{c,sq}$ of the SQUID, and recording the time τ_{sw} it takes from the beginning of the ramp for a voltage to appear across the SQUID. From τ_{sw} and the ramp rate dI/dt, one can calculate the switching current I_{sw}, the point the SQUID phase particle escapes from the well. I_{sw} though is not exactly $I'_{c,sq}$, due to thermal activation or quantum tunneling of the phase particle out of the local minima (I consider the effect of thermal activation on $I'_{c,sq}$ in Ch. 2.2.2). To account for the fluctuating $I'_{c,sq}$, one must repeat the ramping measurement many times to find the full I_{sw} distribution. The measurement process is summarized in Fig. 2-8.

Fig. 2-9 shows the measured switching current I_{sw} as a function of f_{sq}. One clearly sees the expected cosine dependence of $I_{sw} \approx I'_{c,sq}$ on f_{sq}, along with the width of I_{sw} due to noise processes and quantum tunneling. There are two other strong features

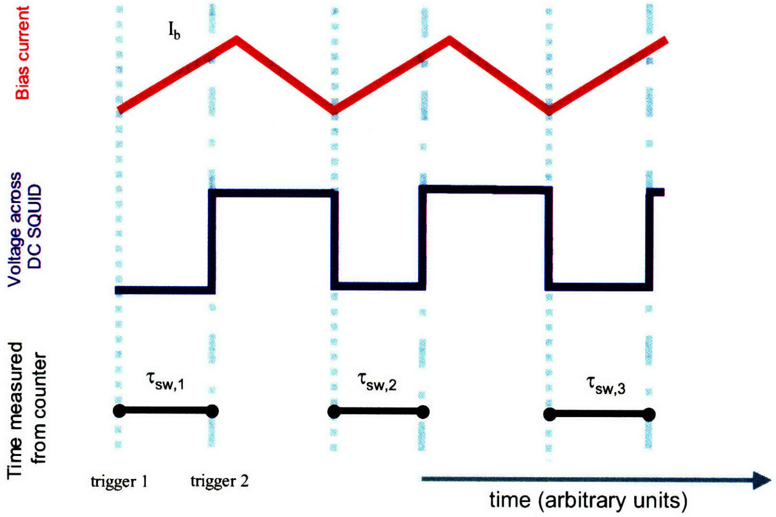

Figure 2-8: Timing of switching measurement. $I'_{c,sq}$ is measured by ramping I_b significantly higher than the maximum of $I'_{c,sq}$, and by measuring the time from the beginning of the ramp to the appearance of a non-zero voltage across the SQUID, the current I_{sw} at which the SQUID phase particle escapes from the well is measured. To fully account for a fluctuating $I'_{c,sq}$, the switching measurement is repeated many times.

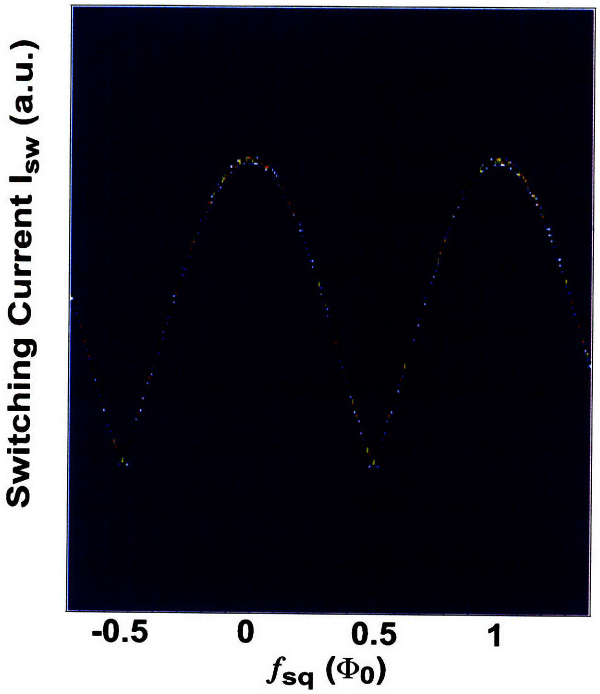

Figure 2-9: The measured SQUID switching current I_{sw} as a function of f_{sq}. Note the expected cosine dependence of $I_{sw} \approx I'_{c,sq}$ on f_{sq}, along with the width of I_{sw} due to noise processes and quantum tunneling. Data shown here was taken at 15mK.

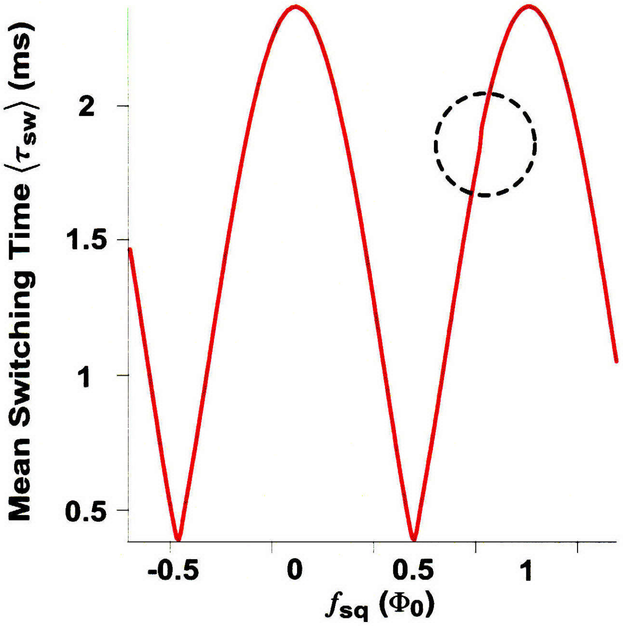

Figure 2-10: Mean DC SQUID switching time $\langle \tau_{\mathrm{sw}} \rangle$ as a function of flux in the presence of the qubit (mean of data in Fig. 2-9). The step due to the qubit is visible in the circled region. Data shown here was taken at 15mK.

in Fig. 2-9. The first is the variation of the width of I_{sw} with f_{sq}, which is maximal for high switching currents. This is due to the changing barrier height with I_b that the SQUID phase particle must cross to escape (see Ch. 2.2.2), combined with a longer time for escape to occur during the ramp for higher switching currents. The second strong feature is the double-valued switching currents at the minima in I_{sw}. This feature is due to the self-inductance of the SQUID, which has been ignored here for clarity of presentation. In the limit of large self-inductance, the potential energy of the SQUID will be an infinite series of parabolas, centered at integer values of Φ_0 [42]. It is this multi-valued potential energy which leads to multiple switching currents.

When the qubit is placed inside the DC SQUID, f_{sq} becomes $f_{\mathrm{sq}} + \mathrm{M}I_3/\Phi_0$, where I_3 is the circulating current generated by the qubit; i.e., the current through the smaller junction, and M is the mutual inductance between the SQUID and the qubit. On each side of the avoided crossing the ground states have opposite circulating currents, changing the flux seen by the SQUID by $\approx \pm\, 3\, \mathrm{m}\Phi_0$. This causes a step-like structure near f=1/2, which is hard to see when plotting the full switching distribution

(Fig. 2-9), but is clearly visible when plotting the mean of the switching distribution (Fig. 2-10). A zoom-in of the step-like structure is seen in Fig. 2-11. The white dashed line represents $\mathrm{I_{sw}}$ when there is no qubit, the green dashed line represents $\mathrm{I_{sw}}$ when the qubit has a counter-clockwise circulating current, in this case when the qubit is in the ground state when $\delta f > 0$, and the red dashed line represents $\mathrm{I_{sw}}$ when the qubit has a clockwise circulating current, in this case when the qubit is in the ground state when $\delta f < 0$. When, for instance, the ground state to the left of $f = 1/2$ is driven to the excited state, τ_{sw} will be suppressed by approximately 40 μs. To be able to distinguish the two circulating current states, the switching histogram must be narrower than the separation between the two switching current levels.

There is indeed a "double" step-like structure seen in Fig. 2-11. The reason for the extra step on the left is that while the SQUID is ramped, a circulating current in the SQUID (self-inductance of the SQUID has been neglected here for clarity) tilts the qubit potential, which can cause population transfer from the left well to the right well via quantum tunneling [47]. As will be seen in Ch. 2.2.3, a modified readout performed orders of magnitude faster than the one discussed here will remove this resonant tunneling feature from the readout.

One might be wondering at this point how quantum measurement theory affects the above discussion; i.e., what happens when you measure a superposition of circulating currents? Shouldn't the superposition states at $f = 1/2$ give a bi-modal distribution due to the projective nature of quantum measurement? The textbook projective measurement in fact only comes about when the system and measurement apparatus stay completely entangled for the duration of the measurement; i.e., the joint qubit-SQUID system can never be written as a product state before the joint wavefunction collapses. What is indeed being done with the SQUID in these experiments is an expectation value measurement, where the average of the circulating currents is measured, due to a loss of entanglement between the qubit and the SQUID while $\mathrm{I_b}$ is ramped. It can be shown that entanglement is not expected to last throughout the measurement in systems with design parameters like the ones for the device used here [46]. Let me now turn to the switching current histogram due

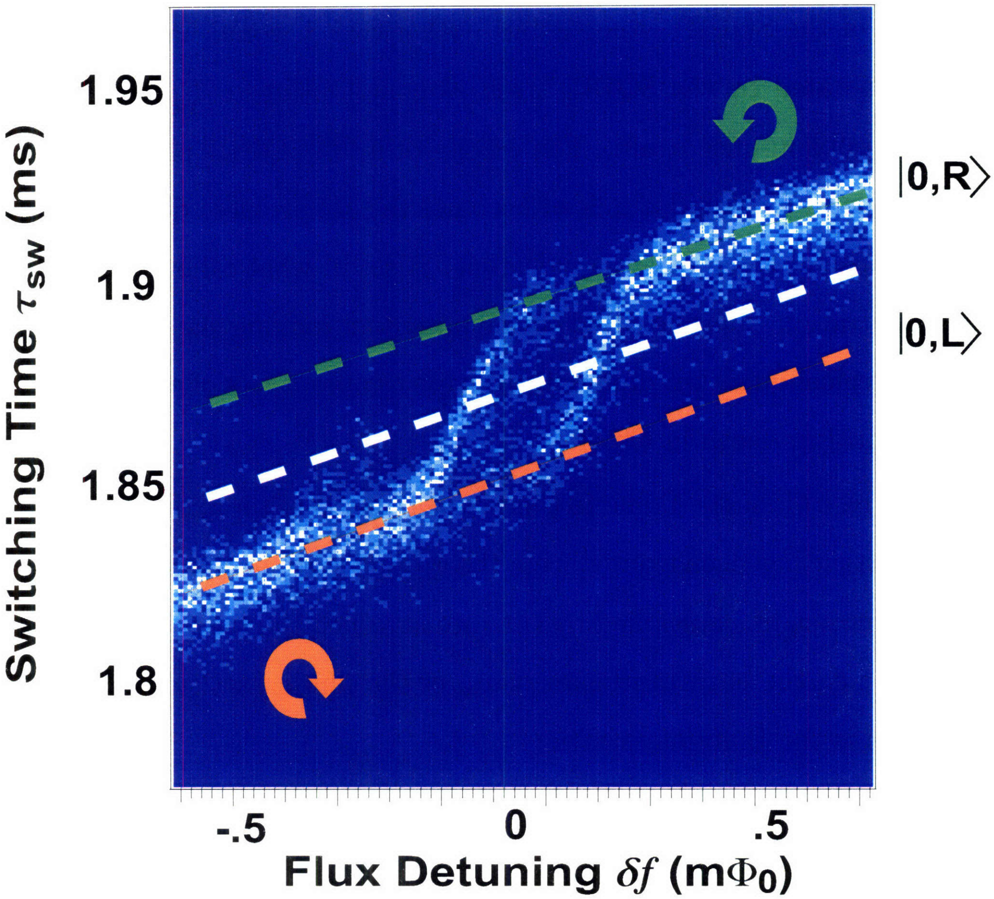

Figure 2-11: DC SQUID switching time τ_{sw} as a function of flux near the qubit step. The full switching distribution of the circled region in Fig. 2-10 is shown. The circulating currents due to the qubit increase or decrease the flux seen by the SQUID, altering I_{sw} of the SQUID, creating a step-like structure in I_{sw} that can be used to distinguish the qubit eigenstates. The right-most step is due to the two-level qubit, whereas the left step is due to resonant tunneling during the measurement ramp (see text). Data shown here was taken at 15mK.

to thermal activation.

2.2.2 The Switching Current Distribution

In the derivation of a 1D potential for the SQUID, I have assumed that the self-inductance of the SQUID is negligible. Otherwise, I would have had to account for the flux generated by the SQUID itself as contributing to f_{sq}, turning the problem into a 2D problem once again. The escape of a 2D SQUID phase particle has been studied at length [52], and it indeed becomes the 1D problem derived above when the self-inductance of the SQUID is negligible. Also, in what follows I will only consider thermal activation from the tilted cosine potential, making the discussion most useful above the typical quantum-dominated escape temperatures of $\approx$ 50mK, a regime that will be studied in depth in Ch. 4.

The 1D rate of escape Γ due to thermal activation is approximately the probability that the particle has been excited from the ground state to the state with energy equal to the barrier height, multiplied by the rate at which the particle attempts to get out of the well; i.e., the natural frequency ω_{sq} of the phase particle in the well [48]. The former term is the Boltzmann ratio:

$$\frac{\exp(-\mathrm{E}_{\text{top of well}}/\mathrm{kT})}{\exp(-E_{\text{bottom of well}}/\mathrm{kT})} = \exp(-\Delta\mathrm{U}/\mathrm{kT}), \tag{2.21}$$

where ΔU(see Fig. 2-12) is the barrier the phase particle must overcome to enter the finite voltage state. From Ref. [49] one finds the rate

$$\Gamma = a(\omega/2\pi)\exp(-\Delta\mathrm{U}/\mathrm{kT}), \tag{2.22}$$

where a is a correction that depends on the amount of damping in the equivalent single junction. For a nice summary of escape rates for the different damping limits, and for both quantum and classical limits, see the paper by Garg [50]. With the goal of fitting experimental escape-rate data to this expression in mind, one first needs to find the functional form for ΔU and ω_{sq}.

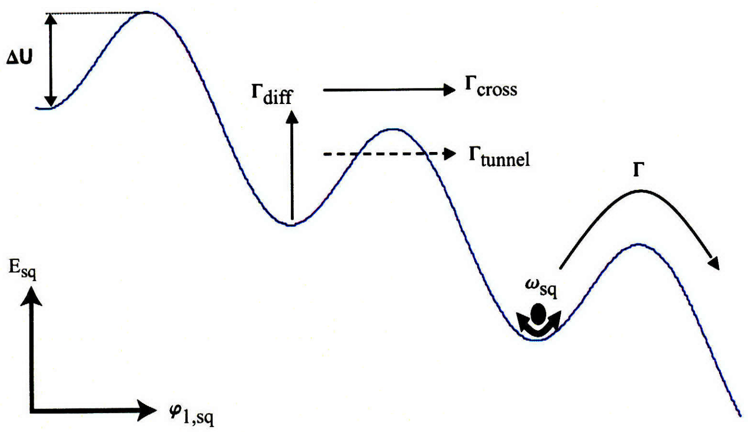

Figure 2-12: Thermal activation in a DC SQUID. Switching of the SQUID can occur before $I_b = I'_{c,sq}$ due to thermal excitation of the phase particle out of a local minimum. The rate of escape Γ is in general due to classical activation and quantum tunneling processes, Γ_{cross} and Γ_{tunnel}, but here I ingore quantum tunneling, so that $\Gamma = \Gamma_{cross}$. Γ_{cross} is related to the height of the barrier presented to the SQUID phase particle, as well as the rate of escape attempts, determined by ΔU and ω_{sq} respectively.

A potential minimum and the closest maximum to its right, labeled $\varphi_{1,sq,min}$ and $\varphi_{1,sq,max}$ respectively (see Fig. 2-12), can be found by taking the 1st derivative of U and setting it equal to zero, upon which one obtains the condition

$$I'_{c,sq}\sin(\varphi_{1,sq,min}) = I_b \tag{2.23}$$

and, so,

$$\varphi_{1,sq,min} = \arcsin(\frac{I_b}{I'_{c,sq}}) \text{ and } \varphi_{1,sq,max} = -\arcsin(\frac{I_b}{I'_{c,sq}}) + \pi. \tag{2.24}$$

The natural frequency ω_{sq} as a function of I_b can now be calculated by setting the second derivative of U (evaluated at the minimum of the metastable well) equal to $M_{sq}\omega_{sq}^2$, where $M_{sq} = \left(\frac{\Phi_0{}^2}{(2\pi)^2}\right) C_{sq}$ [51]:

$$\frac{d^2U}{d\varphi^2} = \min_{\varphi_{1,sq}}[-\cos(\varphi)] = \frac{\Phi_0 I'_{c,sq}}{2\pi}\sqrt{1-\left(\frac{I_b}{I'_{c,sq}}\right)^2} \equiv M_{sq}\omega_{sq}^2,$$

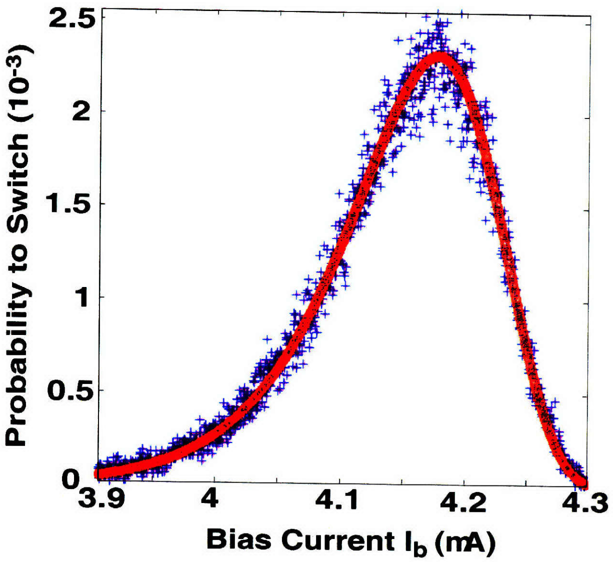

Figure 2-13: Histogram of DC SQUID switching current at a single flux bias. The SQUID was biased at a maximum of I_{sw} and the data was taken at 2K. Data is shown as blue + signs, and the theoretical fit is shown as a solid red line.

and so,

$$\omega_{sq} = \left(\frac{2\pi I'_{c,sq}}{\Phi_0 C}\right)^{1/2}\left[1-\left(\frac{I_b}{I'_{c,sq}}\right)^2\right]^{1/4}. \tag{2.25}$$

To find the barrier ΔU over which the phase particle must be activated to observe a switching event, one subtracts the potential energy at its minimum from the potential energy at its adjacent maximum:

$$\Delta U = \frac{\Phi_0 I'_{c,sq}}{2\pi}\left(\frac{I_b}{I'_{c,sq}}\left[2\sin^{-1}\left(\frac{I_b}{I'_{c,sq}}\right)-\pi\right]+2\cos\left[\sin^{-1}\left(\frac{I_b}{I'_{c,sq}}\right)\right)\right]. \tag{2.26}$$

To fit the histogram, one finally needs an expression for the histogram as a function of the escape rate. By considering the probability of switching in a small interval of time dt, one finds

$$P(I_b) = \frac{1}{\Gamma dI/dt}\left[1-\int_0^{I_b} P(i)di\right] \tag{2.27}$$

where $P(i)$ is the probability of switching at bias current i and dI/dt is the ramp rate of the bias current I_b.

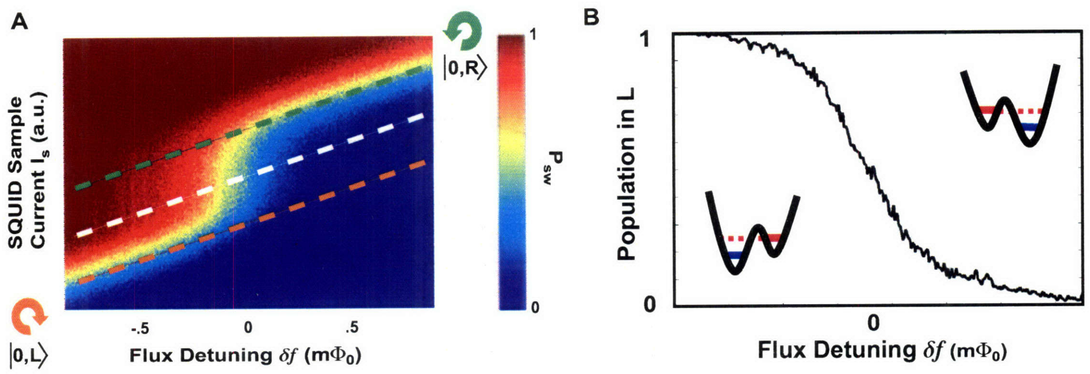

Figure 2-14: (**A**) Rapid readout cumulative histogram of DC SQUID switching current as a function of flux in the presence of the qubit. The colorscale shows the cumulative switching probability P_{sw}. The circulating currents due to the qubit increase or decrease the flux seen by the SQUID, altering I_{sw} of the SQUID, creating a step-like structure in P_{sw}. Data shown here was taken at 15mK. (**B**) A single slice taken along the center dashed line in (A) gives $|0, L\rangle$ and $|0, R\rangle$ populations as a function of flux detuning.

Fig. 2-13 shows the fit obtained with $T = 2K$, $C_{sq} = 3pF$, and $I_{c,sq} = 5.5\mu A$. These values agree well with expectations from thermometry (1.9K) and device designs (2pF and $5.5\mu A$).

2.2.3 Rapid Readout

Experimentally it takes roughly $20\mu s$ for the voltage across the SQUID to develop when it switches, due to the 50kHz bandwidth of the bias-T the SQUID readout line is attached to (see Ch. 2.3.2). To do the switching time measurement discussed earlier, one must go significantly slower than this for the voltage development to look instantaneous. However, running the experiment at say 100Hz would not allow one to see effects that decay away on the microsecond timescale or faster, e.g., Rabi oscillations. To have rapid ramps, on the order of nanoseconds, one must rely on simply noting whether a switching event has occurred or not during the ramp, and repeat the experiment many times to yield the cumulative switching probability P_{sw} for a given ramp height. Note though, one must now repeat the ensemble measurement at all the ramp heights necessary to find the full cumulative switching distribution

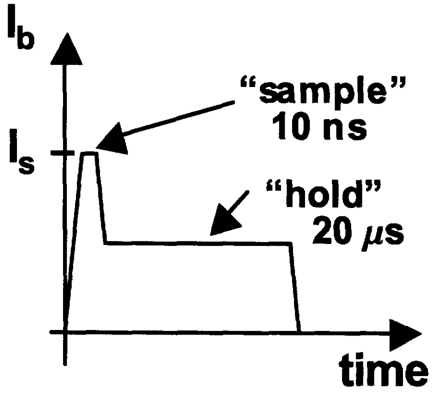

Figure 2-15: Rapid readout pulse. The SQUID is now ramped in 10ns, losing the ability to distinguish exactly when the SQUID switches. One now records a cumulative switching history of the qubit by repeating the ensemble measurement at each pulse height I_s.

at a given *f*. This is in contrast to the timed SQUID measurement discussed earlier, where one ramped the current above the maximum possible switching current, and found the entire switching distribution with one set of ensemble measurements.

The qubit step measured via the rapid readout is seen in Fig. 2-14. Instead of using a triangle waveform to ramp the SQUID, the pulse shape seen in Fig. 2-15 is now used. The sample part of the pulse provides the bias current to the SQUID, while the hold part of the pulse allows a DC voltage to be held across the SQUID in the case of switching. Though the ramp is only 5ns, and the hold only 20μs, one cannot repeat the readout at a rate faster than 10kHz, so that the qubit has a chance to relax to the ground state after each measurement. To make the measurements less time consuming, I will in fact only ramp the current over the center line pictured in Fig. 2-14, since all the information about the qubit state is contained along that line. Notice also the lack of a "double" step (Fig. 2-11) due to quantum tunneling during the rapid measurement (Fig. 2-14), since the ramp now happens so quickly.

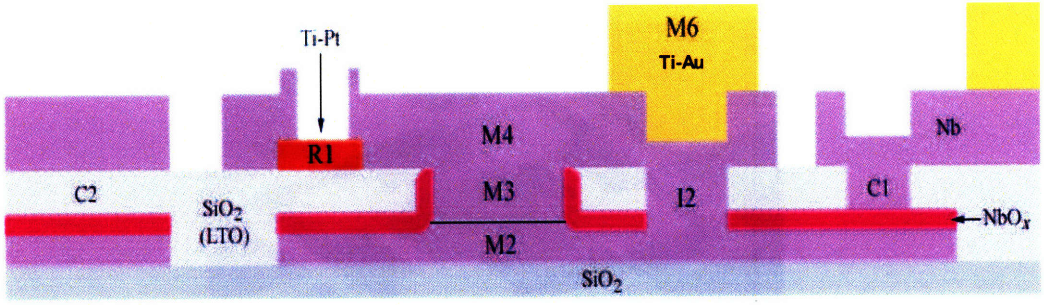

Figure 2-16: Summary of fabrication layers in device. The qubit and surrounding SQUID circuitry are made with a fully-planarized niobium trilayer process and optical lithography.

2.3 Implementation

I will now summarize the process used to create the PC qubit and SQUID circuitry, which has previously been thoroughly explained by Daniel Nakada, who made the device and helped develop the fabrication scheme for this doctoral thesis [53]. I will also describe the setup used for experimentation on the qubit, which was mostly in place before I used it [54].

2.3.1 Device Fabrication and Parameters

The device used for all experiments was fabricated at Lincoln Laboratory using a fully-planarized niobium trilayer process and optical lithography. Fig. 2-16 provides a brief overview of the fabrication process. Let me just focus in Fig. 2-16 on the center section where one sees M2, M3, and M4, which form a single Josephson junction. The process begins with a thermally oxidized Si wafer, and upon that is grown the trilayer of Nb, Al/AlO$_x$, and Nb. The pillars that form the cross section of the junctions are then made with 350-nm I-line lithography. Photoresist is spun on and the mask defines what M3 portions will not be etched away. To help protect the pillars against the next etch of M2, a Niobium Pentoxide (Nb_2O_5) layer is grown via anodization. The M2 layer is then defined with lithography and etched away. Silicon dioxide is then laid everywhere and is planarized. One then lays down the 2nd wiring layer M4,

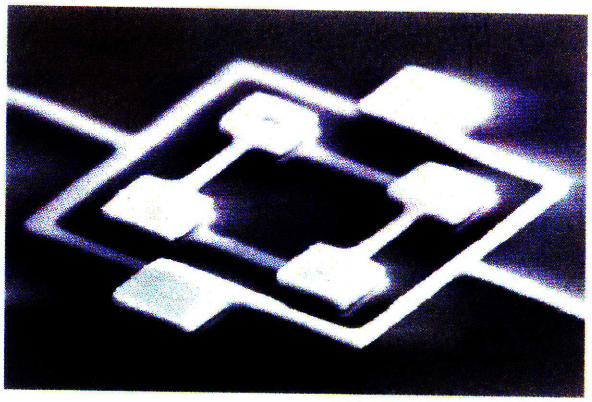

Figure 2-17: SEM image of a PC qubit. The inner loop is the qubit, with three JJ's and one via to connect the different fabrication layers (upper right corner). The outer loop is the measurement SQUID, with 2 JJ's and two leads for measurement.

and uses lithography once again to define its structure before etching.

The device used here has a critical current density $J_c \approx 160\,\mathrm{A/cm^2}$, and the characteristic Josephson and charging energies are $E_J \approx (2\pi\hbar)300\,\mathrm{GHz}$ and $E_C \approx (2\pi\hbar)0.65\,\mathrm{GHz}$ respectively ($E_C = e^2/2C$). The ratio of the qubit JJ areas is $\alpha \approx 0.84$, with $0.42\mu m^2$ cross-section larger JJ's, and $\Delta_{0,0} \approx (2\pi\hbar)10\,\mathrm{MHz}$ (see Ch. 3 for characteristic decoherence times and Ch. 5 for a complete energy level characterization.) The qubit loop area is $16 \times 16\ \mu m^2$, and its self inductance is $L_q \approx 30$ pH. The SQUID Josephson junctions each have a cross-section of $1.1\mu m^2$. The SQUID loop area is $20 \times 20\ \mu m^2$, and its self inductance is $L_S \approx 30$ pH. The SQUID junctions were shunted with 2pF on-chip capacitors. The mutual coupling between the qubit and the SQUID is $M \approx 25$ pH. Finally, the widths of the M2 and M4 wiring layers are $0.8\mu m$ and $1.5\mu m$ respectively, with a thickness of 200nm. Note that for Nb the penetration depth λ_0 at zero temperature is 85nm, the critical temperature T_c=9.25K, and the energy gap Δ_0=1.5meV. An SEM image of a PC qubit can be seen in Fig. 2-17.

2.3.2 Experimental Setup

All experiments were performed in an Oxford Kelvinox 400 dilution refrigerator. The base temperature for the experiments was typically 15mK. Four layers of cryoperm-10 μ-metal shielding were installed in the Kelvinox to provide magnetic shielding.

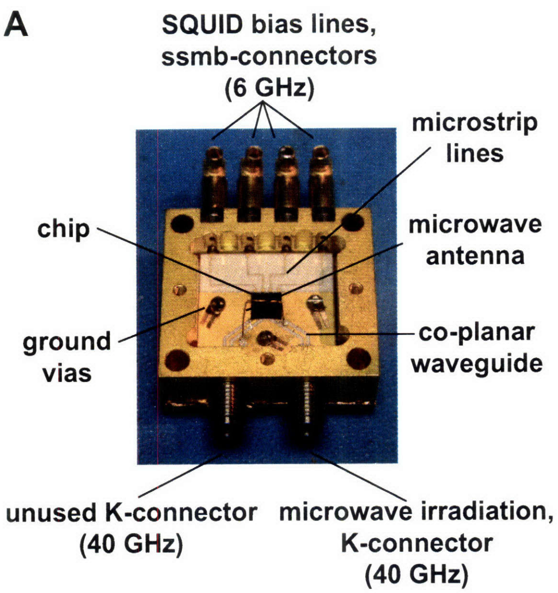

Figure 2-18: Microwave package for device. (**A**) The qubit and DC SQUID chip is mounted at the center of the package. Readout electronics are connected to the SQUID using 4 ssmb connectors, via microstrip lines and wirebonds, and RF microwaves are applied to the qubit via a small loop connected to a co-planar waveguide, which is connected to the K-connector at the bottom right. (**B**) DC magnetic flux is applied to the qubit via a small solenoid in the shape of a bobbin, that is mounted on the the bottom of the lid that seals the package, and sits directly above the qubit when the package is closed.

The qubit and surrounding SQUID circuit are on a 5 x 5 mm^2 chip, which is mounted in a closed microwave package, as seen in Fig. 2-18. The package is made of oxygen-free high conductivity Cu and then Au-plated. The chip itself is attached directly to the package, within a small cutout of the alumina substrate used for external wiring (Fig. 2-18A). Four ssmb panel mounts on the package are used for the SQUID readout. The ssmb lines connect to the chip via microstrip lines, which are attached to the SQUID via wirebonds. One of two K-connectors is used for radio frequency (RF) microwave irradiation of the qubit. The connector is attached directly to a co-planar waveguide, and a small loop of wire (~1cm long) connected from the waveguide centerline to ground, in the vicinity of the qubit, is used as an antenna. A niobium wire coil is mounted to the lid so that it sits directly above the qubit when the package is closed(Fig. 2-18B). This coil is used to provide the DC magnetic field.

The package is placed within an aluminum can to shield it from magnetic flux noise as well as 50mK blackbody radiation, and is thermally anchored to the mixing chamber (see Fig. 2-19).

The slow SQUID readout current and voltage lines utilize a Constantan Nomax loom with 24-twisted pairs, that goes to an RC filter bank (50kHz cutoff) at the 1K pot. The loom is then thermally anchored at every stage, until it breaks out into a D-sub connector at the mixing chamber. From the D-sub the SQUID current and voltage pairs split to two bias-T's, whose outputs subsequently go through stainless steel powder filters (acting as 1GHz low-pass filters) and then resistor boxes (to increase the impedance seen by the SQUID and hence lower the current noise it sees), via Cu-Cu coax on the way to the package. The bias-T's allow for the rapid readout lines to share the powder filters, resistor boxes, and package connections. The rapid readout voltage line was never implemented, as it would require a cryogenic amplifier, and so the RF input of that bias-T is just terminated with 50Ω.

The rapid SQUID readout current line and RF microwave line are made of 3 types of semirigid coaxial cables. Ag plated BeCu inner with stainless steel (SS) outer is used from room temperature to the 1K pot, SS inner with SS outer coax is used from the 1K pot to the mixing chamber, and Cu inner with Cu outer coax is used from the mixing chamber to the package. This setup minimizes heat transfer in the first leg while providing decent electrical conductivity, maximizes thermal isolation in the second leg at a cost of poor electrical conductivity, and maximizes electrical and thermal conductivity in the final leg. Each line is also attenuated at the 1K pot (40dB on SQUID line and 10dB on microwave line) and mixing chamber (10dB on SQUID line and 6dB on microwave line), for thermalization of the inner coax conductor and for reduction of Johnson-Nyquist noise produced at higher temperatures. The SQUID line is additionally connected to the bias-T shared with the slow SQUID current line, before the bias-T output is connected via Cu-Cu coax to a stainless steel powder filter and a resistor box that are located below the mixing chamber. Thermal anchoring of the outer conductors of these lines are also performed at 4K, still, and 50mK stages.

The NbTi DC magnetic flux line is filtered at the 1K pot by 100Ω resistors, and

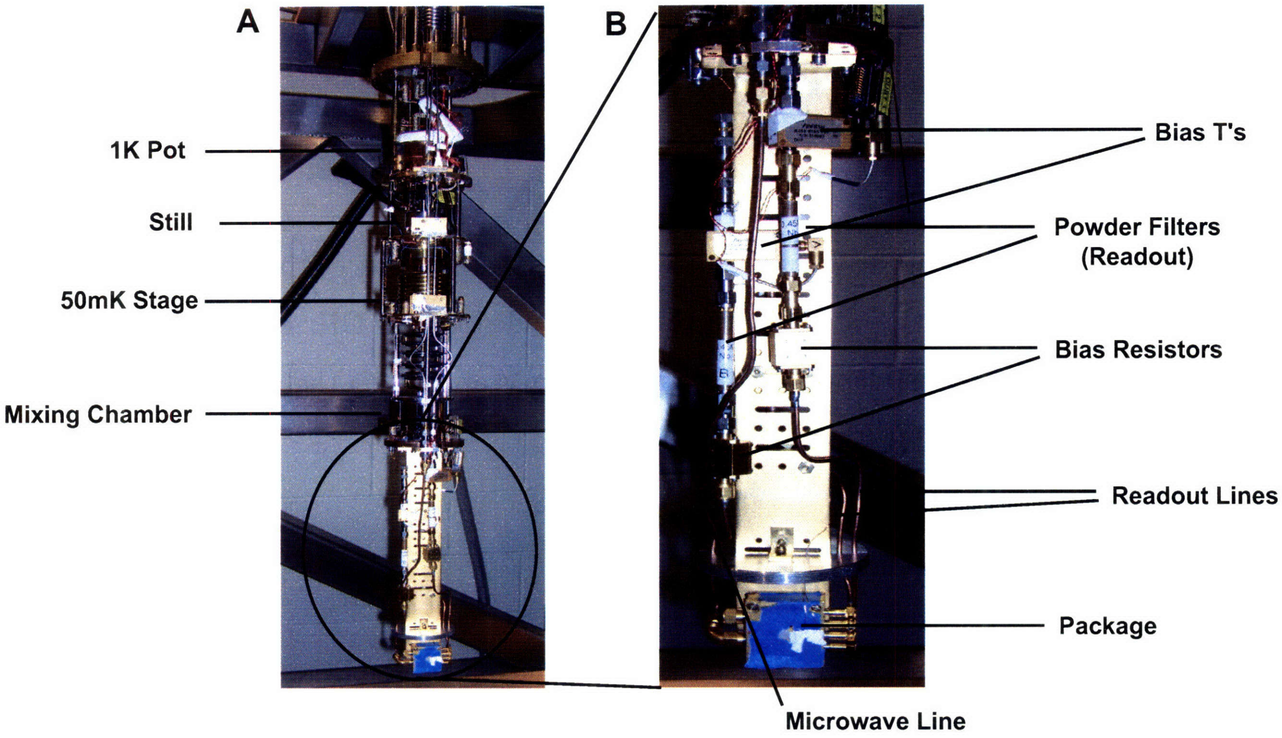

Figure 2-19: Picture of dilution refrigerator insert. (**A**) The entire dilution refrigerator insert is shown. The 1K pot, still, 50mK, and mixing chambers stages are labeled. (**B**) A zoom-in of the insert below the mixing chamber. One sees the bias-T's, powder filters, and resistor boxes for the readout lines, along with the microwave line. Not pictured is the powder filter for the magnet line, which is on the back of the probe.

then thermally anchored at every stage before passing through a powder filter below the mixing chamber, just before it reaches the DC flux solenoid mounted on the package lid.

Outside the refrigerator, the SQUID voltage line goes to a low-noise AD624 battery powered instrumentation amplifier. An Agilent 53132A Universal Counter is then used to record the time between the start of a triangle ramp and switching (slow measurement), or the total number of switches within an allotted gate time (rapid measurement). The slow SQUID current ramp is performed with an Agilent 33250A Arbitrary Waveform Generator, which passes through a 100kΩ bias resistor before being optically isolated using a Burr-Brown ISO100 device. The rapid SQUID current line is attached directly to the 33250A. The microwave generators used throughout this work are the Agilent E8257C PSG Analog Signal Generators. At times the SRS

DG535 Four Channel Digital Delay/Pulse Generator was also used as a trigger for experiment timing. Finally, the DC magnetic flux bias is provided by a Yokogawa 7651 Programmable DC Source, which passes through a 10kΩ resistor on the way to the refrigerator.

In the setup just described, 1 μA of current applied to the magnet coil produced .58 mΦ_0 in the qubit loop, which corresponded to 1.67 GHz energy splitting between the two-level model diabatic states. 12.2 mV applied to the microwave antenna corresponded to 1 mΦ_0 in the qubit loop.

2.4 Summary

In this chapter I have reviewed the basic principles of the PC qubit, how it is measured, and how experiments on the PC qubit are experimentally realized. The discussion began with the derivation of the PC qubit Hamiltonian of the PC qubit, which required a review of Josephson junctions. While the full Hamiltonian was numerically solved, I focused on the analytic solution of the lowest two eigenstates of the qubit, which create an ideal two-level quantum system. From there I reviewed magnetic flux measurements with a DC SQUID, accounting for thermal noise with a simple escape model. A faster version of the standard (slower) DC SQUID readout was then introduced. The rapid readout will be used for the remainder of this thesis because it allows for the study of rapidly decaying quantum coherent phenomena. I finally summarized the lithographic technique used to create the qubit/SQUID device, along with the experimental configuration used to study the qubit.

Chapter 3

Large Amplitude Driving with a Single Avoided Crossing: Quasiclassical Coherence

In this chapter I will present a new coherent quasiclassical regime of the strongly driven PC qubit. Thus far I have not considered the effects of driving the PC qubit with microwave radiation, and as such I will begin the chapter with a discussion of previous work in the strongly driven qubit, with a review of the necessary theoretical concepts. I will then present the new quasiclassical regime, along with a new perturbative theory that is used to explain it. All of the discussion in this chapter will involve only a single avoided crossing, with the qubit behaving like a two-level system (Fig. 2-5). In Ch. 4 and Ch. 5 I will discuss the implications of the full energy level spectrum of the qubit (Fig. 2-3), which has many more than 2 energy levels and 1 avoided crossing.

3.1 Introduction

A common experiment used to study the coherence of a quantum system is Rabi oscillations [55], where population coherently oscillates between two energy levels with energy spacing ΔE due to an oscillating applied field. In typical Rabi oscillations,

$\hbar\omega=\Delta E$, where ω is the driving-field angular frequency, and the driving amplitude A (parameterized in units of energy), is much smaller than ΔE. The population of the two levels then oscillates at a Rabi frequency $\omega_{\rm R} = {\rm A}/2\hbar \ll \Delta E/\hbar = \omega$. By watching the decay of these oscillations in time, one can study the decoherence of the quantum system. Rabi oscillations have been studied at length in superconducting Josephson devices [40, 56, 57, 58, 59, 60, 61, 62].

In a system such as a PC qubit, coherent quantum dynamics can also be investigated at driving frequencies much less than ΔE, and at strong driving amplitudes $\mathrm{A} \approx \Delta E \gg \hbar\omega$. In this case, the transitions occur via the Landau-Zener (LZ) process at a level crossing [63, 64]. Acting in an analogous way to a coherent beamsplitter in optics, LZ transitions between the energy levels create a quantum superposition of the ground and excited states. Each period of the microwave drive will induce two sequential LZ transitions, with a phase accumulated between them, inducing quantum mechanical interference. The latter leads to Stueckelberg oscillations [65], analogous to the interference patterns seen in a Mach-Zehnder interferometer [66, 67, 68]. Mach-Zehnder-type interference is a signature of temporal coherence complementary to Rabi oscillations, the time between sequential LZ transitions clocking the dynamics similarly to Rabi pulse width.

Under such strong driving, the PC qubit will exhibit multiphoton resonances, whereby transitions from the ground state to the excited state occur only at flux detunings such that $\Delta E = \mathrm{n}\hbar\omega$. In this chapter I will consider two limits of this strongly driven regime of the PC qubit. I will begin with a discussion of the case where resonances do not overlap, where one can analytically solve for the dynamics of the qubit due to the highly separated resonances [66]. I will then consider the case of overlapping resonances, where coherent dynamics are still observed, despite the quasiclassical nature of the transitions. A new perturbative approach has been developed to study the qubit's dynamics in this limit, and excellent agreement between theory and experiment is observed.

3.2 Discrete Resonance Limit

When strongly driven transitions from the ground state to the excited state can be attributed to a unique number of photons, n, one can make a resonance approximation that reduces the problem to the standard Rabi oscillation calculation. One then invokes the Rotating Wave Approximation (RWA) (see App. A.1 for a review of the RWA), allowing for the analytic solution of the dynamics of the strongly driven PC qubit. In this section I will begin by reviewing the resonance and RWA approximations for the PC qubit, and then present the experimental realization of the well-separated resonance regime. A useful analogy to Mach-Zehnder interference that will be utilized throughout the thesis will also be reviewed.

3.2.1 Rotating Frame Calculation

While being irradiated at angular frequency ω and amplitude A (in energy units), the PC qubit's Hamiltonian in the two-level approximation can be written as

$$H = -\frac{1}{2}\begin{pmatrix} \varepsilon + \mathrm{A}\cos(\omega t) & \Delta_{0,0} \\ \Delta_{0,0} & -\varepsilon - \mathrm{A}\cos(\omega t) \end{pmatrix} = -\frac{1}{2}\left[(\varepsilon + \mathrm{A}\cos(\omega t))\sigma_z + \Delta_{0,0}\sigma_x\right], \tag{3.1}$$

where ε is the DC magnetic flux detuning in units of energy, and $\Delta_{0,0}$ is the static coupling between diabatic states (see Eq. 2.13).

This Hamiltonian is different than the typical Hamiltonian (Eq. A.1) considered when a two-level system is driven by microwaves, e.g., in atomic physics:

$$H_{\mathrm{atomic}} = -\frac{1}{2}\begin{pmatrix} \varepsilon & \mathrm{A}\cos(\omega t) \\ \mathrm{A}\cos(\omega t) & -\varepsilon \end{pmatrix} = -\frac{1}{2}\left[\varepsilon\sigma_z + \mathrm{A}\cos(\omega t)\sigma_x\right], \tag{3.2}$$

In the typical two-level system the stationary states are σ_z eigenstates and coupled only when radiation is applied. Here though, the PC qubit's eigenstates are not always σ_z eigenstates (due to the permanent static coupling $\Delta_{0,0}$ along σ_x), and driving is along σ_z. In the case of Eq. 3.2 one can only use the RWA to analytically solve the problem when the amplitude of driving is small. Due to the nature of Eq. 3.1, it is in fact possible to find an analytic solution for the PC qubit at all driving amplitudes. The ability to solve for large driving amplitudes does not come for free though. As I will now show, one will have to assume that a new, renormalized driving amplitude is kept small, and that multiphoton resonances cannot overlap.

It is often convenient to solve time-dependent problems by going to a rotating frame such that the time-dependence is removed. Here I will remove the time dependence in Eq. 3.1 by making two sets of transformations. The rotations I will make are such that the effective Hamiltonian is $\tilde{H} = R_z(-\phi)HR_z(\phi) - \frac{\sigma_z}{2}\hbar(d\phi/dt)$ and $|\tilde{\Psi}\rangle = R_z(-\phi)|\Psi\rangle$, where $R_z(-\phi) = \exp(-i\frac{\sigma_z}{2}\phi)$. By first going to a frame whose orientation is rotating around z as $\phi = \lambda \sin\omega t$, where $\lambda = \mathrm{A}/\hbar\omega$, the qubit Hamiltonian becomes [69]

$$\tilde{H} = -\frac{1}{2}\begin{pmatrix} \varepsilon & \sum_{k=-\infty}^{k=\infty}\Delta_{0,0}J_k(\lambda)\exp(ik\omega t) \\ \sum_{k=-\infty}^{k=\infty}\Delta_{0,0}J_k(\lambda)\exp(-ik\omega t) & -\varepsilon \end{pmatrix}, \quad (3.3)$$

where the J_k are Bessel functions of the first kind of order k, and their generating function, $e^{(x(t-1/t)/2)} = \sum_{k=-\infty}^{k=\infty} J_k(x)t^k$, has been used. In analogy to the 1-photon RWA (see App. A.1), k corresponds to the number of photons involved in the transition between eigenstates. To study the behavior of the n-photon process, one first ignores all off-resonant terms; i.e. all photon modes with energy $k\hbar\omega$ not equal to $\varepsilon = n\hbar\omega$

$$\tilde{H} = -\frac{1}{2}\begin{pmatrix} \varepsilon & \Delta_{0,0}J_n(\lambda)[\exp(-in\omega t) + \exp(in\omega t)] \\ \Delta_{0,0}J_n(\lambda)[\exp(in\omega t) + \exp(-in\omega t)] & -\varepsilon \end{pmatrix} \quad (3.4)$$

This resonance approximation will not be suitable when the resonances start to overlap, and a new theory will be needed (see Ch. 3.3). Continuing with the non-overlapping resonances case, one makes the RWA by ignoring the second off-diagonal terms in Eq. 3.4, and by going to a frame whose orientation is rotating around z as

$\phi = n\omega t$, one has

$$\tilde{\tilde{H}} = -\frac{1}{2}\begin{pmatrix} \varepsilon_{\mathrm{n}} & \Delta_{0,0}\mathrm{J}_{\mathrm{n}}(\lambda) \\ \Delta_{0,0}\mathrm{J}_{\mathrm{n}}(\lambda) & -\varepsilon_{\mathrm{n}} \end{pmatrix}, \tag{3.5}$$

where $\varepsilon_n \equiv \varepsilon - n\hbar\omega$. Note that since all rotations have been around z, nothing has been changed from the perspective of the z measurement the SQUID makes. This will be computationally convenient when I calculate the dynamics of σ_z eigenstates resulting from $\tilde{\tilde{H}}$ shortly, since there will be no need to rotate these eigenstates back to the lab frame.

Ignoring the second off-diagonal terms in Eq. 3.4 is identical to the step made in going from Eq. A.1 to Eq. A.2 in the standard RWA, where one requires that $\mathrm{A} << \varepsilon$ in Eq. 3.2 (for a proof of this requirement in the standard RWA see Appendix A). The equivalent constraint here is that $\Delta_{0,0}\mathrm{J}_{\mathrm{n}}(\lambda) << \varepsilon$. Here the coefficient in front of the oscillating terms is $\Delta_n \equiv \Delta_{0,0}J_n(\lambda)$; whereas for the typical Rabi problem, it is just the amplitude A of the driving field. The reason for the difference is the starting Hamiltonians (Eq. 3.1 and Eq. 3.2). In the typical Rabi problem, radiation naturally couples transversely (along σ_x), and only one rotation is needed to remove the time-dependence in the Hamiltonian. For the PC qubit, radiation is coupled longitudinally (along σ_z), with a static transverse coupling term, and an extra rotation is needed to first bring the driving onto σ_x, effectively convolving the static coupling and driving terms, and resulting in an effective renormalized driving amplitude.

By going to a rotating frame such that a system with longitudinal driving of amplitude A is transformed to one with transverse driving of amplitude Δ_{n}, one can solve the strongly driven PC qubit for any A by keeping the renormalized amplitude Δ_{n} small. This is a key point, so let me reiterate it. No one knows how to solve the standard two-level, strong driving problem analytically (Eq. 3.2), but for the PC qubit (Eq. 3.1), by effectively changing the driving amplitude from A to Δ_{n} via a z rotation, one can study the PC qubit driven by large A as long as $\Delta_{0,0}$ is small or ω is large. Keep in mind though, this only works when the resonances do not overlap, a necessary requirement to get to Eq. 3.4.

The two-level system described in Eq. 3.5 has eigenvalues

$$\tilde{\tilde{E}}_{\pm} = \pm\frac{1}{2}\sqrt{\varepsilon_{\mathrm{n}}^2 + \Delta_{\mathrm{n}}^2} \tag{3.6}$$

with eigenstates given by

$$|\tilde{\tilde{\Psi}}_{-}\rangle = \cos\frac{\chi}{2}|0,\mathrm{R}\rangle + \sin\frac{\chi}{2}|0,\mathrm{L}\rangle \text{ and } |\tilde{\tilde{\Psi}}_{+}\rangle = -\sin\frac{\chi}{2}|0,\mathrm{R}\rangle + \cos\frac{\chi}{2}|0,\mathrm{L}\rangle \tag{3.7}$$

where $\chi = \tan^{-1}(\frac{\Delta_n}{\varepsilon_n})$, and the states $|0,\mathrm{R}\rangle$ and $|0,\mathrm{L}\rangle$ are the uncoupled σ_z eigenstates. As mentioned earlier, since all rotations have been around z, nothing has been changed from the perspective of the z measurement the SQUID makes. Hence I will permanently drop all notation indicating a rotated wavefunction, since the rotated nature is not observable in the experiment.

Since $\Delta_{0,0} \ll \varepsilon$ during a typical experiment, the initial state, say on the right side of f=1/2, is approximately

$$|\Psi(0)\rangle = |0,\mathrm{R}\rangle = \cos\frac{\chi}{2}|\Psi_{-}\rangle - \sin\frac{\chi}{2}|\Psi_{+}\rangle. \tag{3.8}$$

The state at some later time t can simply be written as

$$|\Psi(t)\rangle = e^{-\frac{i}{\hbar}E_{-}t}\cos\frac{\chi}{2}|\Psi_{-}\rangle - e^{\frac{i}{\hbar}E_{+}t}\sin\frac{\chi}{2}|\Psi_{+}\rangle. \tag{3.9}$$

The probability for being in the excited state, $\mathrm{p_n}(t)$, can then be written as

$$\begin{aligned} \mathrm{p_n}(t) &= |\langle 0,\mathrm{L}|\Psi(t)\rangle|^2 \\ &= \frac{\Delta_{\mathrm{n}}^2}{\varepsilon_{\mathrm{n}}^2 + \Delta_{\mathrm{n}}^2}\sin^2\frac{\sqrt{\varepsilon_{\mathrm{n}}^2 + \Delta_{\mathrm{n}}^2}\,t}{2}. \end{aligned} \tag{3.10}$$

which has the same form as the standard Rabi expression, except for the driving amplitude being renormalized.

One can also show that the steady state excited state population is

$$\begin{aligned} \mathrm{p}_{\mathrm{n}}^{(\infty)} &= \lim_{T\to\infty} \frac{1}{T} \int_0^T dt \, |\langle 0, \mathrm{L} | \Psi(t) \rangle|^2 \\ &= \frac{1}{2} \frac{\Delta_{\mathrm{n}}^2}{\varepsilon_{\mathrm{n}}^2 + \Delta_{\mathrm{n}}^2} = \frac{1}{2} \frac{\Delta_{0,0}^2 \mathrm{J}_{\mathrm{n}}^2(\frac{\mathrm{A}}{\hbar\omega})}{(\varepsilon - n\hbar\omega)^2 + \Delta_{0,0}^2 \mathrm{J}_{\mathrm{n}}^2(\frac{\mathrm{A}}{\hbar\omega})}. \end{aligned} \tag{3.11}$$

3.2.2 Accounting For Decoherence

Up to this point I have treated the PC qubit as a perfectly isolated quantum system. The PC qubit however is always interacting with its environment, constantly re-establishing equilibrium with its surroundings. As such, the PC qubit experiences both a trend towards equilibrium among its eigenstate populations, known as relaxation, as well as a loss of coherence when in a superposition of eigenstates, known as dephasing. The PC qubit also experiences inhomogeneous broadening, a lower frequency version of dephasing. There are many elegant, highly mathematical models which can be used to understand the origins of decoherence in systems such as the PC qubit [70, 71], but here I will focus on a more intuitive picture of decoherence. For simplicity, the following discussion of decoherence will be for the two-level model of the PC qubit only. Since $\Delta_{0,0} \ll \varepsilon$ during a typical experiment, I will also limit the discussion of decoherence to what happens for σ_z eigenstates.

Relaxation is the process whereby populations in the ground and excited state adjust until the transition rates from one state to the other have reached their steady-state equilibrium [72]. For the PC qubit, transitions between the two states can occur classically via thermal activation over the barrier, or via quantum mechanical tunneling through the barrier. Relaxation stems from a coupling element between the ground and excited state, along σ_x, and results in an exponential decay towards equilibrium of eigenstate populations. The excited state falls to the ground state at the characteristic rate denoted by Γ_1 ($1/\mathrm{T}_1$), and the rate of excitation from the ground state to the excited state is denoted by Γ_1'.

For relaxation to occur, energy must also be absorbed or emitted by the environment. This energy can come in the form of thermal noise; i.e., a continuum of environmental modes, or as individual photons; i.e., another two-level system embedded in the solid state of the qubit. Quantized environmental modes could also provide coupling between levels when there is none in the isolated system, e.g., a fluctuating two-level system in the environment could flip back and forth, causing fluctuations in the junction's critical current and hence $\Delta_{0,0}$. The exact nature of the environmental modes contributing to relaxation is an ongoing part of superconducting qubit research [73].

Dephasing is the process whereby phase information in a superposition state is lost over time due to random phase kicks from the environment. These random events couple into the PC qubit along the σ_z axis, via mutual inductance to the qubit, resulting in an exponential decay of coherence at a characteristic rate Γ_2 ($1/\mathrm{T}_2$). The source of these fluctuations could be anything from current noise in the dc flux bias or microwave lines, to flux generated from other two-level systems in the environment. Which noise source dominates dephasing in the PC qubit is still an active research topic [74].

It is interesting to note that the dephasing rate Γ_2 is actually a multivariate function, given by $\Gamma_2 = \Gamma_\phi + \Gamma_1/2$, where Γ_ϕ is the pure dephasing rate, a characteristic rate of the dephasing process by itself [72]. This result is most easily understood by thinking about a σ_x eigenstate allowed to evolve under a purely σ_z Hamiltonian, where there is no dephasing mechanism, just relaxation, and the relaxation rate Γ_1' from the ground to excited state is negligible. The σ_x eigenstate will clearly evolve into the σ_z ground state, and so dephasing has in fact occurred with no dephasing mechanism.

In the setup studied here, it will be seen that $\Gamma_2 \gg \Gamma_1$. As such, decoherence can be introduced into previous discussions of the strongly driven qubit by simply assuming the decay of the excited state at the rate Γ_2. With a normalized exponential decay, Eq. 3.11 becomes

$$
\begin{aligned}
\mathrm{p}_{\mathrm{n}}^{(\infty)} &= \int_0^{\infty} dt\, \Gamma_2 \exp(-\Gamma_2 t)\, |\langle 0, \mathrm{L}|\Psi(t)\rangle|^2 \\
&= \frac{1}{2}\frac{\Delta_{\mathrm{n}}^2}{\varepsilon_{\mathrm{n}}^2 + \Delta_{\mathrm{n}}^2 + \Gamma_2^2} = \frac{1}{2}\frac{\Delta_{0,0}^2 \mathrm{J}_{\mathrm{n}}^2(\frac{\mathrm{A}}{\hbar\omega})}{(\varepsilon - n\hbar\omega)^2 + \Delta_{0,0}^2 \mathrm{J}_{\mathrm{n}}^2(\frac{\mathrm{A}}{\hbar\omega}) + \Gamma_2^2}.
\end{aligned}
\tag{3.12}
$$

One immediately sees from this expression that if the qubit is driven for a long time, the excited state population will be a "Bessel Staircase", which consists of a series of resonances along the f axis, as well as a Bessel dependence along the A or ω axes. Compared to Eq. 3.11, dephasing broadens the resonances, with a new width of $2\sqrt{\Delta_{\mathrm{n}}^2 + \Gamma_2^2}$.

The exponential decays associated with relaxation and dephasing were just assumed to have Lorentzian linewidths. However, when a dephasing process occurs on timescales longer than the time it takes to complete a single measurement of the system, the center of those Lorentzian resonances may start to drift randomly. This kind of broadening is known as inhomogeneous broadening, and it will be the dominant noise source in this work. The exact shape of the inhomogeneously broadened resonances depends on the underlying mechanism, and as I will show shortly, in these experiments it takes on a Gaussian lineshape.

3.2.3 Experimental Realization

To study the qubit's response to large driving I have utilized the pulse sequence shown in Figure 3-1. A sinusoidal microwave pulse of frequency ν, amplitude V (A$\propto$ V), and width Δt, was applied to the qubit. A static magnetic flux detuning, δf_{dc}, was also applied, giving a total flux detuning in time of $\delta f = \delta f_{\mathrm{dc}} - \Phi_{\mathrm{rf}} \sin 2\pi\nu t$, where Φ_{rf} is proportional to the source voltage V. The state of the qubit was determined with the rapid readout pulse (see Ch. 2.2.3), approximately 100ns after the end of the microwave pulse.

The repetition rate for the experiment was 10 kHz, with typically 1000 measurements made at each bias point. The qubit is indeed disturbed by the measurement,

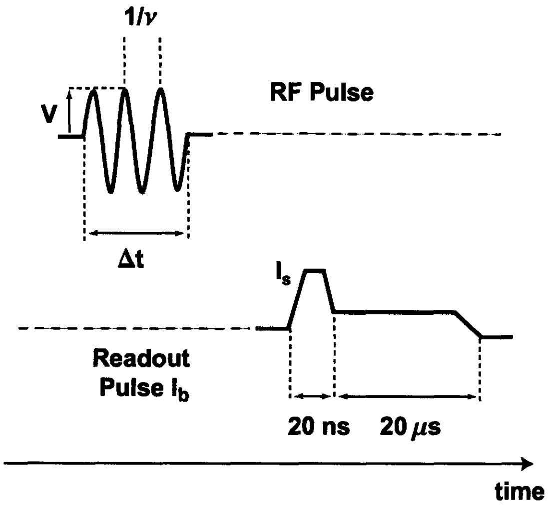

Figure 3-1: Pulse sequence for large amplitude driving experiments. A sinusoidal microwave pulse of frequency ν, amplitude V ($A \propto V$), and width Δt is followed within 100ns by the rapid SQUID readout pulse (see Fig. 2-15).

and takes $\sim 5\,\text{ms}$ for the post-measurement excited state population to relax to the ground state. However, a $100\,\mu s$ repetition period was achieved here, by cooling the qubit after each measurement (see Ch. 5 for an in-depth discussion of cooling). With our qubit, cooling takes less than $1\,\mu s$ to reset the qubit, and actually causes there to be less population in the excited state than in equilibrium.

Figure 3-2 shows the measured qubit population in the left well as a function of V and δf_{dc}, for $\nu = 270$ MHz. One immediately sees the Bessel staircase derived in Ch. 3.2.2 (Eq. 3.12). Fig. 3-2 shows photon transitions from n=1 photons to n=44 photons. Along a line of constant δf_{dc}, on-resonance, one sees the Bessel-function dependence $J_n^2(A/h\nu)$ expected when Γ_2 is the dominant term in Eq. 3.12. Population transfer due to qubit driving first appears at amplitudes that vary linearly with δf_{dc}, and symmetrically about the qubit step. This diagonal threshold arises because Bessel functions' first lobe maxima grow linearly with V as n is increased. I will now discuss a nice analogy which provides physical insight into where Eq. 3.12 and Fig. 3-2 come from. The analogy comes from optics and will be utilized throughout this thesis.

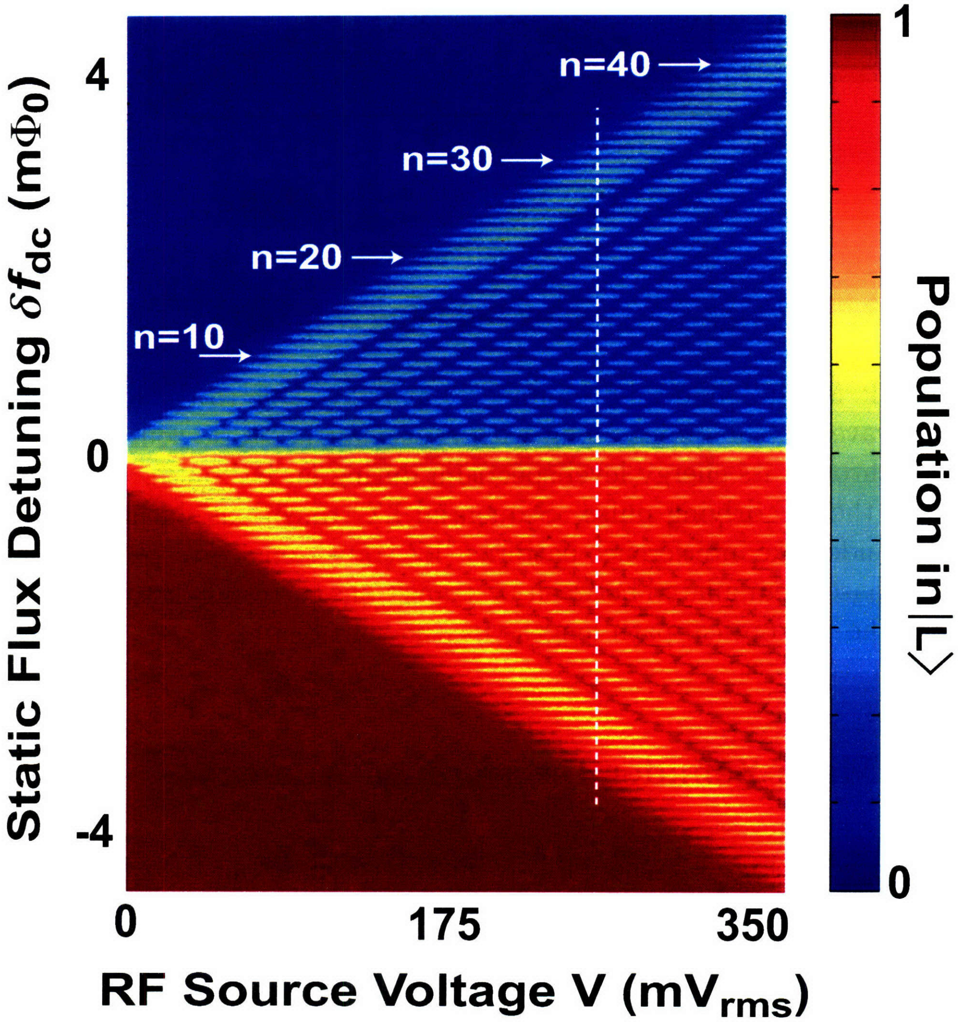

Figure 3-2: Measured qubit population, strongly driven at $\nu = 270\,\text{MHz}$. The Bessel ladder (Eq. 3.12) is observed, with multiphoton resonances up to $n = 44$ visible. One can also see the n=1 Bessel function out to 14 lobes. A pulse of duration $\Delta t = 3\,\mu s$ was used. Data shown here was taken at 15mK, and the qubit was pre-cooled before each measurement (see Ch. 4 on cooling).

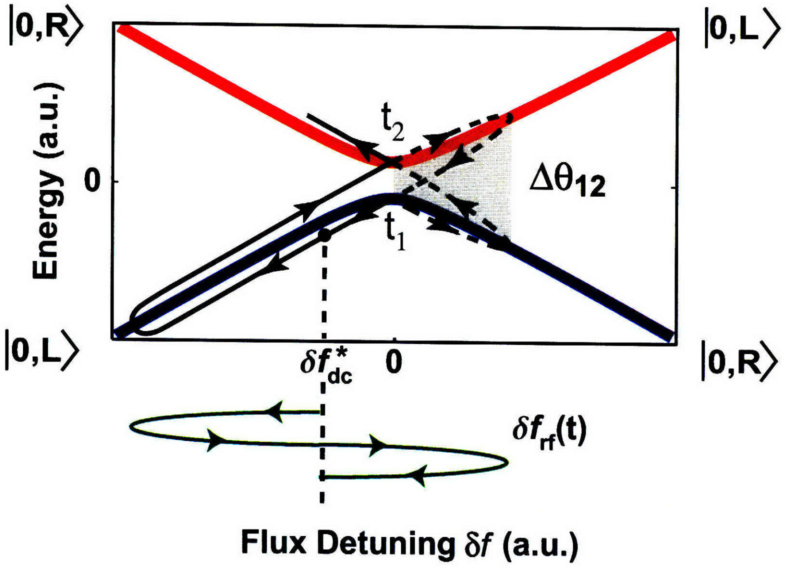

Figure 3-3: Mach-Zehnder interferometer analogy. Due to the longitudinal coupling of microwaves to the qubit, along with a permanent static coupling $\Delta_{0,0}$, the qubit is swept through its energy level spectrum during an RF pulse. Pictured here is one period of the RF driving pulse. Sequential LZ transitions during one period create Mach-Zehnder-like interference patterns. LZ transitions correspond to beamsplitters, and the phase accumulated between LZ transitions corresponds to the phase difference between the two optical path lengths for the split beams.

3.2.4 Mach-Zehnder Interference Analogy

As illustrated in Fig. 3-3, the qubit is initially prepared in the ground state at static flux detuning $\delta f_{\rm dc} = \delta f_{\rm dc}{}^*$. The qubit is driven longitudinally with a time-dependent flux $\delta f(t) = \delta f^*_{\rm dc} - \Phi_{\rm rf}\sin 2\pi\nu t$. As discussed in Ch. 3.2.1, the PC qubit is different than the typical atomic system in that microwaves couple to the qubit longitudinally, with a permanent static transverse coupling $\Delta_{0,0}$. Thus when an RF pulse is applied to the qubit, the microwaves are sweeping the qubit through the two-level energy system, inducing sinusoidal excursions with angular frequency $\omega = 2\pi\nu$ through the energy bands about $\delta f_{\rm dc}{}^*$ as pictured in Fig. 3-3. Visualizing the microwaves as sweeping the qubit through it's energy level spectrum will be a useful concept throughout this thesis.

Under the influence of these microwaves, the qubit state is swept through the avoided crossing at time t_1, where it undergoes an LZ transition, and it is subsequently in a coherent superposition of the two diabatic states. The LZ transition can be described by the transformation

$$|\Psi_f\rangle = \begin{pmatrix} t & r \\ r & t \end{pmatrix} |\Psi_i\rangle \tag{3.13}$$

where $|\Psi_i\rangle$ is the state before the LZ transition, $|\Psi_f\rangle$ is the state after the LZ transition, $\mathrm{t} = \exp(\frac{-\pi\Delta_{0,0}^2}{\hbar v})$, $v = \mathrm{d}(\mathrm{E}_+ - \mathrm{E}_-)/\mathrm{dt}$, and $|\mathrm{r}|^2 = 1 - |\mathrm{t}|^2$. It will be useful to keep in mind two limits of the LZ transition throughout this thesis. When the microwaves sweep the qubit through an avoided crossing slowly, compared to the magnitude of the avoided crossing, the qubit state adiabatically evolves from one diabatic state to the other (t=0, r=1 since $\frac{\pi\Delta_{0,0}^2}{\hbar v} \gg 1$). When the sweep through the crossing is much faster than the avoided crossing strength, the qubit state is unchanged (t=1, r=0 since $\frac{\pi\Delta_{0,0}^2}{\hbar v} \ll 1$). Typically, a situation between these two limits will be realized. It is in this regime that one speaks of non-adiabatic control of a qubit.

For times $t_1 < t < t_2$, the superposition state created after the first LZ transition accumulates a relative phase $\Delta\theta_{12}$, which mediates quantum interference at the second LZ transition at time t_2 (this is clear since if $\Delta\theta_{12} = 0$, the state in at t_1 will be the same state out at t_2, due to the reversibility of the unitary transformation in Eq. 3.13). The sequence of two LZ transitions, repeated many times during the RF pulse, is analogous to a cascade of Mach-Zehnder interferometers [66]. The LZ transitions correspond to beamsplitters, and the phase accumulated between LZ transitions corresponds to the phase difference between the two optical path lengths for the split beams.

One now expects Mach-Zehnder-type interference fringes in the qubit population due to changes in $\Delta\theta_{12}$, associated with changes in A, ω, and δf_{dc}. One also expects interference due to the total roundtrip phase θ, associated with changes in δf_{dc} and ω, whenever multiple periods of RF fall within a microwave pulse (the roundtrip phase interference pattern is identified as a multiphoton resonance condition θ=2πn). The two dimensional interference pattern just described is exactly the Bessel staircase derived in Eq. 3.12 and demonstrated in Fig. 3-2. Consider a vertical slice at constant

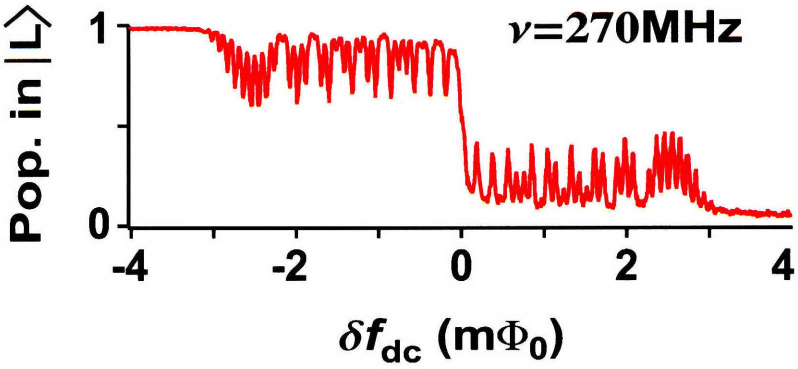

Figure 3-4: Measured qubit population, strongly driven at $\nu = 270\,\text{MHz}$. Slice taken along the dashed line in Fig. 3-2, at V=240mV$_{\text{rms}}$. Resonances arise from a constructive roundtrip phase θ=2πn, and the envelope on top of the resonances is Mach-Zehnder-like interference from the phase $\Delta\theta_{12}$ accumulated between LZ transitions.

A and ω, as in Fig. 3-4. One clearly sees multiphoton resonances due to the roundtrip phase interference, as a function of δf_{dc}. One also sees an envelope on top of the resonances, due to $\Delta\theta_{12}$ varying between constructive and destructive interference, as a function of δf_{dc}.

Of course, to have a coherent interference effect, one needs to evade decoherence. To have interference from varying θ one needs coherence over at least one full period of the RF drive. On the other hand, to have interference from varying $\Delta\theta_{12}$, one only needs coherence from t_1 to t_2. In Fig. 3-2 and Fig. 3-4, coherence times are longer than the period of the RF drive, since interference from both $\Delta\theta_{12}$ and θ is observed. I will now present results where coherence is still preserved between LZ transitions, but not over an entire driving period. This will remove the individual resonances along δf_{dc}, but keep the Mach-Zehnder interference fringes varying with V and δf_{dc}, resulting in the first observation of a coherent quasiclassical regime in superconducting qubits.

3.3 A New Coherent Quasiclassical Regime

When strongly driven transitions from the ground state to the excited state result from the absorption of many different photon modes; i.e., multiple values of n simultaneously, one is in a "quasiclassical" limit. There one can no longer make the resonance approximation made in Ch. 3.2.1 because now the linewidths of the resonances overlap. In this section I will show the experimental realization of the multi-moded transition regime, where coherent effects are still observed. I will then present a new perturbative treatment of the qubit's ground state to excited state transition rate, which will allow description of the qubit in the overlapping resonance limit.

One must be careful to separate T_2 effects from inhomogeneous broadening, because it is only when the resonances overlap due to dephasing that mutli-moded transitions actually occur. By comparing the new transition rate theory to experimental results, I will show that resonances indeed overlap due to dephasing, proving that the qubit is truly in the quasiclassical limit. The high accuracy of the perturbative theory will also become evident. The work in this section is based on published material [75].

3.3.1 Experimental Realization

Fig. 3-5 shows the qubit's response when driven at $\nu = 90$ MHz. The individual photon resonances are no longer distinguishable because the resonance widths exceed the resonance spacing. Nonetheless, interference fringes are still observed along the V and $\delta f_{\rm dc}$ axes, indicating that coherent interference is still occurring due to $\Delta\theta_{12}$. However, it is not clear at this point whether driving at $\nu = 90$ MHz is too slow for coherence to be preserved over a full cycle of the microwaves, destroying the roundtrip interference condition on θ that yields the resonance condition, or whether one is still in the discrete resonance limit, and the resonances are just blurred out by inhomogeneous broadening. In the former, $\nu T_2 \leq 1$, and multiple photon modes contribute to each resonance, whereas in the latter, a single photon mode is still responsible for every transition, and it is just inhomogeneous broadening that is

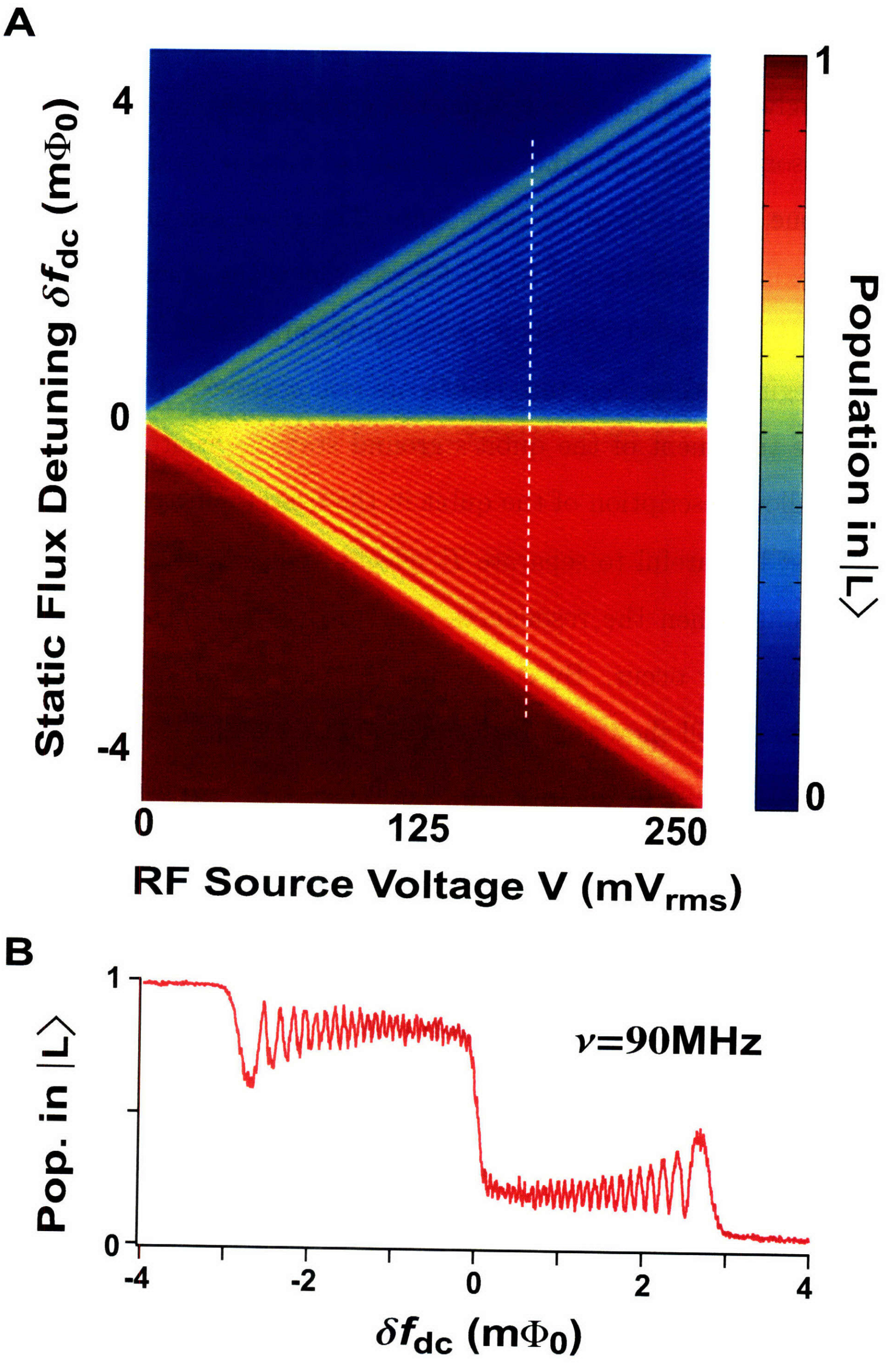

Figure 3-5: (A) Measured qubit population, strongly driven at $\nu = 90\,\text{MHz}$. Data shown here was taken at 15mK, and the qubit was pre-cooled before each measurement (see Ch. 4 on cooling). Coherent behavior is still observed even though multiphoton resonances can no longer be discerned. A pulse of duration $\Delta t = 3\,\mu\text{s}$ was used. (B) Slice taken along the dashed line in Fig. 3-5A, at V=171mV$_{\text{rms}}$. A and B should be contrasted to the $\nu = 270\,\text{MHz}$ case, where multiphoton resonances are still discernible (Fig. 3-2 and Fig. 3-4).

making the resonances overlap.

Assuming $\nu T_2 \leq 1$, I will now proceed to summarize a new theory that is valid when multiple photon modes contribute to transitions at a single static flux detuning. By then comparing this new theory with Fig. 3-5 (see Ch. 3.3.3), I will show that at $\nu = 90$ MHz the qubit is indeed in the coherent quasiclassical limit.

3.3.2 Transition Rate Calculation

While making the resonance approximation earlier (Ch. 3.2.1), it was assumed that the resonance spacing, before inhomogeneous broadening effects, was wider than the resonance width. To study the case where resonances overlap, and avoid the resonance approximation, one can consider the transition rate from the ground to excited state via perturbation theory [76, 77]. The result will be an example of Fermi's golden rule [78], where the group of final states is due to the linewidth of the excited state arising from dephasing. The theory that follows was developed in collaboration with Leonid Levitov and Andrey Shytov.

Including the effects of dephasing, Eq. 3.1 becomes:

$$H = -\frac{1}{2}\begin{pmatrix} h(t) & \Delta_{0,0} \\ \Delta_{0,0} & -h(t) \end{pmatrix}. \tag{3.14}$$

Here, $h(t) = \varepsilon + \delta\varepsilon(t) + A\cos\omega t$ is the energy detuning from an avoided crossing modulated by the driving field in the presence of classical noise $\delta\varepsilon(t)$. By going to a frame whose orientation is rotating around z with $\phi(t) = \frac{1}{\hbar}\int_0^t h(\tau)d\tau$, the Hamiltonian is brought to the form

$$\tilde{H} = -\frac{1}{2}\begin{pmatrix} 0 & \Delta(t) \\ \Delta^*(t) & 0 \end{pmatrix}, \tag{3.15}$$

where $\Delta(t) = \Delta_{0,0}e^{-i\phi(t)}$. This transformation has brought the problem into the interaction picture. First order perturbation theory in $\Delta(t)$ then gives the rate of transitions between the ground and excited state, denoted by W, as [78]

$$W = \frac{d}{d(t'-t)}|A_{t,t'}|^2 \tag{3.16}$$

where $A_{t,t'} = \frac{1}{\hbar}\int_t^{t'} \Delta(t_1)dt_1$.

For the first order perturbation approach to be accurate, there should be no oscillatory behavior of the excited state population in time. In the experiments in this thesis, oscillations in the excited state population are not observed because population transfer is slow relative to the dephasing time T_2. Hence, the requirement to use first order perturbation theory here can be written down as $W \ll \Gamma_2 = 1/T_2$. This inequality does not imply that the effect of driving the qubit is weak. The rate W can still be large compared to the relaxation rate Γ_1, leading to the strong deviation of population from equilibrium observed in experiments.

By introducing Bessel functions in the Fourier series of $e^{-i(A/\hbar\omega)\sin\omega t}$ and letting $\delta\phi(t) = \frac{1}{\hbar}\int_0^t \delta\varepsilon(\tau)d\tau$, one has

$$e^{-i\phi(t)} = e^{-i\frac{\varepsilon}{\hbar}t - i\delta\phi(t)} \sum_n J_n(\lambda)e^{i\omega nt}. \tag{3.17}$$

The transition rate can then be written as

$$W = \int_t^{t'}\int_t^{t'} \sum_n \sum_{n'} J_n(\lambda)J_{n'}(\lambda)e^{i\omega(nt_1 - n't_2)}e^{-i\frac{\varepsilon}{\hbar}(t_1-t_2)}e^{-i\delta\phi(t_1-t_2)}dt_1dt_2. \tag{3.18}$$

Averaging over $\delta\phi(t)$ with the help of the white noise model $\langle e^{i\delta\phi(t)-i\delta\phi(t')}\rangle = e^{-\Gamma_2|t-t'|}$ [72], and integrating in Eq. 3.18 as $\int e^{-i(\frac{\varepsilon}{\hbar}-\omega n)\tau - \Gamma_2|\tau|}d\tau = 2\Gamma_2/((\frac{\varepsilon}{\hbar} - n\omega)^2 + \Gamma_2^2)$, one obtains

$$W(\varepsilon, A) = \frac{\Delta_{0,0}^2}{2}\sum_n \frac{\Gamma_2 J_n^2(\lambda)}{(\frac{\varepsilon}{\hbar} - n\omega)^2 + \Gamma_2^2}. \tag{3.19}$$

For large n, Bessel functions can be expressed through the Airy function $\mathrm{Ai}(u) = \frac{1}{\pi}\int_0^\infty \cos(uy + \frac{1}{3}y^3)dy$ as $J_n(\lambda) = a\mathrm{Ai}(a(n-\lambda))$ where $a = (2/\lambda)^{1/3}$. Using the identity

$\cot z = \sum (z - \pi n)^{-1}$, Eq. 3.19 is approximated as

$$W = \frac{\pi a^2 \Delta_{0,0}^2}{2\omega} \mathrm{Im}\, \cot\left(\frac{\pi}{\omega}(\frac{\varepsilon}{\hbar} - i\Gamma_2)\right) \mathrm{Ai}^2\left(\frac{a}{\hbar\omega}(\varepsilon - A)\right) \tag{3.20}$$

There are two main regimes exhibited by this expression: (i) $\nu \geq \Gamma_2$, and (ii) $\nu \leq \Gamma_2$. In case (i) one has a sum of non-overlapping resonances. For each value of ε, the sum in Eq. 3.19 is dominated by the term with n the nearest integer to $\varepsilon/\hbar\omega$, giving rise to resonances of strength $J_n^2(\lambda)$, the Bessel ladder of Eq. 3.12.

In contrast, in case (ii), the peaks in Eq. 3.19 are overlapping. Setting cot $= i$ in Eq. 3.20 [79], one obtains

$$W(\varepsilon, A) \approx \frac{\pi a^2 \Delta_{0,0}^2}{2\omega} \mathrm{Ai}^2(a(\varepsilon - A)/\omega). \tag{3.21}$$

The effect of Γ_2 on the Airy function oscillation is small at $\Gamma_2 \leq (2\pi/a)\nu$. Since $a \approx 0.3$ for $\varepsilon/h\nu \leq 50$, this condition is compatible with $\nu \leq \Gamma_2$. Eq. 3.21 can also be obtained by considering just two subsequent passages of a level crossing at a short time separation $|t_2 - t_1| \ll \nu^{-1}$, and ignoring the periodicity of the driving.

Since $\mathrm{Ai}(u < 0)$ oscillates as $\pi^{-1/2}|u|^{-1/4}\cos(\frac{2}{3}|u|^{3/2} - \frac{\pi}{4})$, while $\mathrm{Ai}(u > 0)$ decays exponentially, Eq. 3.21 implies that the transitions occur only for $A \geq \varepsilon$, with a rate which oscillates as a function of $A - \varepsilon$. The oscillations are the same for both integer and non-integer $\varepsilon/\hbar\omega$, confirming that, while the resonances merge into a continuous band, the interference fringes persist at $\nu \leq \Gamma_2$.

To describe the population dynamics in the presence of driving, a rate equation approach will be employed, where the qubit level occupations obey

$$\dot{p}_i = \sum_j g_{ij} p_j \tag{3.22}$$

where $g_{-+} = -g_{++} = W + \Gamma_1$, $g_{+-} = -g_{--} = W + \Gamma_1'$, i,j take on the values -,+ (representing the ground and excited state), and $\Gamma_1 = 1/T_1$, $\Gamma_1' = \Gamma_1 e^{-\varepsilon/k_{\mathrm{B}}T}$, are the down and up relaxation rates as dictated by the detailed balance relation, where k_{B} is the Boltzmann constant, and T is the bath temperature. The magnetization of the stationary state is $m_s = p_- - p_+ = (\Gamma_1 - \Gamma_1')/(2W + \Gamma_1 + \Gamma_1')$, which gives the equilibrium value $m_0 = \tanh \frac{\varepsilon}{2k_BT}$ at weak excitation, $W \ll \Gamma_1$, and $m_s \ll m_0$ at high excitation due to saturation of the transition.

3.3.3 Comparison of Experiment and Theory

I will now study the validity of the perturbative theory just discussed by analyzing the qubit's evolution in time. By fitting theoretical predictions to experimental results I will find best fits for $\Delta_{0,0}, \Gamma_2, \Gamma_1$, and the inhomogeneous broadening width σ. Besides showcasing the accuracy and utility of the perturbative theory, I will also show that $\nu T_2 \approx 1$, proving that a new coherent quasiclassical regime has indeed been observed.

Interference fringes in the excited state population as a function of RF pulse length Δt are shown in Fig. 3-6A. The rate equation (Eq. 3.22) predicts an exponential time dependence for the magnetization,

$$m(\Delta \mathrm{t}) = \mathrm{m_s} + (\mathrm{m_0} - \mathrm{m_s})\mathrm{e}^{-\Gamma\Delta \mathrm{t}}, \quad \Gamma = 2\mathrm{W} + \Gamma_1 + \Gamma_1'. \tag{3.23}$$

Since T_1 here is much longer than the observed transition time, $T_1 \approx 20\,\mu$s [66], I will assume $\Gamma \approx 2W$, allowing for a simple comparison of experimental and theoretical characteristic rates. By fitting exponentials to the qubit population at each flux detuning seen in Fig. 3-6A (four example fits are shown in the inset of Fig. 3-6B), one finds the rate Γ which characterizes how fast the stationary state is approached (Fig. 3-6B).

In Fig. 3-7 I compare the experimental characteristic rate and qubit population with those predicted by the model (Eq. 3.19 and Eq. 3.23). Inhomogeneous broadening is numerically incorporated into the model by assuming a Gaussian broadening mechanism with standard deviation σ. The agreement between the experimental results and the perturbative theory, seen in Fig. 3-7, is remarkable. From the best fits I obtain $\Gamma_2/2\pi = 12 - 18\,\mathrm{MHz}$ ($T_2 \approx 9 - 13\,\mathrm{ns}$), $\sigma/2\pi = 40 - 45\,\mathrm{MHz}$, and $\Delta_{0,0}/2\pi\hbar = 13\,\mathrm{MHz}$. Since $\Gamma_2 = 1/T_2 \approx 90\,\mathrm{MHz}$, the quasiclassical limit has indeed been reached.

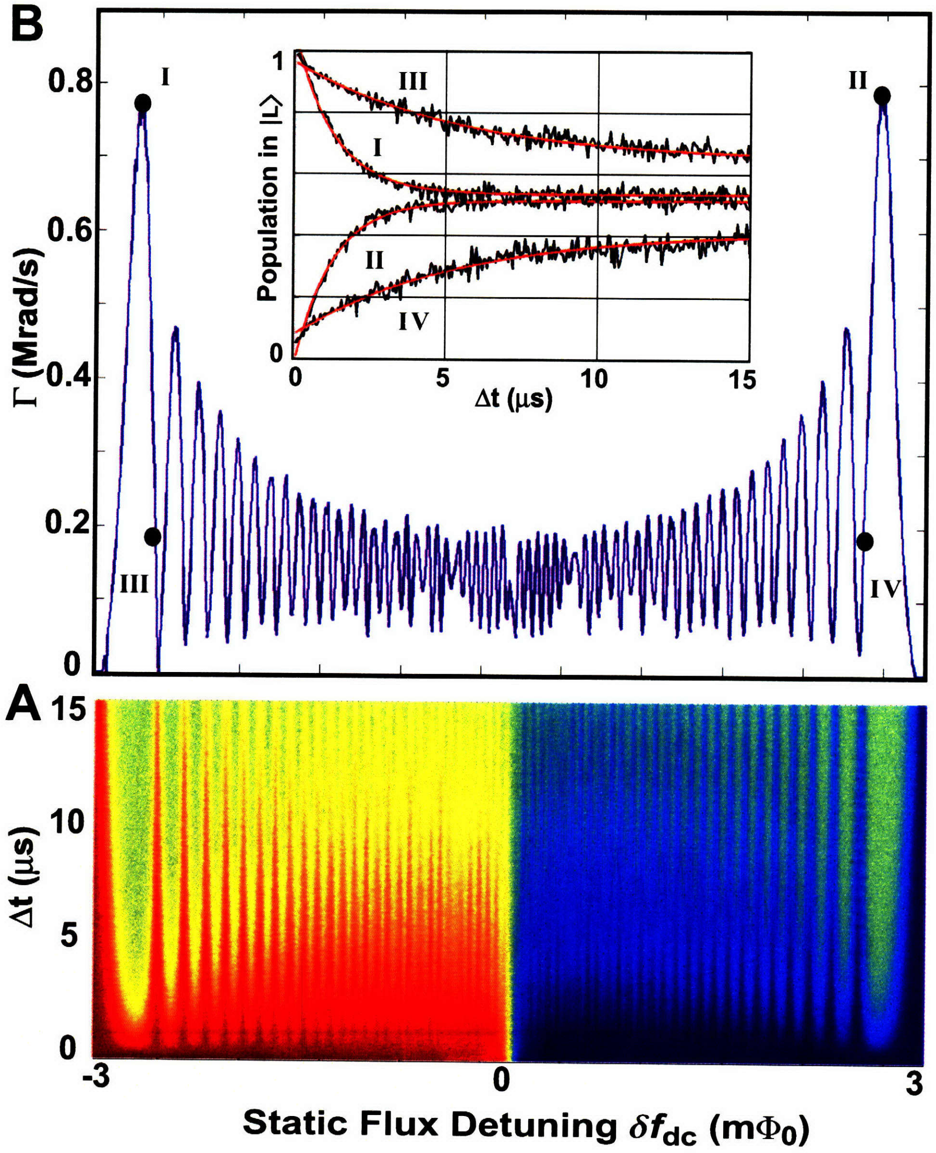

Figure 3-6: (**A**) Temporal evolution of excited state population obtained by varying the pulse width Δt ($\nu = 90\,\mathrm{MHz}$, $V = 171\,\mathrm{mV_{rms}}$). Data shown here was taken at 15mK, and the qubit was pre-cooled before each measurement (see Ch. 4 on cooling). (**B**) The characteristic rate Γ as a function of static flux detuning δf_{dc}, obtained by fitting to the exponential time dependence (Eq. 3.23) (inset shows examples of fits for the points I, II, III and IV).

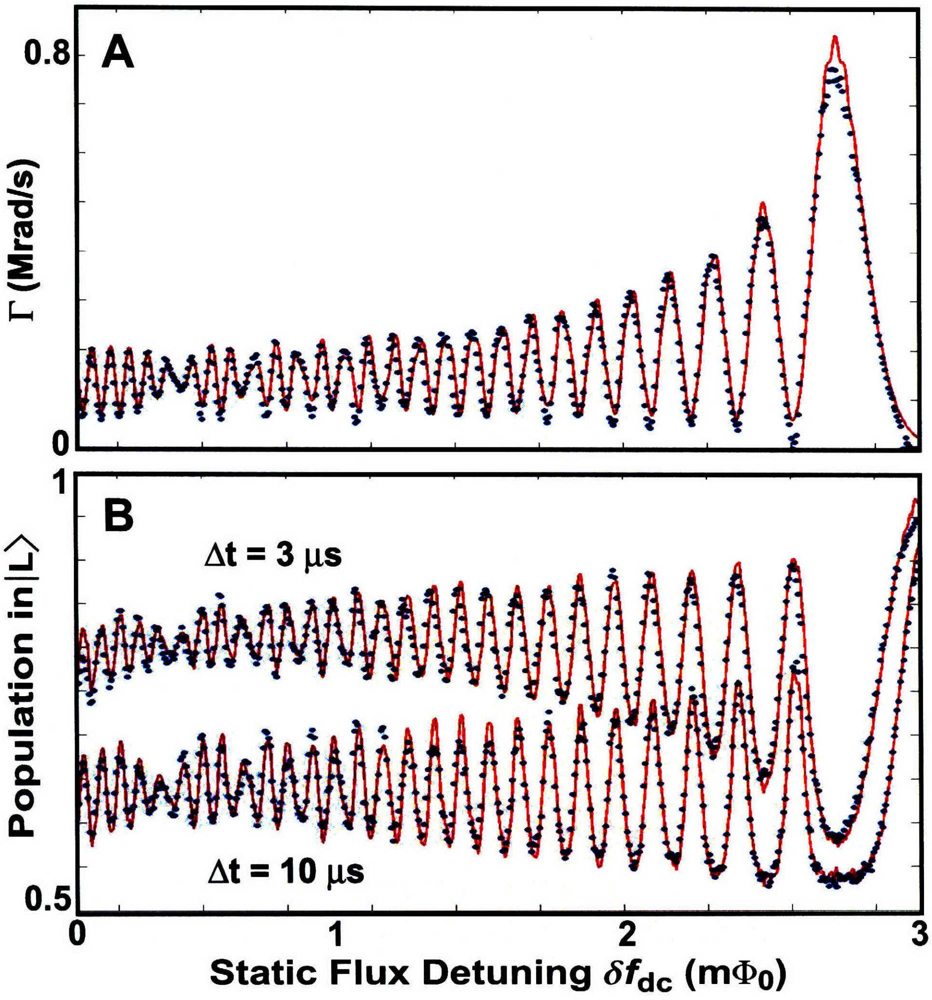

Figure 3-7: Comparison of experiment (blue dots) and theory (red lines). (**A**) The transition rate from the right half of Fig. 3-6B fitted with Γ defined by Eqs. 3.19 and 3.23. (**B**) Left well occupation taken from the right half of Fig. 3-6A, compared to the model, Eq. 3.23.

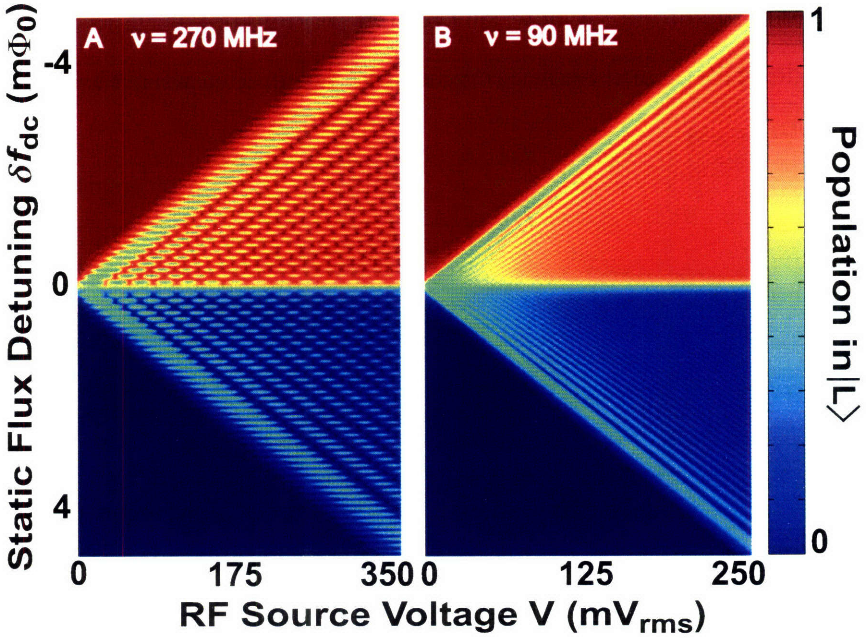

Figure 3-8: Simulation of qubit population using model parameters extracted from data. (**A**) $\nu = 270\,\text{MHz}$. (**B**) $\nu = 90\,\text{MHz}$. These simulations should be compared with the data shown in Fig. 3-2 and Fig. 3-5

By using the fit parameters for the $3\mu s$ magnetization curve, I calculate the qubit population in the multiphoton (Fig. 3-8A) and quasiclassical (Fig. 3-8B) regimes as a function of δf_{dc} and V, which agree remarkably with the data shown in Fig. 3-2 and Fig. 3-5.

3.4 Summary

I have just demonstrated a new quasiclassical regime of coherent quantum dynamics of a qubit, realized at low driving frequencies in the strong driving limit. Coherent transitions between qubit states occur via the LZ process when the system is swept through an energy-level avoided crossing. The quantum interference mediated by repeated transitions gives rise to an oscillatory dependence of the qubit population on the driving field amplitude and static flux detuning. These interference fringes, which at high frequencies consist of individual multiphoton resonances, persist even for driving frequencies near the dephasing rate Γ_2, where individual resonances are no longer distinguishable. A new theoretical model that is valid in the quasiclassical regime was described, and shows remarkable agreement with the observations.

Chapter 4

Large Amplitude Driving with an Additional Crossing: Microwave Cooling

Thus far I have only considered the two lowest levels of the PC qubit. If one drives the qubit strong enough, higher energy levels and avoided crossings can be accessed (Fig. 2-3). In this chapter I present a new method for cooling two-level quantum systems, which utilizes an additional, higher-energy avoided crossing to remove unwanted excited state population. I will begin with a background discussion on atomic sideband cooling that is analogous to the cooling performed here on the PC qubit. I will then discuss how cooling works in the PC qubit, and then finally quantify exactly how much cooling is being performed and on what timescales.

4.1 Introduction

Quantum-coherent phenomena, from superconductivity to Rabi oscillations, are all destroyed by high temperatures. However, by cooling the quantum system under study, one can reduce the thermal noise to the point where coherence can persist over the time scale of the experiments. Conventionally, the entire system under study is cooled with ^{3}He or ^{3}He-^{4}He cryogenic techniques [80]. Although this straightforward

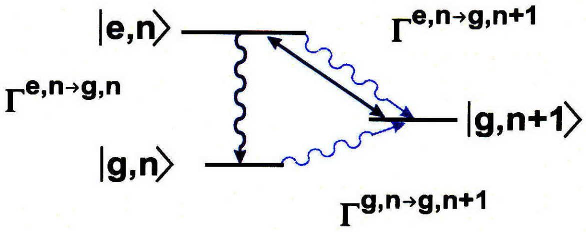

Figure 4-1: Diagram of atomic sideband cooling. External excitation transfers the thermal population from state $|\mathrm{g}, \mathrm{n}+1\rangle$ to state $|\mathrm{e}, \mathrm{n}\rangle$ (straight line), from which it decays into the ground state $|\mathrm{g}, \mathrm{n}\rangle$. Wavy lines represent spontaneous relaxation and absorption, where $\Gamma^{\mathrm{e,n}\rightarrow\mathrm{g,n}} \gg \Gamma^{\mathrm{e,n}\rightarrow\mathrm{g,n+1}}, \Gamma^{\mathrm{g,n}\rightarrow\mathrm{g,n+1}}$ is required for cooling from n+1 to n.

approach has advantages, such as cooling ancillary electronics, it also has drawbacks. In particular, poor heat conduction at millikelvin temperatures limits the lowest temperatures attainable.

A fundamentally different approach to cooling has been developed and implemented in quantum optics [81]. The key idea is that the degrees of freedom of interest may be cooled individually, without relying on thermal conduction between the refrigerator and the experiment. By such directed cooling processes, the temperature of individual quantum states can be reduced by many orders of magnitude with little effect on the temperature of surrounding degrees of freedom.

In one successful approach known as sideband cooling [82], the unwanted thermal population of an excited state is eliminated by driving it via a resonant sideband transition to a higher excited state, whose population quickly relaxes into the ground state. The three-level system just described is illustrated in Fig. 4-1, and results from a two-level atomic system (TLAS) confined as a simple harmonic oscillator (SHO) from a trap potential, where the goal is to cool the excited state population in the SHO degree of freedom. Using the notation $|\mathrm{TLAS\ state, SHO\ state}\rangle$ with TLAS states $|\mathrm{g}\rangle, |\mathrm{e}\rangle$ and SHO states $|\mathrm{n}\rangle$ with $\mathrm{n} = 0, 1, 2, \ldots$, one drives population from the TLAS ground state with higher SHO energy, $|\mathrm{g}, \mathrm{n}{+}1\rangle$, to the TLAS excited-state with lower SHO energy, $|\mathrm{e}, \mathrm{n}\rangle$, from which it relaxes to the TLAS ground state with with lower SHO energy $|\mathrm{g}, \mathrm{n}\rangle$ (see Fig. 4-1). One has thus moved population from the

SHO state with quantum number n+1 to the SHO state with quantum number n, hence cooling the SHO degree of freedom. For cooling to be effective, the relaxation rate between $|\mathrm{e, n}\rangle$ and $|\mathrm{g, n}\rangle$, $\Gamma^{\mathrm{e,n}\rightarrow\mathrm{g,n}}$, must be much faster than both the decay rate from $|\mathrm{e, n}\rangle$ to $|\mathrm{g, n+1}\rangle$, $\Gamma^{\mathrm{e,n}\rightarrow\mathrm{g,n+1}}$, and the rate from $|\mathrm{g, n}\rangle$ to $|\mathrm{g, n+1}\rangle$, $\Gamma^{\mathrm{g,n}\rightarrow\mathrm{g,n+1}}$. Note also that the TLAS represents internal atomic states, whereas the SHO levels are external trap states.

I will now present a method of cooling the PC qubit analogous to sideband cooling just described. The idea will be to cool the two-level system of the PC qubit discussed thus far in the thesis, consisting of the states $|\Psi_-\rangle$ and $|\Psi_+\rangle$, by driving unwanted thermal population in the excited state $|\Psi_+\rangle$ to a third level that decays rapidly to the ground state $|\Psi_-\rangle$ of the two-level system. In contrast to conventional atomic sideband cooling, internal degrees of freedom of the PC qubit will be cooled by using ancillary internal states. In Ch. 4.2 I will consider how cooling is achieved in the PC qubit, focusing on a qualitative understanding of the cooling process. In Ch. 4.3 I will then consider cooling more quantitatively, with a study of the amount of thermally excited population that is actually being cooled and on what timescales. The work in this section is based on published material [83].

4.2 Cooling the PC Qubit

When the qubit is in equilibrium with its environment, some population is thermally excited from the ground state $|\Psi_-\rangle$ to the excited state $|\Psi_+\rangle$ according to $p_+/p_- = \exp[-(E_+ - E_-)/k_\mathrm{B}T_\mathrm{bath}]$, where $p_\pm$ are the qubit populations for energy levels $E_\pm$, k_B is the Boltzmann constant, and T_bath is the bath temperature. To cool the qubit subsystem below T_bath, in analogy to atomic sideband cooling, an RF flux of amplitude V and frequency ν is applied, driving the thermal population in $|\Psi_+\rangle$ to an ancillary state, from which it quickly relaxes to the ground state $|\Psi_-\rangle$.

In the case where $\delta f_\mathrm{dc} < 0$, see Fig. 4-2, thermal population in $|0, \mathrm{R}\rangle$ ($|\Psi_+\rangle$) is driven to the ancillary state $|1, \mathrm{L}\rangle$, from which it quickly relaxes to the ground state $|0, \mathrm{L}\rangle$ ($|\Psi_-\rangle$). The hierarchy of relaxation and absorption rates required for efficient

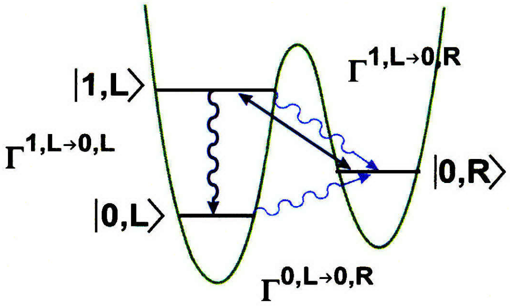

Figure 4-2: Diagram of sideband cooling in the PC qubit (illustrated for $\delta f_{\rm dc} < 0$). External excitation transfers the thermal population from state $|0,\mathrm{R}\rangle$ to state $|1,\mathrm{L}\rangle$ (straight line), from which it decays to the ground state $|0,\mathrm{L}\rangle$. Wavy lines represent spontaneous relaxation and absorption, where $\Gamma^{1,\mathrm{L}\to 0,\mathrm{L}} \gg \Gamma^{1,\mathrm{L}\to 0,\mathrm{R}}, \Gamma^{0,\mathrm{L}\to 0,\mathrm{R}}$ is required for cooling from R to L.

cooling, $\Gamma_1^{1L\to 0L} \gg \Gamma^{1L\to 0R}, \Gamma^{0L\to 0R}$, is achieved in the PC qubit system due to a relatively weak tunneling between wells, which inhibits the inter-well relaxation and absorption processes, $|1,\mathrm{L}\rangle$ to $|0,\mathrm{R}\rangle$ and $|0,\mathrm{L}\rangle$ to $|0,\mathrm{R}\rangle$, compared with the relatively strong intra-well relaxation process $|1,\mathrm{L}\rangle$ to $|0,\mathrm{L}\rangle$. The same cooling description applies when $\delta f_{\rm dc} > 0$, with the potential tilted in the opposite sense, and the labels R and L simply interchanged.

The cooling procedure illustrated in Fig. 4-2 is generalized to the energy-band diagram shown schematically in Fig. 4-3. For a particular static flux detuning $\delta f_{\rm dc} = \delta f_{\rm dc}^{*} < 0$, and driving amplitude increasing from $V = 0$, population transfer from $|0,\mathrm{L}\rangle$ to $|0,\mathrm{R}\rangle$ first occurs when the $\Delta_{0,0}$ avoided crossing is first reached. As discussed in Ch. 3, this population transfer arises from an LZ transition. As the amplitude V is further increased past $\Delta_{0,0}$, Mach-Zehnder-like interference due to the repeated action of oscillating through $\Delta_{0,0}$ arises as in Fig. 3-8. As the amplitude is further increased however, the adjacent avoided crossing $\Delta_{1,0}$ is reached, inducing LZ transitions between levels $|0,\mathrm{R}\rangle$ and $|1,\mathrm{L}\rangle$. This action now provides a mechanism for populating the ancillary state $|1,\mathrm{L}\rangle$ that is used in the cooling process. (The interesting behavior observed upon increasing V further until the $\Delta_{0,1}$ crossing is also reached is the subject of Ch. 5.2).

The corresponding qubit population as a function of static flux detuning $\delta f_{\rm dc}$

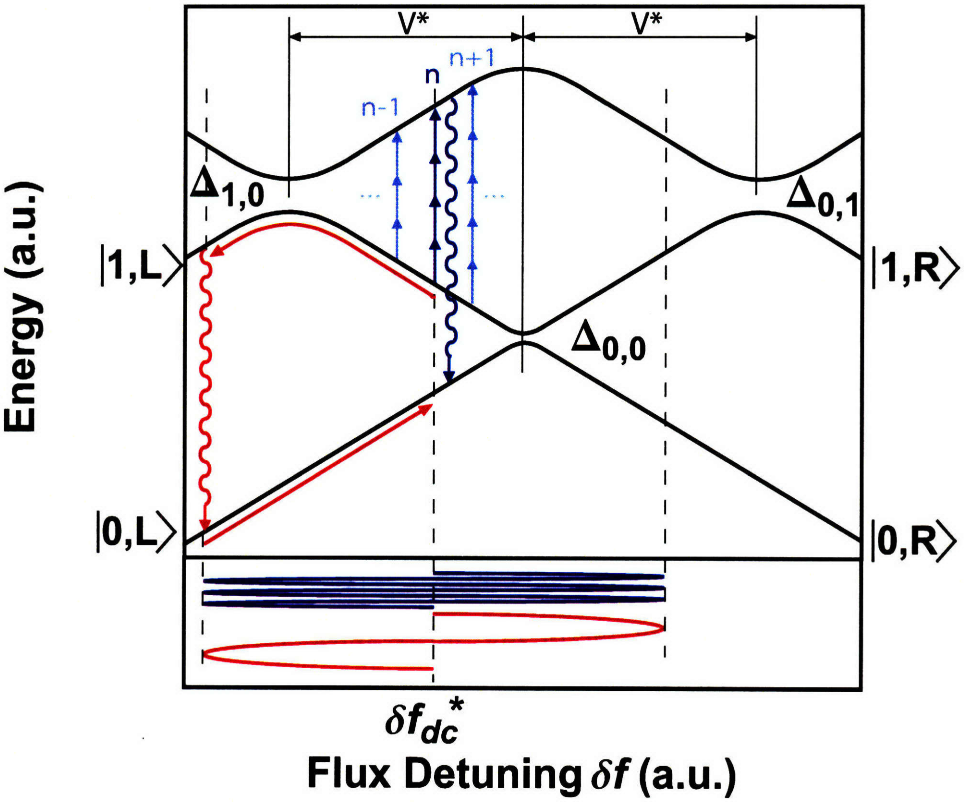

Figure 4-3: Energy level schematic explaining cooling of the PC qubit via an additional avoided crossing $\Delta_{1,0}$. The resonant and adiabatic sideband cooling regimes are illustrated. $|0R\rangle \rightarrow |1L\rangle$ transitions are resonant at high driving frequency ν (blue lines) and occur via adiabatic passage at low ν (red lines). $\Delta_{0,0}$ and $\Delta_{1,0}$ are the tunnel splittings between $|0R\rangle$ - $|0L\rangle$ and $|0R\rangle$ - $|1L\rangle$, respectively. The amplitude V* shown is the amplitude at which cooling will begin to occur no matter the starting static flux detuning δf_{dc}, which also happens to be the optimal cooling amplitude (see Ch. 4.3).

and amplitude V is shown in Fig. 4-4 when driven at $\nu = 160\,\mathrm{MHz}$. Consider the behavior for a given flux detuning $\delta f_{\mathrm{dc}} = \delta f^*_{\mathrm{dc}}$, as shown by the horizontal dashed line in Fig. 4-4. As the amplitude of the RF source voltage is increased from V=0, the population stays in the ground state $|0,\mathrm{L}\rangle$ until $\mathrm{V}=\mathrm{V}_1$ is reached. At this point $\Delta_{0,0}$ is reached, and LZ transitions begin to transfer population from $|0,\mathrm{L}\rangle$ to $|0,\mathrm{R}\rangle$. As the amplitude V is further increased past $\Delta_{0,0}$, Mach-Zehnder-like interference due to the repeated action of oscillating through $\Delta_{0,0}$ is observed. It is when $\mathrm{V}=\mathrm{V}_2$ that $\Delta_{1,0}$ is reached, inducing transitions between levels $|0,\mathrm{R}\rangle$ and $|1,\mathrm{L}\rangle$. However, due to the fast relaxation rate from $|1,\mathrm{L}\rangle$ to $|0,\mathrm{L}\rangle$, most of the population transferred from $|0,\mathrm{R}\rangle$ to $|1,\mathrm{L}\rangle$ is quickly transferred to $|0,\mathrm{L}\rangle$. One has thus cooled the two-level system approximately defined by $|0,\mathrm{L}\rangle$ and $|0,\mathrm{R}\rangle$ at δf^*_{dc}. One can actually see in Fig. 4-4 the regime where $\Delta_{0,1}$ is reached (right edge), causing an increase in population again in $|0,\mathrm{R}\rangle$ (see Ch. 5.2 for a discussion of this regime).

Fig. 4-5 shows the qubit step before and after applying a cooling pulse at several frequencies, for $T_{\mathrm{bath}} = 300$ mK. The $|0,\mathrm{R}\rangle \rightarrow |1,\mathrm{L}\rangle$ transition rate can be described by a product of a resonant factor and an oscillatory Airy factor, in direct analogy to the discussion in Ch. 3.3.2 for the $|0,\mathrm{L}\rangle \rightarrow |0,\mathrm{R}\rangle$ transition. The resonant factor dominates at high frequencies (800 and 400 MHz), where well-resolved resonances of n-photon transitions are observed, as illustrated in Fig. 4-3 (transition in blue) and shown in Fig. 4-5 (top traces and inset). The cooling is thus maximized near the detuning values matching $\mathrm{E}_{1,\mathrm{L}} - \mathrm{E}_{0,\mathrm{R}} = nh\nu$ (downward arrows in Fig. 4-5). This should be contrasted with Fig. 3-4, where transitions are pushed away from equilibrium in the opposite sense.

At intermediate frequencies (400 and 200 MHz), the Airy factor becomes more prominent and accounts for the oscillations that modulate the intensity of the n-photon resonances. Below $\nu = 200\,\mathrm{MHz}$, although individual resonances are no longer discernible, the modulation envelope persists due to the coherence of the LZ dynamics at the $\Delta_{1,0}$ avoided crossing. The $|0,\mathrm{R}\rangle$ to $|1,\mathrm{L}\rangle$ transition becomes weak near the zeros of the modulation envelope, where less efficient cooling is observed, or even slight heating (e.g., upward arrows in Fig. 4-5, 800 and 400 MHz). This is a result of

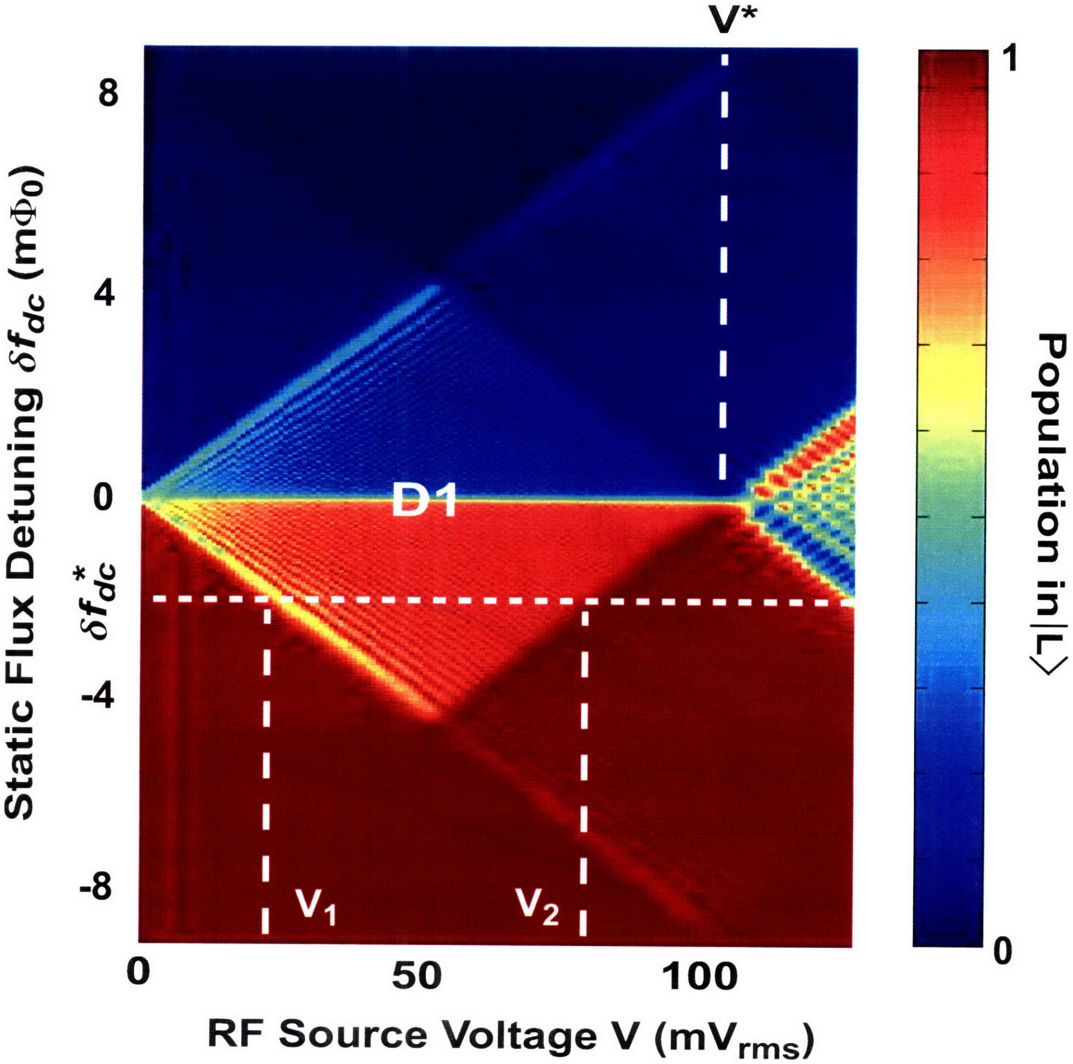

Figure 4-4: Measured qubit population, strongly driven at $\nu = 160\,\mathrm{MHz}$. For $\delta f_{\mathrm{dc}} < 0$ the back side of region D1 is due to coupling between $|0,\mathrm{R}\rangle$ and $|1,\mathrm{L}\rangle$ mediated by $\Delta_{1,0}$. For a constant $\delta f_{\mathrm{dc}} = \delta f^*_{\mathrm{dc}}$, one sees the onset of population transfer at V=V$_1$, and cooling of the excited state population after V=V$_2$. V=V* is the amplitude of optimal cooling (see Fig. 4-8). Data shown here was taken at $T_{\mathrm{bath}} = 15\,\mathrm{mK}$, and the qubit was in fact pre-cooled before each measurement.

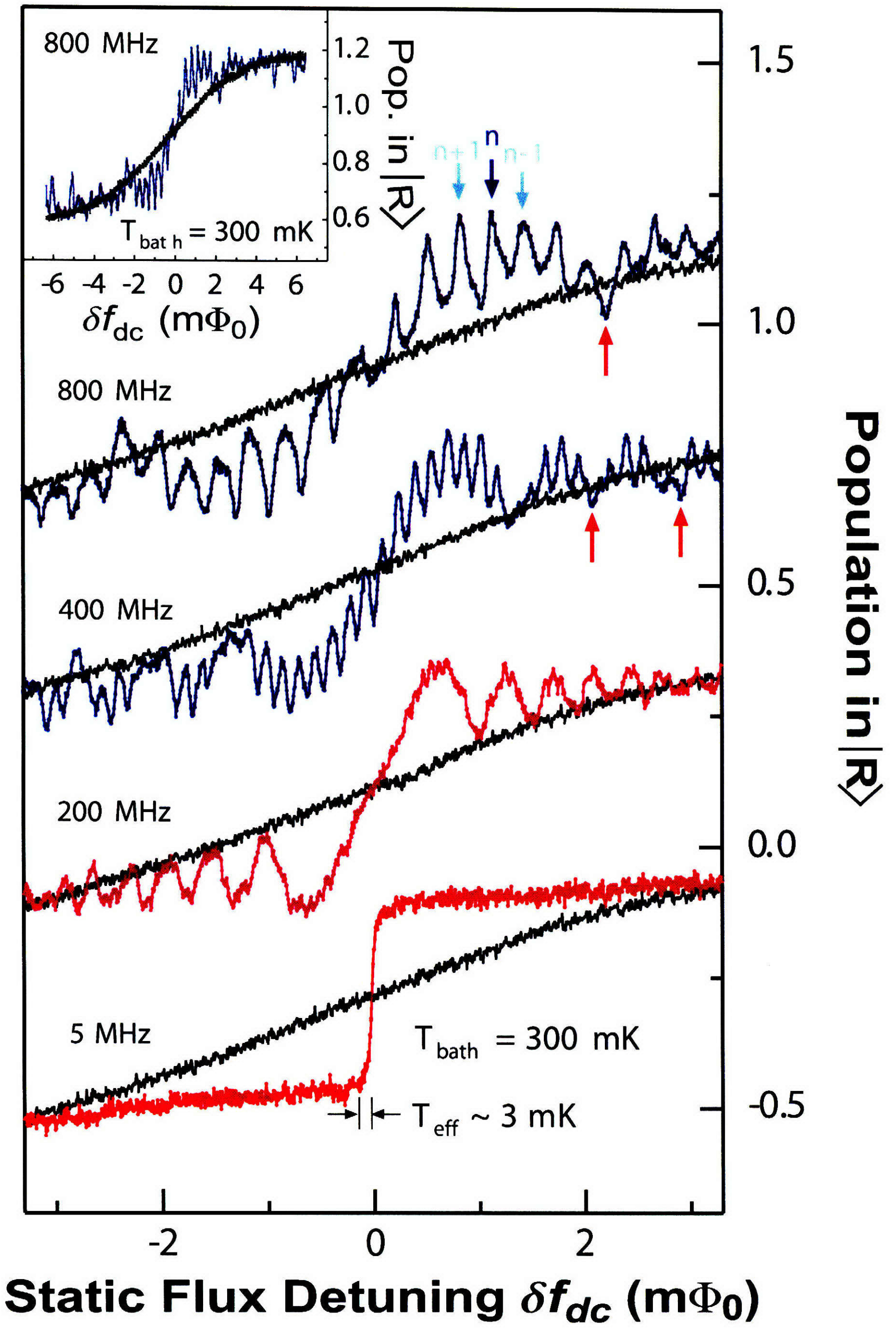

Figure 4-5: Cooling induced by RF pulses with driving frequencies ν = 800, 400, 200 and 5 MHz, with V=V*. Population in $|\mathrm{R}\rangle$ versus static flux detuning δf_{dc} for the cooled qubit and for the qubit in thermal equilibrium with the bath (black lines, $T_{\mathrm{bath}} = 300\,\mathrm{mK}$). Measurements for ν = 800, 200 and 5 MHz are displaced vertically for clarity. (Inset) Population in $|\mathrm{R}\rangle$ versus δf_{dc} over a wider range of flux detuning; ν = 800 MHz.

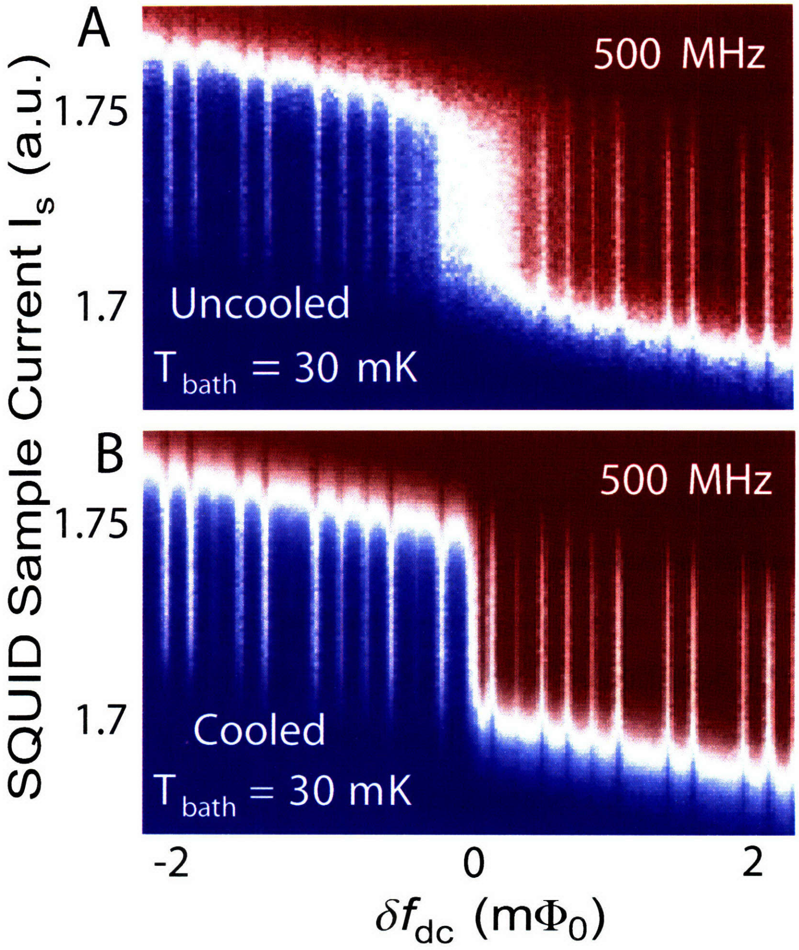

Figure 4-6: Verification of cooling to the ground state. Spectroscopy of (**A**) uncooled and (**B**) cooled qubit (5 MHz, 3-μs cooling pulse) at $T_{\text{bath}} = 30$ mK. The cumulative switching-probability distributions as a function of I_s and δf_{dc} under 500-MHz RF excitation are shown. The effective temperature of the cooled qubit is 3mK.

the $|0, \mathrm{L}\rangle$ to $|0, \mathrm{R}\rangle$ transition rate which, although relatively small, $\Delta_{0,0}^2 \ll \Delta_{1,0}^2$, acts to excite the qubit when the usually dominant $|0, \mathrm{R}\rangle$ to $|1, \mathrm{L}\rangle$ transition rate vanishes. At low frequencies [$\nu \leq \nu_0 = (\Delta_{1,0}^3/A^*)^{1/2}/h \approx 10\,\mathrm{MHz}$], the state $|1, \mathrm{L}\rangle$ is reached via adiabatic passage (Fig. 4-3, red lines) and the population transfer and cooling become conveniently independent of static flux detuning (see $\nu = 5$ MHz in Fig. 4-5).

To determine whether the observation of a sharp qubit step proves that the system makes transitions to the ground state, as opposed to populating an excited state with the same circulating current as the ground state, the excitation spectra of the "pre-cooled" qubit and of the qubit in thermal equilibrium with the bath were measured (Fig. 4-6). In the former, a weak RF excitation was applied immediately after the cooling pulse (time-lag less than 100 ns), well before the system equilibrates by warming up to the bath temperature (see discussion of cooled qubit equilibration times in Ch. 4.3). By comparing the excitation spectra of the equilibrium and cooled systems one sees that, although cooling markedly reduces the step width, the excitation spectrum remains unchanged. Because the RF excitation is resonant with the $|\Psi_-\rangle$ to $|\Psi_+\rangle$ transition only, this strongly indicates that the population in a cooled qubit is indeed in the ground state.

Thus far, I have only considered the basic mechanism behind cooling, and a qualitative measure of whether cooled population actually goes to the ground state. I will now turn to a more quantitative characterization of the cooling process. I will focus on the definition of temperature, and study what temperatures are actually being achieved via cooling. I will then study the dependence of the cooled temperature on driving parameters, and finally consider the utility of cooling by studying the timescales involved in the cooling process.

4.3 Quantifying Cooling

Under equilibrium conditions, the two-level qubit populations exhibit a thermally-broadened qubit step, given by $m_0 = p_- - p_+ = \tanh \frac{\varepsilon}{2k_B T_{\mathrm{bath}}}$ (see Ch. 3.3.2), where ε is the static flux detuning δf_{dc} in units of energy. Up to this point though, it has been assumed that the SQUID measurement of the qubit is a single shot measurement; i.e., one can perfectly distinguish the two circulating currents eigenstates. This has been a valid assumption thus far, since temperatures have been kept low enough, but as the bath temperature increases, the SQUID distribution increases, reducing the fidelity F of the measurement. The measured equilibrium qubit step is then measured to be

$$\text{Pop. in } |\mathrm{R}\rangle = \frac{1}{2}(1 + \mathrm{F}\mathrm{m}_0). \tag{4.1}$$

When an RF field is applied, the qubit is no longer in equilibrium with the bath,

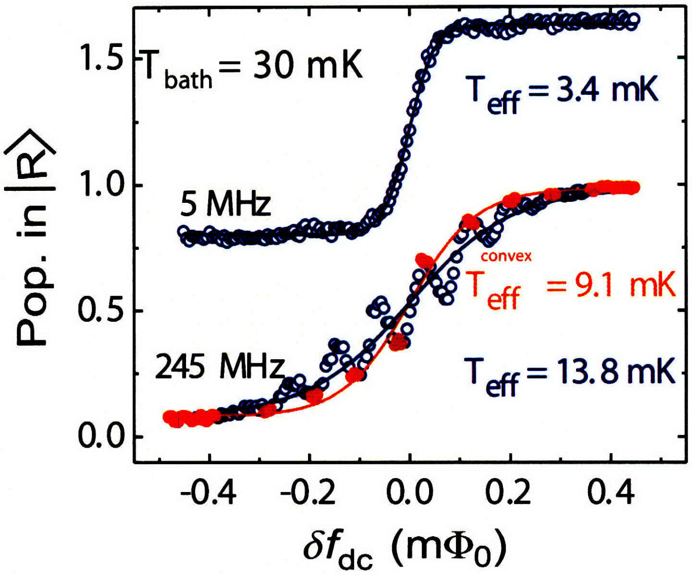

Figure 4-7: Definition of effective temperature T_{eff} of qubit. Qubit steps measured at $\nu = 5$ and 245 MHz (circles) and best fits to Eq. 4.1. At 245 MHz, the aggregate temperature fitting (blue, $T_{\text{eff}} = 13.8$ mK) and the convex fitting (orange, $T_{\text{eff}} = 9.1$ mK) are shown. $T_{\text{bath}} = 30$ mK and V=V*.

but it can still be well-characterized by an effective temperature T_{eff} using Eq. 4.1 with T_{eff} instead of T_{bath}. This is illustrated in Fig. 4-7 for $\nu = 5$ MHz and $\nu = 245$ MHz ($T_{\text{bath}} = 30$ mK). At $\nu = 5$ MHz, the qubit step clearly follows Eq. 4.1, as shown with a fit line for $T_{\text{eff}} = 3.4$ mK. At 245 MHz, individual multiphoton resonances are evident, and the population in $|\text{R}\rangle$ is a non-monotonic function of δf_{dc}. In this case, T_{eff} is still a useful parameter to quantify the effective cooling, but it should be interpreted as an aggregate temperature over all detunings. Alternatively, because the cooling is maximized at individual resonances, one may perform a convex fitting of Eq. 4.1, where only the solid (orange) symbols are taken into account to determine the effective temperature at the resonance detunings. The convex effective temperature $T_{\text{eff}}^{\text{convex}} = 9.1$ mK is smaller than the aggregate value $T_{\text{eff}} = 13.8$ mK. Throughout this work I will only refer to the more conservative effective temperature obtained using the aggregate definition.

Fig. 4-8 shows the variation of T_{eff} about $V = V^*$, the region marked in Fig. 4-4, for $\nu = 5$ MHz and $\nu = 245$ MHz (insets show the raw data). As seen in these

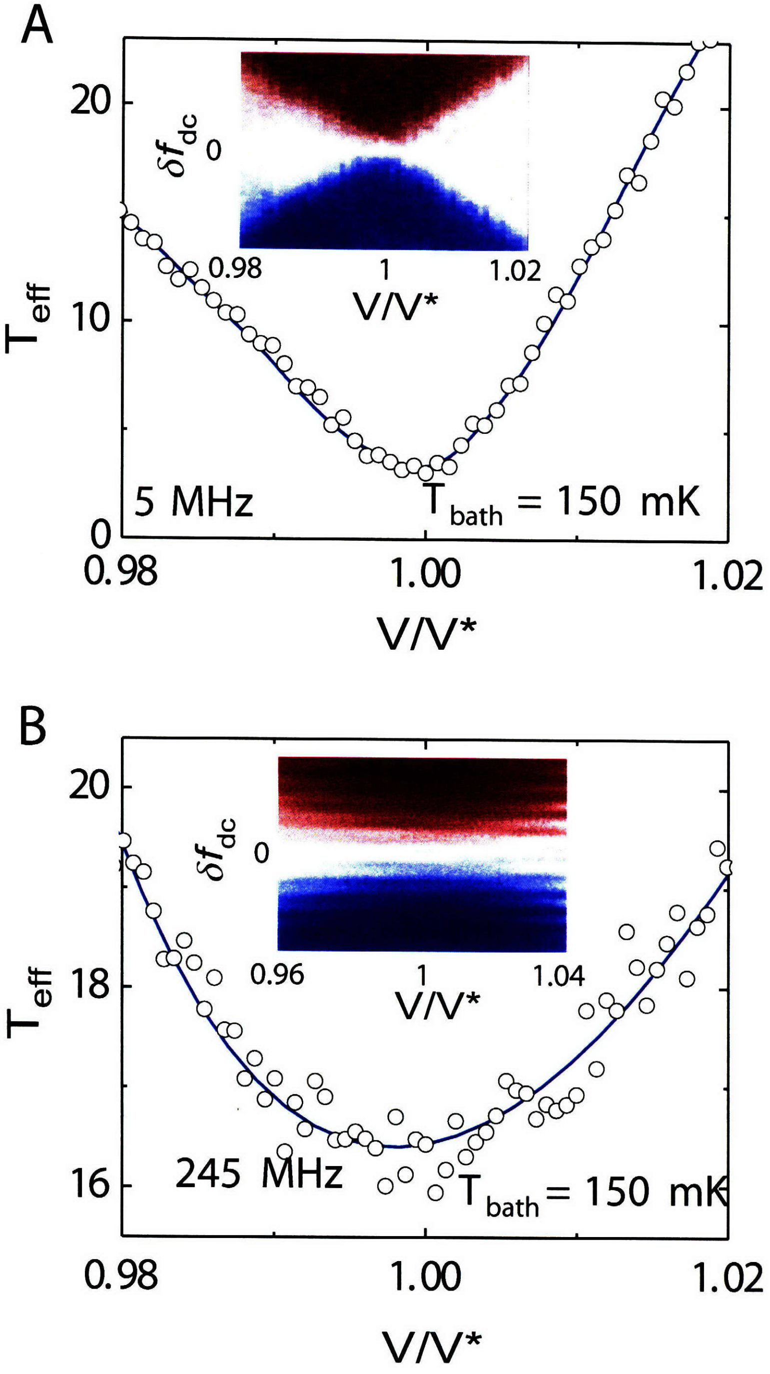

Figure 4-8: (Insets) Detail of the region $V \approx V^*$ (Fig. 4-4) for (**A**) $\nu = 5$ MHz and (**B**) $\nu = 245$ MHz. In each case, T_{eff} is extracted from the qubit step. Lines are guides for the eye; Δt = 3 μs, $T_{\text{bath}} = 150$ mK.

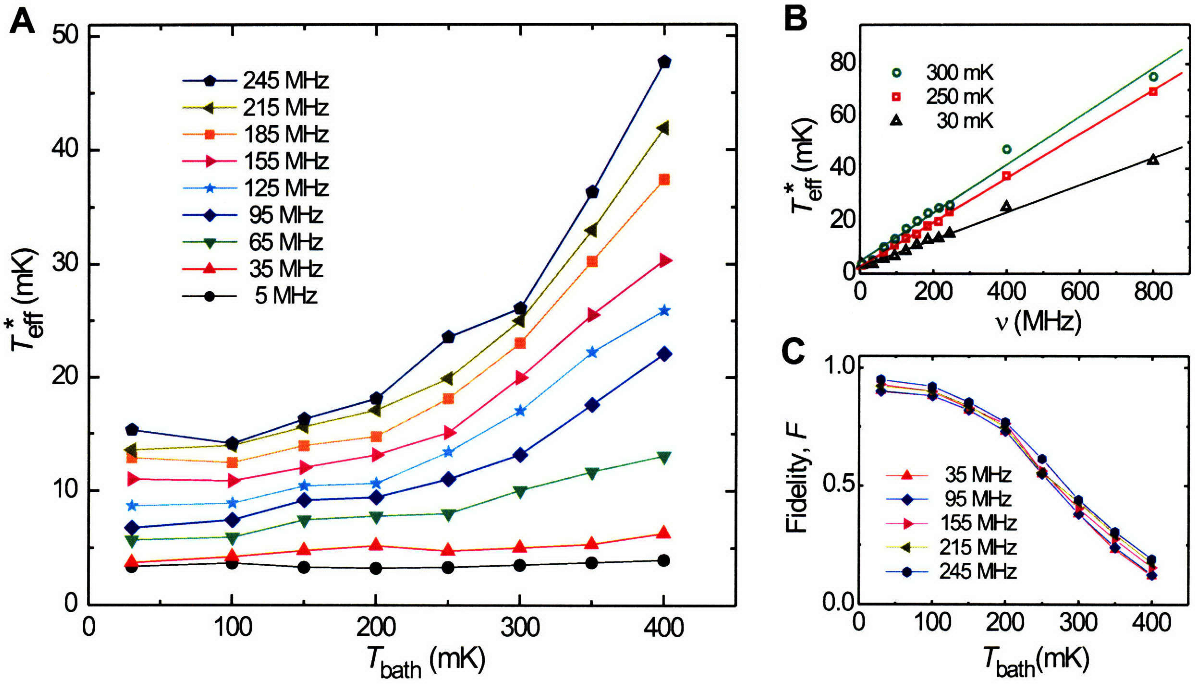

Figure 4-9: Effective temperature $T^*_{\rm eff}$ and measurement fidelity F. (**A**) $T^*_{\rm eff}$ versus $T_{\rm bath}$ at the indicated driving frequencies ν. $T^*_{\rm eff}$ increases with $T_{\rm bath}$ at high ν, but remains constant at low ν. (**B**) $T^*_{\rm eff}$ versus ν for different $T_{\rm bath}$. Lines are linear fits. (**C**) F versus $T_{\rm bath}$ at the indicated ν. A pulse width Δt = 3 μs was used, with V=V*, in all cases.

figures, $T_{\rm eff}$ typically presents a minimum, where the cooling is most efficient and from which V^* can be determined. This can be understood as the amplitude at which only one side avoided crossing is reached for any static flux detuning within the two-level approximation. Once two side avoided crossings are reached, the effects of cooling are destroyed due to transitions at the third crossing.

Figure 4-9, A and B, summarize the dependence of $T^*_{\rm eff} = T_{\rm eff}(\mathrm{V}^*)$ on the dilution refrigerator temperature $T_{\rm bath} = 30 - 400$ mK for several frequencies ν, spanning the resonant sideband to the adiabatic passage limits, with a fixed pulse width Δt = 3 μs. In Fig. 4-9A, at large ν, $T^*_{\rm eff}$ exhibits a monotonic increase with $T_{\rm bath}$, which becomes less pronounced as ν decreases, due to a decreasing fraction of uncooled

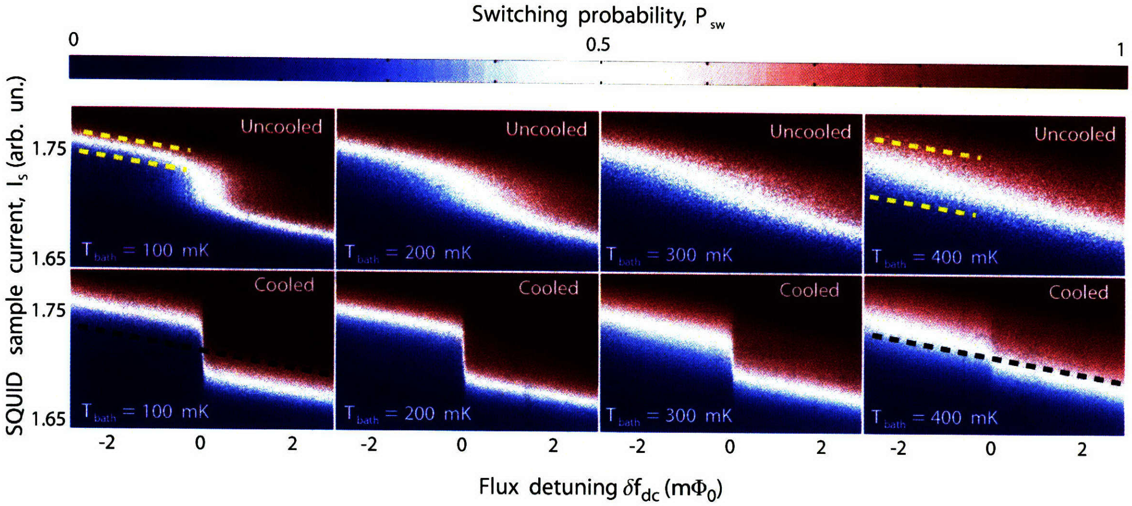

Figure 4-10: Cumulative switching distribution of the qubit as a function of I_s and δf_{dc} of the qubit in equilibrium with the bath (top) and of the cooled qubit (bottom) at different T_{bath}. The cooling pulse has $\Delta t = 3$ μs, and $\nu = 5$ MHz. Although the cooled qubit step remains sharp ($T_{eff} \sim 3$ mK), the readout SQUID switching distribution broadens as T_{bath} increases (yellow dashed lines), reducing the readout fidelity F (along the dashed black lines).

qubit step portions with decreasing ν. In the adiabatic passage limit, e.g. $\nu = 5$ MHz, $T^*_{eff} \approx 3$ mK is practically constant and reaches values that, notably, can be more than two orders of magnitude smaller than T_{bath}. In Fig. 4-9B, T^*_{eff} is observed to increase linearly with ν for different values of T_{bath}. The apparent cooling limit of $T^*_{eff} \approx 3$ mK is consistent with the inhomogeneously broadened linewidth observed in these experiments (see Ch. 3.3.3), which likely places a lower limit on the measurable minimum temperature, but is not a fundamental cooling limit.

Fig. 4-9C displays the measurement-fidelity F versus T_{bath}. Although the qubit is effectively cooled, $T^*_{eff} \ll T_{bath}$, over the range of T_{bath} in Fig. 4-9, A and B, the readout SQUID is not actively cooled, and its switching current distribution broadens with T_{bath}. The full 2D cumulative switching distribution of the SQUID near the qubit step is shown in Fig. 4-10. One can see the cooled qubit step, while the SQUID distribution broadens as T_{bath} is raised. At high temperatures, the fidelity F, defined in Eq. 4.1, becomes too small to discriminate the two qubit states, independent of the qubit's effective temperature. The fidelity F is observed to be larger than 0.8 for

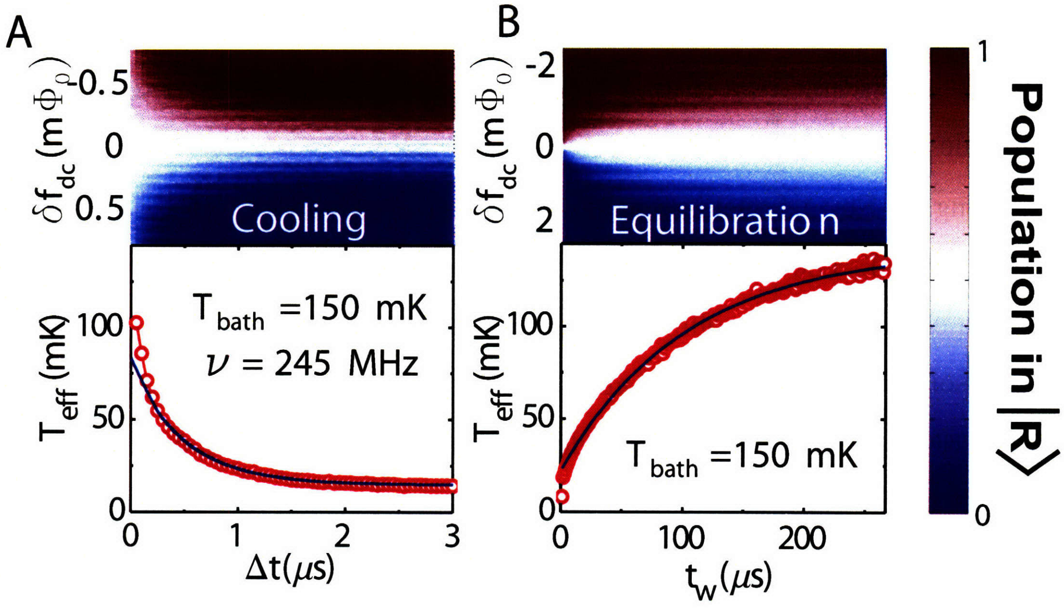

Figure 4-11: Dynamics of qubit cooling and equilibration. (**A**) (Upper panel) Population in $|\mathrm{R}\rangle$ as a function of δf_{dc} and cooling pulse width $\Delta\mathrm{t}$ ($\nu = 245$ MHz). (Lower panel) T_{eff} versus $\Delta\mathrm{t}$ extracted from upper panel (circles) and exponential fit (blue line) with $\sim$ 1-μs time constant. (**B**) (Upper panel) Population in $|\mathrm{R}\rangle$ as a function of δf_{dc} and waiting time t_{w} after the cooling pulse ($\Delta\mathrm{t} = 3$ μs and $\nu = 5$ MHz). (Lower panel) T_{eff} versus t_{w} extracted from upper panel (circles) and exponential fit (blue line) with $\sim$ 100-μs time constant. $T_{\mathrm{bath}} = 150$ mK.

$T_{\mathrm{bath}} < 100$ mK, remains above 0.5 at ^{3}He refrigerator temperatures, but drops to $F \approx 0.1$ at $T_{\mathrm{bath}} = 400$ mK, limiting one's ability to measure the qubit state at higher temperatures.

The cooling and equilibration dynamics of the qubit are summarized in Fig. 4-11 and Fig. 4-12 ($T_{\mathrm{bath}} = 150$ mK). Cooling a qubit in equilibrium with the bath requires a characteristic cooling time. In turn, a cooled qubit is effectively colder than its environment, a non-equilibrium condition, which over a characteristic equilibration time will thermalize to the environmental bath temperature. This relation between cooling and equilibration times determines the facility of cooling the qubit and performing operations while still cold. Fig. 4-11, A and B, show the time evolution of cooling and warming up of the qubit step. The top panels show the population in $|\mathrm{R}\rangle$ as a function of δf_{dc} and cooling-pulse length $\Delta\mathrm{t}$ (Fig. 4-11A, $\nu = 245$ MHz), and as a function of δf_{dc} and waiting-time t_{w} after pre-cooling with a 5 MHz pulse (Fig. 4-11B).

Note the difference in the time scales, where it is observed that substantial cooling is accomplished within 1 μs (Fig. 4-11A), but equilibration occurs over a much longer time scale (Fig. 4-11B).

Fitting to Eq. 4.1 yields T_{eff} as a function of Δt and t_w (Fig. 4-11, A and B, bottom panels). The near exponential behavior of T_{eff} versus Δt and t_w allows one to infer the characteristic cooling and equilibration times as defined by an exponential fitting (solid blue lines), which are summarized in Fig. 4-12. Notably, the cooling characteristic time is nearly independent of both ν and T_{bath} and, on average, is about 500 ns. It is this quick cooling time that allows a repetition rate between experiments of 10kHz, rather than the 200Hz used before cooling was developed, necessary for post-measurement relaxation to occur naturally over $\sim$ 5ms. In contrast, at the base temperature of the dilution refrigerator, the equilibration time is about three orders of magnitude longer, 300 μs, and remains one order of magnitude longer at 250 mK, a temperature that is accessible with ^{3}He refrigerators. The decrease of the equilibration time with increasing T_{bath} is simply due to the Boltzmann factor described in Ch. 3.3.2. The large discrepancy between equilibration and cooling times allows for the straightforward implementation of pre-cooling, with little concern for a loss of cooling between the pre-cooling pulse and the experiment.

4.4 Summary

I have just presented the first demonstration of microwave-induced cooling in a superconducting flux qubit. The thermal population in the first-excited state of the qubit was driven to a higher-excited state by way of a sideband transition. Subsequent relaxation into the ground state resulted in cooling. Effective temperatures as low as $T_{\text{eff}} \approx 3$ millikelvin are achieved for bath temperatures $T_{\text{bath}} = 30 - 400$ millikelvin, a cooling factor between 10 and 100. This demonstration provides an analog to optical cooling of trapped ions and is generalizable to other solid-state quantum systems. Active cooling of qubits, applied to quantum information science, provides a means for rapid qubit-state preparation with improved accuracy, and for suppressing decoher-

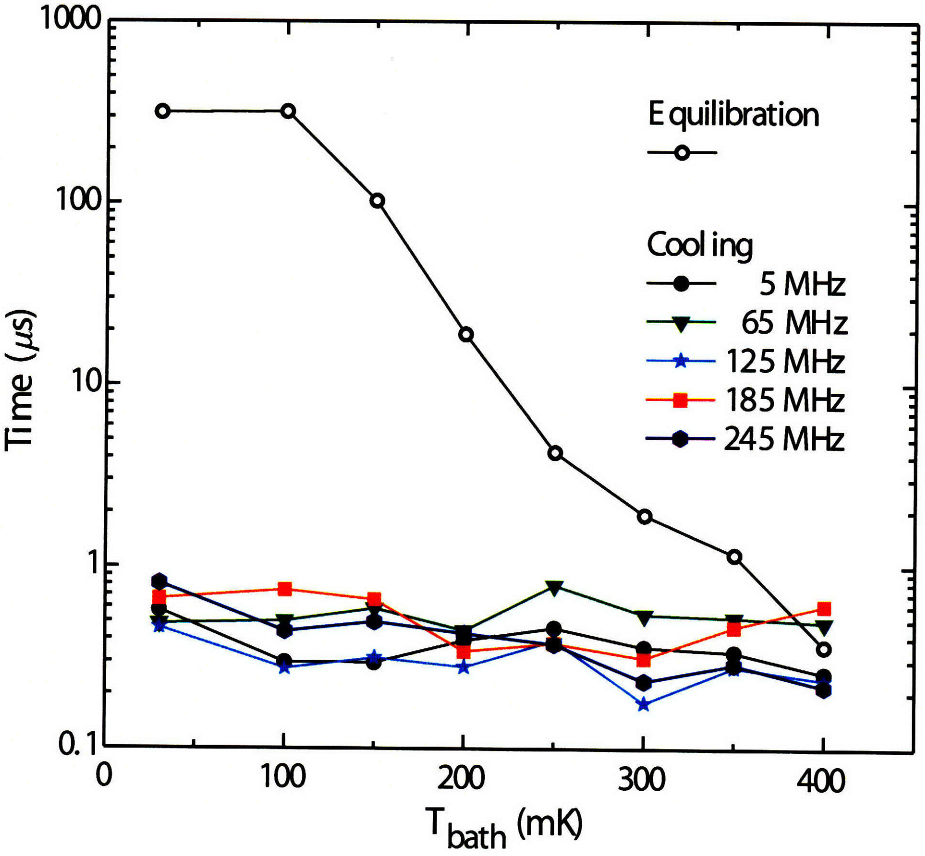

Figure 4-12: Characteristic equilibration and cooling times for different T_{bath}. Cooling is performed at the indicated frequencies and equilibration follows a cooling pulse of $\Delta \mathrm{t} = 3$ μs and $\nu = 5$ MHz. Characteristic times are found via the procedure outlined in Fig. 4-11.

ence in multi-qubit systems. Pre-cooling of the PC qubit was an integral part of the experiments done in Ch. 3 and Ch. 5, as it allowed for better state preparation and less wait time between experiments, and is now a standard part of most experiments done in our laboratory.

Chapter 5

Large Amplitude Driving with Many Avoided Crossings: Amplitude Spectroscopy

Thus far I have only considered the lowest 4 levels of the PC qubit, with a pair of side avoided crossings flanking the main two-level system of the qubit. If one drives the qubit strong enough, even higher energy levels and avoided crossings can be accessed (Fig. 2-3). In this chapter I will discuss a new form of spectroscopy, dubbed "amplitude spectroscopy", that is achieved by increasing the driving amplitude as far as possible. The technique can be used to characterize the full energy level spectrum of the PC qubit, just by studying the qubit population as a function of driving amplitude. Ch. 5 is truly a culmination of the previous work I have presented in Ch. 3 and Ch. 4, and as such I will refer back to the concepts discussed there regularly.

5.1 Introduction

The energy-level structure of a quantum system plays a fundamental role in determining its behavior and manifests itself in a discrete absorption and emission spectrum. Conventionally, spectra are probed via frequency spectroscopy whereby the frequency ν of a harmonic driving field is varied to fulfill the condition $\Delta E = h\nu$, where the driving field is resonant with level separation ΔE and h is Planck's constant. Although this technique has been successfully employed in a variety of physical systems, including natural and artificial atoms [39, 84, 85], its application is not universally straightforward, because it generally requires scanning a broad range of frequencies nominally at a fixed amplitude. This becomes particularly challenging for frequencies in the range of 10's and 100's of gigahertz due to dispersion and increased attenuation.

Here, I introduce amplitude spectroscopy, an alternative approach to characterizing the multi-level energy spectrum of the PC qubit, that circumvents the challenge of high frequencies. Amplitude spectroscopy, in contrast to frequency spectroscopy, probes the energy level structure of a quantum system via its response to driving-field amplitude rather than frequency. It is generally applicable to systems with energy-level avoided crossings that can be traversed using an external control parameter. Such longitudinal excursions throughout the energy level diagram would typically be realized by strongly driving the system with an external field at a fixed frequency, which may be several orders of magnitude lower than the energy-level spacing. In this limit, the system evolves adiabatically, except in the vicinity of energy-level avoided crossings where LZ-type quantum-coherent transitions occur. The quantum interference between repeated LZ transitions gives rise to interference fringes that encode information about the system's energy spectrum. By trading amplitude for frequency, the amplitude spectroscopy approach allows one to probe quantum systems with strong coupling to external fields, such as solid-state artificial atoms, over extraordinarily wide bandwidths, bypassing the limitations of a frequency-based approach.

The rest of this chapter will be broken up into two main parts. In Ch. 5.2 I will consider the basic mechanisms behind amplitude spectroscopy. I will focus on a qualitative understanding of what happens when driving amplitude is strong enough to sweep the qubit through many avoided crossings. The observed qubit population will be the result of many of the concepts introduced in Ch. 3 and Ch. 4, now just being realized at higher avoided crossings. In Ch. 5.3 I will move on to a quantitiatve characterization of the energy spectrum of the PC qubit. From the observed qubit population as a function of driving amplitude, I will reconstruct a portion of the qubit's energy spectrum. The work in this section is based on material recently submitted for publication [86].

5.2 Diamonds: Accessing an Entire Energy Manifold

Fig. 5-1A displays the amplitude spectroscopy of the qubit driven towards saturation. Driving frequency ν was chosen such that, throughout the driving cycle, $h\nu$ is generally much smaller than the instantaneous energy-level spacing, while the speed at which the qubit is swept through avoided crossings is large enough to make the evolution through avoided crossings non-adiabatic. As previously discussed (Ch. 3 and Ch. 4), LZ transitions drive the system into coherent superpositions of energy eigenstates associated with different wells. Four primary "spectroscopy diamonds" with large population contrast, centered about $\delta f_{\mathrm{dc}} = 0$ (D1, D2, D3, and D4), are observed in the data; they are flanked by eight fainter diamonds, as shown in Fig. 5-1A. The diamond structures and the interference patterns within them result from the interplay between driving parameters and the energy level spectrum of the qubit. The energy spectrum is characterized by three features: avoided crossing locations, energy level slopes, and avoided crossing sizes, as shown in Fig. 5-1B. The diamond shapes and inner interference patterns will allow for a full characterization of these features, and hence the energy level spectrum. Before extracting spectroscopic information, let me describe how the diamonds come about.

Fig. 5-1A shows the measured qubit population as a function of driving amplitude, while Fig. 5-1B shows the energy level diagram with a description of the physical processes involved in creating the diamonds (for $\delta f_{\mathrm{dc}}^{*} <0$). As the amplitude of the RF source voltage is increased from V=0, the population stays in the ground state $|0,\mathrm{L}\rangle$ until $\mathrm{V}=\mathrm{V}_1$ is reached. At this point $\Delta_{0,0}$ is reached, and LZ transitions begin to transfer population from $|0,\mathrm{L}\rangle$ to $|0,\mathrm{R}\rangle$. This event, occurring at different amplitudes

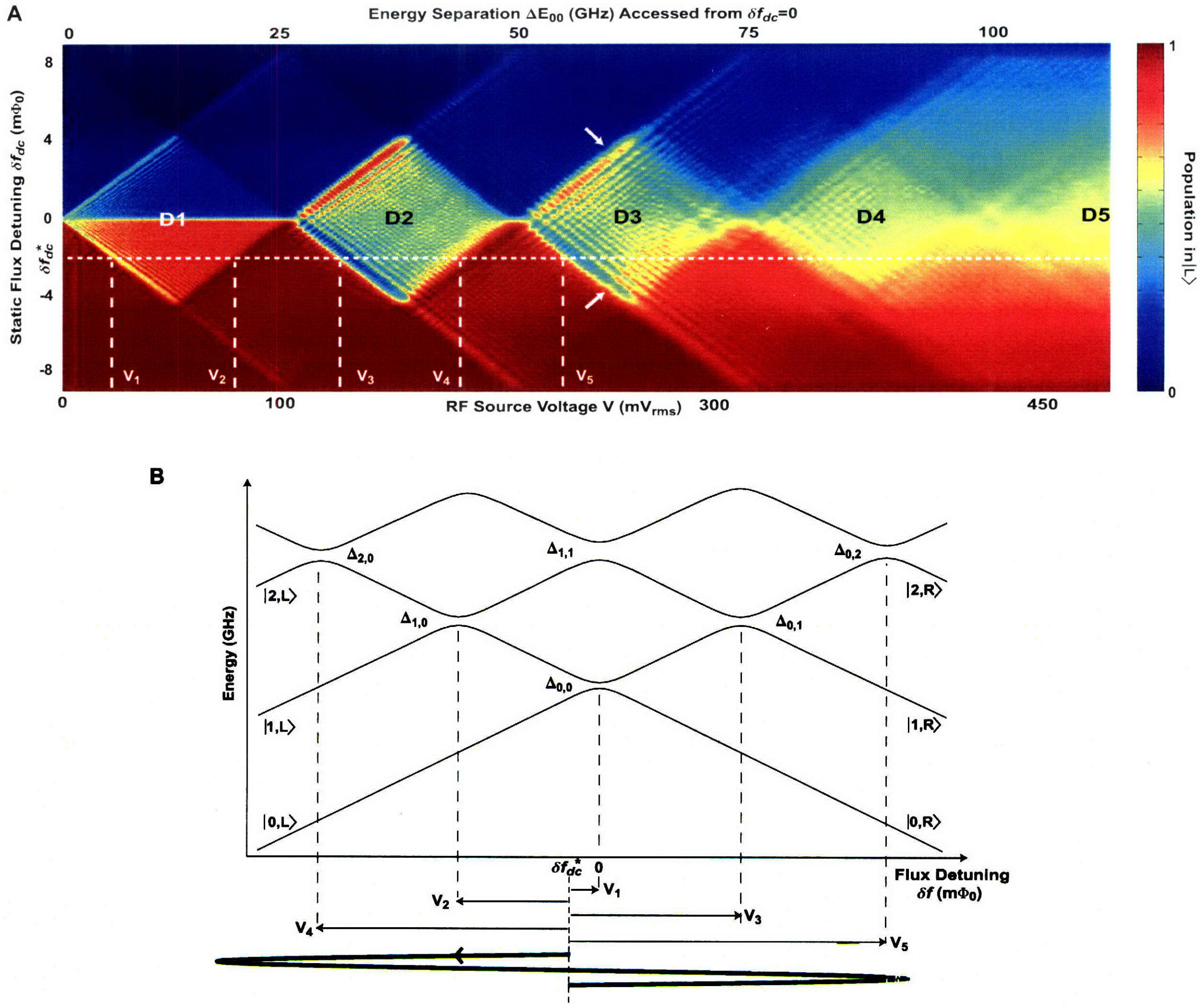

Figure 5-1: (**A**) Amplitude spectroscopy with long-pulse driving towards saturation. The qubit is driven at a fixed frequency $\nu = 0.160$ GHz ($\Delta\mathrm{t} = 3\,\mu$s), while amplitude V is swept for each static flux detuning δf_{dc}. The diamond edges signify the driving amplitude V for each value of δf_{dc} when an avoided level crossing is first reached (amplitudes $V_1 - V_5$ for $\delta f_{\mathrm{dc}} = \delta f^*_{\mathrm{dc}}$). The main diamond regions, symmetric about $\delta f_{\mathrm{dc}} = 0$, are labeled D1 to D5. Arrows indicate signatures of transverse mode coupling (see Fig. 5-9). Top axis: the $|0,\mathrm{L}\rangle - |0,\mathrm{R}\rangle$ energy spacing $\Delta E_{0,0}$ accessed by V from $\delta f_{\mathrm{dc}} = 0$. (**B**) Schematic energy-level diagram illustrating the relation between the driving amplitude V and the avoided crossing positions for a particular static flux detuning $\delta f_{\mathrm{dc}} = \delta f^*_{\mathrm{dc}}$. The arrows represent the amplitudes $V_1 - V_5$ of the RF field at which the illustrated avoided crossings are reached, marking the onset of the diamond regions in (A).

for different values of δf_{dc} create the front side of diamond 1. As the amplitude V is further increased past $\Delta_{0,0}$, Mach-Zehnder-like interference due to the repeated action of oscillating through $\Delta_{0,0}$ is observed (see Ch. 3 for an in-depth discussion of this region).

As the amplitude is further increased however, the adjacent avoided crossing $\Delta_{1,0}$ is reached, inducing transitions between levels $|0,\mathrm{R}\rangle$ and $|1,\mathrm{L}\rangle$. This happens when $\mathrm{V}=\mathrm{V}_2$. However, due to the fast relaxation rate from $|1,\mathrm{L}\rangle$ to $|0,\mathrm{L}\rangle$, most of the population transferred from $|0,\mathrm{R}\rangle$ to $|1,\mathrm{L}\rangle$ is quickly transferred to $|0,\mathrm{L}\rangle$. One has thus cooled the two-level system approximately defined by $|0,\mathrm{L}\rangle$ and $|0,\mathrm{R}\rangle$ at $\delta f^{*}_{\mathrm{dc}}$ (see Ch. 4 for an in-depth discussion of this region). This marks the back of the first diamond.

For $V_2 < V < V_3$ (see Fig. 5-1, A and B), the saturated population depends on the competition between transitions at $\Delta_{0,0}$ and $\Delta_{1,0}$, on fast intrawell relaxation, and to a lesser extent on much slower interwell relaxation processes. Because in this experiment $\Delta_{0,0} \ll h\nu \approx \Delta_{1,0}$, the result is dominated by the dynamics at the $\Delta_{1,0}$ crossing. Although transitions $|0,\mathrm{L}\rangle \rightarrow |0,\mathrm{R}\rangle$ are induced at the $\Delta_{0,0}$ crossing, stronger transitions at $\Delta_{1,0}$ convert a substantial fraction of that population to $|1,\mathrm{L}\rangle$. This excited population quickly relaxes back to $|0,\mathrm{L}\rangle$, thus suppressing the net population transfer. For the combinations of δf_{dc} and V where interference between successive passages through $\Delta_{1,0}$ is instead destructive, signatures of transitions due to $\Delta_{0,0}$ are visible, albeit with reduced contrast (detail, Fig. 5-2A, and upward arrows in Fig. 4-5).

At even larger amplitudes, transitions to additional excited states become possible. When $V > V_3$, the qubit can make transitions between $|0,\mathrm{L}\rangle$ and $|1,\mathrm{R}\rangle$, marking the front side of diamond D2 (see Fig. 5-1, A and B). The backside of this diamond is marked by the amplitude $V = V_4$ that reaches $\Delta_{2,0}$, allowing transitions between $|0,\mathrm{R}\rangle$ and $|2,\mathrm{L}\rangle$. This description can be extended straightforwardly to the remainder of the spectrum. In this device, explicit signatures of coherent multi-path traversal between the $\delta f < 0$ and $\delta f > 0$ regions of the energy-level diagram (e.g., via avoided crossings $\Delta_{1,1}$ and $\Delta_{2,2}$, $\ldots$) were not found.

There are two remarkable features associated with the amplitude spectroscopy shown in Fig. 5-1A. First, one is able to probe the qubit continuously over extraordinarily wide bandwidths using a single driving frequency of only 0.16 GHz. The highest diamond (D5) in Fig. 5-1A results from transitions to energy levels more than 100 GHz$\times h$ above the ground state. Even at such high energy levels, the PC qubit retains its energy-level structure in the presence of the strong driving used to access them.

Second, diamond D2 (see Fig. 5-1A) exhibits strong population inversion, due to competition between transitions at avoided crossings $\Delta_{0,1}$ and $\Delta_{1,0}$, combined with fast intrawell relaxation to $|0,\mathrm{L}\rangle$ and $|0,\mathrm{R}\rangle$. The transition rates at $\Delta_{0,1}$ and $\Delta_{1,0}$ exhibit strong oscillatory behavior due to LZ interference, constructive or destructive, depending on the values of δf_{dc} and V. As seen in Fig. 5-2A, the competition between these rates leads to a checkerboard pattern symmetric about $\delta f_{\mathrm{dc}} = 0$ with alternating regions of strong population inversion and efficient cooling. For detunings $\delta f_{\mathrm{dc}} < 0$ at fixed frequency ν, there exist certain amplitudes V for which the interference conditions at $\Delta_{0,1}$ result in a strong transition from $|0,\mathrm{L}\rangle \rightarrow |1,\mathrm{R}\rangle$. When followed by fast intrawell relaxation to $|0,\mathrm{R}\rangle$, this transiently inverts the population. As the qubit is subsequently driven through $\Delta_{1,0}$, if these driving conditions keep the population in $|0,\mathrm{R}\rangle$, the net result is strong population inversion in saturation. Conversely, when the conditions are reversed for $\delta f_{\mathrm{dc}} < 0$, and lead to a build-up of population in state $|0,\mathrm{L}\rangle$, the result is strong cooling. Both the inversion and cooling effects are symmetric about $\delta f_{\mathrm{dc}} = 0$ and are present in the interference patterns in D2 (Fig. 5-2A) and in the higher diamonds (Fig. 5-1A). The population inversion observed here is incoherent, and can serve as a pump, in analogy to a pump in a single-atom laser [87].

5.3 Characterizing the Energy Level Spectrum

In this section I will derive the main features of the energy spectrum of the PC qubit by analyzing the amplitude dependence of the driven qubit population. I will begin by analyzing the diamonds shown in Fig. 5-1A, which were taken using a pulse width $\Delta t = 3\mu s$. This pulse width corresponds to a qubit population that is approaching saturation (see Fig. 3-6). Analysis of higher diamonds though becomes easier when the pulse width considered is shorter, and so I will later proceed to extract energy spectrum information from scans with Δt on the order of nanoseconds.

5.3.1 Long-time Analysis

As discussed in Ch. 5.2, the onset of each diamond is associated with transitions at a particular avoided crossing. The diamond boundaries thus signify the avoided crossing locations. However, since the first avoided crossing is defined to be at $\delta f_{\mathrm{dc}} = 0\mathrm{m}\Phi_0$, and it is assumed that the energy level spectrum is symmetric, it is simplest to find higher crossing locations just from the ending point of diamonds. These are the amplitudes where a qubit biased at $\delta f_{\mathrm{dc}} = 0\mathrm{m}\Phi_0$ just reaches the next avoided crossing. A linear relation between V and Φ_{rf} exists, and the frequency-dependent conversion factor α between RF flux and source voltage is found to be $\alpha = 0.082\mathrm{m}\Phi_0/\mathrm{mV}_{\mathrm{rms}}$, inferred from the slope of the front edge of the first diamond (see Fig. 5-2A). From the ending locations of diamonds, and the conversion factor α, I obtain the avoided crossing locations $\delta f_{q,q'}$, in units of $\mathrm{m}\Phi_0$, listed in Fig. 5-7.

Given the linear nature of the energy level spectra away from the avoided crossings, one can find an expression for the energy-level separation as a function of static flux detuning in these regions. The energy-level separation between states $|q, \mathrm{L}\rangle$ and $|q',\mathrm{R}\rangle$ can be written as $\Delta E_{q,q'} \equiv h(|m_q| + |m_{q'}|)(\delta f_{\mathrm{dc}} - \delta f_{q,q'})$, which is proportional to the net flux detuning from the location $\delta f_{q,q'}$ of the avoided crossing $\Delta_{q,q'}$, and to the sum of the magnitudes of the energy-level slopes m_q and $m_{q'}$. Because the relative phase accumulated between the $|q, \mathrm{L}\rangle$ and $|q', \mathrm{R}\rangle$ components of the wave function over repeated LZ transitions is sensitive to $\Delta E_{q,q'}$, the slopes can be derived from the interference patterns which arise when varying δf_{dc} (see Ch. 3.2.4). The theory that follows was developed in collaboration with Mark Rudner and Leonid Levitov [88].

The interference between sequential LZ transitions at an isolated avoided crossing

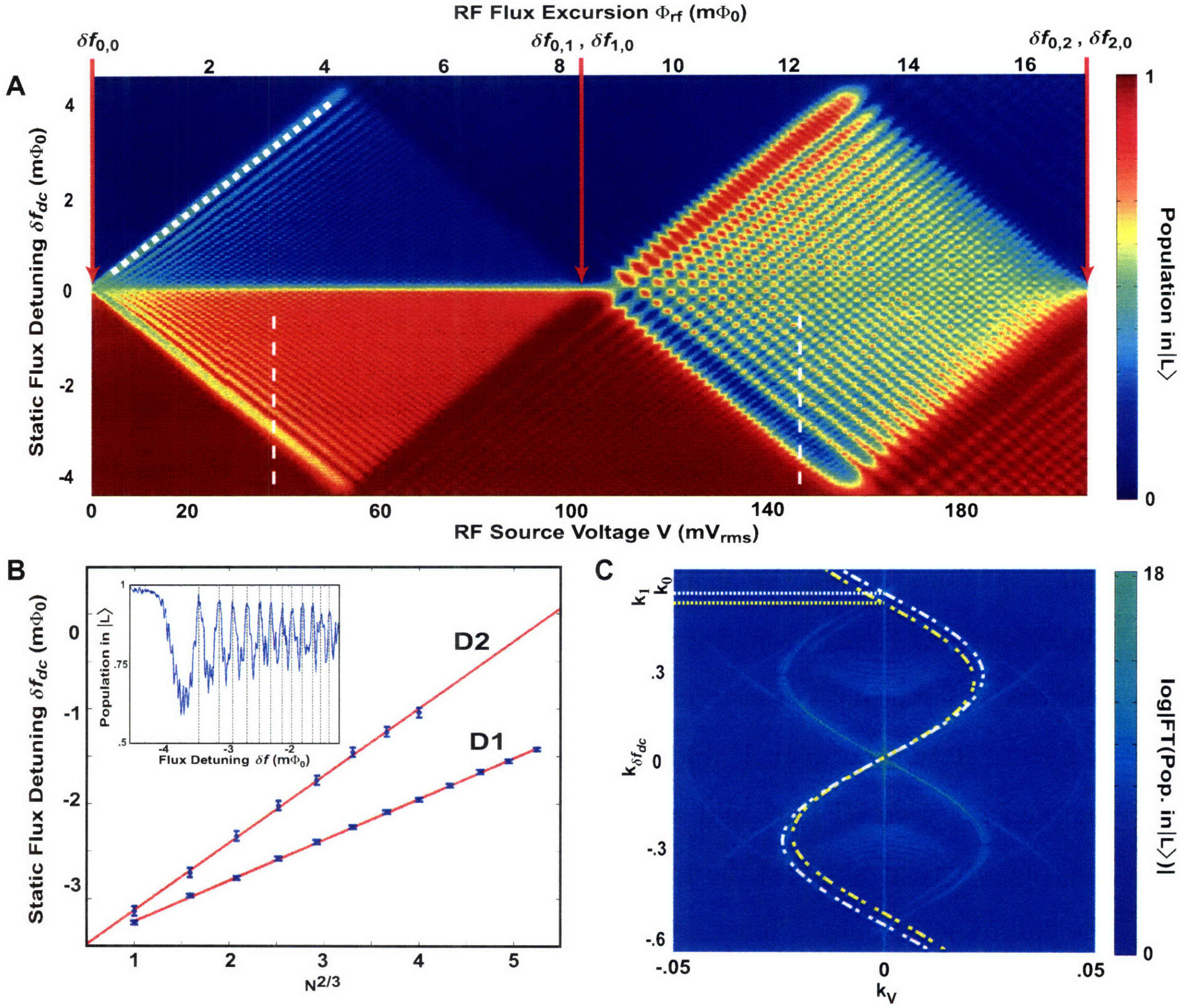

Figure 5-2: Energy-level slopes and avoided crossing locations. (**A**) Detail of diamonds D1 and D2 (Fig. 5-1A) showing interference patterns due to single (D1) and multiple (D2) avoided crossings (see text). Diamond D2 exhibits strong population inversion. Arrows mark the location of the avoided crossing positions. Energy-level slopes are extracted in (B) from the interference fringes (dashed white lines) at 43 mV$_{\text{rms}}$ (D1) and 150 mV$_{\text{rms}}$ (D2). The flux-to-voltage conversion factor is determined by the front side of D1 (dotted white line). (**B**) Determination of the energy-level slopes for levels $|0,L\rangle$, $|0,R\rangle$, $|1,L\rangle$, and $|1,R\rangle$. Detuning location of the Nth interference-node (see inset) vs. $N^{2/3}$ at the voltages marked with dashed lines in (A) and their corresponding linear fits (red line). Inset: Vertical slice from diamond D1 (43 mV$_{\text{rms}}$). Interference nodes N used in the main panel are indicated by dotted lines. (**C**) 2D Fourier transform of both diamonds in (A). The sinusoids with wavenumbers k_0 and k_1 are contributions from diamonds D1 and D2, respectively, and are related to the energy-level slopes (see Ch. 5.3.1).

is sensitive to the relative phase

$$\phi = 2\pi \int_{t_1}^{t_2} \Delta E(t')\, dt' \tag{5.1}$$

accumulated by the two components of the wave function between the first and second traversals of the avoided crossing (see Ch. 3.2.4). Here $\Delta E(t')$ is the instantaneous diabatic energy level separation at time t', and $t_{1,2}$ are the times of the first and second traversals, respectively. Note that the energy ΔE is measured in frequency units (GHz), and this is why the expression contains the factor 2π rather than $1/\hbar$. The Nth node in the interference pattern occurs when a relative phase of $2\pi N$ is picked up during the qubit's excursion beyond the avoided crossing.

For demonstration, I will focus on the interference in the first diamond where the driving $\delta f(t) = -\delta f_{\rm dc} + \alpha V \cos\omega t$ sweeps the qubit through only the lowest avoided crossing $\Delta_{0,0}$. Using the definition of the energy level slopes, for times near the maximum of the cosine driving flux one gets

$$\Delta E(t) \approx 2|m_0|(\alpha V - \delta f_{\rm dc}) - |m_0|\alpha V\, \omega^2 t^2, \tag{5.2}$$

where the driving $\delta f(t)$ near the maximum of $\cos\omega t$ has been fit to a parabola. This second order Taylor series approximation is valid since I am only considering RF amplitudes that have not swept the qubit too far past $\Delta_{0,0}$.

By setting $\Delta E(t_*) = 0$, one finds the initial and final crossing times $t_{1,2} = \mp t_*$, with $t_* \equiv \sqrt{\frac{2(\alpha V - \delta f_{\rm dc})}{\alpha V \omega^2}}$. In the parabolic approximation to the driving signal, the phase accumulated between crossings is

$$\begin{aligned} \phi &= 2\pi \int_{-t_*}^{t_*} \left(2|m_0|(\alpha V - \delta f_{\rm dc}) - |m_0|\alpha V\, \omega^2 t'^2\right) dt' && (5.3) \\ &= 2|m_0|\, \frac{8\pi}{3}\, (\alpha V - \delta f_{\rm dc})\, t_*. && (5.4) \end{aligned}$$

Using the quantization condition for interference, $\phi = 2\pi N$, and the definition of t_*, the values of static flux detuning $\{\delta f_{\rm dc}^{(N)}\}$ where interference occurs with driving source voltage V are found to be

$$2\pi N = 2|m_0|\,\frac{8\pi\sqrt{2}}{3}\,\frac{(\alpha V - \delta f_{\rm dc}^{(N)})^{3/2}}{(\alpha V)^{1/2}\omega}. \tag{5.5}$$

Rearranging Eq. (5.5) and using $\omega = 2\pi\nu$ one has

$$\delta f_{\rm dc}^{(N)} = \alpha V - \left(\frac{3\pi\nu}{2\sqrt{2}}\frac{\sqrt{\alpha V}}{2|m_0|}\right)^{2/3} N^{2/3}, \tag{5.6}$$

where the prefactor to $N^{2/3}$ is identified with the fit parameter $s_{0,0}$.

Expression (5.6) can be generalized to any avoided crossing $\Delta_{q,q'}$ by making the replacement $2|m_0| \to |m_q| + |m_{q'}|$. The detuning locations of the nodes (inset, Fig. 5-2B) thus follow the power-law $s_{qq'}N^{2/3}$ with a prefactor $s_{qq'}$ related to the energy-level slopes:

$$|m_q| + |m_{q'}| = a\nu\sqrt{\alpha V/s_{qq'}^3}\,\left(\frac{\rm GHz}{\rm m\Phi_0}\right), \tag{5.7}$$

where $a = 3\pi/2\sqrt{2}$. Fig. 5-2B shows the $N^{2/3}$ power-law fits to the nodes of the vertical slices in diamonds D1 and D2 which are used to extract m_0 and m_1 (Fig. 5-2A, dashed vertical lines), where it is assumed that $|m_q| = |m_{q'}| \equiv m_q$ for $q = q'$ in this system. The slopes are obtained sequentially from the fitted values $s_{qq'}$ in Eq. 5.7, starting with $2m_0 = 2.88$ GHz/mΦ_0, followed by $m_0 + m_1 = 2.534$ GHz/mΦ_0; their values are summarized in Fig. 5-7.

The amplitude spectroscopy plots in Fig. 5-1A and Fig. 5-2A display structure on several scales. On the largest scale, the boundaries of the "spectroscopy diamonds" are readily identifiable. The interiors of the diamonds are textured by fringes arising from the interference between successive LZ transitions at a single or multiple avoided crossings. On an even smaller scale, these fringes are composed of a series of horizontal multiphoton resonance lines. In order to extract information from these small scale structures, it is helpful to apply a transformation that is able to invert length scales; the two-dimensional Fourier transform (2DFT) provides this service. Using Fourier analysis, the apparently complicated mesh of overlapping Bessel functions is transformed to a pair of sinusoids, Fig. 5-2C, with periodicity related to the energy level slopes, $k_V = \pm \alpha g \sin(k_{\delta f_{\rm dc}}/g)$, where $g = 2(|m_q| + |m_{q'}|)/\nu$ [89]. The sinusoid associated with $q = q' = 0$ arises from the transitions at $\Delta_{0,0}$, while the second sinusoid with $q = 0$, $q' = 1$ and $q = 1$, $q' = 0$ is degenerate and arises from the transitions at $\Delta_{0,1}$ and $\Delta_{1,0}$.

I will now summarize the theory for the Fourier analysis of the diamonds, which was developed in collaboration with Mark Rudner, Leonid Levitov, and Andrey Shytov [89]. The analytic treatment that follows is applicable to the perturbative driving regime $\Delta^2/\hbar\omega A \ll 1$ (see Ch. 3.3), where Δ is the splitting at the largest traversed avoided crossing and the driving amplitude $A = 2|m_0|\Phi_{\rm RF}$ is expressed in energy units. In the device used here, for the driving frequencies employed, this condition is satisfied in the first two diamonds, where one finds good agreement between the analytical treatment, numerics, and the data. For higher diamonds, where the dynamics are non-perturbative, more complicated behavior is observed. The numerical approach can still be employed, but in practice it is found that in such cases it is more efficient to extract the desired information directly from the short-time dynamics (see Ch. 5.3.2).

For simplicity, let's consider the internal structure of the first diamond, which arises from repeated passages through a single weak avoided crossing. As discussed in Ch. 3, the "Bessel staircase" structure seen in the front half of diamond 1 (Fig. 5-1A), can be understood as a combination of multiphoton resonance lines and Mach-Zehnder interference fringes. The internal structure of the first diamond reflects the amplitude and detuning dependence of the transition rate

$$W(V, \delta f_{\rm dc}) = \frac{\Delta^2}{2} \sum_{n=-\infty}^{\infty} |J_n(x)|^2 \frac{\Gamma_2}{(2\,h|m_0|\delta f_{\rm dc} - nh\nu)^2 + \Gamma_2^2}, \qquad (5.8)$$

where $x = 2|m_0|\alpha V/\nu$. Eq. 5.8 is the same as Eq. 3.19, with the linear slope relation inserted.

To obtain the Fourier transform of Eq. (5.8),

$$\tilde{W}(k_x, k_{\delta f_{\rm dc}}) = \iint e^{-ik_x x - ik_{\delta f_{\rm dc}} \cdot \delta f_{\rm dc}} \, W(V, \delta f_{\rm dc}) \, dx \, d\delta f_{\rm dc}, \tag{5.9}$$

one can employ the standard formulae

$$J_n(x) = \oint \frac{d\theta}{2\pi} e^{-in\theta} \, e^{ix \sin\theta}, \tag{5.10}$$

$$\frac{\Gamma_2}{\Delta\varepsilon^2 + \Gamma_2^2} = \frac{1}{2} \int_{-\infty}^{\infty} dq \, e^{-iq\Delta\varepsilon} e^{-\Gamma_2 |q|} \tag{5.11}$$

with $\Delta\varepsilon \equiv 2\,h|m_0|\delta f_{\rm dc} - nh\nu$. The Fourier transform of Eq. (5.8) can be found and indeed displays intensity concentrated along the curve

$$k_V = \pm \frac{4|m_0|\alpha}{\nu} \sin\left(\frac{\nu}{4|m_0|} \, k_{\delta f_{\rm dc}} \right), \tag{5.12}$$

with $k_V = \frac{2|m_0|\alpha}{\nu} k_x$ [89].

Most strikingly, the apparently distinct phenomena of interference fringes and multiphoton resonances observed in the real space image are manifested as a single smooth curve in Fourier space. This structure can be understood by considering k_x and $k_{\delta f_{\rm dc}}$ to be smoothly varying functions of the spatial coordinates $(x, \delta f_{\rm dc})$. Through a stationary phase analysis of the Fourier integrals [89], one finds the mapping between real space patches and regions of k-space depicted in Fig. 5-3A.

In numerical simulations it is found that the steady-state magnetization in the second diamond was well reproduced by a simple rate model based on incoherently adding two additional transition rates of a form similar to Eq. (5.8) to account for transitions at the avoided crossings with the left and right first excited states. These additional rates are calculated using values of Δ appropriate for the excited state avoided crossings (approximately 90 MHz), and also take into account the different slopes of the ground and excited state energy bands.

In the above model, the Fourier image of the second diamond is simply the sum of the Fourier transforms of the three relevant transition rates. Due to the different

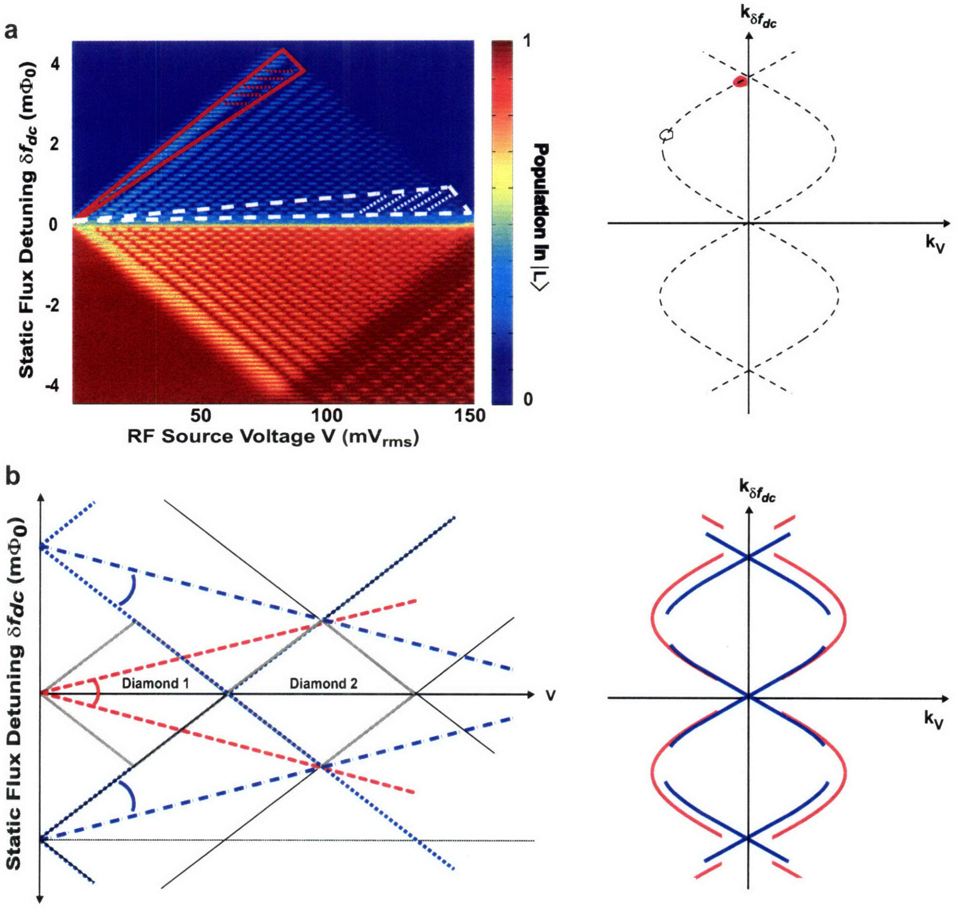

Figure 5-3: Graphical interpretation of 2D Fourier transform technique. (**A**) Diamond 1 at $\nu = 400$ MHz is pictured alongside a schematic of its Fourier transform. On a local scale within the wedge-shaped region of $(V, \delta f_{\rm dc})$ space outlined by a solid red line, the image everywhere looks like a simple series of evenly spaced horizontal bands. Thus the Fourier transform over this region maps to a region of $(k_V, k_{\delta f_{\rm dc}})$ space localized near the $k_{\delta f_{\rm dc}}$ axis as indicated by the red dots. Within the region outlined by the dashed white line, the local periodicity is along the angled interference fringes; the Fourier transforms maps this region to the region of $(k_V, k_{\delta f_{\rm dc}})$ space localized near the extrema of the sinusoid in the k_V direction as indicated by the open white circles. (**B**) The utility of transforming diamonds decreases for higher diamonds, because the Fourier integral samples a smaller sector of the real space image associated with the higher excited states. Due to the mapping between sectors of real space and localized regions of k-space, the sinusoids associated with higher diamonds are not fully developed.

coefficients in the linear dependence of the ground and excited energy bands on static flux bias, the wavelengths of the sinusoids resulting from the ground and excited state crossings differ by the ratio of these slopes. In addition, the real-space integration in the Fourier transform samples a more limited sector of the fringes arising from each of the avoided crossings than in the case of the first diamond (see Fig. 5-3B). As a result, the regions around $\frac{\nu}{2}(|m_1| + |m_0|)^{-1} k_{\delta f_{\rm dc}} = (n + 1/2)\pi$, $k_V = \pm\frac{2\alpha}{\nu}(|m_1| + |m_0|)$ are absent from the sinusoids arising from the excited state crossings, while the regions around $\frac{\nu}{4|m_0|} k_{\delta f_{\rm dc}} = n\pi$, $k_V = 0$ are absent from the sinusoid arising from transitions at the lowest avoided crossing [89].

5.3.2 Short-time Analysis

Amplitude spectroscopy can also be performed over short time scales, providing valuable information about the energy-level spectrum and temporal coherence (Fig. 5-4-Fig. 5-6). Temporal-response measurements are performed by initializing the system to the ground state at detuning $\delta f_{\rm dc}$ and then applying an RF field pulse of a variable length Δt, with fixed frequency and amplitude. The phase of the sinusoid is carefully adjusted to maintain the timing and directionality of the RF-flux excursion through the energy levels between pulses. When the pulse ends abruptly at time Δt, the state of the system is preserved as the flux detuning instantaneously returns to $\delta f_{\rm dc}$ (finite decay-time corrections are discussed below).

This is exemplified in Fig. 5-4A, where parameters are tuned to investigate the $\Delta_{2,0}$ (when $\delta f_{\rm dc} > 0$) and $\Delta_{0,2}$ (when $\delta f_{\rm dc} < 0$) level crossings (Fig. 5-4B). For example, starting in the ground state at positive detuning ($\delta f_{\rm dc} > 0$), the qubit is driven through $\delta f(t) < 0$, diabatically crossing $\Delta_{0,0}$ and $\Delta_{1,0}$ at the beginning of the first quarter-period with no significant population transfer (beginning of region A). Significant population transfer first occurs in region A when $\Delta_{2,0}$ is first reached. The sharp onset of population transfer is followed by brief temporal oscillations. The population becomes stationary after the qubit returns through $\Delta_{2,0}$ in the second quarter period (region B).

In the third quarter-period (region C), the driving pulse takes the qubit through

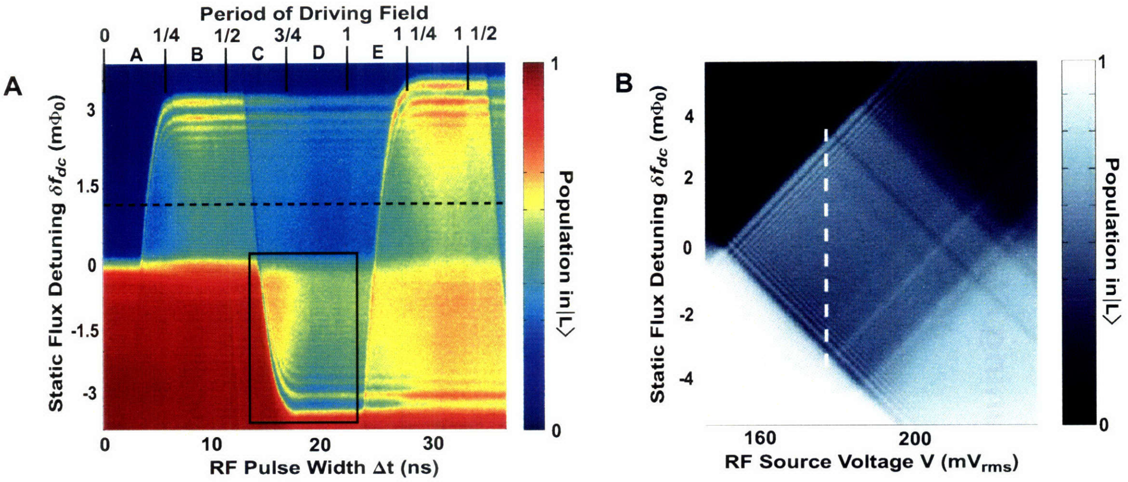

Figure 5-4: (**A**) Qubit response to a short RF pulse of variable length Δt as a function of static flux detuning δf_{dc}, with $V = 181\ \mathrm{mV_{rms}}; \nu = 0.045$ GHz. Top axis: driving field period (regions A-E); the maximum pulse width corresponds to ~1.5 oscillation periods. The scan is performed at an amplitude value in the left side of diamond D3 shown in (B), which reaches all crossings through $\Delta_{0,2}$ and $\Delta_{2,0}$. (**B**) Diamond 3 at $\nu = 45$ MHz. Dashed line indicates the amplitude ($181\mathrm{mV_{rms}}$) at which pulse width scan in (A) was taken.

the excited state avoided crossing $\Delta_{0,2}$ located on the opposite side of the level diagram (positive flux bias, Fig. 5-1B). This event is marked by a second sharp population transfer. The population subsequently remains nearly constant (region D) until a third abrupt population transfer occurs during the first quarter of the second period (region E), which signals the qubit's return through $\Delta_{2,0}$ and the repetition of the driving cycle. The population transfer does not reach its furthest extent in flux during the first half-period (as it does for the subsequent half-periods) because the pulse shape used has slightly lower amplitude for times smaller than 5 ns.

The observed response over short time scales is not symmetric about $\delta f_{\mathrm{dc}} = 0$. When starting in the ground state at static bias $\delta f_{\mathrm{dc}} = \delta f^{*}_{\mathrm{dc}} < 0$, the system is drawn deep into the ground state during the first half-period, without inducing any transitions (see Fig 5-1B). It is only during the second half-period that $\Delta_{0,2}$ is finally reached and significant population transfer occurs. The detailed time dependence of population in this interval is shown in Fig. 5-5. The curved line in Fig. 5-5 marks the pulse width Δt at which the sinusoidal flux excursion first exceeds and, subsequently,

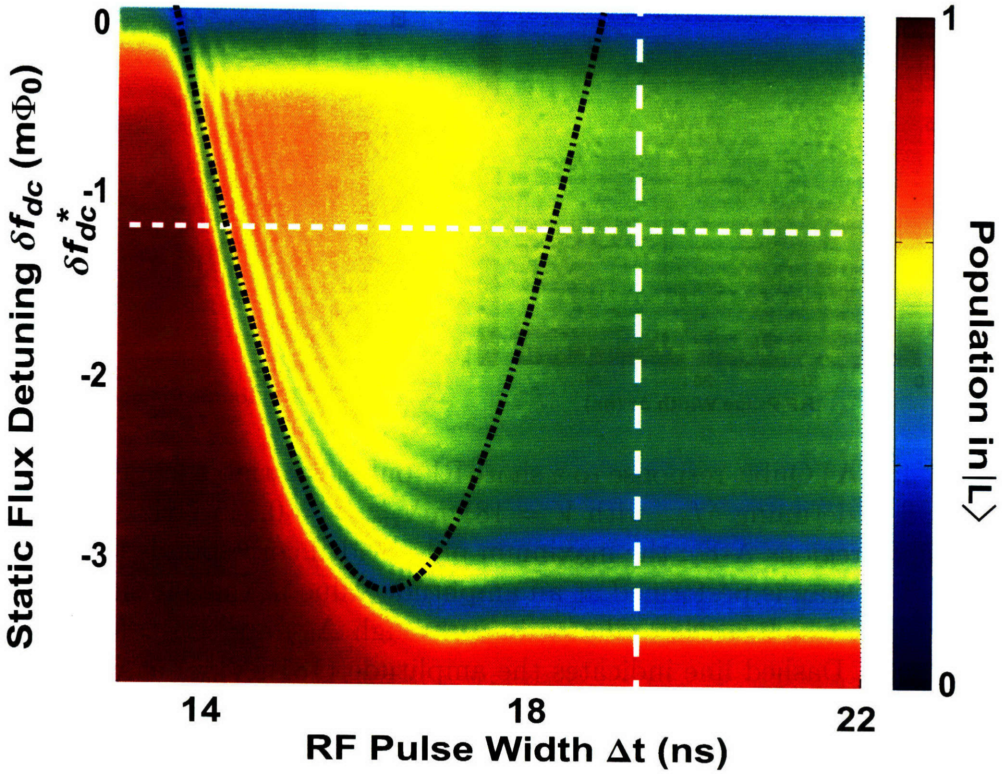

Figure 5-5: Detail of the interference pattern in the boxed region of Fig. 5-4A. The dashed curve marks the pulse width Δt at which the sinusoidal flux-excursion first exceeds and, subsequently, returns through $\Delta_{0,2}$ at flux detunings δf_{dc}. The detail along the two straight, dashed lines is shown in Fig. 5-6.

returns through $\Delta_{0,2}$ for different flux detunings δf_{dc}; the sinusoidal excursion about the specific static flux δf^*_{dc} is correspondingly indicated in Fig. 5-1B by the green sinusoidal curve. The detail along the dashed lines in Fig. 5-5 is shown in Fig. 5-6.

The temporal oscillations displayed in Fig. 5-5 and Fig. 5-6A can be understood qualitatively as a Larmor-type precession, or "ringing," that results after the qubit is swept through the avoided crossing. In a pseudo-spin-1/2 picture where the qubit states are identified with up and down spin states relative to a fictitious z-axis, the qubit precesses about a tipped effective magnetic field which steadily increases in magnitude and rotates toward the z-axis. This picture is consistent with a temporal analysis of the standard LZ problem, in which a linear ramp with velocity v sweeps the qubit through the avoided crossing , followed by an instantaneous return through the crossing at the end of the pulse which preserves the diabatic population.

In the regime where the LZ transition probability is small, a perturbative model to describe these oscillations in terms of the well-known Fresnel integral has been developed in collaboration with Mark Rudner and Leonid Levitov [90]. By linearizing the sinusoidal driving signal near the moment of traversal through the avoided crossing, one arrives at the familiar LZ Hamiltonian $\hat{H}(t) = (1/2)(vt\,\sigma_z + \Delta\sigma_x)$, where v is the sweep velocity and Δ is the splitting at the avoided crossing. The system is then transformed to a non-uniformly rotating frame by $|\,\psi_R(t)\,\rangle = e^{i\phi(t)\sigma_z}|\,\psi(t)\,\rangle$, where $\phi(t) \equiv -\frac{1}{2}\int_0^t vt'\,dt' = -\frac{1}{4}vt^2$. The rotating frame effective Hamiltonian is purely off diagonal (as done in Eq. 3.15)

$$\hat{H}_R = \frac{1}{2}\begin{pmatrix} 0 & \Delta_R(t) \\ \Delta_R^*(t) & 0 \end{pmatrix}, \tag{5.13}$$

with $\Delta_R(t) \equiv \Delta\exp(-ivt^2/2)$.

Proceeding with a perturbative treatment of the system's dynamics by expanding the system's time evolution operator $\hat{U}(t, t_0)$ to first order in Δ, one has

$$\hat{U}(t, t_0) = \hat{1} - \frac{i}{\hbar}\int_{t_0}^{t}\hat{H}_R(t')dt' + \mathcal{O}(\Delta^2). \tag{5.14}$$

This approach is valid when the driving conditions are far from adiabaticity; i.e., $\Delta^2/\hbar\omega A \ll 1$ (as in Ch. 3.3). The probability $P(t) = |\langle\,\Psi_+\,|\hat{U}(t, t_0)|\,\Psi_-\,\rangle|^2$ to find the system in the excited state $|\,\Psi_+\,\rangle$ at time t given that it started in the ground state $|\,\Psi_-\,\rangle$ at $vt_0 \ll -\Delta$ is given by

$$P(t) = \frac{\Delta^2}{4}\left|\int_{t_0}^{t} e^{ivt'^2/2}\,dt'\right|^2. \tag{5.15}$$

In practice, the pulse does not turn off instantly, but, rather, exhibits a transient that is well-approximated by a rapid parabolic decay. Although Eq. 5.15 captures the essential features of the data in Fig. 5-6A, to obtain a quantitative fit one must account for the non-abrupt ending of the pulse. This transient slightly modifies the

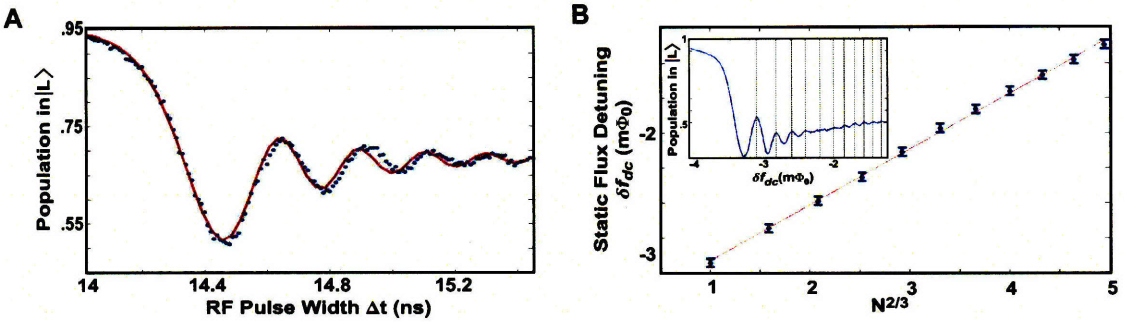

Figure 5-6: (**A**) Temporal oscillations along the horizontal line in Fig. 5-5 at the specific static flux bias $\delta f_{\mathrm{dc}} = \delta f^*_{\mathrm{dc}}$, fitted by a LZ model with damping (red line, see text). (**B**) Nth interference node versus $N^{2/3}$ along the vertical line in Fig. 5-5 and best linear fit. Inset: interference pattern along vertical line in Fig. 5-5 and node locations.

total precession phase accumulated before read-out, and adds a small Mach-Zehnder-type interference due to the finite ramp speed back through the avoided crossing $\Delta_{0,2}$. Remarkable agreement is found between the data and a simulation of the Bloch dynamics of the two level system near $\Delta_{0,2}$, which included longitudinal sinusoidal driving up to time $t = \Delta\mathrm{t}$, followed by a rapid parabolic decay over approximately 2 ns, and intrawell relaxation with a rate of 0.65 ns^{-1} (Fig. 5-6A). The value of $\Delta_{0,2}$ is extracted as a fitting parameter in the simulation and, in this regime, is largely insensitive to the details of the pulse decay and intrawell relaxation.

As in the case of the long-time data, the energy-level slopes can be extracted from the vertical fringes (Fig. 5-5) using the $N^{2/3}$ power-law fitting (Fig. 5-6B) and Eq. 5.7. Eq. 5.7 is used to infer m_2 and m_3 from the sums $m_0 + m_2 = 2.189$ GHz/mΦ_0 and $m_0 + m_3 = 1.929$ GHz/mΦ_0. The short-time amplitude spectroscopy procedure was applied to obtain $\Delta_{q,q'}$ for diamonds D2-D4 and slopes m_q for diamonds D3-D4, and they are presented in Fig. 5-7 ($\Delta_{0,0}$ was previously obtained using the rate-equation approach discussed in Ch. 3.3.3).

Though ignored up to this point, the system's eigenstates are comprised of transverse ($p = 0, 1, 2, \dots$) and longitudinal ($q = 0, 1, 2, \dots$) modes, with diabatic states denoted as $|p, q, \mathrm{L}\rangle$ and $|p', q', \mathrm{R}\rangle$. Since the transverse and longitudinal modes should be decoupled for a symmetric system, I have assumed that only the lowest trans-

Crossing q,q'	Location $\delta f_{q,q'}$ ($m\Phi_0$)	Strength $\Delta_{q,q'}/h$ (GHz)	Slope $m_{q'}$ (GHz/$m\Phi_0$)
0,0	0	0.013 ± 0.001	1.44 ± 0.01
0,1	8.4 ± 0.2	0.090 ± 0.005	1.09 ± 0.03
0,2	17.0 ± 0.2	0.40 ± 0.01	0.75 ± 0.04
0,3	25.8 ± 0.4	2.2 ± 0.1	0.49 ± 0.08

Figure 5-7: Energy spectrum parameters determined using amplitude spectroscopy.

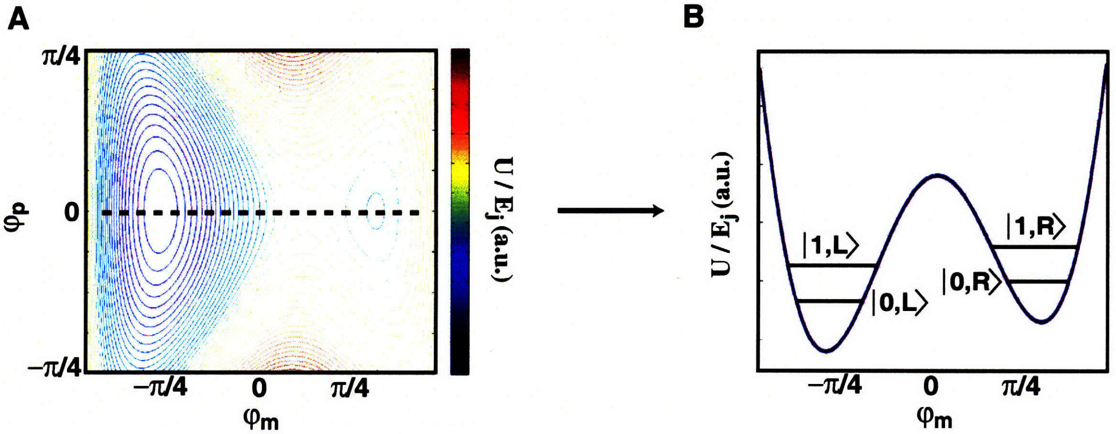

Figure 5-8: (**A**) Contour plot of 2D double-well potential energy for our qubit at $\delta f_0 = 0.46\Phi_0$, far detuned from the symmetry point $\delta f_{\mathrm{dc}} = 0$. When the transverse quantum modes can be ignored, the potential energy can be treated as a 1D double-well along the dashed line pictured. (**B**) 1D double-well potential energy for $\delta f_0 = 0.495\Phi_0$. The wells are slightly tipped to the left and the four lowest energy eigenstates are shown.

verse mode is populated and have used the reduced notation: $|p,q,\mathrm{L}\rangle \rightarrow |q,\mathrm{L}\rangle$, $|p',q',\mathrm{R}\rangle \rightarrow |q',\mathrm{R}\rangle$, and $\Delta_{pq,p'q'} \rightarrow \Delta_{q,q'}$ (Fig. 5-8); i.e., thus far I have assumed the transverse modes to be in their ground state ($p = 0$). However, it was in fact possible to populate excited transverse modes. This population transfer is relatively weak, indicating small deviations from an ideally symmetric double-well potential and longitudinal driving. Signatures of these states appear in diamonds D3 and D4 (e.g., arrows in Fig. 5-1A).

The temporal response to a short RF pulse taken on the front side of diamond D3 is shown in Fig. 5-9A. The front side of diamond D3 (when $\delta f_{\mathrm{dc}} > 0$) results from ac-

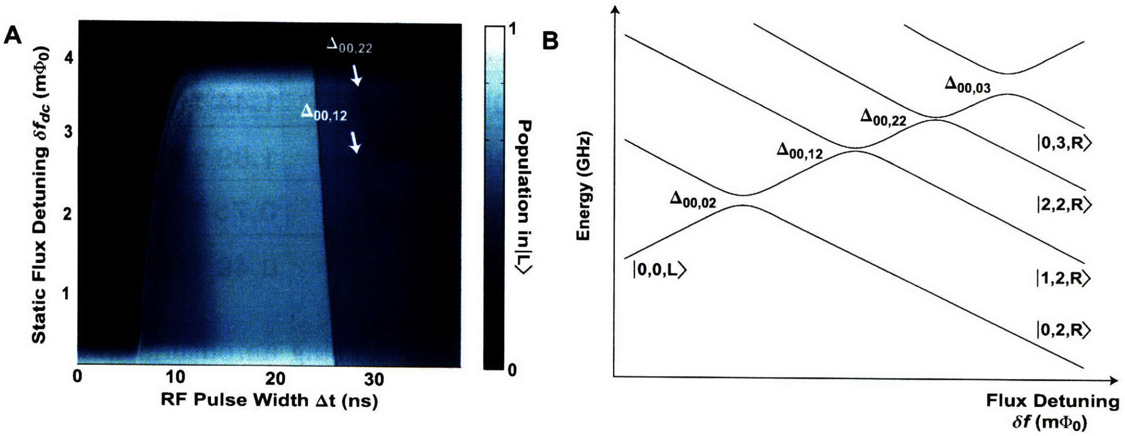

Figure 5-9: Identification of transverse states of the qubit's double-well potential. (**A**) Qubit response to a short RF pulse of variable length Δt as a function of static flux detuning δf_{dc}, with $V = 179$ mV$_{\mathrm{rms}}$; $\nu = 0.025$ MHz. The scan is performed at an amplitude value in the right half of diamond D3, where the crossing $\Delta_{03,00}$ (but not $\Delta_{00,03}$) is reached. The signatures of two crossings with transverse states, $\Delta_{12,00}$ and $\Delta_{22,00}$, are indicated. (**B**) Schematic energy-level diagram showing the locations of the transverse states.

cessing $\Delta_{02,00}$ during the first half-period, where some population is transferred from the right to the left wells (Fig. 5-9A), and I have used the full notation to explicitly indicate both longitudinal and transverse modes. Two weak population transfers are identified during the second half-period between the known positions of the longitudinal avoided crossings $\Delta_{00,02}$ and $\Delta_{00,03}$. This result is in agreement with simulations of the qubit Hamiltonian, which indicate that two transverse modes $|1,2,\mathrm{R}\rangle$ and $|2,2,\mathrm{R}\rangle$ exist in this region, as illustrated in Fig. 5-9B. Although their locations can be identified, the values of $\Delta_{00,12}$ and $\Delta_{00,22}$ are not conclusively determined from this measurement, because the fringe contrast of their temporal oscillations are small compared with those of the adjacent longitudinal crossings $\Delta_{00,02}$ and $\Delta_{00,03}$.

5.4 Summary

I have just demonstrated amplitude spectroscopy, a means of characterizing the energy spectrum of the PC qubit by varying only the RF driving field amplitude. The amplitude spectroscopy technique demonstrated here is generally applicable to systems with traversable avoided crossings, including both artificial and natural atomic systems. The main feature of amplitude spectroscopy is prominent diamonds, which contain interference patterns and population inversion that serve as a fingerprint of the qubit's energy spectrum. By analyzing these features, the energy spectrum of a manifold of states with energies from 0.01 to 120 GHz$\times h$ was determined, using a single driving frequency near 0.1 GHz.

Chapter 6

Summary and Future Work

6.1 Summary

The work presented in this thesis can be summarized by a single picture, Fig. 6-1. The energy spectrum of the PC qubit consists of a sequence of energy levels coupled by avoided crossings. By virtue of the qubit's longitudinal coupling of RF microwaves, one is able to sweep the qubit state through the avoided crossings and induce quantum coherent interference. At relatively weak driving fields, I have explored coherent, quasiclassical dynamics of a single, central avoided crossing that serves as a two-level model for quantum computation and other qubit studies. With slightly higher amplitudes, I have developed a new method of cooling the two-level qubit, by using a higher avoided crossing. Finally, by increasing driving amplitudes even further, I have accessed an entire manifold of energy levels and avoided crossings, and have developed a means of characterizing these features to reconstruct the qubit's energy spectrum.

In Ch. 3 I demonstrated a new quasiclassical regime of coherent quantum dynamics of a qubit. This regime was realized at low driving frequencies in the strong driving limit, with amplitude still small enough that higher avoided crossings were not reached. Coherent transitions between qubit states occurred via the Landau-Zener process when the system was swept through an energy-level avoided crossing. The quantum interference mediated by repeated transitions gave rise to an oscillatory

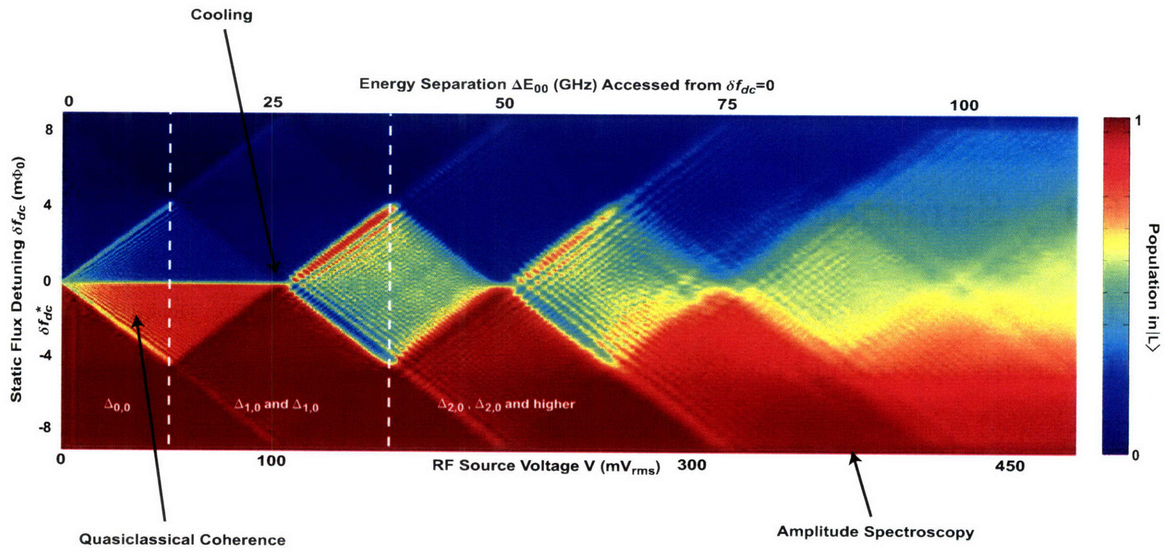

Figure 6-1: Diamonds: A summary of this thesis. The qubit is driven at a fixed frequency $\nu = 0.160$ GHz ($\Delta t = 3\,\mu s$), while amplitude V is swept for each static flux detuning δf_{dc}. Top axis: the $|0,\text{L}\rangle - |0,\text{R}\rangle$ energy spacing $\Delta E_{0,0}$ accessed by V from $\delta f_{\text{dc}} = 0$. Quasiclassical coherence was studied in the two-level approximation, at relatively weak amplitudes. Cooling of the two-level system via a second avoided crossing was accomplished at slightly higher amplitudes, and characterization of many levels and crossings was achieved by studying higher amplitudes.

dependence of the qubit population on the driving field amplitude and static flux detuning. These interference fringes, which at high frequencies consisted of individual multiphoton resonances, persisted even for driving frequencies near the dephasing rate Γ_2, where individual resonances are no longer distinguishable. A new theoretical model that is valid in the quasiclassical regime was described, and showed remarkable agreement with the observations.

In Ch. 4 I presented the first demonstration of microwave-induced cooling in a superconducting flux qubit. The thermal population in the first-excited state of the qubit was driven to a higher-excited state by way of a sideband transition. Subsequent relaxation into the ground state resulted in cooling. Effective temperatures as low as $T_{\text{eff}} \approx 3$ millikelvin were achieved for bath temperatures $T_{\text{bath}} = 30 - 400$ millikelvin, a cooling factor between 10 and 100. This demonstration provides an analog to optical cooling of trapped ions and is generalizable to other solid-state quantum systems. Active cooling of qubits, applied to quantum information science, provides a means for rapid qubit-state preparation with improved accuracy, and for suppressing decoherence in multi-qubit systems. Cooling was instrumental in achieving the results in Chapters 3, 4, and 5.

In Ch. 5 I demonstrated amplitude spectroscopy, a means of characterizing the energy spectrum of the PC qubit by varying only the RF driving field amplitude. The amplitude spectroscopy technique demonstrated is generally applicable to systems with traversable avoided crossings, including both artificial and natural atomic systems. The main feature of amplitude spectroscopy was prominent diamonds, which contain interference patterns and population inversion that serve as a fingerprint of the qubit's energy spectrum. By analyzing these features, the energy spectrum of a manifold of states with energies from 0.01 to 120 GHz$\times h$ was determined, using a single driving frequency near 0.1 GHz.

6.2 Future Work

This thesis has given us a much better understanding of the coherent control of two-level quantum systems possible with large-amplitude driving. The backbone of this thesis was the single crossing work done in Ch. 3, which thoroughly studied the coherent nature of the transitions that occur when strongly driving the two-level qubit. This work was flushed out further in the study of cooling, with a nice overview of all the different frequency regimes displayed in Fig. 4-5. The strongly driven Landau-Zener dynamics were then further explored in a near-sudden approximation in Ch. 5.3.2, where Larmor-type oscillations were explored, with a slight Mach-Zehnder like correction due to finite pulsing. With that said though, Rabi oscillations still hold supreme in any discussion of controlling a two-level quantum system. I believe that an effort to do precise, large amplitude, non-adiabatic control of two-level quantum systems would be a promising line of follow-on research to do in the near future.

As shown in Ch. 4.3, the usefulness of cooling the PC qubit disappears at higher temperatures because the SQUID is not also cooled (see Fig. 4-10). The SQUID is of course a quantum system itself, and hence it should be possible to cool it in a way similar to what was done here for the qubit. Figuring out a way to cool the SQUID would be a very exciting research endeavor, as it may allow for operation of a quantum computer at higher temperatures. Such higher temperature studies could also serve as a useful tool in the study of qubit decoherence and measurement. Proposed schemes to cool the SQUID have in fact already been reported [91], though none have been implemented.

Finally, I believe that in general, superconducting qubits provide a great way to study the fundamentals of quantum physics, but are not fully utilized in this realm. It is the ability to engineer a vast number of Hamiltonians from these circuits that allows for an incredible array of problems to be studied with them. At the current moment, the focus of studies on superconducting qubits is limited to a few circuit configurations, with a major focus on decoherence in these systems, due to their application in quantum computing. I believe that a broader scope of problems and qubits should be considered, with an aim to study fundamental physics like macroscopic quantum physics and measurement theory.

Appendix A

Rotating Wave Approximation: What is it and when is it valid?

In this appendix I will derive the assumptions under which the Rotating Wave Approximation (RWA) is a valid approximation. I will begin with a review of what the RWA is, and then discuss the conditions the RWA is typically claimed to be valid under. I will then review time-dependent perturbation theory, and then use those results to derive the conditions under which the RWA is an accurate approximation.

A.1 Introduction

The response of a two-level quantum system subject to a time-varying electromagnetic field has been of great interest for a very long time [55]. The Hamiltonian for a two-level system defined by σ_z eigenstates, and driven along σ_x at angular frequency ω and amplitude A (parameterized in units of energy), can be written as

$$H = -\frac{1}{2}\begin{pmatrix} \varepsilon & \mathrm{A}\cos(\omega t) \\ \mathrm{A}\cos(\omega t) & -\varepsilon \end{pmatrix} = -\frac{1}{2}\begin{pmatrix} \varepsilon & \frac{\mathrm{A}}{2}[\exp(-i\omega t)+\exp(i\omega t)] \\ \frac{\mathrm{A}}{2}[\exp(i\omega t)+\exp(-i\omega t)] & -\varepsilon \end{pmatrix} \quad (\mathrm{A.1})$$

where ε is the energy spacing between the two eigenstates. It has been known for quite some time that this problem has no closed analytic solution [92, 93]. However, it is well known that if the second term in the off-diagonal elements is ignored, the problem becomes exactly solvable, with the Hamiltonian

$$H = -\frac{1}{2}\begin{pmatrix} \varepsilon & \frac{A}{2}\exp(-i\omega t) \\ \frac{A}{2}\exp(i\omega t) & -\varepsilon \end{pmatrix} \tag{A.2}$$

The transition from Eq. A.2 to Eq. A.1 is the RWA. The name makes more sense if one considers the field felt by the fictitious spin-$\frac{1}{2}$ particle associated with the two-level system. This mapping is achieved by noticing that the Hamiltonian H_s for a spin-$\frac{1}{2}$ particle in a magnetic field can be written as

$$H_s = \gamma\frac{\hbar}{2}(B_x\sigma_x + B_y\sigma_y + B_z\sigma_z) \tag{A.3}$$

where γ is the gyromagnetic ratio of the spin, and the Pauli matrices are defined as

$$\sigma_x = \begin{pmatrix} 0 & 1 \\ 1 & 0 \end{pmatrix};\sigma_y = \begin{pmatrix} 0 & -i \\ i & 0 \end{pmatrix};\sigma_z = \begin{pmatrix} 1 & 0 \\ 0 & -1 \end{pmatrix} \tag{A.4}$$

Before the RWA is made (Eq. A.1), the fictitious spin-$\frac{1}{2}$ particle therefore sees the following magnetic field:

$$\begin{aligned} \mathbf{B} &= \frac{\varepsilon}{\gamma\hbar}\hat{z} + \frac{A}{\gamma\hbar}\cos(\omega t)\hat{x} \\ &= \frac{\varepsilon}{\gamma\hbar}\hat{z} + \overbrace{\frac{A}{2\gamma\hbar}[\cos(\omega t)\hat{x} + \sin(\omega t)\hat{y}]}^{rotating} + \overbrace{\frac{A}{2\gamma\hbar}[\cos(\omega t)\hat{x} - \sin(\omega t)\hat{y}]}^{counter-rotating} \end{aligned} \tag{A.5}$$

After the RWA is made (Eq. A.2), the magnetic field seen by the fictitious spin-$\frac{1}{2}$ particle is

$$\mathbf{B} = \frac{\varepsilon}{\gamma\hbar}\hat{z} + \overbrace{\frac{A}{2\gamma\hbar}[\cos(\omega t)\hat{x} + \sin(\omega t)\hat{y}]}^{rotating} \tag{A.6}$$

It is now clear that going from Eq. A.1 (A.5) to Eq.A.2 (A.6), converts the problem from that of a linearly oscillating drive, equivalent to the sum of two oppositely rotating drives, to that of a solely rotating drive, and hence the name *Rotating* Wave Approximation.

A.2 What assumptions are made in the RWA?

When the RWA is invoked in the literature, it is often casually stated that the approximation is valid if the cosine drive is on resonance; i.e., $\omega = \varepsilon/\hbar$. The argument is that if the two-level is driven on resonance, then the counter-rotating drive at $\omega =$ $-\varepsilon/\hbar$ is considerably off resonance, and hence can be ignored. This requirement almost intuitively makes sense, since when a classical oscillator is driven far off resonance, no power is absorbed by the oscillator, and the external field effectively does nothing and can be ignored. However, I have no intuition for resonance effects that have a dependence on the directionality of the driving field. Resonance is always a scalar phenomenon in the textbook examples, e.g. a driven classical harmonic oscillator, and so this argument falls short for me.

Occasionally I also see statements that the amplitude of the drive must be small when compared to the unperturbed energy separation in order to utilize the RWA; i.e., $A \ll \varepsilon$. Once again I have no intuitive explanation for this condition, and it concerns me that this condition is not always mentioned in the literature when the RWA is invoked. Since my thesis is about the behavior of a qubit when strongly driven, this assumption is of particular interest to me. The goal for the remainder of this appendix is to explicitly determine the assumptions under which the RWA is a valid approximation.

To resolve this issue I will use time-dependent perturbation theory and show that the original problem, with a linear driving field, is similar to the RWA version under certain circumstances. I will do this by calculating the coefficient to be in the ground and excited states when the drives are applied, and show that through second order the linear and rotating drives will approximately give the same answers under a certain set of conditions.

A.3 Time-Dependent Perturbation Theory

The evolution of a two-level quantum state with Hamiltonian H_0 and perturbation V obeys the Schroedinger equation

$$i\hbar\frac{d\Psi}{dt} = (H_o + \lambda V)\Psi \tag{A.7}$$

where λ is a parameter introduced to keep track of the number of times the perturbation enters, and the eigenstates of H_o are given by

$$H_o\Psi_{i,f} = \hbar\omega_{i,f}\Psi_{i,f} \tag{A.8}$$

At time t > 0 the state of the system can be written as a superposition of eigenstates with time dependent coefficients

$$\Psi(t) = \sum_{n=i,f} c_n(t)\exp(-i\omega_n t)\Psi_n, \tag{A.9}$$

where I have chosen to separate out the natural time dependence of the eigenstates from the time dependence due to the perturbation. Combining equations A.7 and A.9, and operating on the left with $\int \Psi_k$, one has

$$i\hbar\dot{c_k} = \lambda\sum_{n=i,f}\exp(-i\omega_{kn}t)V_{kn}c_n \tag{A.10}$$

where $\omega_{kn} \equiv \omega_k - \omega_n$ and $V_{kn} \equiv \langle k|V|n\rangle$. Assuming a solution of the form

$$c_k = c_k^{(0)} + \lambda c_k^{(1)} + \lambda^2 c_k^{(2)} + ... \tag{A.11}$$

and plugging it into Eq. A.10, after collecting terms of the same order in λ one finds that

$$i\hbar\dot{c}_k^{(0)} = 0 \tag{A.12}$$

$$i\hbar\dot{c}_k^{(1)} = \sum_{n=i,f} \exp(-i\omega_{kn}t)V_{kn}c_n^{(0)} \tag{A.13}$$

$$i\hbar\dot{c}_k^{(2)} = \sum_{n=i,f} \exp(-i\omega_{kn}t)V_{kn}c_n^{(1)} \tag{A.14}$$

$$\vdots$$

These are the perturbative equations of motion that I will now use to study the RWA.

A.4 Comparing the Effects of Linear and Rotating Driving Fields

I will now calculate to first order the amplitude of going from the ground state i to the excited state f. By doing this with both the full Hamiltonian (Eq. A.1) and the RWA Hamiltonian (Eq. A.2), I will show that the RWA is a suitable approximation, to first order in the driving field amplitude A, if the system is driven on resonance, and the time t considered is long with respect to the intrinsic time scale, $2\pi\hbar/\varepsilon$.

RWA Hamiltonian Contributions up to 1st order in A

Here $V = V^{RWA}$ where

$$V^{RWA} = \frac{\mathrm{A}}{4}\exp(-i\omega t)|i\rangle\langle f| + \frac{\mathrm{A}}{4}\exp(i\omega t)|f\rangle\langle i|. \tag{A.15}$$

Assuming $c_i^{(0)} = c_i(t = 0) = 1$ and $c_f^{(0)} = c_f(t = 0) = 0$, and since V only couples different eigenstates, one need only consider $k = f$ and $n = i$ in Eq. A.13. Integrating Eq. A.13 from time 0 to t, and plugging in Eq. A.15, one finds

$$c_f^{(1)} = -\frac{i}{\hbar}\int_0^t V_{fi}\exp(-i\omega_{fi}t')c_i^{(0)}dt' = -\frac{i}{\hbar}\int_0^t \frac{\mathrm{A}}{4}\exp(i\omega t')\exp(-i\omega_{fi}t')dt'. \quad \text{(A.16)}$$

Upon integration one has

$$c_f^{(1)} = \frac{\mathrm{A}}{4\hbar}\frac{(1-\exp(i(\omega-\omega_{fi})t)}{(\omega-\omega_{fi})}. \quad \text{(A.17)}$$

To first order in A the probability to be in the excited state is then

$$|(c_f^{(1)})|^2 = \frac{\mathrm{A}^2}{4\hbar^2}\frac{\sin^2\left[\frac{(\omega-\omega_{fi})t}{2}\right]}{(\omega-\omega_{fi})^2}. \quad \text{(A.18)}$$

Full Hamiltonian Contributions up to 1st order in A

Now $V = V^{Linear}$ where

$$\begin{aligned} V^{Linear} =& \frac{\mathrm{A}}{4}\exp(i\omega t)|i\rangle\langle f| + \frac{\mathrm{A}}{4}\exp(i\omega t)|f\rangle\langle i| \\ & \frac{\mathrm{A}}{4}\exp(-i\omega t)|i\rangle\langle f| + \frac{\mathrm{A}}{4}\exp(-i\omega t)|f\rangle\langle i|. \end{aligned} \quad \text{(A.19)}$$

Once again, setting $k = f$ and $n = i$ in equation A.13, integrating both sides from times 0 to t, plugging in Eq. A.19, and using $c_i^{(0)} = 1$, one finds

$$c_f^{(1)} = -\frac{i}{\hbar}\int_0^t V_{fi}\exp(-i\omega_{fi}t')c_i^{(0)}dt' = -\frac{i}{\hbar}\int_0^t \frac{\mathrm{A}}{4}[\exp(i\omega t')+\exp(-i\omega t')]\exp(-i\omega_{fi}t')dt'. \quad \text{(A.20)}$$

Upon integration one then has

$$c_f^{(1)} = \frac{\mathrm{A}}{4\hbar}\left[\frac{(1-\exp(i(\omega-\omega_{fi})t)}{(\omega-\omega_{fi})} - \frac{(1-\exp(-i(\omega+\omega_{fi})t)}{(\omega+\omega_{fi})}\right]. \quad \text{(A.21)}$$

To first order the probability to be in the excited state is

$$|(c_f^{(1)})|^2 = \overbrace{\frac{A^2}{4\hbar^2}\frac{\sin^2\left[\frac{(\omega-\omega_{fi})t}{2}\right]}{(\omega-\omega_{fi})^2}}^{I} + \overbrace{\frac{A^2}{4\hbar^2}\frac{\sin^2\left[\frac{(\omega+\omega_{fi})t}{2}\right]}{(\omega+\omega_{fi})^2}}^{II}$$

$$- \overbrace{\frac{1}{2}\frac{A^2}{4\hbar^2}\left[\frac{1-\cos[(\omega-\omega_{fi})t]-\cos[(\omega+\omega_{fi})t]+\cos(2\omega_{fi}t)}{(\omega-\omega_{fi})(\omega+\omega_{fi})}\right]}^{III} \qquad \text{(A.22)}$$

When are the 1st order contributions to the excited state probability the same?

In the RWA case, the probability to be in the excited state goes like a sinc^2 function centered at ω_{fi} (Eq. A.18). In the linear drive case the probability goes like a sinc^2 function centered at ω_{fi} (term I in Eq. A.22), with another sinc^2 function centered at -ω_{fi} (term II in Eq. A.22), and an interference term (term III in Eq. A.22). Driving at a frequency $\omega \simeq \omega_{fi}$, one can ignore the probability contributed by terms II and III if the width $\delta\omega$ of the main peak of the sinc^2 function centered at ω_{fi}, is much less than $2\omega_{fi}$, the distance to the center of the other sinc^2 function. But since $\delta\omega \simeq \frac{4\pi}{t}$, this inequality can be rewritten as t$\gg \frac{2\pi}{\omega_{fi}}$. So for the RWA to be valid to first order, one must have:

1. $\omega \simeq \omega_{fi} = \frac{\varepsilon}{\hbar}$
2. t$\gg \frac{2\pi}{\omega_{fi}} = \frac{2\pi\hbar}{\varepsilon}$

These two requirements are both related to driving on resonance. The first condition is the standard statement of being on resonance, and the second condition ensures that the driving field is left on for long enough, so that to the two-level system, the driving field has a definite single frequency. Only then can the drive truly be deemed on resonance.

To summarize what has been done so far, I have found two conditions which amount to driving on resonance, that make the full and RWA Hamiltonians give the same observable results to first order in A. I will now proceed in a similar manner as above, and calculate the 2nd order contributions to the populations of the two states. I will find a third and final requirement one must meet to be able to legitimately use the RWA.

RWA Hamiltonian Contributions up to 2nd order in A

Here $V = V^{RWA}$ where

$$V^{RWA} = \frac{\mathrm{A}}{4}\exp(-i\omega t)|i\rangle\langle f| + \frac{\mathrm{A}}{4}\exp(i\omega t)|f\rangle\langle i| \tag{A.23}$$

With $c_i^{(1)} = 0$ since $c_f^{(0)} = 0$, $c_f^{(1)}$ given by Eq. A.17, and V only coupling different eigenstates, one need only consider $k = i$ and $n = f$ in Eq. A.14. Integrating both sides of Eq. A.14 to time t, plugging in Eq. A.23, and using $c_f^{(1)}$ given by Eq. A.17, one finds

$$\begin{aligned} c_i^{(2)} &= -\frac{i}{\hbar}\int_0^t V_{if}\exp(-i\omega_{if}t')c_f^{(1)}dt' \\ &= -\frac{i}{\hbar}\int_0^t \frac{\mathrm{A}}{4}\exp(-i\omega t')\exp(i\omega_{fi}t')\frac{A}{4\hbar}\frac{(1-\exp(i(\omega-\omega_{fi})t')}{(\omega-\omega_{fi})}dt'. \end{aligned} \tag{A.24}$$

Upon integration one has

$$c_i^{(2)} = \frac{\mathrm{A}^2}{16\hbar^2}\left[-\frac{\exp(-i(\omega-\omega_{fi})t)}{(\omega-\omega_{fi})^2} - \frac{t}{(\omega-\omega_{fi})} + \frac{1}{(\omega-\omega_{fi})^2}\right]. \tag{A.25}$$

Full Hamiltonian Contributions up to 2nd order in A

Now $V = V^{Linear}$ where

$$\begin{aligned} V^{Linear} =& \frac{\mathrm{A}}{4}\exp(i\omega t)|i\rangle\langle f| + \frac{\mathrm{A}}{4}\exp(i\omega t)|f\rangle\langle i| \\ & \frac{\mathrm{A}}{4}\exp(-i\omega t)|i\rangle\langle f| + \frac{\mathrm{A}}{4}\exp(-i\omega t)|f\rangle\langle i| \end{aligned} \tag{A.26}$$

Once again, $c_i^{(1)} = 0$ since $c_f^{(0)} = 0$, and $c_f^{(1)}$ given by Eq. A.17, and since V only couples different eigenstates, one need only consider $k = i$ and $n = f$ in Eq. A.14. I do not use $c_f^{(1)}$ given by expression A.21, since I must now honor the constraints found in the first order calculations, requirements 1 and 2, when searching for the final constraints from higher order contributions. Integrating both sides of Eq. A.14 to time t, plugging in Eq. A.26, and using $c_f^{(1)}$ given by expression A.17, one finds

$$\begin{aligned} c_i^{(2)} &= -\frac{i}{\hbar}\int_0^t V_{if}\exp(-i\omega_{if}t')c_f^{(1)}dt' \\ &= -\frac{i}{\hbar}\int_0^t \frac{\mathrm{A}}{4}[\exp(-i\omega t')+\exp(i\omega t')]\exp(i\omega_{fi}t')\frac{A}{4\hbar}\frac{(1-\exp(i(\omega-\omega_{fi})t')}{(\omega-\omega_{fi})}dt'. \end{aligned} \tag{A.27}$$

Upon integration one then has

$$\begin{aligned} c_i^{(2)} = \frac{\mathrm{A}^2}{16\hbar^2}[&\frac{\exp(i(\omega+\omega_{fi})t)}{(\omega+\omega_{fi})(\omega-\omega_{fi})} - \frac{\exp(-i(\omega-\omega_{fi})t)}{(\omega-\omega_{fi})^2} - \frac{\exp(2i\omega t)}{2\omega(\omega-\omega_{fi})} - \frac{t}{(\omega-\omega_{fi})} \\ &- \frac{1}{(\omega+\omega_{fi})(\omega-\omega_{fi})} + \frac{1}{(\omega-\omega_{fi})^2} + \frac{1}{2\omega(\omega-\omega_{fi})}]. \end{aligned} \tag{A.28}$$

When are the 2nd order contributions to the ground state amplitude the same?

The 2nd order contributions from the two different drives are the same when

$$\frac{\mathrm{A}^2}{16\hbar^2}\left[\frac{\exp(i(\omega+\omega_{fi})t)}{(\omega+\omega_{fi})(\omega-\omega_{fi})} - \frac{\exp(2i\omega t)}{2\omega(\omega-\omega_{fi})} - \frac{1}{(\omega+\omega_{fi})(\omega-\omega_{fi})} + \frac{1}{2\omega(\omega-\omega_{fi})}\right] = 0. \tag{A.29}$$

In the most stringent limit of requirement 1 above one has $\omega = \frac{\varepsilon}{\hbar}$, in which case Eq. A.29 always holds. When considering the case of being slightly off-resonance, one can do a Taylor series expansion around $\omega = \frac{\varepsilon}{\hbar}$ and find that this equality is approximately valid when $\frac{A}{\hbar\omega} \simeq \frac{\mathrm{A}}{\varepsilon} \ll 1$. And so the regime so far in which the RWA is valid is:

1. $\omega \simeq \omega_{fi} = \frac{\varepsilon}{\hbar}$
2. t$\gg \frac{2\pi}{\omega_{fi}} = \frac{2\pi\hbar}{\varepsilon}$

3. $A \ll \varepsilon$

The third requirement for the validity of the RWA is quite interesting, in that it is coincidentally the same requirement typically used to justify the validity of keeping only the first order terms when using perturbation theory. And so the derivation here contrasts the case where you get the third condition by invoking the ad hoc restriction that the problem be accurately solved by going only to first order in A [94].

Appendix B

Reprint of "Implementation Schemes for the Factorized Quantum Lattice-Gas Algorithm for the One Dimensional Diffusion Equation Using Persistent-Current Qubits"

D. M. Berns and T. P. Orlando, "Implementation Schemes for the Factorized Quantum Lattice-Gas Algorithm for the One Dimensional Diffusion Equation using Persistent-Current Qubits," *Quant. Info. Process.* 4, 1 (2005).

Quantum Information Processing, Vol. 4, No. 4, October 2005 (© 2005)
DOI: 10.1007/s11128-005-6492-z

Implementation Schemes for the Factorized Quantum Lattice-Gas Algorithm for the One Dimensional Diffusion Equation Using Persistent-Current Qubits

David M. Berns[1,3] and T. P. Orlando[2]

Received January 14, 2005; accepted May 4, 2005

We present two experimental schemes that can be used to implement the Factorized Quantum Lattice-Gas Algorithm for the 1D Diffusion Equation with Persistent-Current (PC) Qubits. One scheme involves biasing the PC Qubit at multiple flux bias points throughout the course of the algorithm. An implementation analogous to that done in Nuclear Magnetic Resonance (NMR) Quantum Computing is also developed. Errors due to a few key approximations utilized are discussed and differences between the PC Qubit and NMR systems are highlighted.

KEY WORDS: Quantum Lattice-Gas; flux qubit; diffusion; quantum computation.

PACS: 03.67.Lx; 85.25.Cp.

1. INTRODUCTION

Most algorithms designed for quantum computers will not best their classical counterparts until they are implemented with thousands of qubits. For example, the factoring of binary numbers with a quantum computer is estimated to be faster than a classical computer only when the length of the number is greater than about 500 digits.(1) Accounting for error correction circuitry(2) would bring the size of the needed quantum computer to be in the thousands of qubits. In contrast, the Factorized Quantum Lattice-Gas Algorithm (FQLGA)(3) for fluid dynamics simulation, even

---

[1] Department of Physics, Massachusetts Institute of Technology, Cambridge, MA 02139, USA.
[2] Department of Electrical Engineering and Computer Science, Massachusetts Institute of Technology, Cambridge, MA 02139, USA.
[3] To whom correpondence should be addressed. E-mail: dmb@MIT.edu

when run on a quantum computer significantly smaller than the one just discussed, has significant advantages over its classical counterparts.

The FQLGA is the quantum version of classical lattice-gases (CLG).(4) The CLG are an extension of classical cellular automata with the goal of simulating fluid dynamics without reference to specific microscopic interactions. The binary nature of the CLG lattice variables is replaced for the FQLGA by the Hilbert space of a two-level quantum system. The results of this replacement are similar to that of the lattice–Boltzmann model, but with a few significant differences.(5) The first is the exponential decrease in required memory. The second is the ability to simulate arbitrarily small viscosities.

As of today there is a plethora of qubits to choose from when designing a quantum computer, and a promising class is superconducting qubits based on Josepshon junction circuits.(6–10) One major advantage of any of these superconducting systems is the ability to precisely engineer the quantum Hamiltonian, which extends from single qubit design to multi-qubit coupling arrangements to measurement engineering. The quantum computer considered here will be built using the Persistent-Current Qubit (PC Qubit).(6)

The goal of this paper is to show how one can implement a 1D version of the FQLGA with the PC Qubit. To this end we will begin by reviewing the algorithm, specifically the one that simulates the diffusion equation, without a loss of generality in understanding the essence of the algorithm or its general requirements. We will then review the PC qubit and show explicitly how to implement the algorithm with this system. Some important differences between the PC qubit and the two-state system studied in Nuclear Magnetic Resonance Quantum Computation (NMRQC)(11) will be shown to allow for some interesting new techniques in implementing quantum logic. We will also show how to implement the algorithm with the PC qubit in a very analogous way to NMRQC schemes(12) with a few significant differences.

2. FQLGA FOR THE 1D DIFFUSION EQUATION

The first thing one must do in the FQLGA is to define a lattice. Each lattice point n will represent a unique position in the simulated fluid. The simulation will contain a finite number of lattice points, hence space is discretized in the simulation.

Next one must encode the mass density ρ of the fluid at each lattice site. In the FQLGA this is done by building at each lattice site a set $\{i\}$ of coupled qubits. Each qubit represents the motion of particles on the microscopic level in one of a finite set of directions. For the diffusion equation in one dimension, at any point in your fluid, there are only two possible directions for each particle to be moving, to the left and to the right. Hence, only two qubits are needed to specify the mass density ρ^n at each lattice site. This intuitive reasoning does not extrapolate to higher dimensional simulations because even in two dimensions there would be an infinite number of directions particles could travel in. In higher dimensions one must adhere to much more mathematical conditions to decide on the small set of directions one must include for a faithful simulation.(4) The probability P of a particle to be participating in the motion assigned to each qubit will be encoded in the probability amplitude of the qubit being in its excited state $|1\rangle$. The state of a qubit is thus set to

$$|\Psi_i{}^n\rangle = \sqrt{1 - P_i{}^n}|0\rangle + \sqrt{P_i{}^n}|1\rangle, \tag{1}$$

where i is the qubit index, n is the lattice site index, and $|0\rangle$ is the ground state of the qubit. For the 1D problem considered here, $i = \{1, 2\}$ and $n = \{1, N\}$, where N is the number of lattice sites used in the simulation. One can easily conceive of fluids of multiple phases with multiple types of interactions even in one dimension, in which the size of $\{i\}$ would be much larger, but this will not be considered here. The mass density ρ is then calculated by summing the occupation probabilities for all qubits at a node. At time t=0 in a 1D simulation the occupation probabilities $P_1{}^n$ and $P_2{}^n$ are set to $\rho^n/2$, which is the condition for local equilibrium in the fluid.(13)

Now that the fluid is initialized, one must account for the interaction of particles in the fluid. These collisions are encoded by the application of a unitary transformation to the coupled systems at each lattice site. For the 1D diffusion equation this unitary transformation is

$$\sqrt{\text{swap}} = \frac{1}{2}\begin{pmatrix} 2 & 0 & 0 & 0 \\ 0 & 1+i & 1-i & 0 \\ 0 & 1-i & 1+i & 0 \\ 0 & 0 & 0 & 2 \end{pmatrix}. \tag{2}$$

The basis for computation is the set of four product states: $|0\rangle|0\rangle$, representing no particles at the site, $|0\rangle|1\rangle$, representing the existence of only a particle moving to the right at the site, $|1\rangle|0\rangle$, representing the existence of only a particle moving to the left at the site, and $|1\rangle|1\rangle$, representing particles moving in both directions at the site. To conserve particle number there can be coupling only between the middle two states. The identity transformation on the first and last states corresponds to no collisions and a perfectly elastic collision, respectively. Transformation of the middle two states was something that never existed in the classical algorithm because there was no superposition of these two states.

After collision the states of the qubits at each lattice site are in general entangled, and we denote that state as $|\Upsilon^n\rangle$. The state of each qubit is then measured, and the process described thus far is repeated many times to achieve an ensemble average. Upon completion of these measurements one will have found the post-collision outgoing occupation probabilities, denoted by $P_i{}^n$ once again, and hence the post-collision state of each qubit, denoted by $|\chi_i{}^n\rangle$. Note that the occupation probabilities now represent something very different than before the collision. The particles have now interacted and are ready to move to the next lattice site.

One must now "stream" the occupation probabilities to their new lattice sites. This is done in a classical computer by storing the occupation probabilities at each lattice site that are coming from adjacent lattice sites due to collisions. More precisely, $P_1{}^n$ becomes $P_1{}^{n+1}$ and $P_2{}^n$ becomes $P_2{}^{n-1}$. Periodic boundary conditions are assumed when streaming at the edges of the fluid.

To find the mass density ρ^n at $t=1$ one simply adds the occupation probability for both qubits at site n once streaming has been done. One time step of the algorithm has now been completed. To simulate the next time step simply start the above procedure all over again except now setting the initial states with the new occupation probabilities just found.

The algorithm can be summarized by four major steps, which are illustrated in Fig. 1. The first step encodes the initial state of the fluid by quantum mechanically setting the state $|\Psi_i{}^n\rangle$ of each qubit at each lattice site. The second step transforms the two-qubit product state at each lattice site to in general an entangled state, whose state is denoted by $|\Upsilon^n\rangle$. Third one makes a projective measurement of the post-collision states $|\chi_i{}^n\rangle$, and one must repeat the first three steps to find the outgoing occupation probabilities $P_i{}^n$. In the fourth and final step one streams the mass density with the appropriate post-collision occupation probabilities, from the left with particles representing positive momentum, and from the right with particles representing negative momentum, and the mass density is calculated. Subsequent time steps are identical except for a change in the initial mass density profile, i.e., initial qubit states in the first step.

3. PERSISTENT-CURRENT QUBIT

The fundamental unit of quantum logic we will use to implement the algorithm is the PC Qubit.(14) It consists of a superconducting loop that is interrupted by three Josephson junctions, pictured as x's in Fig. 2(a). The magnetic flux Φ is the only control field for our qubit, and as shown in the figure, is usually denoted by $f=\Phi/\Phi_o$, where $\Phi_o=h/2e$ is a single flux

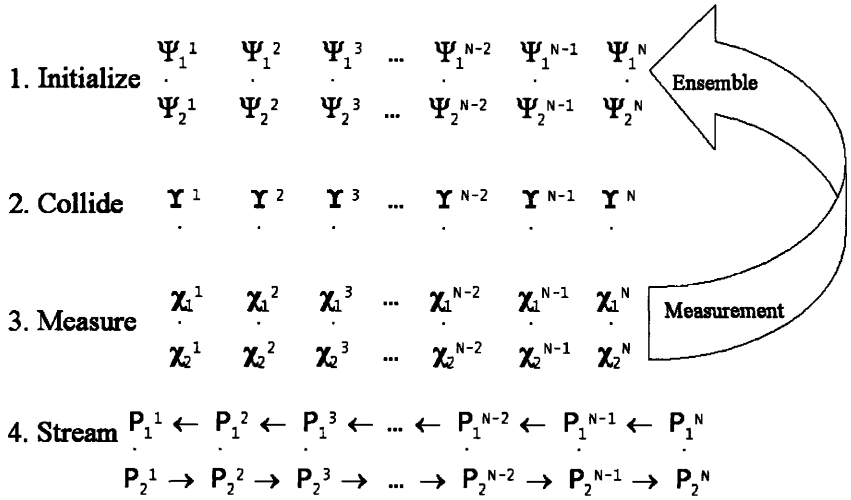

Fig. 1. General summary of the four major steps that comprise one time step of the 1D FQLGA fluid dynamics simulation. The sequence of initialization of mass density, collision of particles, and measurement of post-collision states is repeated many times to make an ensemble measurement. Propagation between collisions is accomplished by storing the adjacent occupation probabilities for a given site in a classical computer, where the mass density is then calculated for this time step. Subsequent time steps utilize these "streamed" occupations when initializing again for the next set of collisions and "streaming".

quantum, h is Planck's constant, and e is the magnitude of the charge of an electron. Physically, a Josephson junction is a small layer of insulator sandwiched between superconductors, so our system is a superconducting loop interrupted by three layers of insulator about 1 nm thick. For single qubit manipulation the magnetic flux through the loop will be modified. The flux seen by a DC SQUID magnetometer, a combination of applied flux and qubit-induced flux, will serve as our measurement variable.

The Hamiltonian of the qubit is derived by considering a circuit element model of our system, which consists of three Josepshon junctions, where two junctions have the same cross-sectional area, and the third is smaller by a factor of α. The constituent relations for an ideal Josephson junction are

$$I = I_C \sin(\varphi), \tag{3a}$$

$$V = \frac{\Phi_o}{2\pi}\frac{\mathrm{d}\varphi}{\mathrm{d}t} \tag{3b}$$

where I is the current through the junction, V the voltage across the junction, I_C the maximum current the junction can hold without a voltage

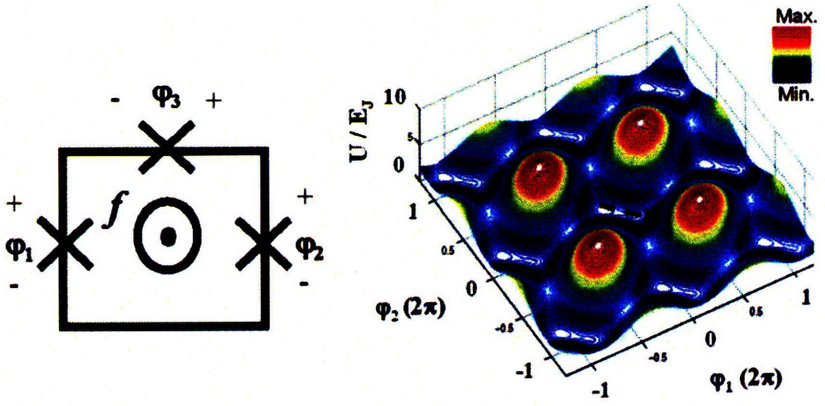

Fig. 2. (a) Schematic drawing of the PC Qubit. The x's represent Josephson junctions, with all connecting leads made of the same superconductor that is part of the junctions. The sign conventions chosen when summing phases are shown, and the magnetic flux penetrating the loop (in units of Φ_o) is labeled by f. (b) The potential energy of the full Hamiltonian for the PC Qubit is plotted when the system is biased at $f = 0.495\Phi_o$. The phase particle sees an infinite 2D lattice with unit cells resembling a double well potential.

appearing across it, $\varphi = \theta_1 - \theta_2$, and $\theta_{1,2}$ is the gauge-invariant phase that characterizes the superconductor condensate on the $+, -$ side of the junction, respectively. Note that I_c is a function linear in the cross-sectional area of the junction, and hence the third junction has a lower I_c by a factor of α.

The energy associated with an ideal Josephson junction is found by integrating the power from time $t=0$ to some final time t_o, which is equivalent to an integral from zero phase to some phase φ. The energy it takes to set the phase of a Josephson junction to φ is

$$E = \int_o^{t_o} (I_c \sin\varphi') \left(\frac{\Phi_o}{2\pi} \frac{\mathrm{d}\varphi'}{\mathrm{d}t} \right) \mathrm{d}t = \frac{\Phi_o I_c}{2\pi} \int_o^{\varphi} \sin\varphi' \mathrm{d}\phi' = E_j(1 - \cos\varphi), \quad (4)$$

where $E_j = \Phi_o I_c / 2\pi$.

By including the charging energies due to the capacitance of the junctions, the Hamiltonian of our circuit is$^{(14)}$

$$H = \frac{P_p^2}{2M_p} + \frac{P_m^2}{2M_m} + E_j[2 + \alpha - 2\cos(\varphi_p)\cos(\varphi_m) - \alpha\cos(2\pi f + 2\varphi_m)], \quad (5)$$

where $\varphi_p = \varphi_1 + \varphi_2$, $\varphi_m = \varphi_1 - \varphi_2$, $P_p = M_p \mathrm{d}\varphi_p/\mathrm{d}t$, $P_m = M_m \mathrm{d}\varphi_m/\mathrm{d}t$, $M_p = (\Phi_o/2\pi)^2 2C$, and $M_m = (\Phi_o/2\pi)^2 2C(1+2\alpha)$. The number of degrees of freedom in the problem was reduced by the fluxoid quantization condition[(15)]

$$\varphi_1 + \varphi_3 - \varphi_2 = 2\pi n + \frac{2\pi \Phi}{\Phi_o}, \tag{6}$$

which forces the sum of the gauge invariant phases to be proportional to the amount of flux quanta modulo an integer multiple of 2π.

We have chosen to associate the capacitive energy, the first two terms in (5), with the kinetic energy, and the ideal Josephson energy, the last four terms in Eq. (5), with the potential energy. The potential energy is that of an infinite lattice of double wells, as seen in Fig. 2(b). The arrow in the plot shows the direction one would take to traverse from one side of a double well to another.

Although quantum mechanics plays a foremost role in deriving the constitutive relations for the superconducting circuit elements, the Hamiltonian for the circuit itself so far has been classical. The quantum version of the circuit can be understood by imagining a phase "particle" in the potential shown in Fig. 2(b). The behavior of this "particle" is analogous to a particle with an anisotropic mass moving in a 2D periodic potential, and so there exist energy bands in a $\vec{k}$-space, which is here related to the charge stored capacitively by the Josephson junctions. By properly choosing E_j/E_c, where $E_c = e^2/2C$, one can remove any $\vec{k}$ (and hence charge) dependence in the energy of the system, and hence can reduce the problem to that of an effective double well. What we have done is choose parameters such that tunneling between adjacent double wells can be neglected relative to the tunneling within a double well in the tight-binding solution(intra-well tunneling typically about 10^4 times more likely), making the solution effectively that of a single double well.

By considering only the lowest two levels of the double well, the equivalent Hamiltonian is

$$\hat{H} = \Phi_o I_p \left(f - \tfrac{1}{2}\right) \hat{\sigma}_z - \tau \hat{\sigma}_x, \tag{7}$$

where $\pm I_p$ are the eigenvalues of circulating current for the two $\hat{\sigma}_z$ eigenstates and τ is the tunneling element from one side of the double well to the other. The energies of the two eigenstates along with a sketch of the double well as a function of applied flux are shown in Fig. 3. One significant difference between this qubit and the one used in NMRQC is the presence of the $\hat{\sigma}_x$ term. The implication of such a term is that the energy of the eigenstates as well as the eigenstates themselves change as the bias field is modified. In Fig. 3 we see that at the classical degeneracy point $f = 1/2$ the qubit's eigenstates are $\hat{\sigma}_x$ eigenstates, while far from $f = 1/2$,

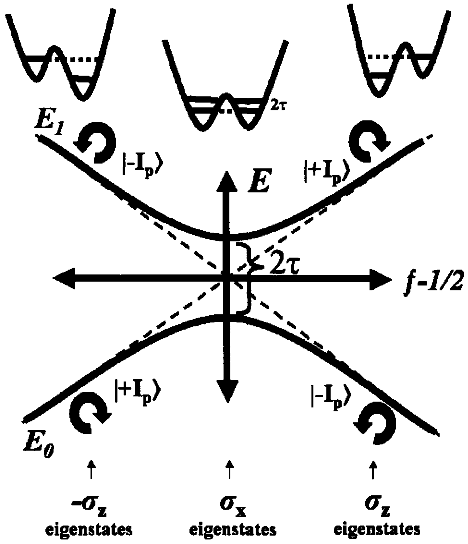

Fig. 3. The energy levels of the PC Qubit are shown as a function of f. The eigenstates of the system change with f and are labeled on the plot. The change in the potential of the phase particle is also depicted at the top of the plot. The energy difference between the states at $f = 1/2$ is seen to be twice the intra-well tunnelling.

but still far from $f = 1$, the eigenstates are those of $\hat{\sigma}_z$. The same thing happens for $f < 1/2$, but now the eigenstates have switched energies, i.e., the ground state here is the first excited state of $\hat{\sigma}_z$ and vice versa.

The PC Qubit has some advantages over other superconducting qubits.(14,16) Charge fluctuations, a consequence of trapped substrate charge, are deemed inconsequential through the choice of parameters used when designing the PC Qubit circuit. Also, flux noise has been reduced in this system over other flux qubits since this system has a smaller loop.

A typical conceptual misconception can be addressed at this point. The two different states used in computation are not related to single Cooper pair behavior. Rather, they are macroscopically distinct states described by the circulating current due to millions of Cooper pairs, characterized by different average induced fluxes when in a magnetic field.

As seen in Sec. 2, the qubits will need to be coupled. For the PC Qubit we have discussed thus far, just as microwaves can only be coupled in through $\hat{\sigma}_z$, coupling between qubits can only be of the form $\hat{\sigma}_z\hat{\sigma}_z$. Slight modifications of the aforementioned qubit design does allow for different coupling, despite the fact that the structures are still completely planar.(14)

4. IMPLEMENTATION WITH THE PC QUBIT

We now show how one can use the PC Qubit to simulate the 1D diffusion equation. In Sec. 4.1, we elaborate on a scheme based upon changing the flux bias points of the qubits during the algorithm, which will lead to a very general initialization scheme, but a less general collision. In Sec. 4.2, we discuss a more general collision, analogous to that done in NMRQC, and how to initialize the qubits before this general collision. Note that the two implementations differ solely in the way single lattice sites are treated. In both cases one has N qubit pairs fabricated monolithically that are initialized, transformed, and measured simultaneously.

4.1. The Multiple Bias Point Implementation

The first of the four steps of the algorithm is initializing each qubit at each node. As discussed in Sec. 2, each qubit must be initialized into a state of real and positive phase in its own Hilbert space. This set of states consists of all those lying on the real phase geodesic between the ground and first excited states on the Bloch sphere. The ground state of the PC Qubit as a function of applied flux coincidentally also occupies exactly this geodesic on the Bloch sphere, as discussed in Sec. 3. Initialization can thus be accomplished while staying in the ground state by adiabatically changing the applied magnetic flux, as depicted in Fig. 3.

The flux used to set the state of one qubit will be affected by the state of the other qubit and its bias current. This permanent inductive coupling can be accounted for by slightly adjusting the applied flux to compensate for the flux introduced by the other qubit and its bias line. On the other hand, by initializing into the ground state we have avoided the detrimental effects of dephasing and relaxation, as well as the errors found in a typical NMR initialization scheme.(12) We emphasize that the initialization portion of the algorithm is identical for any simulation, whether it be for a different equation, a multi-phase simulation, or in a different number of dimensions.

The second step of the algorithm is the collision. Here we study a very specific unitary transformation, the $\sqrt{\text{swap}}$ described in Sec. 2. This matrix simply "half-way" swaps the middle two (first and second excited) computational states of the coupled system. In NMRQC, the coupled eigenstates are exactly those computational states, but there are no direct matrix elements connecting these states.(17) When the PC Qubits are coupled, the first and second excited states of the four-level system, denoted as $|1\rangle$ and $|2\rangle$, respectively, are in general not the same as the computational basis states the $\sqrt{\text{swap}}$ intends to affect. However, the DC bias fields of each qubit can be tuned to make these two sets of eigenstates coincide. Once this is done, one can then implement the $\sqrt{\text{swap}}$ by simply oscillating the magnetic field bias at the frequency corresponding to the energy difference between the middle two eigenstates. This is just a Rabi oscillation between the middle two eigenstates, and since one wants to only "half-way" swap the states, the radiation should only be left on for a quarter of a Rabi period.

Besides finding the appropriate bias points such that the middle two eigenstates of the coupled system are very similar to the middle two computational states, one must also verify that the coupling between these states in the presence of an oscillating magnetic field is non-zero. The results of these calculations are shown in Fig. 4. The bias point of qubit 1, f_1, must be chosen to be far from 1/2, but not too far. In these calculations we take $f_1 = 0.508$. In the figure, we see that when qubit 2 is biased at around $f_2 = 0.51$, the first two system excited states are very similar to the middle two computational states, with overlap elements of about 0.97. At this same bias point one sees a Rabi matrix element of about 0.02, which is more than sufficient for our purposes.

This approximate swap has been incorporated into simulation of the FQLGA for the 1D diffusion equation and the results are pictured in Fig. 5. Snapshots of three different times have been shown, for both an ideal simulation and one including the error introduced due to the approximate collision. At time $t = 0$ one can see that we have initialized our fluid to a gaussian profile. Later time steps of the ideal implementation show the expected spreading due to diffusion, while conserving the total number of particles. Increase in the diffusion constant of the approximate collision when compared to the ideal simulation results from the enhanced population in the $|00\rangle$, $|01\rangle$, and $|10\rangle$ states relative to the $|11\rangle$ state due to extra matrix elements in the approximate swap that couple the four states. The matrix elements are actually enhanced more in the upper triangle elements than in the lower triangle elements(with respect to the anti-diagonal), which gives rise to the slight drift to the right that is observed in the simulation.

Even with an ideal swap operator, an interesting timing issue arises upon non-adiabatically switching the bias fields from the initialization settings to the proper settings to do a Rabi oscillation between the two

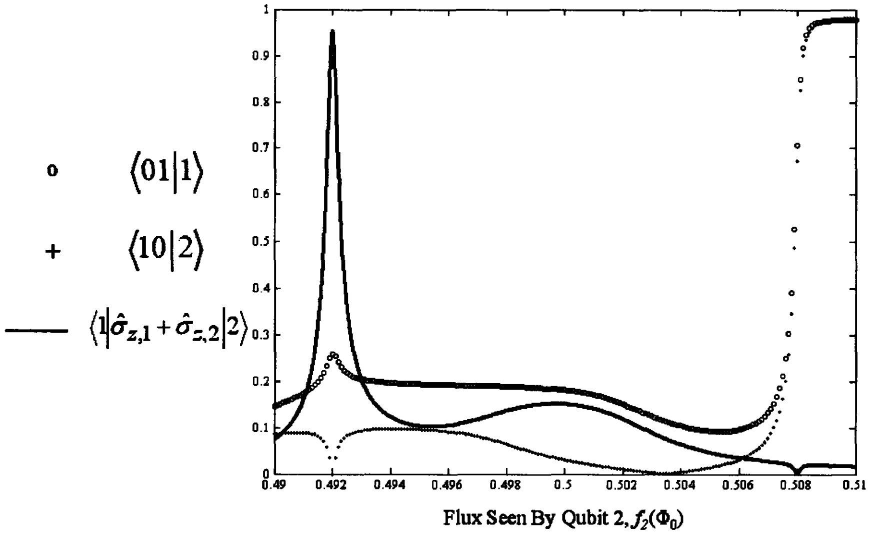

Fig. 4. The overlap between the first (second) excited state $|1\rangle$ ($|2\rangle$) of the PC Qubit coupled system and the $|01\rangle$ ($|10\rangle$) computational state are plotted when qubit 1 is biased at $f = 0.508$. The coupling between $|1\rangle$ and $|2\rangle$ in the presence of an AC magnetic field is also plotted. Qubit coupling equal to τ (same for both qubits) was assumed in the calculation.

middle product states. We first illustrate this timing issue and then show how it can be made negligible by making a larger ensemble measurement.

Once the applied fluxes are changed to those appropriate to perform the approximate swap, the initialized states will most likely not be eigenstates anymore, and hence will begin to precess due to a time-independent perturbation. Assuming things can not be accurately controlled at these timescales, one will have now introduced a random phase difference between the two qubits due to this Larmor precession. This effect is pictured in Fig. 6. The states before the bias fields are switched lie along the same geodesic. Upon changing the magnetic flux seen by each qubit, the qubits begin to precess, out of phase.

The effect of this phase difference δ on the algorithm will be to alter the fraction of particles at each lattice site, post-collision, that are "moving" to the right and to the left. The results of measuring the post-collision occupation probabilities having accounted for a constant phase difference is summarized by

$$P_1 = P_{1,\ \delta=0} + \gamma \sin(\delta), \tag{8a}$$

$$P_2 = P_{2,\ \delta=0} - \gamma \sin(\delta). \tag{8b}$$

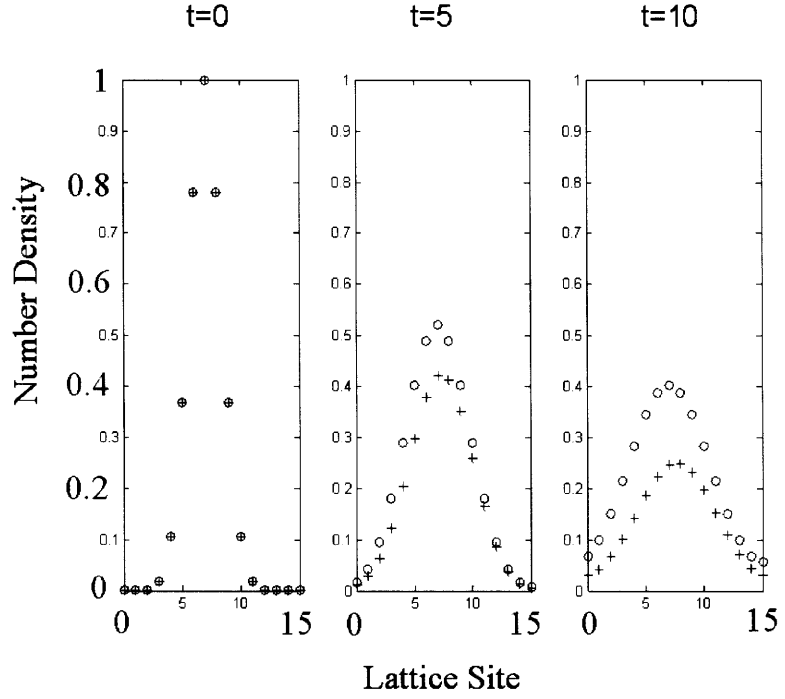

Fig. 5. The results of the FQLGA are simulated having accounted for the approximate nature of the collision proposed in Sec. 4.1 (+). Qubit coupling equal to τ (same for both qubits) was assumed in the approximate swap simulation. The ideal results of the FQLGA are also shown (o).

The effect of this error on the simulation is effectively averaged away when an ensemble is measured, since δ is randomly different for each member of the ensemble. These results are shown in Fig. 7. One can see small random deviations from the ideal simulation that can be made infinitesimally small by measuring a larger ensemble (an ensemble average of 1000 repeated measurements was simulated here).

In summary, an initialization scheme has been developed that is not available to qubits with only one term in their Hamiltonian. This initialization scheme is limited only by the precision of the current source used to create the magnetic field that biases the qubit. The scalability of this scheme relative to those used in NMRQC is an interesting question, but is not resolved here. The collision implementation is also unique to qubits with multiple term Hamiltonians, but the unitary transform implemented is unique to the diffusion equation, and fortuitously simple. A collision

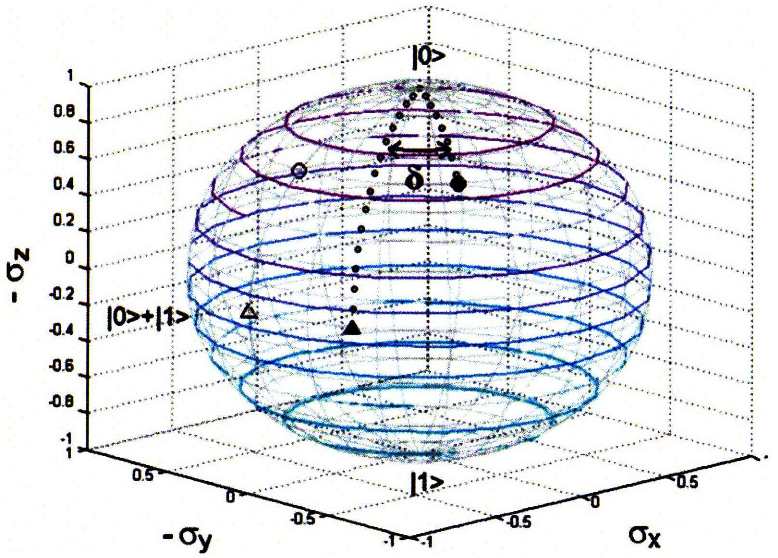

Fig. 6. The unfilled circle and triangle represent two typical initialized states at one lattice point, both on the same north pole to south pole geodesic, before their flux bias is changed to perform the collision. The filled circle and triangle represent the same states after imprecise bias changing has occurred. Imprecisely timed Larmor precession introduces a random phase difference δ between the two states. The unfilled triangle corresponds to the $-\sigma_x$ ground state.

scheme that could be generalized to any unitary transformation would be much more useful.

4.2. Generalized NMRQC-like Implementation

Generalization of the above implementation to any fluid dynamics, i.e., any unitary transformation, can be done in an analogous way to NMRQC schemes. Generalization of the collision transformation consists of using a universal set of quantum computation gates, and decomposing all transformations into a sequence of these.(2) In NMRQC collision is performed by a sequence of single qubit unitary transformations and coupled free evolution. In this section, we will begin by discussing the single qubit rotations needed for a general decomposition, and briefly mention the role they could play in initialization. We will then explore the free evolution of a coupled PC Qubit system, and then show how to combine the single and coupled pulses to implement the collision of the 1D FQLGA for the diffusion equation.

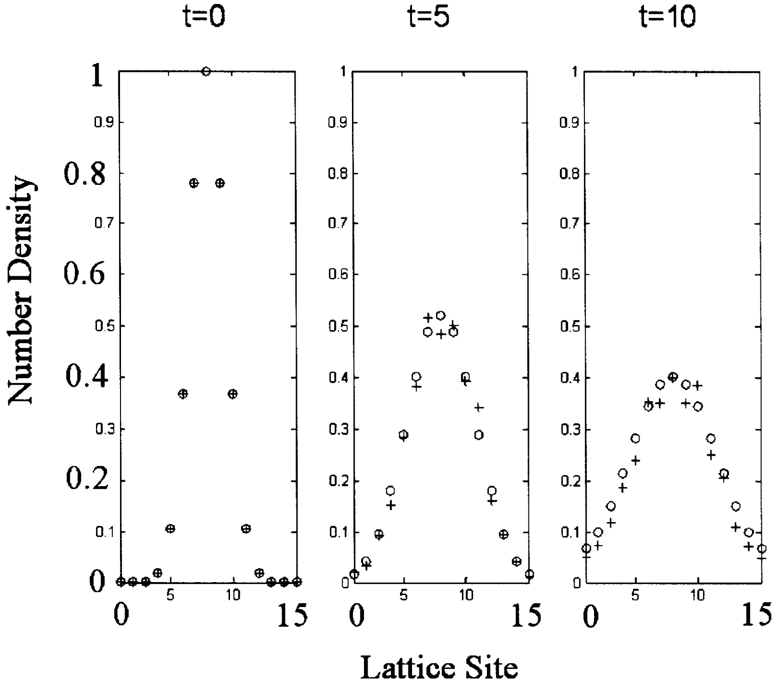

Fig. 7. The results of the FQLGA are simulated having accounted for a random phase difference introduced before the collision for each member of the measurement ensemble (+). The ideal results of the FQLGA are also shown (o).

Single qubit transformations can most easily be achieved in a rotating frame, since here the frequency of precession can be much lower than the Larmor timescale. For this implementation we will only study the case where our qubit is biased at $f = 1/2$. This discussion is easily generalized to any bias point, but the mathematical notation can get quite cumbersome. The Hamiltonian of the PC Qubit in an applied AC field is

$$\hat{H} = w_o \hat{I}_x + g_o \cos(w_o t + \phi)\hat{I}_z, \tag{9}$$

where w_o is the frequency of the applied field, g_o is proportional to the amplitude of the applied field, ϕ is the phase of the applied field, and $\hat{I}_i = \hbar\hat{\sigma}_i/2$.

In the frame rotating about $\hat{I}_x$ this Hamiltonian becomes

$$\tilde{\hat{H}} = \tfrac{1}{2} g_o[\cos(\phi)\hat{I}_z + \sin(\phi)\hat{I}_y]. \tag{10}$$

The quantum state will now precess in this frame about the axis defined by ϕ, with the angle through which the state has precessed given by

$\theta = g_o t/2$. It will be convenient to only consider the set of two rotations defined by $\phi = 0$ and $\pi/2$, which are rotations about $\hat{I}_z$ and $\hat{I}_y$, respectively. These rotations, denoted as $R_z(\theta)$ and $R_y(\theta)$, respectively, can be used in conjunction to bring the qubit state to any point on the Bloch sphere in the rotating frame.

One can use these single qubit rotations not only as part of the collision, but also for initializing, since they can bring the qubit state to anywhere on the Bloch sphere. As already discussed in Sec. 4.1, the ground state of a coupled PC Qubit system is not in general the product of single qubit ground states. Thus, when initializing a qubit via $R_z(\theta)$ and $R_y(\theta)$, one is not starting rotation from the single qubit ground state. However, since the ground state is very close to a product of single qubit ground states, this difference is nearly negligible. In Fig. 8, we show the effects of incorporating this error into the algorithm when the coupling constant is taken to be 1/10 of the qubit resonant frequencies, a rather exaggerated estimate since the coupling is usually much smaller. The diffusion constant is decreased by this approximation, due to the enhanced population in the $|11\rangle$ state relative to the $|00\rangle$ state from the coupling.

The other gate operation needed to form a universal set for general decomposition is coupled free evolution. It is easiest to go to a co-rotating frame where one can have a coupled Hamiltonian only, i.e., no single qubit terms, that is time-independent. In NMRQC this is done by going to the frame where both qubits are rotated around the $\hat{z}$ axis. However, since our coupling does not commute with our single qubit terms, a different method will be used. For notational convenience only, we consider the case where both qubits are biased at $f = 1/2$, where our Hamiltonian is

$$\hat{H} = w_o^1 \hat{I}_x^1 + w_o^2 \hat{I}_x^2 + \frac{2\pi}{\hbar} J_{12} [\hat{I}_z^1 \hat{I}_z^2]. \tag{11}$$

In the co-rotating frame where both qubits are rotating around the $\hat{x}$ axis, one has the Hamiltonian

$$\hat{H} = \frac{\pi}{\hbar} J_{12} [\hat{I}_z^1 \hat{I}_z^2 + \hat{I}_y^1 \hat{I}_y^2] \tag{12}$$

as long as $w_o^1 = w_o^2$. This constraint of $w_o^1 = w_o^2$ imposes limitations on some NMRQC initialization schemes which use frequency selective initialization.

One can now rewrite the unitary collision transformation in the following suggestive way:

$$\sqrt{\text{swap}} = \exp\left[-i\frac{\pi}{8}(\hat{\sigma}_z^1 \hat{\sigma}_z^2 + \hat{\sigma}_y^1 \hat{\sigma}_y^2)\right] \exp\left[-i\frac{\pi}{8}\hat{\sigma}_x^1 \hat{\sigma}_x^2\right]. \tag{13}$$

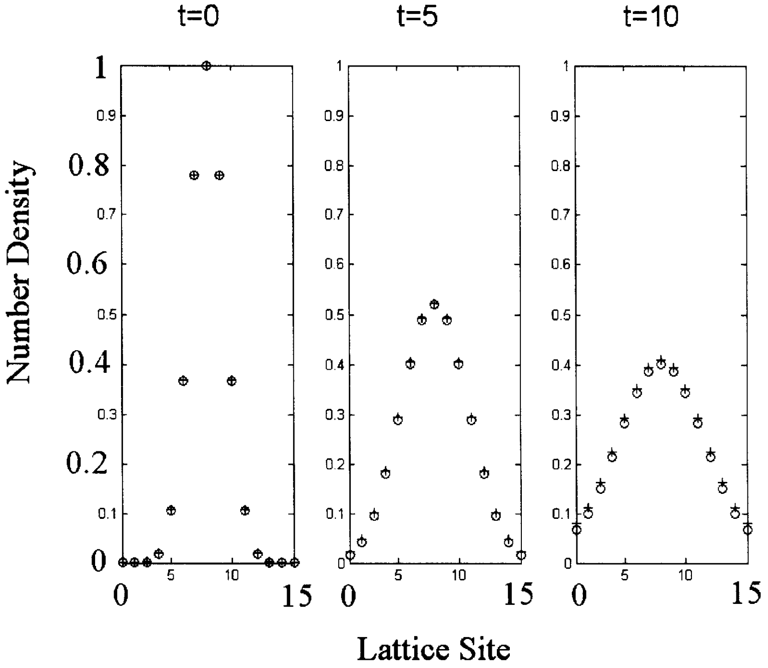

Fig. 8. The results of the FQLGA are simulated for NMR-like single qubit pulse initialization, where errors arise from initializing a coupled ground state that is not a product state (+). The ideal results of the FQLGA are also shown (o).

The first term is just free evolution in the co-rotating frame. The second term can be written as:

$$\begin{aligned}\exp\left[-i\frac{\pi}{8}\hat{\sigma}_x^1\hat{\sigma}_x^2\right] &= R_y^1\left(\frac{\pi}{2}\right)R_y^2\left(\frac{\pi}{2}\right)\\ &\quad\times\exp\left[-i\frac{\pi}{8}\hat{\sigma}_z^1\hat{\sigma}_z^2\right]R_y^1\left(-\frac{\pi}{2}\right)R_y^2\left(-\frac{\pi}{2}\right),\end{aligned}\tag{14}$$

where the middle term can be written as:

$$\begin{aligned}\exp\left[-i\frac{\pi}{8}\hat{\sigma}_z^1\hat{\sigma}_z^2\right] &= \exp\left[-i\frac{\pi}{8}\left(\hat{\sigma}_z^1\hat{\sigma}_z^2+\hat{\sigma}_y^1\hat{\sigma}_y^2\right)\right]R_z^1(\pi)\\ &\quad\times\exp\left[-i\frac{\pi}{8}\left(\hat{\sigma}_z^1\hat{\sigma}_z^2+\hat{\sigma}_y^1\hat{\sigma}_y^2\right)\right]R_z^1(\pi).\end{aligned}\tag{15}$$

Hence one can perform a decomposition of the collision transformation into a sequence of single qubit rotations and coupled free evolution.

In summary, we have shown that the PC Qubit can implement the unitary transform that performs collisions in the 1D FQLGA for the diffusion equation by a single and coupled qubit evolution decomposition. The single qubit rotations were shown to be feasible for qubit initialization as well, with a slight approximation due to the coupled ground state that is not a product state. The coupled free evolution was seen to require identical qubit frequencies over a lattice site, making initialization a bit more challenging.

5. CONCLUSIONS

In this paper, we have shown that the implementation of the FQLGA for the 1D diffusion equation is feasible with PC Qubits. We began by considering the simplest scheme possible using the PC Qubit. This consisted of first initializing the qubits while keeping them in their ground state, and then performing the collision by quickly changing their flux bias points and then performing a single $\pi/2$ pulse. This initialization technique could prove useful, but the way we have implemented the collision is not easily generalized to other collisions. We needed to develop a more general collision scheme, and then see how we could initialize in conjunction with that new scheme.

A more general collision transformation was then discussed by decomposing the unitary matrix into a sequence of single qubit rotations and coupled free evolution. We first developed single qubit rotations for the PC Qubit that could be used as part of the collision decomposition as well as for initializing the occupation probabilities. The initialization was considered only approximate due to the permanent non-commuting coupling between qubits. For the coupled free evolution we saw that transforming to a rotating frame analogously to NMRQC set a strong but feasible constraint on the frequencies of our qubits. Ultimately one would like to remove the constraint of equal frequencies, so that frequency-selective initialization can be done analogously to the NMRQC implementation, alongside the very general collision scheme. One would then also need to account for initialization pulses rotating states from a non-product ground state.

ACKNOWLEDGEMENTS

The authors would like to thank Debra Chen and Jeff Yepez for valuable discussions. This work was supported by the AFOSR/NM grant FA 9550-04-1-0221.

REFERENCES

1. K. Berggren, Quantum Computing with Superconductors, *Proc. IEEE* **92**(10), 1630 (2004).
2. M. A. Nielsen and I. L. Chuang, *Quantum Computation and Quantum Information* (Cambridge Univ. Press, Cambridge, 2000).
3. J. Yepez, *Quantum Computing and Quantum Communications*, Lecture Notes in Computer Science, Vol. 1509, (Springer-Verlag, (1999) p. 35.
4. D. A. Wolf-Gladrow, *Lattice-Gas Cellular Automata and Lattice Boltzmann Models*, edited by A. Dold et al. (Springer, Berlin, 2000).
5. J. Yepez, An efficient quantum algorithm for the one-dimensional Burgers equation, quant-ph/0210092.
6. I. Chiorescu et al., Coherent Dynamics of a Superconducting Flux Qubit, *Science* **299**, 1869 (2003).
7. J. R. Friedman et al., Quantum Superposition of Distinct Macroscopic States, *Nature* **406**, 43 (2000).
8. Y. A. Pashkin et al., Quantum Oscillations in Two Coupled Charge Qubits, *Nature* **421**, 823 (2003).
9. J. M. Martinis et al., Rabi Oscillations in a Large Josephon-Junction Qubit, *Phys. Rev. Lett.* **89**, 117901 (2002).
10. D. Vion et al., Manipulating the Quantum State of an Electrical Circuit, *Science* **296**, 886 (2002).
11. I. L. Chuang et al., Bulk Quantum Computation with Nuclear Magnetic Resonance: Theory and Experiment, *Proc. R. Soc. Lond. A* **454**, 447 (1998).
12. M. Pravia et al., Experimental Demonstration of Quantum Lattice Gas Computation, *Quant. Infor. Processing* **2**, 97 (2003).
13. J. Yepez, Quantum Lattice-Gas Model for the Diffusion Equation, *Intl. J. Mod. Phys. C* **12** (9) 1285 (2001).
14. T.P. Orlando et al., Superconducting Persistent-Current Qubit, *Phys. Rev. B* **60**, 15398 (1999).
15. T.P. Orlando and K.A. Delin, *Foundations of Applied Superconductivity* (Addison-Wesley Reading, MA, UK, 1991).
16. D.J. Van Harlingen et al., Decoherence in Josepshon-junction qubits due to critical-current fluctuations, *Phys. Rev. B* **70**, 064517 (2004).
17. G. P. Berman et al., Simulation of the Diffusion Equation on a Type-II Quantum Computer, *Phys. Rev. A* **66**, 012310 (2002).

Appendix C

Other Selected Reprints

D. M. Berns, W. D. Oliver, S. 0. Valenzuela, A. V. Shytov, K. K. Berggren, L. S. Levitov, and T. P. Orlando, "Coherent Quasiclassical Dynamics of a Persistent Current Qubit," *Phys. Rev. Lett.* 97, 150502 (2006).

S. O. Valenzuela, W. D. Oliver, D. M. Berns, K. K. Berggren, L. S. Levitov, and T. P. Orlando, "Microwave-Induced Cooling of a Superconducting Qubit," *Science* 314, 1589 (2006).

D. M. Berns, M. S. Rudner, S. O. Valenzuela, K. K. Berggren, W. D. Oliver, L. S. Levitov, and T. P. Orlando, "Amplitude Spectroscopy of a Solid-State Artificial Atom," Submitted for publication (2008), arXiv:0805.1552.

M. S. Rudner, A. V. Shytov, L. S. Levitov, D. M. Berns, W. D. Oliver, S. O. Valenzuela, and T. P. Orlando, "Quantum Phase Tomography of a Strongly Driven Qubit," Submitted for publication (2008), arXiv:0805.1555.

Coherent Quasiclassical Dynamics of a Persistent Current Qubit

D. M. Berns,[1,*] W. D. Oliver,[2] S. O. Valenzuela,[3] A. V. Shytov,[4] K. K. Berggren,[2,†] L. S. Levitov,[1] and T. P. Orlando[5]
[1]*Department of Physics, Massachusetts Institute of Technology, Cambridge, Massachusetts 02139, USA*
[2]*MIT Lincoln Laboratory, 244 Wood Street, Lexington, Massachusetts 02420, USA*
[3]*MIT Francis Bitter Magnet Laboratory, Cambridge, Massachusetts 02139, USA*
[4]*Physics Department, Brookhaven National Laboratory, Upton, New York 11973-5000, USA*
[5]*Department of Electrical Engineering and Computer Science, Massachusetts Institute of Technology, Cambridge, Massachusetts 02139, USA*

(Received 26 May 2006; published 11 October 2006)

A new regime of coherent quantum dynamics of a qubit is realized at low driving frequencies in the strong driving limit. Coherent transitions between qubit states occur via the Landau-Zener process when the system is swept through an energy-level avoided crossing. The quantum interference mediated by repeated transitions gives rise to an oscillatory dependence of the qubit population on the driving-field amplitude and flux detuning. These interference fringes, which at high frequencies consist of individual multiphoton resonances, persist even for driving frequencies smaller than the decoherence rate, where individual resonances are no longer distinguishable. A theoretical model that incorporates dephasing agrees well with the observations.

DOI: 10.1103/PhysRevLett.97.150502 PACS numbers: 03.67.Lx, 03.65.Yz, 85.25.Cp, 85.25.Dq

Macroscopic quantum systems coherently driven by external fields provide new insights into the fundamentals of quantum mechanics and hold promise for use in quantum information science [1,2]. Superconducting Josephson devices are model quantum systems [3] that can be manipulated by rf driving fields, and recent years have seen rapid progress in the understanding of their quantum dynamics [4–13]. Quantum coherence of these systems can be probed by temporal Rabi oscillations [4,7–13]. There, the driving-field frequency ν equals the energy-level separation $\Delta E/\hbar$, and the population of the two levels oscillates at a frequency ω_R much smaller than ΔE. In the weak driving limit, $\hbar\omega_R \approx A \ll \Delta E = h\nu$, where A is the driving amplitude parameterized in units of energy.

Coherent quantum dynamics can also be investigated at driving frequencies much less than $\Delta E/\hbar$, and at strong driving amplitude $A \approx \Delta E \gg h\nu$. In this case, the transitions occur via the Landau-Zener (LZ) process at a level crossing [14,15]. Acting as a coherent beam splitter, LZ transitions create a quantum superposition of the ground and excited states and, upon repetition, induce quantum mechanical interference. The latter leads to Stueckelberg or Ramsey-type oscillations [16,17] in analogy to a Mach-Zehnder (MZ) interferometer [18,19]. These oscillations are also related to photoassisted transport [20–22] and Rabi oscillations observed in the multiphoton regime [7,13]. MZ-type interference is a unique signature of temporal coherence complementary to Rabi oscillations, with the time between sequential LZ transitions clocking the dynamics similarly to the Rabi pulse width.

In this Letter, we report a new *quasiclassical* regime, where coherence is still observed at driving frequencies in the classical domain, $\nu T_2 \lesssim 1$ [23], where T_2 is the dephasing rate. This occurs because the interval between consecutive LZ transitions, relevant for MZ interference, is only a fraction of the driving-field period. We investigate the crossover between the multiphoton and quasiclassical regimes, demonstrating that coherent MZ-type interference fringes in the qubit population persist for frequencies $\nu T_2 \lesssim 1$ even though individual multiphoton resonances can no longer be resolved. This behavior should be contrasted with driven Rabi oscillations, where at low driving frequency, $\nu T_2 \lesssim 1$, there is no signature of coherence. The crossover between the two regimes, $\nu T_2 \sim 1$, is also influenced by inhomogeneous broadening resulting from repeated measurements, as discussed below.

In our experiment we utilize a persistent-current (PC) qubit [24]: a superconducting loop interrupted by three Josephson junctions (JJ), one of which has a reduced cross-sectional area [Fig. 1(a)]. A time-dependent magnetic flux $f(t) = f^{\mathrm{dc}} + f^{\mathrm{ac}}(t)$ controls the qubit. For $f(t) \approx \Phi_0/2$, the qubit exhibits a double-well potential profile with individual wells representing diabatic circulating-current states, $|0\rangle$ and $|1\rangle$, with energies $\pm\epsilon \propto \pm\delta f$, where $\delta f \equiv f^{\mathrm{dc}} - \Phi_0/2$ is the flux detuning. These states are coupled with a tunneling energy Δ. The driving and readout pulse sequence is illustrated in Fig. 1(b). Qubit transitions are driven by a microwave flux $f^{\mathrm{ac}} \propto A\cos 2\pi\nu t$, with A, parameterized in units of energy, proportional to the microwave source voltage V_{rms}. The qubit state is read out with a dc SQUID, whose switching current I_{SW} depends on the flux generated by the qubit and, thereby, the qubit circulating-current state. The device was fabricated at Lincoln Laboratory using a fully planarized niobium trilayer process and optical lithography. The device has a critical current density $J_c \approx 160$ A/cm^2, and the characteristic Josephson and charging energies are $E_J \approx (2\pi\hbar)300$ GHz and $E_C \approx (2\pi\hbar)0.65$ GHz, respectively. The ratio of the qubit JJ areas is $\alpha \approx 0.84$, and $\Delta \approx (2\pi\hbar)10$ MHz. The experiments were performed in a di-

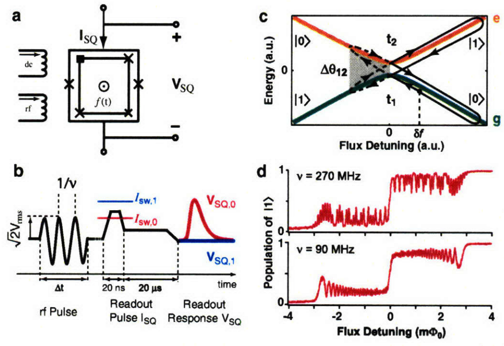

FIG. 1 (color). (a) Schematic of the PC qubit surrounded by a dc SQUID readout. dc and rf fields control the state of the qubit. (b) A rf pulse of duration $\Delta t \gg \nu^{-1}$ drives the qubit, and its state is inferred from the voltage V_{SQ} across the SQUID pulsed with current I_{SQ}. (c) The qubit experiences two Landau-Zener transitions over a single rf period, accumulating a relative phase $\Delta\theta_{12}$ between them. (d) The resulting interference fringes in qubit population for $\nu = 270$ and 90 MHz, and $V_{rms} = 240$ and 171 mV, respectively, (vertical lines on Fig. 2).

lution refrigerator at a base temperature of 20 mK. The device was magnetically shielded, and all electrical lines were carefully filtered and attenuated to reduce noise (see Ref. [18] for details).

The qubit dynamics in the strongly driven limit is influenced by quantum interference at sequential LZ transitions. As illustrated in Fig. 1(c), the qubit is initially prepared in the ground state at flux detuning δf, and, after a first LZ transition at time t_1, it is in a coherent superposition of the two diabatic states. For times $t_1 < t < t_2$, the superposition state accumulates a relative phase $\Delta\theta_{12}$, which mediates the quantum interference at the second LZ transition at time t_2. The sequence of two LZ transitions, repeated many times during the rf pulse, is analogous to a cascade of MZ interferometers. One expects MZ-type interference fringes in the qubit population due to changes in $\Delta\theta_{12}$ associated with changes in V_{rms} and δf, which are indeed observed [Fig. 1(d)].

Figure 2 presents the measured qubit population of state $|1\rangle$ (color scale) as a function of V_{rms} and δf for high- and low-frequency driving, $\nu = 270$ and 90 MHz, respectively. Population transfer due to qubit driving appears at V_{rms} exceeding a threshold value which varies linearly with $|\delta f|$ and symmetrically about the qubit step. For high-frequency driving, $\nu T_2 \gtrsim 1$, the individual multiphoton resonances are distinguishable and form a "Bessel ladder" [18] [Fig. 2(a)]. The population of state $|1\rangle$ for the nth-photon resonance follows a Bessel-function dependence, $J_n^2(A/h\nu)$. The range of δf in Fig. 2(a) accommodates photon transitions with n = 1-45, which together define coherent MZ interference-fringe bands of discrete resonances.

In contrast, for low-frequency driving, $\nu T_2 \lesssim 1$, the individual photon resonances are no longer distinguishable because the resonance widths exceed the resonance spacing [Fig. 2(b)]. Nonetheless, the MZ interference-fringe bands, a signature of coherence in the strongly driven regime, indicate that the coherent interference mediating the population transfer persists.

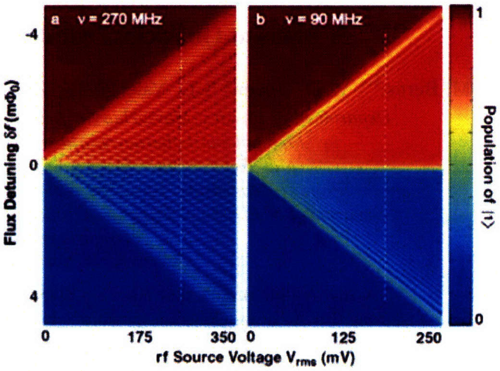

FIG. 2 (color). Measured qubit population at strong driving in two regimes. (a) $\nu = 270$ MHz. Multiphoton resonances of order up to $n = 45$ can be discerned ($\nu T_2 > 1$). (b) $\nu = 90$ MHz. Individual resonances are no longer distinguishable ($\nu T_2 \lesssim 1$), but coherent interference is still observed. Vertical lines indicate the scans displayed in Fig. 1(d). A pulse of duration $\Delta t = 3\ \mu s$ was used in both cases.

To understand these results we consider a driven qubit subject to the effects of decoherence:

$$\mathcal{H} = -\frac{1}{2}\begin{pmatrix} h(t) & \Delta \\ \Delta & -h(t) \end{pmatrix}. \qquad (1)$$

Here, $h(t) = \epsilon + \delta\epsilon(t) + A\cos 2\pi\nu t$ is the energy detuning from an avoided crossing modulated by the driving field in the presence of classical noise $\delta\epsilon(t)$. By a gauge transformation, the Hamiltonian is brought to the form

$$\mathcal{H} = -\frac{1}{2}\begin{pmatrix} 0 & \Delta(t) \\ \Delta^*(t) & 0 \end{pmatrix}, \qquad \Delta(t) = \Delta e^{-i\phi(t)}, \qquad (2)$$

where $\phi(t) = \int_0^t h(\tau)d\tau$ (we set $\hbar = 1$ while developing our model, and restore it in the final results). Perturbation theory gives the rate of LZ transitions between the states $|0\rangle$ and $|1\rangle$:

$$W = \lim_{\delta t \to \infty} |A_{t,t'}|^2/\delta t, \qquad A_{t,t'} = \frac{1}{2}\int_t^{t'} \Delta(t')dt', \qquad (3)$$

where $\delta t = t' - t > 0$, and the limit physically means that δt is large compared to T_2.

For the perturbation approach to be valid, the change of qubit population must be slow on the scale of T_2. This condition can be written down as $W \ll \Gamma_2 = 1/T_2$. We stress that this inequality does not imply that the effect of driving the qubit is weak. The rate W can still be large compared to the inelastic relaxation rate Γ_1, leading to the strong deviation of population from equilibrium observed in our experiment.

To evaluate W, we write the expression in Eq. (3) as

$$W = \frac{1}{4}\int \langle \Delta(t+\tau)\Delta^*(t)\rangle d\tau, \qquad \Delta(t) = \Delta e^{-i\phi(t)}. \quad (4)$$

By introducing Bessel functions in the Fourier series of $e^{-i(A/\omega)\sin\omega t}$, $\omega = 2\pi\nu$, we have

$$e^{-i\phi(t)} = e^{-i\epsilon t - i\delta\phi(t)}\sum_n J_n(x)e^{i\omega n t}, \qquad x = \frac{A}{\omega}.$$

We average over $\delta\phi(t)$ with the help of the white noise model $\langle e^{i\delta\phi(t)-i\delta\phi(t')}\rangle = e^{-\Gamma_2|t-t'|}$, and integrate in (4) as $\int e^{-i(\epsilon-\omega n)\tau-\Gamma_2|\tau|}d\tau = 2\Gamma_2/[(\epsilon-\omega n)^2+\Gamma_2^2]$ to obtain

$$W(\epsilon, A) = \frac{\Delta^2}{2}\sum_n \frac{\Gamma_2 J_n^2(x)}{(\epsilon-\omega n)^2+\Gamma_2^2}. \quad (5)$$

For large n, Bessel functions can be expressed through the Airy function $\mathrm{Ai}(u) = \frac{1}{\pi}\int_0^\infty \cos(uy + \frac{1}{3}y^3)dy$ as $J_n(x) = a\mathrm{Ai}[a(n-x)]$, $a = (2/x)^{1/3}$. Using the identity $\cot z = \sum_n (z-\pi n)^{-1}$ we approximate Eq. (5) as

$$W = \frac{\pi a^2\Delta^2}{2\omega}\,\mathrm{Im}\cot\left[\frac{\pi}{\omega}(\epsilon - i\Gamma_2)\right]\mathrm{Ai}^2\left[\frac{a}{\omega}(\epsilon - A)\right]. \quad (6)$$

There are two main regimes exhibited by this expression: (i) $\nu \gtrsim \Gamma_2$, and (ii) $\nu \lesssim \Gamma_2$. In case (i), we have a sum of nonoverlapping resonances. For each value of ϵ, the sum is dominated by the term with n the nearest integer to ϵ/ω, giving rise to resonances of strength $J_n^2(x)$, the Bessel ladder of Ref. [18].

In contrast, in case (ii), the peaks in Eq. (5) are overlapping. Setting cot= i in Eq. (6) [23], we obtain

$$W(\epsilon, A) \approx \frac{\pi a^2\Delta^2}{2\omega}\mathrm{Ai}^2[a(\epsilon - A)/\omega]. \quad (7)$$

The effect of Γ_2 on the Airy function oscillation is small at $\Gamma_2 \lesssim (2\pi/a)\nu$. Since $a \approx 0.3$ for $\epsilon/h\nu \lesssim 50$, this condition is compatible with $\nu \lesssim \Gamma_2$. Equation (7) can also be obtained by considering just two subsequent passages of a level crossing at a short time separation $|t_2 - t_1| \ll \nu^{-1}$[see Fig. 1(c)], and ignoring the periodicity of the driving.

Since $\mathrm{Ai}(u<0)$ oscillates as $\pi^{-1/2}|u|^{-1/4}\cos(\frac{2}{3}|u|^{3/2} - \frac{\pi}{4})$, while $\mathrm{Ai}(u>0)$ decays exponentially, Eq. (7) implies that the transitions occur only for $A \gtrsim \epsilon$, with a rate which oscillates as a function of $A - \epsilon$. The oscillations are the same for both integer and noninteger $\epsilon/h\nu$, confirming that, while the resonances merge into a continuous band, the interference fringes persist at $\nu \lesssim \Gamma_2$, in agreement with our observations.

To describe the population dynamics in the presence of driving, we employ a rate equation approach, in which the qubit level occupations $p_{0,1}$ obey $\dot{p}_i = \sum_j g_{ij}p_j$, where

$$g_{01} = -g_{11} = W + \Gamma_1, \qquad g_{10} = -g_{00} = W + \Gamma_1'. \quad (8)$$

Here, $\Gamma_1 = 1/T_1$, $\Gamma_1' = \Gamma_1 e^{-\beta\epsilon}$ are the down and up relaxation rates. The magnetization of the stationary state is $m_s = p_0 - p_1 = (\Gamma_1 - \Gamma_1')/(2W + \Gamma_1 + \Gamma_1')$, which gives the equilibrium value $m_0 = \tanh\frac{1}{2}\beta\epsilon$ at weak excitation, and $m_s \ll m_0$ at high excitation.

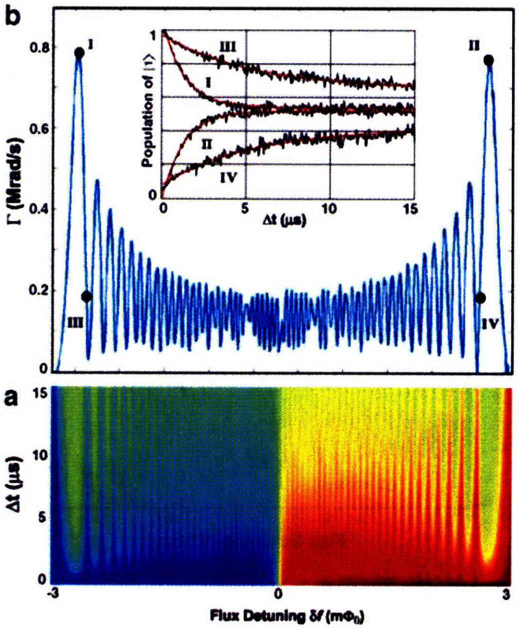

FIG. 3 (color). (a) Time evolution of excited state population ($\nu = 90$ MHz, $V_{\mathrm{rms}} = 171$ mV) obtained by varying the pulse width Δt. (b) The characteristic rate Γ as a function of flux detuning δf obtained by fitting to the exponential time dependence [Eq. (9)] (inset shows examples of fits for the points I, II, III and IV).

To validate this model, we investigate the interference fringes in the excited state population as a function of rf pulse length Δt [Fig. 3(a)]. The rate equation predicts an exponential time dependence for the magnetization,

$$m(\Delta t) = m_s + (m_0 - m_s)e^{-\Gamma\Delta t}, \qquad \Gamma = 2W + \Gamma_1 + \Gamma_1'. \quad (9)$$

By fitting exponentials [Eq. (9)] to the qubit population at each flux detuning, we find the rate Γ which characterizes how fast the stationary state is approached [Fig. 3(b)]. Since our $T_1 \approx 20$ μs [18] is much longer than the observed transition time, we have $\Gamma \approx 2W$. Comparing the extracted Γ at points I and II in Fig. 3(b) with Eq. (7), we obtain $\Delta/2\pi\hbar = 13$ MHz.

We now compare the experimental characteristic rate Γ with the quantity $2W$ [Eq. (5)] in Fig. 4(a), and the observed qubit population with that predicted by the model [Eqs. (5) and (9)] in Fig. 4(b). From the best fits we obtain $\Gamma_2/2\pi = 12$–18 MHz ($T_2 \approx 9$–13 ns), consistent with the transition between the multiphoton and quasiclassical regimes of Fig. 2: 270 MHz $> \Gamma_2 = 1/T_2 \gtrsim 90$ MHz.

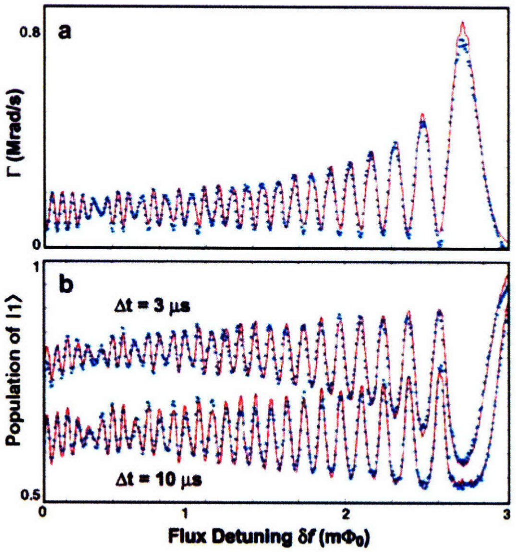

FIG. 4 (color). Comparison of experiment (blue) and theory (red). (a) The transition rate from the right half of Fig. 3(b) fitted with Γ defined by Eqs. (5) and (9). (b) State $|1\rangle$ occupation taken from Fig. 3(a), compared to the model, Eq. (9).

Inhomogeneous broadening is incorporated into the model by assuming a Gaussian broadening mechanism with standard deviation $\sigma/2\pi = 40$–45 MHz. The resulting power-broadened linewidth is approximately 150 MHz, consistent with the linewidth observed in Fig. 2(a). Best fits in Fig. 4 are obtained with slightly different values of Γ_2 and σ within the ranges above. By using the fit parameters for the 3 μs magnetization curve, we can calculate the qubit population in the multiphoton [Fig. 5(a)] and quasiclassical [Fig. 5(b)] regimes as a function of δf and $V_{\rm rms}$.

In conclusion, we have observed quantum coherent qubit dynamics at strong driving for frequencies smaller than the dephasing rate. In this limit, well-resolved multiphoton transitions merge into a continuous band, while the Mach-Zehnder-like coherent interference pattern persists. A simple model of a driven two-level system subject to decoherence is in remarkable agreement with the observed interference patterns.

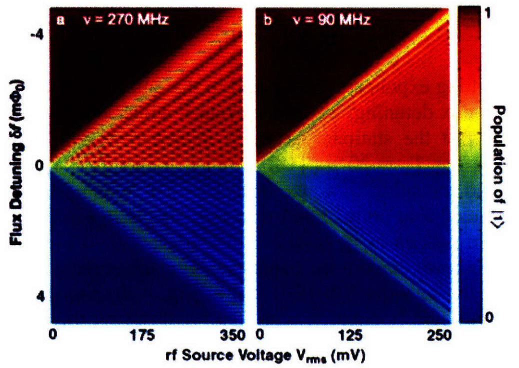

FIG. 5 (color). Simulation of qubit population using model parameters extracted from data. (a) $\nu = 270$ MHz. (b) $\nu = 90$ MHz.

We thank V. Bolkhovsky, G. Fitch, D. Landers, E. Macedo, R. Slattery, and T. Weir at MIT Lincoln Laboratory for fabrication and technical assistance and D. Cory, A. J. Kerman, and S. Lloyd for helpful discussions. This work was supported by AFOSR (No. F49620-01-1-0457) under the DURINT program. The work at Lincoln Laboratory was sponsored by the U. S. DOD under Air Force Contract No. FA8721-05-C-0002. A. V. S. acknowledges support by U. S. DOE under Contract No. DEAC 02-98 CH 10886.

---

*Electronic address: dmb@mit.edu

†Present address: EECS Department, Massachusetts Institute of Technology, Cambridge, Massachusetts 02139, USA.

[1] J. E. Mooij, Science **307**, 1210 (2005).
[2] Y. Makhlin, J. Diggins, and A. Shnirman, Rev. Mod. Phys. **73**, 357 (2001).
[3] J. Clarke *et al.*, Science **239**, 992 (1988).
[4] Y. Nakamura, Y. A. Pashkin, and J. S. Tsai, Nature (London) **398**, 786 (1999).
[5] J. R. Friedman *et al.*, Nature (London) **406**, 43 (2000).
[6] C. H. van der Wal *et al.*, Science **290**, 773 (2000).
[7] Y. Nakamura, Y. A. Pashkin, and J. S. Tsai, Phys. Rev. Lett. **87**, 246601 (2001).
[8] D. Vion *et al.*, Science **296**, 886 (2002).
[9] Y. Yu *et al.*, Science **296**, 889 (2002).
[10] J. M. Martinis *et al.*, Phys. Rev. Lett. **89**, 117901 (2002).
[11] I. Chiorescu *et al.*, Science **299**, 1869 (2003).
[12] B. L. T. Plourde *et al.*, Phys. Rev. B **72**, 060506 (2005).
[13] S. Saito *et al.*, Phys. Rev. Lett. **96**, 107001 (2006).
[14] A. V. Shytov, D. A. Ivanov, and M. V. Feigel'man, Eur. Phys. J. B **36**, 263 (2003).
[15] A. Izmalkov *et al.*, Europhys. Lett. **65**, 844 (2004).
[16] E. C. G. Stueckelberg, Helv. Phys. Acta **5**, 369 (1932).
[17] N. F. Ramsey, Phys. Rev. **76**, 996 (1949).
[18] W. D. Oliver *et al.*, Science **310**, 1653 (2005).
[19] M. Sillanpää *et al.*, Phys. Rev. Lett. **96**, 187002 (2006).
[20] P. K. Tien and J. P. Gordon, Phys. Rev. **129**, 647 (1963).
[21] L. P. Kouwenhoven *et al.*, Phys. Rev. Lett. **73**, 3443 (1994).
[22] Y. Nakamura, and J. S. Tsai, J. Supercond. **12**, 799 (1999).
[23] We emphasize that the crossover between high and low frequencies in this case occurs at $\nu T_2 \sim 1$ rather than at $\omega T_2 \sim 1$. This can be inferred from the expression $\mathrm{Im}\cot[\pi(\epsilon - i\Gamma_2)/\omega]$, Eq. (6), which describes multiphoton resonances broadening. At large Γ_2 this gives $1 + 2e^{-2\pi\Gamma_2/\omega}\cos(2\pi\epsilon/\omega) + O(e^{-4\pi\Gamma_2/\omega})$. The cosine modulation is exponentially suppressed at $\nu \lesssim \Gamma_2$, whereby transitions are no longer due to a single photon mode.
[24] T. P. Orlando *et al.*, Phys. Rev. B **60**, 15 398 (1999).

Microwave-Induced Cooling of a Superconducting Qubit

Sergio O. Valenzuela,[1]* William Oliver,[2] David M. Berns,[3] Karl K. Berggren,[2]†
Leonid S. Levitov,[3] Terry P. Orlando[4]

We demonstrated microwave-induced cooling in a superconducting flux qubit. The thermal population in the first-excited state of the qubit is driven to a higher-excited state by way of a sideband transition. Subsequent relaxation into the ground state results in cooling. Effective temperatures as low as ≈3 millikelvin are achieved for bath temperatures of 30 to 400 millikelvin, a cooling factor between 10 and 100. This demonstration provides an analog to optical cooling of trapped ions and atoms and is generalizable to other solid-state quantum systems. Active cooling of qubits, applied to quantum information science, provides a means for qubit-state preparation with improved fidelity and for suppressing decoherence in multi-qubit systems.

Cooling dramatically affects the quantum dynamics of a system, suppressing dephasing and noise processes and revealing an array of lower-energy quantum-coherent phenomena, such as superfluidity, superconductivity, and the Josephson effect. Conventionally, the entire system under study is cooled with ^{3}He-^{4}He cryogenic techniques. Although this straightforward approach has advantages, such as cooling ancillary electronics and providing thermal stability, it also has drawbacks. In particular, limited cooling efficiency and poor heat conduction at millikelvin temperatures limit the lowest temperatures attainable.

A fundamentally different approach to cooling has been developed and implemented in quantum optics (*1*–*4*). The key idea is that the degrees of freedom of interest may be cooled individually, without relying on heat transfer among different parts of the system. By such directed cooling processes, the temperature of individual quantum states can be reduced by many orders of magnitude with little effect on the temperature of surrounding degrees of freedom. In one successful approach, called sideband cooling (*5*–*8*), the unwanted thermal population of an excited state $|1\rangle$ is eliminated by driving a resonant sideband transition to a higher excited state $|2\rangle$, whose population quickly relaxes into the ground state $|0\rangle$ (Fig. 1A). The two-level subsystem of interest, here $\{|0\rangle, |1\rangle\}$, is efficiently cooled if the driving-induced population transfer to state $|0\rangle$ is faster than the thermal repopulation of state $|1\rangle$. The sideband method, originally used to cool vibrational states of trapped ions and atoms, allows several interesting extensions (*1*–*4*, *9*–*12*). For example, the transition to an excited state can be achieved by nonresonant processes, such as adiabatic passage (*9*), or by adiabatic evolution in an optical potential (*10*–*12*). Other approaches, such as optical molasses and evaporative cooling, have been developed to cool the translational degrees of freedom of atoms to nanokelvin temperatures, establishing the basis for the modern physics of cold atoms (*13*).

Superconducting qubits are mesoscopic artificial atoms (*14*) that exhibit quantum-coherent dynamics (*15*) and host a number of phenomena known to atomic physics and quantum optics, including coherent quantum superpositions of distinct macroscopic states (*16*, *17*), time-dependent Rabi oscillations (*18*–*24*), coherent coupling to microwave cavity photons (*25*–*27*), and Stückelberg oscillations via Mach-Zehnder interferometry (*28*–*30*). In a number of these experiments, qubit state preparation by a dc pulse or by thermalization with the bath was used. It is tempting, however, to extend the ideas and benefits of optical cooling to solid-state qubits, because they present a high degree of quantum coherence, a relatively strong coupling to external fields, and tunability, a combination rarely found in other fundamental quantum systems.

We demonstrate a solid-state analog to optical cooling by using a niobium persistent-current qubit (*31*), a superconducting loop interrupted by three Josephson junctions (*32*). When the qubit loop is threaded with a dc magnetic flux $f_q \approx \Phi_0/2$, where $\Phi_0 \equiv h/2e$ is the flux quantum (h is Planck's constant), the qubit's potential energy exhibits a double-well profile (Fig. 1A), which can be tilted by adjusting the flux detuning, $\delta f_q = f_q - \Phi_0/2$, away from zero. The lowest-energy states of each

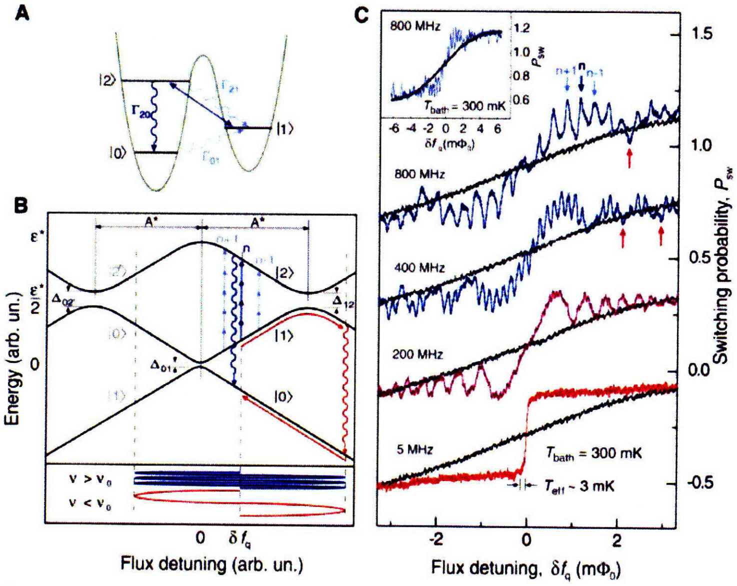

Fig. 1. Sideband cooling in a flux qubit. (**A**) External excitation transfers the thermal population from state $|1\rangle$ to state $|2\rangle$ (straight line) from which it decays into the ground state $|0\rangle$. Wavy lines represent spontaneous relaxation and absorption, $\Gamma_{20} >> \Gamma_{21},\Gamma_{01}$. The double well is the flux-qubit potential comprising energy levels. (**B**) Schematic band diagram illustrating the resonant and adiabatic sideband cooling of the ac-driven qubit. $|1\rangle \rightarrow |2\rangle$ transitions are resonant at high driving frequency ν (blue lines) and occur via adiabatic passage at low ν (red lines). Δ_{01} and Δ_{12} are the tunnel splittings between $|0\rangle$ and $|1\rangle$ and between $|1\rangle$ and $|2\rangle$. (**C**) Cooling induced by ac-pulses with driving frequencies ν = 800, 400, 200, and 5 MHz. State $|0\rangle$ population P_{sw} versus flux detuning δf_q for the cooled qubit and for the qubit in thermal equilibrium with the bath (black lines, T_{bath} = 300 mK). Measurements for ν = 800, 200, and 5 MHz are displaced vertically for clarity. (Inset) P_{sw} versus δf_q over a wider range of flux detuning; ν = 800 MHz.

---

[1] Massachusetts Institute of Technology (MIT) Francis Bitter Magnet Laboratory, Cambridge, MA 02139, USA. [2] MIT Lincoln Laboratory, 244 Wood Street, Lexington, MA 02420, USA. [3] Department of Physics, MIT, Cambridge, MA 02139, USA. [4] Department of Electrical Engineering and Computer Science, MIT, Cambridge, MA 02139, USA.

*To whom correspondence should be addressed. E-mail: sov@mit.edu

†Present address: Department of Electrical Engineering and Computer Science, MIT, Cambridge, MA 02139, USA.

well are the diabatic qubit states of interest, $|0\rangle$ and $|1\rangle$, characterized by persistent currents I_q with opposing circulation, whereas the higher-excited states in each well, e.g., $|2\rangle$, are ancillary levels that form the "sideband transition" with the qubit. In contrast to conventional sideband cooling, which aims to cool an "external" harmonic oscillator (e.g., ion trap potential) with an "internal" qubit (e.g., two-level system in an ion), our demonstration aims to cool an "internal" qubit by using an ancillary "internal" oscillator-like state [supporting online material (SOM) Text].

When the qubit is in equilibrium with its environment, some population is thermally excited from the ground-state $|0\rangle$ to state $|1\rangle$ according to $p_1/p_0 = \exp[-(\varepsilon_1 - \varepsilon_0)/k_B T_{\text{bath}}]$, where $p_{0,1}$ are the qubit populations for energy levels $\varepsilon_{0,1}$, k_B is the Boltzmann constant, and T_{bath} is the bath temperature. To cool the qubit subsystem below T_{bath}, in analogy to optical pumping and sideband cooling, a microwave magnetic flux of amplitude A and frequency ν targets the $|1\rangle \rightarrow |2\rangle$ transition, driving the state $|1\rangle$ thermal population to state $|2\rangle$, from which it quickly relaxes to the ground state $|0\rangle$. The hierarchy of relaxation and absorption rates required for efficient cooling, $\Gamma_{20} >> \Gamma_{21}, \Gamma_{01}$, is achieved in our system owing to a relatively weak tunneling between wells, which inhibits the interwell relaxation and absorption processes, $|2\rangle \rightarrow |1\rangle$ and $|0\rangle \rightarrow |1\rangle$, compared with the relatively strong intrawell relaxation process, $|2\rangle \rightarrow |0\rangle$. This three-level system behavior is markedly different from the population saturation observed in two-level systems.

The cooling procedure illustrated in Fig. 1A is generalized to the energy-band diagram shown schematically in Fig. 1B. The diabatic-state energies

$$\varepsilon_{1,0} = \pm I_q \delta f_q, \quad \varepsilon_{2',2} = \varepsilon^* \pm I_q \delta f_q \qquad (1)$$

are linear in the flux detuning δf_q, with the energy $\varepsilon^* \approx 25$ GHz and $I_q = 1.44$ GHz/mΦ_0 in our device, and exhibit avoided crossings $\Delta_{01} \approx 12$ MHz and $\Delta_{12} = \Delta_{02'} \approx 100$ MHz due to quantum tunneling through the double-well barrier (Fig. 1A). The diabatic levels exchange roles at each avoided crossing, and the energy band is symmetric about $\delta f_q = 0$ (*33*).

Under equilibrium conditions, the average level populations exhibit a thermally broadened "qubit step" about $\delta f_q = 0$, the location of the $|0\rangle$ to $|1\rangle$ avoided crossing. This is determined from the switching probability P_{sw} of the measurement superconducting quantum interference device (SQUID) magnetometer, which follows the $|0\rangle$ state population (*32*)

$$P_{\text{sw}} = \frac{1}{2}(1 + F m_0), \quad m_0 = \tanh\frac{\varepsilon}{2k_B T} \qquad (2)$$

where F is the fidelity of the measurement, $m_0 = p_0 - p_1$ is the equilibrium magnetization that results from the qubit populations $p_{0,1}$, $T = T_{\text{bath}}$, and $\varepsilon = \varepsilon_1 - \varepsilon_0 \propto \delta f_q$ as inferred from Eq. 1. In the presence of microwave excitation targeting the $|1\rangle \rightarrow |2\rangle$ transition, the resultant cooling, which we will later quantify in terms of an effective temperature $T_{\text{eff}} < T_{\text{bath}}$, acts to increase the ground-state population and, thereby, sharpen the qubit step. This cooling signature is evident in Fig. 1C, where we show the qubit step before and after applying a cooling pulse at several frequencies for $T_{\text{bath}} = 300$ mK.

The cooling presented in Fig. 1, B and C, exhibits a rich structure as a function of driving frequency and detuning, resulting from the manner in which state $|2\rangle$ is accessed. The $|1\rangle \rightarrow |2\rangle$ transition rate can be described by a product of a resonant factor and an oscillatory Airy factor (*30*). The former dominates at high frequencies (800 and 400 MHz), where well-resolved resonances of n-photon transitions are observed, as illustrated in Fig. 1B (transition in blue) and Fig. 1C (top traces and inset). The cooling is thus maximized near the detuning values matching $\varepsilon_2 - \varepsilon_1 = nh\nu$ (downward arrows in Fig. 1C). At intermediate frequencies (400 and 200 MHz), the Airy factor becomes more prominent and accounts for the Stückelberg-like oscillations that modulate the intensity of the n-photon resonances (*28*, *30*). Below $\nu = 200$ MHz, although individual resonances are no longer discernible, the modulation envelope persists due to the coherence of the Landau-Zener dynamics at the Δ_{12} avoided crossing (*30*). The $|1\rangle \rightarrow |2\rangle$ transition becomes weak near the zeros of the modulation envelope, where we observe less efficient cooling, or even slight heating (e.g., upward arrows in Fig. 1C, 800 and 400 MHz). This is a result of the $|0\rangle \rightarrow |1\rangle$ transition rate which, although relatively small, $\Delta_{01}^2 \ll \Delta_{12}^2$, acts to excite the qubit when the usually dominant $|1\rangle \rightarrow |2\rangle$ transition rate vanishes. At low frequencies [$\nu \lesssim \nu_0 = (\Delta_{12}^3/A^*)^{1/2} \approx$ 10 MHz], the state $|2\rangle$ is reached via adiabatic passage (Fig. 1B, red lines) and the population transfer and cooling become conveniently independent of detuning (see $\nu = 5$ MHz in Fig. 1C).

Maximal cooling occurs near an optimal driving amplitude (Fig. 2). Figure 2A shows the $|0\rangle$ state population P_{sw} measured as a function of the microwave amplitude A and flux detuning δf_q for frequency $\nu = 5$ MHz. The adiabatic passage regime, realized at this frequency, is particularly simple to interpret, although higher frequencies allow for an analogous interpretation. Cooling and the diamond feature of size $A^* = \varepsilon^*/2I_q$ can be understood in terms of the energy band diagram (Fig. 1B). For amplitudes $0 \leq A \leq A^*/2$, population transfer between states $|0\rangle$ and $|1\rangle$ occurs when $A > |\delta f_q|$, such that the sinusoidal flux reaches the Δ_{01} avoided crossing; this defines the front side of the observed spectroscopy diamond symmetric about the qubit step. For amplitudes $A^*/2 \leq A \leq A^*$, the Δ_{12} ($\Delta_{02'}$) avoided crossing dominates the dynamics, resulting in a second pair of thresholds $A = A^* - |\delta f_q|$, which define the back side of the diamond. As the diamond narrows to

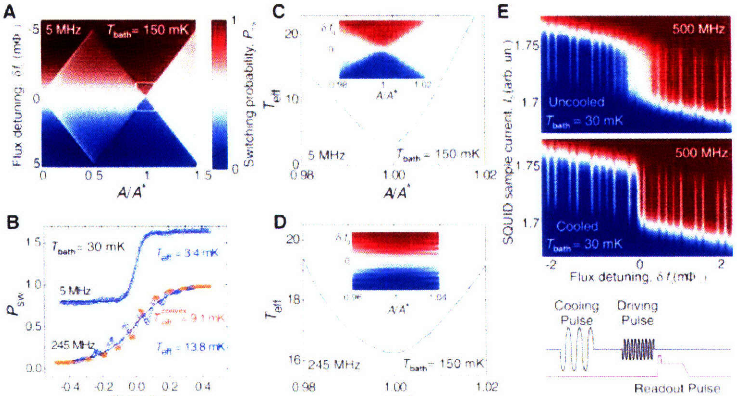

Fig. 2. Optimal cooling parameters and effective temperature. (**A**) State $|0\rangle$ population P_{sw} versus flux detuning, $-A^*/2 \lesssim \delta f_q \lesssim A^*/2$, and driving amplitude A with $\nu = 5$ MHz, $t_p = 3$ μs, and $T_{\text{bath}} = 150$ mK. Optimal conditions for cooling are realized at $A = A^*$, where A^* is defined in Fig. 1B. (**B**) Effective temperature T_{eff}. Qubit steps measured at $\nu = 5$ and 245 MHz (circles) and best fits to Eq. 2. At 245 MHz, the aggregate temperature fitting (blue, $T_{\text{eff}} = 13.8$ mK) and the convex fitting (orange, $T_{\text{eff}} = 9.1$ mK) are shown. $T_{\text{bath}} = 30$ mK. (**C** and **D**) (Inset) Detail of the region $A \approx A^*$ [white box in (A)] for $\nu = 5$ MHz (top) and $\nu = 245$ MHz (bottom). In each case, T_{eff} is extracted from the qubit step as in (B). Lines are guides for the eye; $t_p = 3$ μs, $T_{\text{bath}} = 150$ mK. (**E**) Spectroscopy of uncooled (top) and cooled (middle) qubit (5 MHz, 3-μs cooling pulse) at $T_{\text{bath}} = 30$ mK. Cumulative switching-probability distribution as a function of I_s and δf_q under 500-MHz ac excitation.

the point $A = A^*$, cooling is observed. There only one of the two side avoided crossings is reached and, thereby, strong transitions with relaxation to the ground state result for all δf_q, yielding the sharpest qubit step. For $A > A^*$, both side avoided crossings Δ_{12} and $\Delta_{02'}$ are reached simultaneously when $|\delta f_q| \lesssim A - A^*$, leading again to a large population transfer between $|0\rangle$ and $|1\rangle$.

When an ac field is applied, the qubit is no longer in equilibrium with the bath, but it can still be well characterized by an effective temperature T_{eff} using Eq. 2 with $T = T_{\mathrm{eff}}$. This is illustrated in Fig. 2B for $\nu = 5$ MHz and $\nu = 245$ MHz ($T_{\mathrm{bath}} = 30$ mK). At $\nu = 5$ MHz, the qubit step clearly follows Eq. 2, as shown with a fit line for $T_{\mathrm{eff}} = 3.4$ mK. At 245 MHz, individual multiphoton resonances are evident, and P_{sw} is a nonmonotonic function of δf_q. In this case, T_{eff} is still a useful parameter to quantify the effective cooling, but it should be interpreted as an aggregate temperature over all frustrations. Alternatively, because the cooling is maximized at individual resonances, one may perform a convex fitting of Eq. 2, where only the solid (orange) symbols are taken into account to determine the effective temperature at the resonance detunings. The convex effective temperature $T_{\mathrm{eff}}^{\mathrm{convex}} = 9.1$ mK is smaller than the aggregate value $T_{\mathrm{eff}} = 13.8$ mK. In the remainder of the paper, we refer to the more conservative effective temperature obtained using the aggregate definition.

Figure 2, C and D, show the variation of T_{eff} about $A = A^*$ for $\nu = 5$ MHz and $\nu = 245$ MHz, respectively, in the region marked with a white rectangle in Fig. 2A (insets show the raw data). As seen in these figures, T_{eff} typically presents a minimum, where the cooling is most efficient and from which A^* can be determined.

To determine whether the observation of a sharp qubit step proves that the system makes transitions to the ground state, as opposed to selectively populating an excited state with the same magnetization, we measured the excitation spectra of the "precooled" qubit and of the qubit in thermal equilibrium with the bath (Fig. 2E). In the former, a weak ac excitation was applied immediately after the cooling pulse (time lag less than 100 ns), well before the system equilibrates by warming up to the bath temperature (see below). By comparing the excitation spectra of the equilibrium and cooled systems (Fig. 2E, $T_{\mathrm{bath}} = 30$ mK), we note that, although cooling markedly reduces the step width, making the qubit much colder, the excitation spectrum remains unchanged. Because the ac excitation is resonant with the $|0\rangle \rightarrow |1\rangle$ transition only, this strongly indicates that the population in a cooled qubit is in the ground state.

Figure 3, A and B, summarize the dependence of $T_{\mathrm{eff}}^* = T_{\mathrm{eff}}(A^*)$ on the dilution refrigerator temperature $T_{\mathrm{bath}} = 30$ to 400 mK for several frequencies ν, spanning the resonant to the adiabatic passage limits, with a fixed pulse width $t_p = 3$ μs. In Fig. 3A, at large ν, T_{eff}^* exhibits a monotonic increase with T_{bath}, which becomes less pronounced as ν decreases. In the adiabatic passage limit, e.g., $\nu = 5$ MHz, $T_{\mathrm{eff}}^* \approx 3$ mK is practically constant and reaches values that, notably, can be more than two orders of magnitude smaller than T_{bath}. In Fig. 3B, T_{eff}^* is observed to increase linearly with ν for different values of T_{bath}. Because the number of resonances in the qubit-step region is inversely proportional to ν, the cooling at the individual resonances depends only weakly on ν when using the convex definition $T_{\mathrm{eff}}^{\mathrm{convex}}(A^*)$.

Figure 3C displays the measurement-fidelity F versus T_{bath}. Although the qubit is effectively cooled, $T_{\mathrm{eff}}^* \ll T_{\mathrm{bath}}$, over the range of T_{bath} in Fig. 3, A and B, the readout SQUID is not actively cooled, and its switching current distribution broadens with T_{bath} (fig. S2). At high temperatures, the fidelity F, defined in Eq. 2, becomes too small to discriminate the two qubit states; this is independent of the qubit's effective temperature, which remains ~3 mK at all values of T_{bath}. We observe that the fidelity F is larger than 0.8 for $T_{\mathrm{bath}} < 100$ mK, remains above 0.5 at ^{3}He refrigerator temperatures, but drops to $F \approx 0.1$ at $T_{\mathrm{bath}} = 400$ mK, limiting our ability to measure the qubit state at higher temperatures (SOM Text).

The cooling and equilibration dynamics of the qubit are summarized in Fig. 4 ($T_{\mathrm{bath}} = 150$ mK). Cooling a qubit in equilibrium with the bath requires a characteristic cooling time. In turn, a cooled qubit is effectively colder than its environment, a nonequilibrium condition, which over a characteristic equilibration time will thermalize to the environmental bath temperature. This relation between cooling and equilibration times determines the facility of cooling the qubit and performing operations while still cold. Figure 4, A and B, show the time evolution at cooling and warming up of the qubit step. The top panels show P_{sw} as a function of δf_q and cooling-pulse length t_p (Fig. 4A, $\nu = 245$ MHz), and as a function of δf_q and waiting-time t_w after

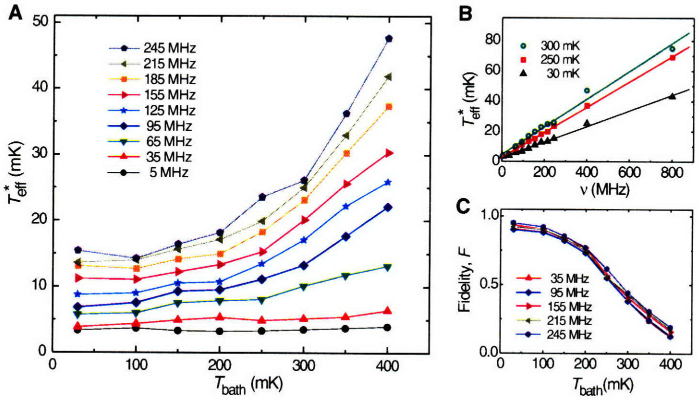

Fig. 3. Effective temperature T_{eff}^* for $A = A^*$ and measurement fidelity F. **(A)** T_{eff}^* versus T_{bath} at the indicated driving frequencies ν. T_{eff}^* increases with T_{bath} at high ν, but remains constant at low ν. **(B)** T_{eff}^* versus ν for different values of T_{bath}. Lines are linear fits. **(C)** F versus T_{bath} at the indicated ν. A pulse width $t_p = 3$ μs was used in all cases.

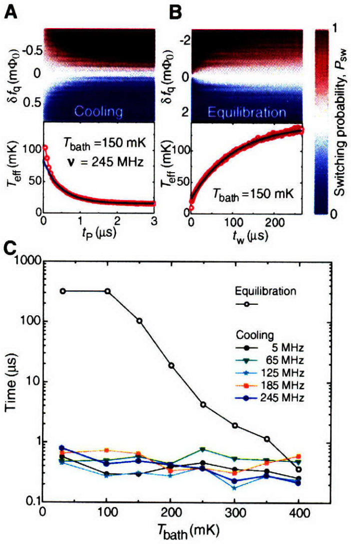

Fig. 4. Dynamics of cooling and equilibration. **(A)** (Upper panel) State $|0\rangle$ population P_{sw} as a function of δf_q and cooling pulse width t_p (ν = 245 MHz). (Lower panel) T_{eff} versus t_p extracted from upper panel (circles) and exponential fit (blue line) with ~1-μs time constant. **(B)** (Upper panel) State $|0\rangle$ population P_{sw} as a function of δf_q and waiting time t_w after the cooling pulse (t_p = 3 μs and ν = 5 MHz). (Lower panel) T_{eff} versus t_w extracted from upper panel (circles) and exponential fit (blue line) with ~100-μs time constant. T_{bath} = 150 mK. **(C)** Characteristic equilibration and cooling times for different T_{bath}. Cooling is performed at the indicated frequencies.

precooling with a 5-MHz pulse (Fig. 4B) (for t_p and t_w definition, see fig. S1). Note the difference in the time scales, where it is observed that substantial cooling is accomplished within 1 μs (Fig. 4A), but equilibration occurs over a much longer time scale (Fig. 4B). Fitting to Eq. 2 yields T_{eff} as a function of t_p and t_w (Fig. 4, A and B, bottom panels). The near-exponential behavior of T_{eff} versus t_p and t_w allows one to infer the characteristic cooling and equilibration times as defined by an exponential fitting (solid blue lines), which are summarized in Fig. 4C. Notably, the cooling characteristic time is nearly independent of both ν and T_{bath} and, on average, is about 500 ns. In contrast, at the base temperature of the dilution refrigerator, the equilibration time is about three orders of magnitude longer, 300 μs, and remains one order of magnitude longer at 250 mK, a temperature that is accessible with ^{3}He refrigerators.

The minimum qubit effective temperature demonstrated in this work was estimated to be $T_{eff} \approx 3$ mK. This value is consistent with the inhomogeneously broadened linewidth observed in the experiment, which likely places a lower limit on the measurable minimum temperature. The microwave-induced cooling presented here can be applied to problems in quantum information science, including ancilla-qubit reset for quantum error-correcting codes and quantum-state preparation, with implications for improved fidelity and decoherence in multi-qubit systems. This approach, realized in a superconducting qubit, is generalizable to other solid-state qubits and can be used to cool other on-chip elements, e.g., the qubit circuitry or resonators.

References and Notes

1. S. Chu, *Rev. Mod. Phys.* **70**, 685 (1998).
2. C. N. Cohen-Tannoudji, *Rev. Mod. Phys.* **70**, 707 (1998).
3. W. D. Phillips, *Rev. Mod. Phys.* **70**, 721 (1998).
4. D. Leibfried, R. Blatt, C. Monroe, D. Wineland, *Rev. Mod. Phys.* **75**, 281 (2003).
5. D. J. Wineland, R. E. Drullinger, F. L. Walls, *Phys. Rev. Lett.* **40**, 1639 (1978).
6. W. Neuhauser, M. Hohenstatt, P. Toschek, H. Dehmelt, *Phys. Rev. Lett.* **41**, 233 (1978).
7. I. Marzoli, J. I. Cirac, R. Blatt, P. Zoller, *Phys. Rev. A.* **49**, 2771 (1994).
8. C. Monroe *et al.*, *Phys. Rev. Lett.* **75**, 4011 (1995).
9. H. Perrin, A. Kuhn, I. Bouchoule, C. Salomon, *Europhys. Lett.* **42**, 395 (1998).
10. V. Vuletić, C. Chin, A. J. Kerman, S. Chu, *Phys. Rev. Lett.* **81**, 5768 (1998).
11. A. J. Kerman, V. Vuletić, C. Chin, S. Chu, *Phys. Rev. Lett.* **84**, 439 (2000).
12. G. Morigi, J. Eschner, C. H. Keitel, *Phys. Rev. Lett.* **85**, 4458 (2000).
13. C. E. Wieman, D. E. Pritchard, D. J. Wineland, *Rev. Mod. Phys.* **71**, S253 (1999).
14. J. Clarke, A. N. Cleland, M. H. Devoret, D. Esteve, J. H. Martinis, *Science* **239**, 992 (1988).
15. Y. Makhlin, G. Schön, A. Shnirman, *Rev. Mod. Phys.* **73**, 357 (2001).
16. J. R. Friedman, V. Patel, W. Chen, S. K. Tolpygo, J. E. Lukens, *Nature* **406**, 43 (2000).
17. C. H. van der Wal *et al.*, *Science* **290**, 773 (2000).
18. Y. Nakamura, Y. A. Pashkin, J. S. Tsai, *Nature* **398**, 786 (1999).
19. Y. Nakamura, Y. A. Pashkin, J. S. Tsai, *Phys. Rev. Lett.* **87**, 246601 (2001).
20. D. Vion *et al.*, *Science* **296**, 886 (2002).
21. Y. Yu, S. Han, X. Chu, S.-I. Chu, Z. Wang, *Science* **296**, 889 (2002).
22. J. M. Martinis, S. Nam, J. Aumentado, C. Urbina, *Phys. Rev. Lett.* **89**, 117901 (2002).
23. I. Chiorescu, Y. Nakamura, C. J. P. M. Harmans, J. E. Mooij, *Science* **299**, 1869 (2003).
24. S. Saito *et al.*, *Phys. Rev. Lett.* **96**, 107001 (2006).
25. I. Chiorescu *et al.*, *Nature* **431**, 159 (2004).
26. A. Wallraff *et al.*, *Nature* **431**, 162 (2004).
27. J. Johansson *et al.*, *Phys. Rev. Lett.* **96**, 127006 (2006).
28. W. D. Oliver *et al.*, *Science* **310**, 1653 (2005).
29. M. Sillanpää, T. Lehtinen, A. Paila, Yu. Makhlin, P. Hakonen, *Phys. Rev. Lett.* **96**, 187002 (2006).
30. D. M. Berns *et al.*, *Phys. Rev. Lett.* **97**, 150502 (2006).
31. T. P. Orlando *et al.*, *Phys. Rev. B* **60**, 15398 (1999).
32. Materials and methods are available as supporting material on *Science* Online.
33. For negative δf_q, levels $|0\rangle$ and $|1\rangle$ exchange roles, and level $|2'\rangle$ plays the role of level $|2\rangle$. Unless explicitly noted, the discussions herein refer to positive δf_q.

34. We thank A. J. Kerman, D. Kleppner, and A. V. Shytov for helpful discussions; and V. Bolkhovsky, G. Fitch, D. Landers, E. Macedo, P. Murphy, R. Slattery, and T. Weir at MIT Lincoln Laboratory for technical assistance. This work was supported by Air Force Office of Scientific Research (grant F49620-01-1-0457) under the DURINT program and partially by the Laboratory for Physical Sciences. The work at Lincoln Laboratory was sponsored by the U.S. Department of Defense under Air Force Contract No. FA8721-05-C-0002.

Supporting Online Material
www.sciencemag.org/cgi/content/full/314/5805/1589/DC1
Materials and Methods
SOM Text
Figs. S1 and S2

17 August 2006; accepted 19 October 2006
10.1126/science.1134008

U-Pb Isotopic Age of the StW 573 Hominid from Sterkfontein, South Africa

Joanne Walker,[1] Robert A. Cliff,[1]* Alfred G. Latham[2]

Sterkfontein cave, South Africa, has yielded an australopith skeleton, StW 573, whose completeness has excited great interest in paleoanthropology. StW 573, or "Little Foot," was found 25 meters below the surface in the Silberberg Grotto. ^{238}U-^{206}Pb measurements on speleothems immediately above and below the fossil remains, corrected for initial ^{234}U disequilibrium, yield ages of 2.17 ± 0.17 million years ago (Ma) and $2.24^{+0.09}_{-0.07}$ Ma, respectively, indicating an age for StW 573 of close to 2.2 Ma. This age is in contrast to an age of ~3.3 Ma suggested by magnetochronology and ages of ~4 Ma based on ^{10}Be and ^{26}Al, but it is compatible with a faunal age range of 4 to 2 Ma.

Sterkfontein, 50 km northwest of Johannesburg, is part of a world heritage site dubbed the Cradle of Humankind because it has produced about one-third of the world's known early hominid fossils (*1*). The Sterkfontein deposits formed in the lower levels of the pre-Cambrian Malmani dolomite (*2*) and are divided into stratigraphic members (members 1 to 6 from the base), correlating the deposits to a layer-cake stratigraphy (*3*, *4*). StW 573 comprises a skull, foot, tibia, radius, humerus, and other arm and hand bones (*5*, *6*). With its combination of human and ape-like features, this fossil has the potential to provide new insights into the evolution of early hominids, such as their degree of adaptation to bipedalism (*5*–*7*). The fossil is found within member 2 in the Silberberg Grotto, where the deposits comprise calcified breccias interlayered with flowstones, of which three flowstone layers are associated with StW 573 (Fig. 1). The skeleton is cemented in breccia on the flank of a former talus slope (*4*, *5*). The lower leg bones are separated from the remainder of the skeleton by part of flowstone layer 2C. This is due to partial slumping of the middle section of the skeleton before the formation of this flowstone (*5*). The flowstones are intact and show no signs of postdepositional faulting that would indicate later disturbance, and they are considered to lie in their original stratigraphic order.

Previous work on the age of StW 573 has been based on several types of evidence: fauna, stratigraphic position relative to an independently dated horizon, electron spin resonance (ESR), paleomagnetism, and cosmogenic isotopes. StW 573 was initially dated at 3.5 to 3.0 million years ago (Ma) according to the stratigraphic separation between members 2 and 4 (*7*, *8*) and the presence of a *Chasmaporthetes* specimen within the member 2 deposits (*6*) that was likened to a specimen at the Miocene-Pliocene site of Langebaanweg, South Africa (*9*). It was estimated that the intervening member 3 deposit, which is ~8 m in thickness (*10*), would have taken 300,000 to 500,000 years to accumulate (*7*, *8*). Member 4 was dated at 2.8 to 2.4 Ma through faunal correlation studies with dated East African assemblages (*11*–*13*) and at

---

[1] School of Earth and Environment, University of Leeds, Leeds LS2 9JT, UK. [2] School of Archaeology, Classics, and Egyptology, University of Liverpool, Liverpool L69 3GS, UK.

*To whom correspondence should be addressed. E-mail: bob@earth.leeds.ac.uk

Amplitude Spectroscopy of a Solid-State Artificial Atom

D. M. Berns,[1] M. S. Rudner,[1] S. O. Valenzuela,[2] K. K. Berggren,[3,*] W. D. Oliver,[3,†] L. S. Levitov,[1] and T. P. Orlando[4]

[1]*Department of Physics, Massachusetts Institute of Technology, Cambridge MA 02139*
[2]*MIT Francis Bitter Magnet Laboratory, Cambridge, MA 02139*
[3]*MIT Lincoln Laboratory, 244 Wood Street, Lexington, MA 02420*
[4]*Department of Electrical Engineering and Computer Science,*
Massachusetts Institute of Technology, Cambridge, MA 02139

(Dated: May 11, 2008)

The energy-level structure of a quantum system plays a fundamental role in determining its behavior and manifests itself in a discrete absorption and emission spectrum [1]. Conventionally, spectra are probed via frequency spectroscopy [1, 2] whereby the frequency ν of a harmonic driving field is varied to fulfill the conditions $\Delta E = h\nu$, where the driving field is resonant with the level separation ΔE (h is Planck's constant). Although this technique has been successfully employed in a variety of physical systems, including natural [1, 2] and artificial [3, 4, 5, 6, 7, 8, 9, 10, 11, 12, 13] atoms and molecules, its application is not universally straightforward, and becomes extremely challenging for frequencies in the range of 10's and 100's of gigahertz. Here we demonstrate an alternative approach, whereby a harmonic driving field sweeps the atom through its energy-level avoided crossings at a fixed frequency, surmounting many of the limitations of the conventional approach. Spectroscopic information is obtained from the amplitude dependence of the system response. The resulting "spectroscopy diamonds" contain interference patterns and population inversion that serve as a fingerprint of the atom's spectrum. By analyzing these features, we determine the energy spectrum of a manifold of states with energies from 0.01 to 120 GHz$\times h$ in a superconducting artificial atom, using a driving frequency near 0.1 GHz. This approach provides a means to manipulate and characterize systems over a broad bandwidth, using only a single driving frequency that may be orders of magnitude smaller than the energy scales being probed.

Spectroscopy has historically been used to obtain a wide range of information on atomic and nuclear properties [1, 2]. Early on, the determination of spectral lines helped elucidate the principles of quantum mechanics through studies of the hydrogen atom and facilitated the discovery of electron and nuclear spin. Since then, several spectroscopy techniques to determine absolute transition frequencies (or, equivalently, wavelengths) have been developed, involving the emission, absorption, or scattering (e.g. Raman) of radiation. The advent of tunable, coherent radiation sources at microwave and optical frequencies led to the age of modern atomic spectroscopy, where a primary approach is to identify absorption spectra as the source frequency is varied [1, 2].

The study of artificial atoms at cryogenic temperatures, whose spectra extend into the microwave and millimeter wave regimes (10-300 GHz), faces different challenges. Stable tunable microwave sources in excess of 70 GHz exist, but are expensive, and generally require multipliers which are inefficient and intrinsically noisy [14]. Frequency dependent dispersion and attenuation, tight tolerances to control impedance, and multi-mode or restricted-bandwidth performance of transmission lines and waveguides [14], limit the application of broadband frequency spectroscopy in these systems. Despite these challenges, superposition states in superconducting [3, 4, 5] and semiconducting artificial atoms [6] have been probed directly up to several 10's of GHz. A number of leading groups have developed alternative techniques, e.g., resonant- and photon-assisted tunneling [7, 8], which can be used to access spectroscopic information in specific systems at even higher frequencies, though each has its own advantages and limitations and may not be easily applicable to other systems.

"Amplitude spectroscopy," introduced in this manuscript, probes the energy level structure of a quantum system via its response to driving-field amplitude rather than frequency (Fig. 1A). It is applicable to systems with energy-level avoided crossings that can be traversed using an external control parameter. For a generic artificial atom, such longitudinal excursions throughout the energy level diagram (Fig. 1C) are realized by strongly driving the system with an external field at a fixed frequency, which may be several orders of magnitude lower than the energy-level spacing. In this limit, the system evolves adiabatically, except in the vicinity of energy-level avoided-crossings where Landau-Zener-type quantum coherent transitions occur. The quantum interference between repeated Landau-Zener transitions gives rise to interference fringes that encode information about the system's energy spectrum. By trading amplitude for frequency, the amplitude spectroscopy approach allows one to probe quantum systems with strong coupling to external fields, such as solid-state artificial atoms, over extraordinarily wide bandwidths, bypassing many of the limitations of a frequency-based approach.

We demonstrate amplitude spectroscopy with a superconducting qubit, a solid-state artificial atom exhibiting discrete energy states [7] that can be strongly coupled to external radio frequency (RF) fields while preserving quantum coherence [9]. Artificial atoms are natural systems for probing a wide range of quantum effects: coherent superpositions of macroscopic states [3, 4, 5], Rabi oscillations [9, 10, 11, 12, 13, 15, 16, 17, 18], incoherent Landau-Zener transitions [19], Stückelberg oscillations [20, 21, 22, 23], microwave cooling [24, 25, 26], and cavity quantum electrodynamics [27,

---

[*] Present address: EECS Department, MIT
[†] Electronic address: oliver@ll.mit.edu

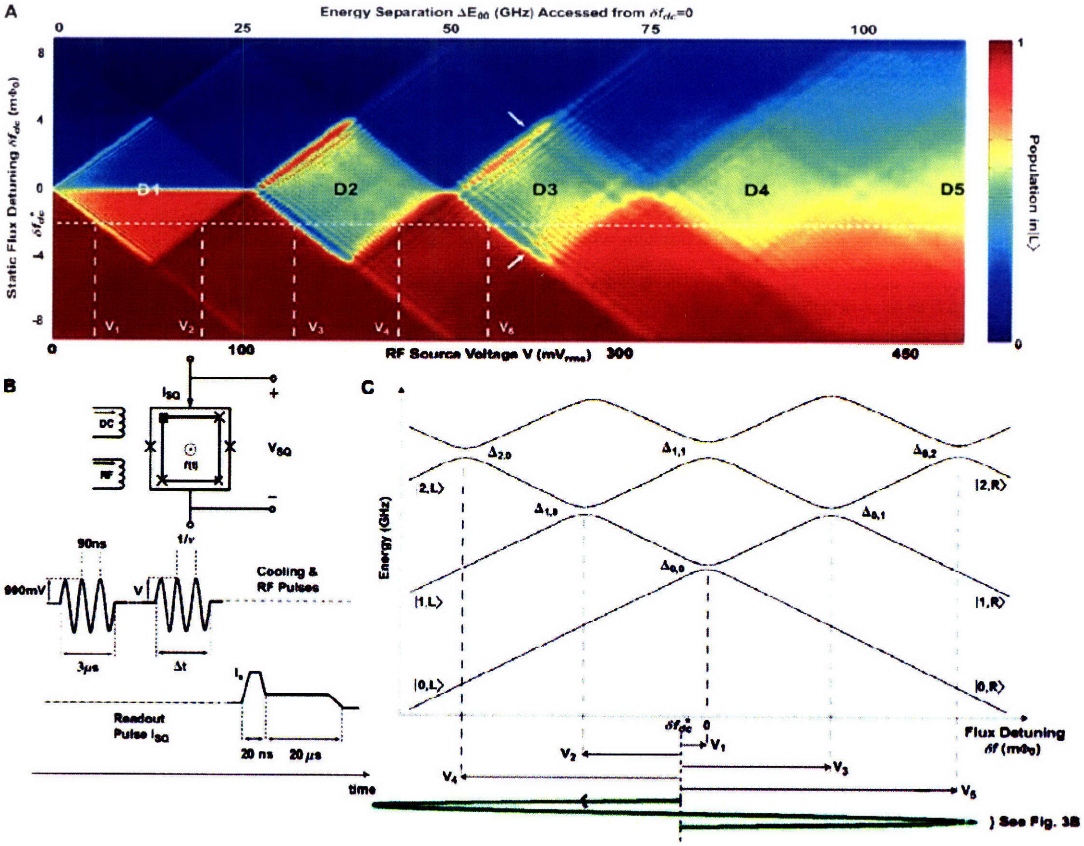

FIG. 1: Amplitude spectroscopy with long-pulse driving towards saturation. (**A**) Amplitude spectroscopy diamonds. The qubit is driven at a fixed frequency $\nu = 0.160$ GHz, while amplitude V is swept for each static flux detuning $\delta f_{\rm dc}$. Color scale: net qubit population in state $|q, L\rangle$, where L (R) labels diabatic states of the left (right) well of the qubit double-well potential, and $q = 0, 1, 2, ...$ labels the longitudinal modes. The diamond edges signify the driving amplitude V for each value of $\delta f_{\rm dc}$ when an avoided level crossing is first reached (amplitudes $V_1 - V_5$ for $\delta f_{\rm dc} = \delta f^*_{\rm dc}$). The main diamond regions, symmetric about $\delta f_{\rm dc} = 0$, are labeled D1 to D5. Arrows indicate signatures of transverse mode coupling (see Fig. 4). Top axis: the $|0,{\rm L}\rangle - |0,{\rm R}\rangle$ energy spacing $\Delta E_{0,0}$ accessed by V from $\delta f_{\rm dc} = 0$. (**B**) Schematic of the qubit surrounded by a SQUID magnetometer readout. Static and radio-frequency (RF) fields control the state of the qubit: a 3-μs cooling-pulse followed by an amplitude-spectroscopy pulse of duration Δt and amplitude V. The qubit state is determined with a synchronous readout pulse applied to the SQUID. (**C**) Schematic energy-level diagram illustrating the relation between the driving amplitude V and the avoided crossing positions for a particular static flux detuning $\delta f_{\rm dc} = \delta f^*_{\rm dc}$. The arrows represent the amplitudes $V_1 - V_5$ of the RF field at which the illustrated avoided crossings are reached, marking the onset of the diamond regions in (A).

28, 29] have been demonstrated with these systems. Significant progress has also been made toward their application to quantum information science [30, 31], including state initialization [24], tunable [32, 33, 34] and long-distance [35, 36] coupling, quantum control [37, 38, 39, 40], quantum state tomography [41], and measurement [42, 43, 44].

Our qubit (Fig. 1B) is a niobium superconducting loop interrupted by three Josephson junctions (see also App. A) [45, 46]. The qubit potential has a two-dimensional double-well profile near flux-bias $f \approx \Phi_0/2$, parameterized by the detuning $\delta f \equiv f - \Phi_0/2$, where Φ_0 is the superconducting flux quantum (Fig. A5). The system's energy eigenstates are comprised of transverse $(p = 0, 1, 2, \ldots)$ and longitudinal $(q = 0, 1, 2, \ldots)$ modes, with energies controlled by the flux detuning δf. When the potential is tilted so that resonant interwell tunneling is suppressed, the eigenstates closely approximate the diabatic well states localized in the left (L) and right (R) wells, and are associated with loop currents of opposing circulation. In this limit, the energies of localized states in the left (right) well increase (decrease) approximately linearly with flux detuning (Fig. 1C). Whenever the diabatic states $|p, q, \mathrm{L}\rangle$ and $|p', q', \mathrm{R}\rangle$ are degenerate, resonant interwell tunneling mixes them and opens avoided crossings $\Delta_{pq,p'q'}$.

We drive the qubit longitudinally with a time-dependent flux $\delta f(t) = \delta f_{\mathrm{dc}} - \Phi_{\mathrm{rf}} \sin \omega t$, with a harmonic term of amplitude Φ_{rf}, proportional to the source voltage V, that induces sinusoidal excursions with frequency $\nu = \omega/2\pi$ through the energy bands about a static flux bias δf_{dc}. Because the transverse and longitudinal modes should be decoupled for a symmetric system, we assume initially that only the lowest transverse mode is populated and use the reduced notation: $|p, q, \mathrm{L}\rangle \rightarrow |q, \mathrm{L}\rangle$, $|p', q', \mathrm{R}\rangle \rightarrow |q', \mathrm{R}\rangle$, and $\Delta_{pq,p'q'} \rightarrow \Delta_{q,q'}$ (Fig. A5B). We do observe, however, signatures of weak excitations of transverse modes (see Fig. 4 and related discussion).

Each experiment uses the pulse sequence shown in Fig. 1B, which consists of a harmonic cooling pulse to initialize the qubit to its ground state [24], followed by the desired amplitude spectroscopy pulse. The qubit state is determined with a synchronous readout pulse applied to a superconducting quantum interference device (SQUID) magnetometer (App. A 3). Using this technique, we investigate both the long and short time behavior of our qubit, and infer the energy-level slopes m_q, and the splittings $\Delta_{q,q'}$ and locations $\delta f_{q,q'}$ of avoided crossings to construct the energy level diagram.

Fig. 1A displays the amplitude spectroscopy of the qubit driven towards saturation. We choose a driving frequency ν such that, throughout the driving cycle, $h\nu$ is generally much smaller than the instantaneous energy-level spacing, yet the speed is large enough to make the evolution through avoided crossings non-adiabatic. In this regime, Landau-Zener transitions drive the system into coherent superpositions of energy eigenstates associated with different wells. Four primary "spectroscopy diamonds" with large population contrast, centered about $\delta f_{\mathrm{dc}} = 0$ (D1, D2, D3, and D4), are observed in the data; they are flanked by eight fainter diamonds. The diamond structures result from the interplay between static flux detuning and driving amplitude, which determine when the various avoided crossings are reached. Because the onset of each diamond is associated with transitions at a particular avoided crossing, the diamond boundaries signify the avoided crossing locations. We use the linear relation between V and Φ_{rf} (see Fig. 2A) to obtain the avoided crossing locations $\delta f_{q,q'}$ listed in Table 1.

For a particular static flux detuning $\delta f_{\mathrm{dc}} = \delta f_{\mathrm{dc}}^{*} < 0$ (Figs. 1A and 1C) and driving amplitude increasing from $V = 0$, population transfer from $|0, \mathrm{L}\rangle$ to $|0, \mathrm{R}\rangle$ first occurs when the $\Delta_{0,0}$ avoided crossing is reached at $V = V_1$ (front side of diamond D1, see Fig. 1A). For $V_1 < V < V_2$, interferometric Landau-Zener physics [20, 21, 22, 48] at the $\Delta_{0,0}$ avoided crossing results in the observed fringes (detail, Fig. 2A). At $V = V_2$, the adjacent avoided crossing $\Delta_{1,0}$ is reached, inducing transitions between levels $|0, \mathrm{R}\rangle$ and $|1, \mathrm{L}\rangle$ and marking the back of D1.

For $V_2 < V < V_3$, the saturated population depends on the competition between transitions at $\Delta_{0,0}$ and $\Delta_{1,0}$, on fast intrawell relaxation, and to a lesser extent on much slower interwell relaxation processes. Because in our experiment $\Delta_{0,0} \ll h\nu \approx \Delta_{1,0}$, the result is dominated by the dynamics at the $\Delta_{1,0}$ crossing. Although transitions $|0, \mathrm{L}\rangle \rightarrow |0, \mathrm{R}\rangle$ are induced at the $\Delta_{0,0}$ crossing, stronger transitions at $\Delta_{1,0}$ convert a substantial fraction of that population to $|1, \mathrm{L}\rangle$. This excited population quickly relaxes back to $|0, \mathrm{L}\rangle$, thus suppressing the net population transfer. For the combinations of δf_{dc} and V where interference between successive passages through $\Delta_{1,0}$ is instead destructive, signatures of transitions due to $\Delta_{0,0}$ are visible, albeit with reduced contrast (detail, Fig. 2A).

At even larger amplitudes, transitions to additional excited states become possible. When $V > V_3$, the qubit can make transitions between $|0, \mathrm{L}\rangle$ and $|1, \mathrm{R}\rangle$, marking the front side of diamond D2. The backside of this diamond is marked by the amplitude $V = V_4$ that reaches $\Delta_{2,0}$, allowing transitions between $|0, \mathrm{R}\rangle$ and $|2, \mathrm{L}\rangle$. This description can be extended straightforwardly to the remainder of the spectrum. In this device, we did not find explicit signatures of coherent multipath traversal between the $\delta f < 0$ and $\delta f > 0$ regions of the energy-level diagram (e.g., via avoided crossings $\Delta_{1,1}$ and $\Delta_{2,2}, \ldots$).

There are several remarkable features associated with the amplitude spectroscopy shown in Fig. 1A. First, we are able to probe the qubit continuously over extraordinarily wide bandwidth using a single driving frequency of only 0.16 GHz. The highest diamond (D5) in Fig. 1A results from transitions to energy levels more than 100 GHz$\times h$ above the ground state. Even at such high energy levels, our artificial atom retains its energy-level structure in the presence of the strong driving used to access them.

Second, diamond D2 exhibits strong population inversion due to competition between transitions at avoided crossings $\Delta_{0,1}$ and $\Delta_{1,0}$ combined with fast intrawell relaxation to $|0, \mathrm{L}\rangle$ and $|0, \mathrm{R}\rangle$ (Fig. 2A). The transition rates at $\Delta_{0,1}$ and $\Delta_{1,0}$ exhibit strong oscillatory behavior due to Landau-Zener interference, constructive or destructive, depending on the values of δf_{dc} and V. The competition between these rates leads to a checkerboard pattern symmetric about $\delta f_{\mathrm{dc}} = 0$ with alternating regions of strong population inversion and efficient cooling. Similar checkerboard patterns are present in the higher diamonds. The population inversion observed here is incoherent, and can serve as the pump for a single-atom laser [49].

The energy-level separation $\Delta E_{q,q'} \equiv h(|m_q| + |m_{q'}|)(\delta f_{\mathrm{dc}} - \delta f_{q,q'})$ between states $|q, \mathrm{L}\rangle$ and $|q', \mathrm{R}\rangle$ is proportional to the net flux detuning from the location $\delta f_{q,q'}$ of the avoided crossing $\Delta_{q,q'}$, and to the sum of the magnitudes of the energy-level slopes m_q and $m_{q'}$. Because the relative phase accumulated between the $|q, \mathrm{L}\rangle$ and $|q', \mathrm{R}\rangle$ components of the wave function over repeated Landau-Zener transitions is sensitive to $\Delta E_{q,q'}$, the slopes can be derived from the interference patterns which arise when varying δf_{dc}. The Nth node in the interference pattern occurs when a relative phase of $2\pi N$ is picked up during the qubit's excursion beyond the avoided crossing. The detuning locations of the nodes (inset, Fig. 2B) follow the power-law $s_{qq'} N^{2/3}$ with a prefactor $s_{qq'}$

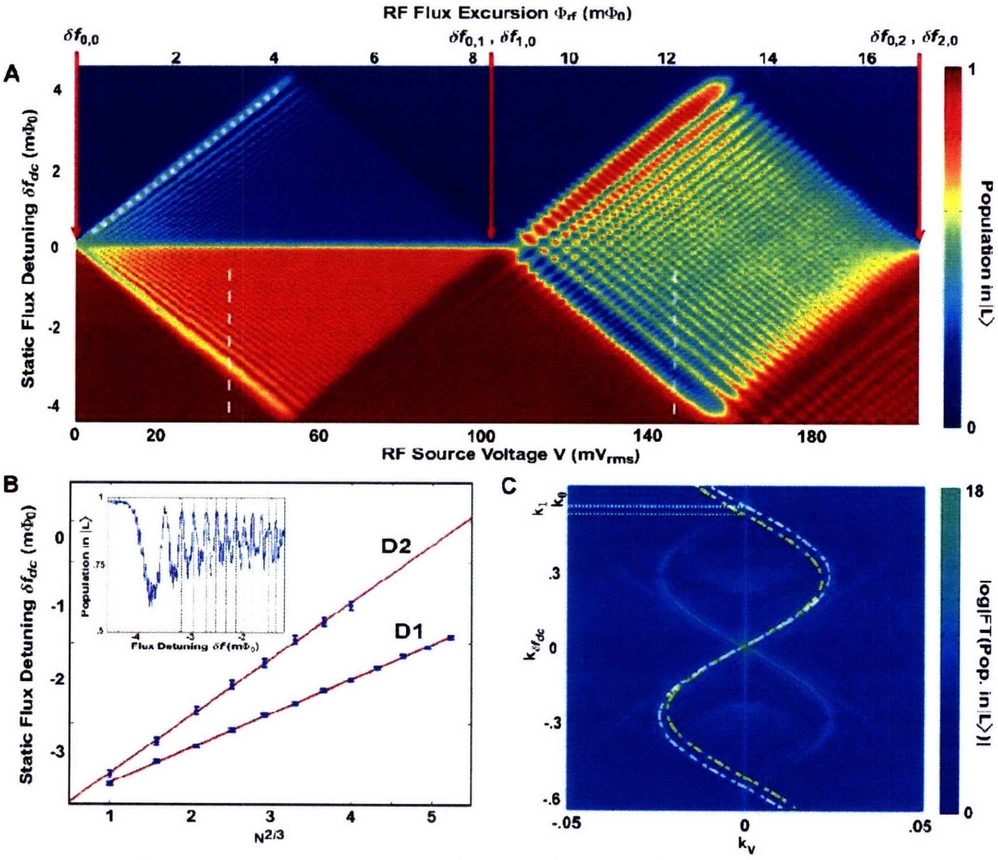

FIG. 2: Energy-level slopes and interference patterns. (**A**) Detail of diamonds D1 and D2 (Fig. 1A) showing interference patterns due to single (D1) and multiple (D2) avoided crossings (see text). Diamond D2 exhibits strong population inversion. Arrows mark the location of the avoided crossing positions. Energy-level slopes are extracted in (B) from the interference fringes (dashed white lines) at 43 $\mathrm{mV_{rms}}$ (D1) and 150 $\mathrm{mV_{rms}}$ (D2). The flux-to-voltage conversion factor is determined by the front side of D1 (dotted white line). (**B**) Determination of the energy-level slopes for levels $|0,L\rangle$, $|0,R\rangle$, $|1,L\rangle$, and $|1,R\rangle$. Detuning location of the Nth interference-node (see inset) vs. $N^{2/3}$ at the voltages marked with dashed lines in (A) and their corresponding linear fits (red line). Inset: Vertical slice from diamond D1 (43 $\mathrm{mV_{rms}}$). Interference nodes N used in the main panel are indicated by dotted lines. (**C**) 2D Fourier transform of both diamonds in (A). The sinusoids with wavenumbers k_0 and k_1 are contributions from diamonds D1 and D2, respectively, and are related to the energy-level slopes (see text).

related to the energy-level slopes (App. B 1):

$$|m_q| + |m_{q'}| = a\nu\sqrt{\alpha V/s_{qq'}^3}\left(\frac{\mathrm{GHz}}{\mathrm{m}\Phi_0}\right), \qquad (1)$$

where $a = 3\pi/2\sqrt{2}$. The factor α is the frequency-dependent conversion factor between RF flux and source voltage; its value $\alpha = 0.082\,\mathrm{m}\Phi_0/\mathrm{mV_{rms}}$ is inferred from the slope of the front edge of the first diamond (Fig. 2A). Fig. 2B shows the $N^{2/3}$ power-law fits to the nodes of the vertical slices in diamonds D1 and D2 which are used to extract m_0 and m_1 (Fig. 2A, dashed vertical lines), where we take $|m_q| = |m_{q'}| \equiv m_q$ for $q = q'$ in our system. The slopes are obtained sequentially from the fitted values $s_{qq'}$ in Eq. 1, starting with $2m_0 = 2.88$ GHz/mΦ$_0$, followed by $m_0 + m_1 = 2.534$ GHz/mΦ$_0$; their values are summarized in Table 1.

The relation between the slopes m_0 and m_1 is most clearly exhibited by the 2D Fourier transform of the diamonds in Fig. 2C (App. B 2). The observed structure in the first two diamonds arises from the underlying "Bessel-function staircases" of multi-photon resonances associated with transitions between the lowest four energy levels, where the n-photon absorption rate depends on driving amplitude through the square of the Nth-order Bessel function [20, 22, 23]. Using Fourier analysis, the apparently complicated mesh of

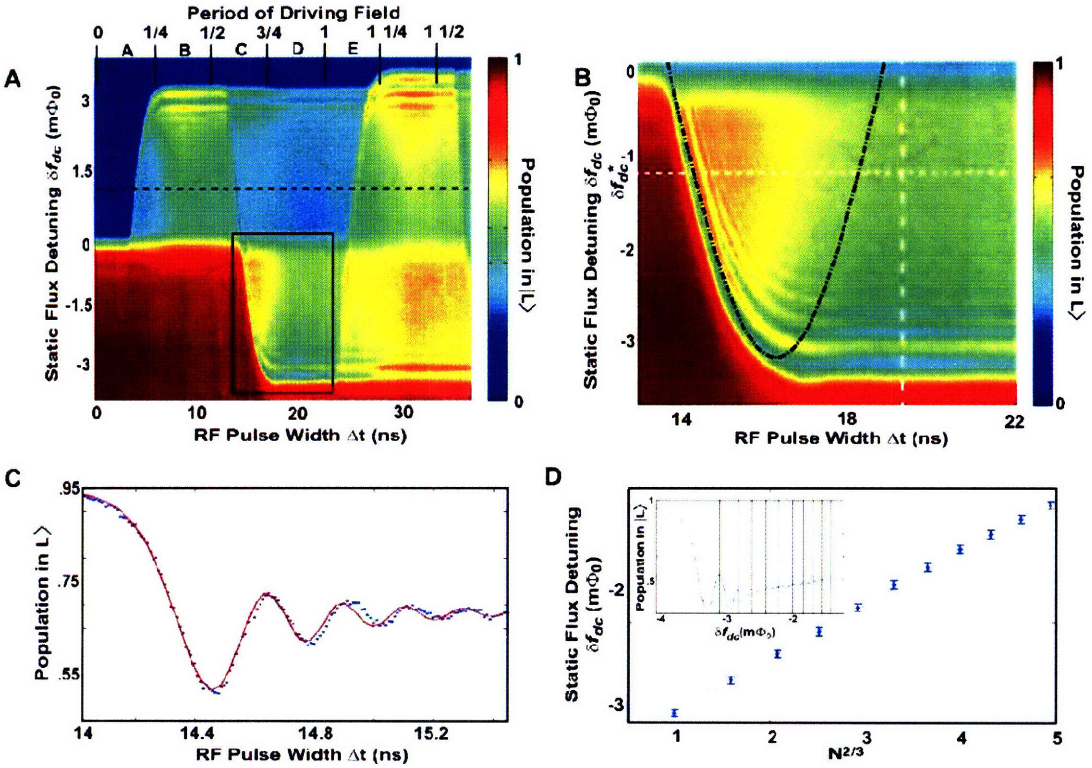

FIG. 3: Amplitude spectroscopy with short-pulse driving. (**A**) Qubit response to a short RF pulse of variable length Δt as a function of static flux detuning δf_{dc}, with $V = 181$ mV$_{\mathrm{rms}}$; $\nu = 0.045$ GHz. Top axis: driving field period (regions A-E); the maximum pulse width corresponds to ~1.5 oscillation periods. The scan is performed at an amplitude value in the left side of diamond D3 (Fig.A11), which reaches all crossings through $\Delta_{0,2}$ and $\Delta_{2,0}$. (**B**) Detail of the interference pattern in the boxed region of (A). The black curve marks the pulse width Δt at which the sinusoidal flux-excursion first exceeds and, subsequently, returns through $\Delta_{0,2}$ at flux detunings δf_{dc}. (**C**) Temporal oscillations along the horizontal line in (B) at the specific static flux bias $\delta f_{\mathrm{dc}} = \delta f^*_{\mathrm{dc}}$, fitted by a Landau-Zener model with damping (red line, see text). (**D**) Nth interference node versus $N^{2/3}$ along the vertical line in (B) and best linear fit. Inset: interference pattern along vertical line in (B) and node locations.

overlapping Bessel functions is transformed to a pair of sinusoids with periodicity related to the energy level slopes, $k_V = \pm\alpha g \sin(k_{\delta f_{\mathrm{dc}}}/g)$, where $g = 2(|m_q| + |m_{q'}|)/\nu$ [50]. The sinusoid associated with $q = q' = 0$ arises from the transitions at $\Delta_{0,0}$, while the second sinusoid with $q = 0$, $q' = 1$ and $q = 1$, $q' = 0$ is degenerate and arises from the transitions at $\Delta_{0,1}$ and $\Delta_{1,0}$. All four diamonds and their individual Fourier transforms are presented in Figs. A6-A10.

Valuable additional information about the energy level spectrum and temporal coherence is gained by performing amplitude spectroscopy over short time scales (Fig. 3). Temporal-response measurements are performed by initializing the system to the ground state at detuning δf_{dc} and then applying an RF field pulse of a variable length Δt, with fixed frequency and amplitude. The phase of the sinusoid is carefully adjusted to maintain the timing and directionality of the RF-flux excursion through the energy levels between pulses.

Crossing q, q′	Location $\delta f_{q,q'}$(mΦ_0)	Coupling $\Delta_{q,q'}/h$ (GHz)	Slope $m_{q'}$ (GHz/mΦ_0)
0, 0	0	0.013 ± 0.001	1.44 ± 0.01
0, 1	8.4 ± 0.2	0.090 ± 0.005	1.09 ± 0.03
0, 2	17.0 ± 0.2	0.40 ± 0.01	0.75 ± 0.04
0, 3	25.8 ± 0.4	2.2 ± 0.1	0.49 ± 0.08

TABLE I: Energy spectrum parameters of a superconducting artificial atom determined using amplitude spectroscopy

When the pulse ends abruptly at time Δt, the state of the system is preserved as the flux detuning instantaneously returns to δf_{dc} (finite decay-time corrections are discussed below).

This is exemplified in Fig. 3, where parameters are tuned to investigate the $\Delta_{2,0}$ level crossing (Fig. A11). For example,

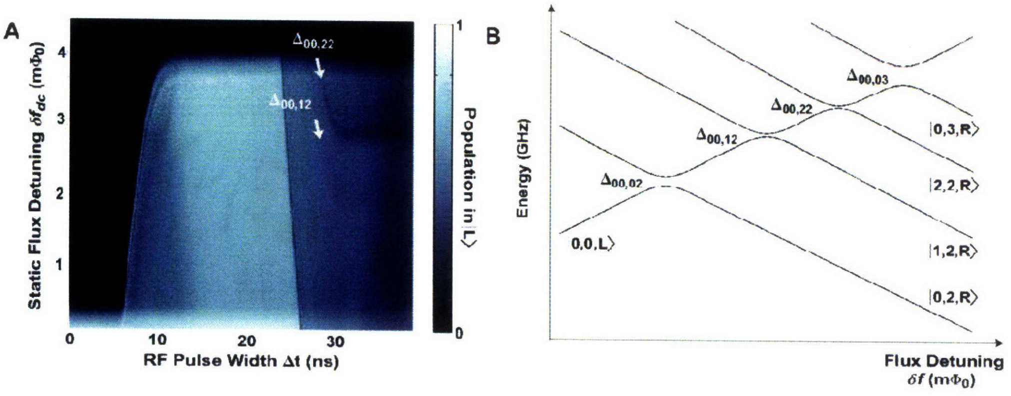

FIG. 4: Identification of transverse states of the qubit's double-well potential. (**A**) Qubit response to a short RF pulse of variable length Δt as a function of static flux detuning $\delta f_{\rm dc}$, with $V = 179$ mV$_{\rm rms}$; $\nu = 0.025$ MHz. The scan is performed at an amplitude value in the right side of diamond D3 (Fig. A12), where the crossing $\Delta_{03,00}$ (but not $\Delta_{00,03}$) is reached. The signatures of two crossings with transverse states, $\Delta_{12,00}$ and $\Delta_{22,00}$, are indicated. (**B**) Schematic energy-level diagram showing the locations of the transverse states.

starting in the ground state at positive detuning ($\delta f_{\rm dc} > 0$), the qubit is driven through $\delta f(t) < 0$, diabatically crossing $\Delta_{0,0}$ and $\Delta_{1,0}$ at the beginning of the first quarter-period with no significant population transfer (beginning of region A). Significant population transfer first occurs in region A when $\Delta_{2,0}$ is reached. The onset of population transfer is followed by brief temporal oscillations, which we use to find the splitting $\Delta_{2,0}$ (see below). The population becomes stationary after the qubit returns through $\Delta_{2,0}$ in the second quarter period (region B).

In the third quarter-period (region C), the driving pulse takes the qubit through the excited state avoided crossing $\Delta_{0,2}$ located on the opposite side of the level diagram (positive flux bias, Fig. 1C). This event is marked by a second sharp population transfer. The population subsequently remains nearly constant (region D) until a third abrupt population transfer occurs during the first quarter of the second period (region E), which signals the qubit's return through $\Delta_{2,0}$ and the repetition of the driving cycle. The population transfer does not reach its furthest extent in flux during the first half-period (as it does for the subsequent half-periods) because our pulse shape has slightly lower amplitude for times smaller than 5 ns.

The observed response over short time scales is not symmetric about $\delta f_{\rm dc} = 0$. When starting in the ground state at static bias $\delta f_{\rm dc} = \delta f_{\rm dc}^* < 0$, the system is drawn deep into the ground state during the first half-period, without inducing any transitions (see Fig 1C). It is only during the second half-period that $\Delta_{0,2}$ is finally reached and significant population transfer occurs. The detailed time dependence of population in this interval is shown in Fig. 3B. The curved line in Fig. 3B marks the pulse width Δt at which the sinusoidal flux excursion first exceeds and, subsequently, returns through $\Delta_{0,2}$ for different flux detunings $\delta f_{\rm dc}$; the sinusoidal excursion about the specific static flux $\delta f_{\rm dc}^*$ is correspondingly indicated in Fig. 1C.

The temporal oscillations displayed in Fig. 3B and Fig. 3C can be understood qualitatively as a Larmor-type precession, or "ringing," that results after the qubit is swept through the avoided crossing. In a pseudo-spin-1/2 picture where the qubit states are identified with up and down spin states relative to a fictitious z-axis, the qubit precesses about a tipped effective magnetic field which steadily increases in magnitude and rotates toward the z-axis. This picture is consistent with a temporal analysis of the standard Landau-Zener problem, in which a linear ramp with velocity v sweeps the qubit through the avoided crossing. In the perturbative (non-adiabatic) limit (B 3), this model yields the transition probability

$$P(t) = \frac{\Delta_{0,2}^2}{4}\left|\int_{t_0}^{t} e^{ivt'^2/2}dt'\right|^2 . \qquad (2)$$

The integral in Eq. 2 often arises in the context of optical diffraction, giving rise to Fresnel oscillations similar to the coherent oscillations observed in Fig. 3C.

Although Eq. 2 captures the essential features of the data in Fig. 3C, to obtain a quantitative fit we must account for the non-abrupt ending of the pulse. This transient slightly modifies the total precession phase accumulated before readout, and adds a small Mach-Zehnder-type interference due to the finite ramp speed back through the avoided crossing $\Delta_{0,2}$. We found remarkable agreement between the data and a simulation of the Bloch dynamics of the two level system near $\Delta_{0,2}$ which included longitudinal sinusoidal driving up to time $t = \Delta t$ followed by a rapid decay over approximately 2 ns, and intrawell relaxation with a rate of 0.65 ns^{-1} (Fig. 3C). The value of $\Delta_{0,2}$ is extracted as a fitting parameter and, in this regime, is largely insensitive to the details of the pulse decay and intrawell relaxation.

As in the case of the long-time data, the energy-level slopes can be extracted from the vertical fringes (Fig. 3B) using the $N^{2/3}$ power-law fitting (Fig. 3D) and Eq. 1. We used Eq. 1 to infer m_2 and m_3 from the sums $m_0 + m_2 = 2.189$ GHz/mΦ_0 and $m_0 + m_3 = 1.929$ GHz/mΦ_0. The short-time amplitude spectroscopy procedure was applied to obtain $\Delta_{q,q'}$ for diamonds D2-D4 and slopes m_q for diamonds D3-D4, and they are presented in Table 1 ($\Delta_{0,0}$ was previously obtained using the rate-equation approach [22]).

So far we have focused only on the strongly coupled longitudinal modes. However, the lack of perfect symmetry allows us to probe excited transverse modes within our driving scheme as well. The population transfer is relatively weak, indicating small deviations from an ideally symmetric double-well potential and longitudinal driving. Signatures of these states appear in diamonds D3 and D4 (e.g., arrows in Fig. 1A and Fig. A13). The temporal response to a short RF pulse taken on the front side of diamond D3 (Fig. A12) is shown in Fig. 4A. The front side of diamond D3 results from accessing $\Delta_{02,00}$ during the first half-period, where some population is transferred from the right to the left wells (Fig. 4A), and we have used the full notation explicitly indicating both longitudinal and transverse modes. Two weak population transfers are identified during the second half-period between the known positions of the longitudinal avoided crossings $\Delta_{00,02}$ and $\Delta_{00,03}$. This result is in agreement with simulations of the qubit Hamiltonian [46], which indicate that two transverse modes $|1,2,\mathrm{R}\rangle$ and $|2,2,\mathrm{R}\rangle$ exist in this region, as illustrated in Fig. 4B. Although we can identify their locations, the values of $\Delta_{00,12}$ and $\Delta_{00,22}$ are not conclusively determined from this measurement, because the fringe contrast of their temporal oscillations are small compared with those of the adjacent longitudinal crossings $\Delta_{00,02}$ and $\Delta_{00,03}$.

The amplitude spectroscopy technique demonstrated here is generally applicable to systems with traversable avoided crossings, including both artificial and natural atomic systems. Due to the sensitivity of interference conditions and transition probabilities to system parameters, it is a useful tool to study and manipulate quantum systems. The technique is extensible to anharmonic excitation, e.g., one can utilize arbitrary-waveform excursions through the energy levels and targeted harmonic excitations to achieve desired transitions. This type of hybrid driving has been very recently demonstrated with Cs [51] and Rb [52] atoms about Feshbach resonances, systems containing weakly-coupled levels that are otherwise challenging to address with a standard frequency-based approach. The amplitude spectroscopy technique is complementary to frequency spectroscopy, allowing the characterization of a quantum system, and, more generally, should open new pathways for quantum control [53].

We thank A. Shytov, J. Bylander, B. Turek, A.J. Kerman, and J. Sage for helpful discussions; V. Bolkhovsky, G. Fitch, E. Macedo, P. Murphy, K. Parrillo, R. Slattery, and T. Weir at MIT Lincoln Laboratory for technical assistance. This work was supported by AFOSR and LPS (F49620-01-1-0457) under the DURINT program, and by the U.S. Government. The work at Lincoln Laboratory was sponsored by the US DoD under Air Force Contract No. FA8721-05-C-0002.

APPENDIX A: SUPPLEMENTARY INFORMATION

1. Device Fabrication and Parameters

The device was fabricated at MIT Lincoln Laboratory. It has a critical current density $J_c \approx 160\,\mathrm{A/cm^2}$, and the characteristic Josephson and charging energies are $E_\mathrm{J} \approx (2\pi\hbar)300\,\mathrm{GHz}$ and $E_\mathrm{C} \approx (2\pi\hbar)0.65\,\mathrm{GHz}$ respectively. The ratio of the qubit JJ areas is $\alpha \approx 0.84$, and $\Delta \approx (2\pi\hbar)10\,\mathrm{MHz}$. The qubit loop area is 16×16 μm^2, and its self inductance is $L_\mathrm{q} \approx 30$ pH. The SQUID Josephson junctions each have critical current $I_{c0} \approx 2$ μA. The SQUID loop area is 20×20 μm^2, and its self inductance is $L_\mathrm{S} \approx 30$ pH. The SQUID junctions were shunted with 2 1-pF on-chip capacitors. The mutual coupling between the qubit and the SQUID is $M \approx 25$ pH.

2. Potential Energy of the PC Qubit

The potential energy of the PC Qubit is a 2D anisotropic periodic potential with double-well structures at each lattice site. After designing for negligible inter-lattice-site tunneling, the potential energy can be visualized as a single double-well, as seen in Fig. A5a. It is convenient to parameterize the potential energy U with phase variables $\varphi_m = (\varphi_1 - \varphi_2)/2$ and $\varphi_p = (\varphi_1 + \varphi_2)/2$, where φ_1 and φ_2 are the phases across junctions 1 and 2, respectively, in Fig.1B. It is also convenient to plot U/E$_\mathrm{j}$, where $\mathrm{E_j} = \Phi_0 \mathrm{I_c}/2\pi$ and I_c is the critical current of the larger junction. When the double-well potential is symmetric and the qubit is driven symmetrically, one can reduce the 2D potential to a 1D double-well along the φ_m direction, as seen in Fig. A5b. This is the longitudinal direction along which the qubit circulating current varies through the phase ϕ_m [46].

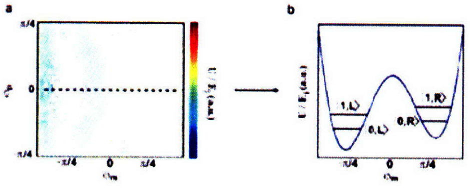

FIG. 5: **2D and 1D double-well potential energies (see text). a,** Contour plot of 2D double-well potential energy for our qubit at $\delta f_0 = 0.46\Phi_0$, far detuned from the symmetry point $\delta f_\mathrm{dc} = 0$. When the transverse quantum modes can be ignored, the potential energy can be treated as a 1D double-well along the dashed line pictured. **b,** 1D double-well potential energy for $\delta f_0 = 0.495\Phi_0$. The wells are slightly tipped to the left and the four lowest energy eigenstates are shown.

3. Qubit Readout

The qubit states are read out using a DC-SQUID, a sensitive magnetometer that distinguishes the flux generated by the qubit persistent currents, I_q. The readout is performed by driving the SQUID with a 20-ns "sample" current I_s followed by a 20-μs "hold" current (Fig. 1B). The SQUID will switch to its normal state voltage V_s if $I_\mathrm{s} > I_\mathrm{sw,L}$ ($I_\mathrm{s} > I_\mathrm{sw,R}$), when the qubit is in state $|L\rangle$ ($|R\rangle$). By sweeping the SQUID current I_s and qubit flux detuning δf_0, while monitoring the presence of a SQUID voltage over many trials, we generate a cumulative switching-current distribution function. From this distribution, we extract a best-estimator line in the space of I_s and δf_0 that allows us to characterize the population of state $|L\rangle$ for a given flux detuning.

4. Implementation

The experiments were performed in a dilution refrigerator at a temperature of approximately 20 mK. The device was magnetically shielded with 4 Cryoperm-10 cylinders and a superconducting enclosure. All electrical leads were attenuated and/or filtered to minimize noise. The electrical temperature of the device in the absence of microwave cooling was approximately 40 mK. After applying the microwave cooling pulse (Fig.1B), the effective temperature of the qubit was less than 3 mK. Microwave cooling enabled the data to be obtained at a repetition rate of 10 kHz, much faster than the intrinsic equilibration rate due to interwell relaxation. For all experiments, the static flux detuning was swept in 6-$\mu\Phi_0$ steps, and the RF amplitude was scanned in 0.5-mV steps (at the source). The pulse width was scanned in steps of 0.005 ns to .1 ns, and each data point comprised an average of 500 to 30,000 trials, depending on the desired resolution.

APPENDIX B: SUPPLEMENTARY DISCUSSION

1. Slope Extraction from Landau-Zener Interference Patterns

The interference between sequential Landau-Zener transitions at an isolated avoided crossing is sensitive to the relative phase

$$\phi = 2\pi \int_{t_1}^{t_2} \Delta E(t')\, dt' \qquad \text{(B1)}$$

accumulated by the two components of the wave function between the first and second traversals of the avoided crossing. Here $\Delta E(t')$ is the instantaneous diabatic energy level separation at time t', and $t_{1,2}$ are the times of the first and second traversals, respectively. We note that the energy ΔE is measured in frequency units (GHz), and this is why the expression contains the factor 2π rather than $1/\hbar$.

For demonstration, we focus on the interference in the first diamond where the driving $\delta f(t) = -\delta f_\mathrm{dc} + \alpha V \cos\omega t$ sweeps the qubit through only the lowest avoided crossing $\Delta_{0,0}$. Using the definition of the energy level slopes given in the text, this gives

$$\Delta E(t) \approx 2|m_0|(\alpha V - \delta f_\mathrm{dc}) - |m_0|\alpha V \omega^2 t^2, \qquad \text{(B2)}$$

where we have fit the driving $\delta f(t)$ near the maximum of $\cos\omega t$ to a parabola.

By setting $\Delta E(t_*) = 0$, we find the initial and final crossing times $t_{1,2} = \mp t_*$, with $t_* \equiv \sqrt{\frac{2(\alpha V - \delta f_\mathrm{dc})}{\alpha V \omega^2}}$. In the parabolic approximation to the driving signal, the phase accumulated between crossings is

$$\begin{aligned} \phi &= 2\pi \int_{-t_*}^{t_*} \left(2|m_0|(\alpha V - \delta f_\mathrm{dc}) - |m_0|\alpha V \omega^2 t'^2\right) dt' && \text{(B3)} \\ &= 2|m_0| \frac{8\pi}{3} (\alpha V - \delta f_\mathrm{dc})\, t_*. && \text{(B4)} \end{aligned}$$

Using the quantization condition for interference, $\phi = 2\pi N$, and the definition of t_*, we find the values of static flux detuning $\{\delta f_\mathrm{dc}^{(N)}\}$ where interference occurs with driving source voltage V:

$$2\pi N = 2|m_0| \frac{8\pi\sqrt{2}}{3} \frac{(\alpha V - \delta f_\mathrm{dc}^{(N)})^{3/2}}{(\alpha V)^{1/2}\omega}. \qquad \text{(B5)}$$

Rearranging Eq. (B5) and using $\omega = 2\pi\nu$ we find

$$\delta f_\mathrm{dc}^{(N)} = \alpha V - \left(\frac{3\pi\nu}{2\sqrt{2}} \frac{\sqrt{\alpha V}}{2|m_0|}\right)^{2/3} N^{2/3}, \qquad \text{(B6)}$$

where the prefactor to $N^{2/3}$ is identified with the fit parameter $s_{0,0}$ in the text.

Expression (B6) can be generalized to any avoided crossing $\Delta_{q,q'}$ by making the replacement $2|m_0| \to |m_q| + |m_{q'}|$, from which we arrive at Eq. (1) in the text.

2. 2D Fourier Transform of Amplitude Spectroscopy Diamonds

The amplitude spectroscopy plots in Figs. 1 and 2 of the main text display structure on several scales. On the largest scale, the boundaries of the "spectroscopy diamonds" are readily identifiable. The interiors of the diamonds are textured by fringes arising from the interference between successive Landau-Zener transitions at a single or multiple avoided crossings. On an even smaller scale, these fringes are composed of a series of horizontal multiphoton resonance lines. In order to extract information from these small scale structures, it is helpful to apply a transformation that is able to invert length scales; the two-dimensional Fourier transform (2DFT) provides this service.

An analytic treatment is presented in detail in Ref. [50]; the main conclusions are presented here. The treatment in Ref. [50] is applicable to the perturbative driving regime $\Delta^2/\hbar v \ll 1$, where Δ is the splitting at the largest traversed avoided crossing and $v = dE/dt$ is the speed of sweeping the qubit through level crossing. In our device for the driving frequencies employed, this condition is satisfied in the first two diamonds, where we find good agreement between the analytical treatment, numerics, and the data. For higher diamonds where the dynamics are non-perturbative, more complicated behavior is observed. The numerical approach can still be employed, but in practice we find that in such cases it is more efficient to extract the desired information directly from the short-time dynamics as described in the discussion of Fig. 3 in the text.

The internal structure of the first diamond arises from repeated passages through a single weak avoided crossing. As discussed in [50], the primary features of the 2D Fourier Transform of qubit magnetization for this perturbative driving regime can be understood by studying the 2DFT of the transition rate at the qubit level crossing. The 2DFT of the transition rate displays intensity concentrated along the curve

$$k_{\tilde{V}} = \pm\frac{2}{\nu}\sin\left(\frac{\nu}{2}k_{\delta\tilde{f}_{\rm dc}}\right), \qquad \text{(B7)}$$

where the flux detuning and the driving signal are measured in the energy units: $\delta\tilde{f}_{\rm dc} = 2|m_0|\delta f_{\rm dc}$ and $\tilde{V} = 2|m_0|\alpha V$. After going back to the physical units, Eq.(B7) gives

$$k_V = \pm\frac{4|m_0|\alpha}{\nu}\sin\left(\frac{\nu}{4|m_0|}k_{\delta f_{\rm dc}}\right), \qquad \text{(B8)}$$

The simplicity of the result can be traced to the fact that the curve (B7) reproduces time evolution of the quantum phase of the qubit [50] which is harmonic for harmonic driving.

Most strikingly, the apparently distinct phenomena of interference fringes and multiphoton resonances observed in the real space image are manifested as a single smooth curve in Fourier space. This structure can be understood by considering k_V and $k_{\delta f_{\rm dc}}$ to be smoothly varying functions of the spatial coordinates $(V, \delta f_{\rm dc})$. Through a stationary phase analysis of the Fourier integrals, one finds the mapping between real space patches and regions of k-space depicted in Fig. A10a.

In numerical simulations we found that the steady-state magnetization in the second diamond was well reproduced by a simple rate model based on incoherently adding two additional transition rates to account for transitions at the avoided crossings with the left and right first excited states. These additional rates are calculated using values of Δ appropriate for the excited state avoided crossings (approximately 90 MHz), and also take into account the different slopes of the ground and excited state energy levels.

In the above model, the Fourier image of diamond two is the sum of the Fourier transforms of the three relevant transition rates. Due to the difference in the dispersion of the lowest and second lowest qubit energy levels versus dc flux bias, for the Δ_{01} and Δ_{10} level crossings we have $\delta\tilde{f}_{\rm dc} = (|m_0| + |m_1|)\delta f_{\rm dc}$, $\tilde{V} = (|m_0| + |m_1|)\alpha V$. This gives a sinusoid

$$k_V = \pm\frac{2(|m_0| + |m_1|)\alpha}{\nu}\sin\left(\frac{\nu}{2(|m_0| + |m_1|)}k_{\delta f_{\rm dc}}\right) \text{(B9)}$$

with the wavelength different from that of (B8) by the ratio of the slopes $2|m_0|/(|m_0| + |m_1|)$. Both sinusoids can be seen in the Fourier transform of the second diamond, shown in Fig. A7, which indicates that the transitions at the Δ_{00} crossing and the Δ_{01} (Δ_{01}) crossings contribute to the observed pattern. From the measured ratio of the sinusoids' wavelengths we obtain the ratio of the slopes of the qubit energy levels m_0/m_1 without any fitting parameters.

In addition, in the Fourier transform of the second diamond the real-space integration samples a more limited sector of the fringes arising from each of the avoided crossings as compared to the case of the first diamond (see Fig. A10b). As a result, the regions around the middle part of a sinusoid, $\frac{\nu}{2(|m_1|+|m_0|)}k_{\delta f_{\rm dc}} \approx (n + 1/2)\pi$, are absent from the sinusoids arising from the Δ_{01} and Δ_{10} crossings, while the regions around the nodes, $\frac{\nu}{4|m_0|}k_{\delta f_{\rm dc}} \approx n\pi$, are absent from the sinusoid arising from transitions at the Δ_{00} crossing.

3. Perturbative Treatment of Fresnel Oscillations

The time-dependent oscillations observed in temporal-response measurements (see Fig. 3C) result from Larmor precession about a tilted axis following the qubit's transit through an avoided crossing. In the regime where the Landau-Zener transition probability is small, we use a perturbative model to relate these oscillations to the well-known Fresnel integral.

By linearizing the sinusoidal driving signal near the moment of traversal through the avoided crossing, t_*, we arrive at the familiar Landau-Zener Hamiltonian $\hat{H}(t) = (\hbar/2)(vt\,\hat{\sigma}^z + \Delta\hat{\sigma}^x)$, where $v = h(|m_q| + |m_{q'}|)\Phi_{\rm RF}\cos\omega t_*$ is the sweep velocity and Δ is the splitting at the avoided crossing. Next, we transform to a non-uniformly rotating frame by $|\,\psi_R(t)\,\rangle = e^{i\phi(t)\hat{\sigma}^z}|\,\psi(t)\,\rangle$, where $\phi(t) \equiv -\frac{1}{2}\int_0^t vt'\,dt' = -\frac{1}{4}vt^2$. The rotating frame Hamiltonian is purely off diagonal, with $\Delta_R(t) \equiv \Delta\exp(-ivt^2/2)$,

$$\hat{H}_R = \frac{\hbar}{2}\begin{pmatrix} 0 & \Delta_R(t) \\ \Delta_R^*(t) & 0. \end{pmatrix}, \qquad \text{(B10)}$$

We now expand the system's time evolution operator $\hat{U}(t, t_0)$ to first order in Δ:

$$\hat{U}(t, t_0) = \hat{1} - \frac{i}{\hbar}\int_{t_0}^{t}\hat{H}_R(t')dt' + \mathcal{O}(\Delta^2). \qquad \text{(B11)}$$

This approach is valid when the driving conditions are far from adiabaticity, i.e. $\Delta^2/v \ll 1$. The probability $P(t) = |\langle\uparrow\ |\hat{U}(t,t_0)|\ \downarrow\rangle|^2$ to find the system in the excited state $|\ \uparrow\rangle$ at time t given that it started in the ground state $|\ \downarrow\rangle$ at $vt_0 \ll -\Delta$ is given by

$$P(t) = \frac{\Delta^2}{4}\left|\int_{t_0}^{t} e^{ivt'^2/2}dt'\right|^2 \qquad \text{(B12)}$$

as given in Eq. (2) of the main text. The oscillatory dependence of this this integral on the final time t can be verified with the help of the Cornu spiral.

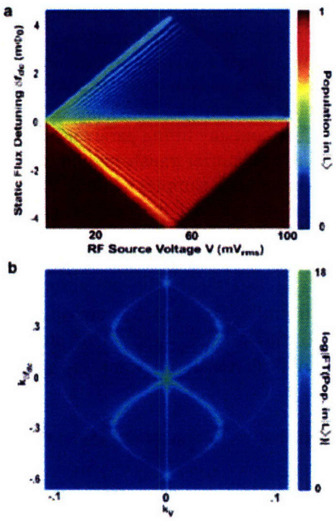

FIG. 6: **Diamond 1 and its 2D Fourier transform. a,** Diamond 1 in Fig.1 in the main text. Driving frequency $\nu = 160$ MHz. **b,** 2D Fourier transform of diamond 1. A single sinusoid is visible, along with its lower harmonics [50].

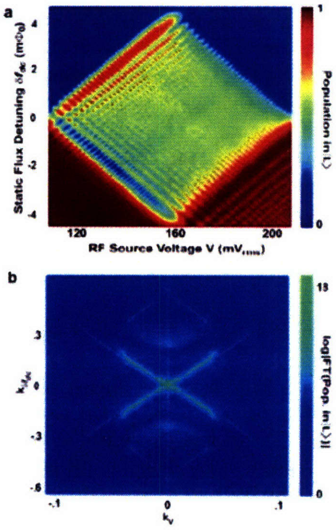

FIG. 7: **Diamond 2 and its 2D Fourier transform. a,** Diamond 2 in Fig.1 in the main text. Driving frequency $\nu = 160$ MHz. **b,** 2D Fourier transform of diamond 2. Two sinusoids are visible with slightly different period due to the multiple energy bands and avoided crossings that lead to diamond 2 [50].

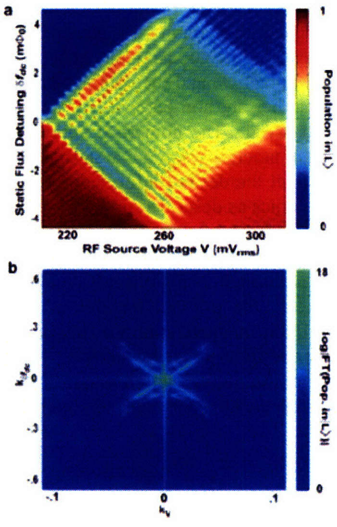

FIG. 8: **Diamond 3 and its 2D Fourier transform. a,** Diamond 3 in Fig.1 in the main text. Driving frequency $\nu = 160$ MHz. **b,** 2D Fourier transform of diamond 3. Because the Fourier transform samples progressively smaller sectors of the diamonds as diamond number increases, the extent of the sinusoids in the $k_{\delta f_{dc}}$ direction is limited [50].

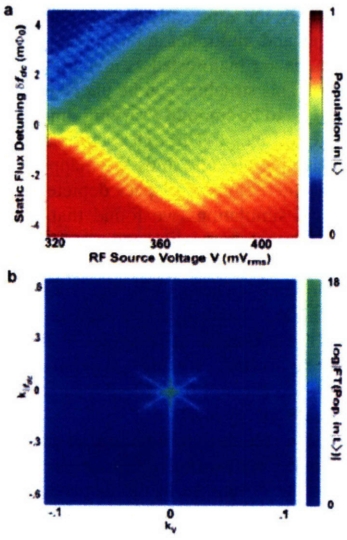

FIG. 9: **Diamond 4 and its 2D Fourier transform. a,** Diamond 4 in Fig.1 in the main text. Driving frequency $\nu = 160$ MHz. **b,** 2D Fourier transform of diamond 4. Because the Fourier transform samples progressively smaller sectors of the diamonds as diamond number increases, the extent of the sinusoids in the $k_{\delta f_{dc}}$ direction is limited [50].

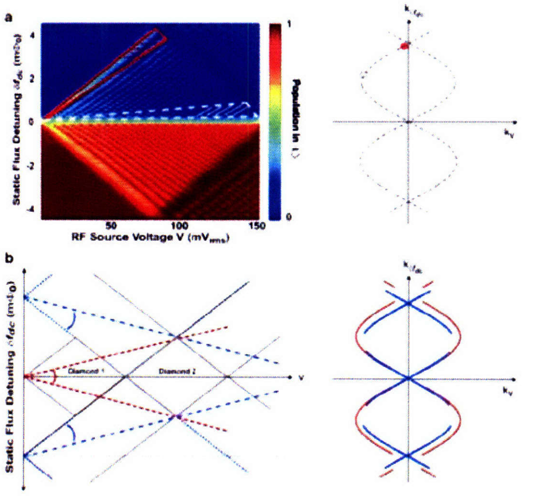

FIG. 10: **Graphical interpretation of 2D Fourier transform technique. a,** Diamond 1 at $\nu = 400$ MHz is pictured alongside a schematic of its Fourier transform. On a local scale within the wedge-shaped region of $(V, \delta f_{\rm dc})$ space outlined by a solid red line, the image everywhere looks like a simple series of evenly spaced horizontal bands. The Fourier transform over this region maps to a region of $(k_V, k_{\delta f_{\rm dc}})$ space localized near the $k_{\delta f_{\rm dc}}$ axis as indicated by the red dot in (B). Within the region outlined by the dashed white line, the local periodicity is along the angled interference fringes; the Fourier transforms maps this region to the region of $(k_V, k_{\delta f_{\rm dc}})$ space localized near the extrema of the sinusoid in the k_V direction as indicated by the open white circle. **b,** The Fourier integral samples a smaller sector of the real space image associated with the higher excited states in higher diamonds. Due to the mapping between sectors of real space and localized regions of k-space, the sinusoids associated with higher diamonds are not fully developed. Only the portion of the sinusoid corresponding to the mapped region in real space is realized in the Fourier image.

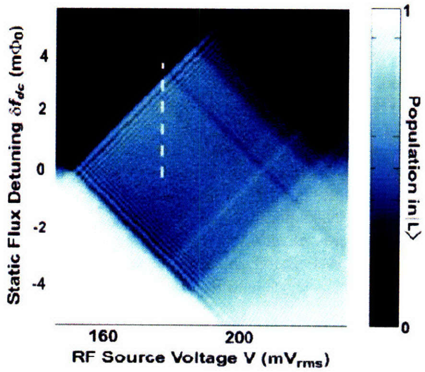

FIG. 11: **Diamond 3 at $\nu = 45$ MHz.** Dashed line indicates the amplitude (181mV$_{\rm rms}$) at which the pulse-width scan in Fig.3 was taken.

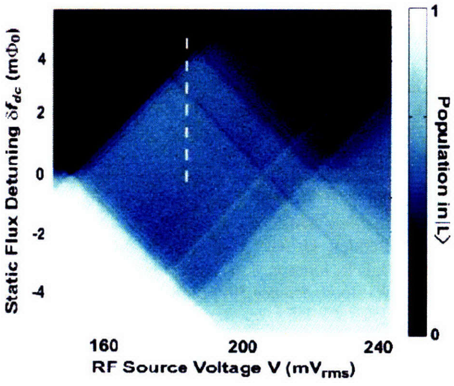

FIG. 12: **Diamond 3 at $\nu = 25$ MHz.** Dashed line indicates the amplitude (179mV$_{\rm rms}$) at which the pulse width scan in Fig.4 was taken.

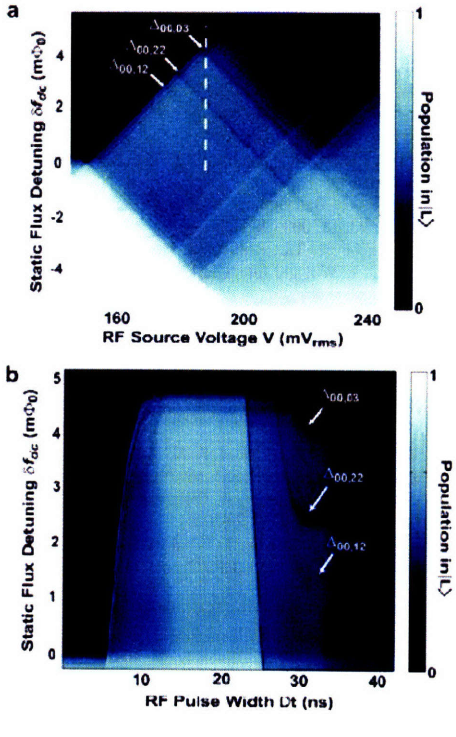

FIG. 13: **Pulse width scan at $\nu = 25$ MHz in diamond 3. a,** Diamond 3 at $\nu = 25$ MHz. Dashed line indicates the amplitude (183mV$_{\rm rms}$) at which the pulse width scan in Fig.A13b was taken. **b,** Pulse width scan in diamond 3 at $\nu = 25$ MHz. A loss of population occurs where the crossings $\Delta_{00,03}$, $\Delta_{22,00}$ and $\Delta_{12,00}$ are reached. This is in contrast to Fig.4A, where crossing $\Delta_{03,00}$ was reached, but never $\Delta_{00,03}$. Also noted are the avoided crossings with which the diagonal lines in the diamond (see a) are attributed.

---

[1] A.L. Schawlow, *Rev. Mod. Phys.* **54**, 697-707 (1982).

[2] R.C. Thompson, *Rep. Prog. Phys.* **48**, 531-578 (1985).

[3] J. R. Friedman, V. Patel, W. Chen, S. K. Tolpygo, J. E. Lukens, *Nature* **406**, 43-46 (2000).

[4] C. H. van der Wal, A. C. J. ter Haar, F. K. Wilhelm, R. N. Schouten, C. J. P. M. Harmans, T. P. Orlando, S. Lloyd, J. E. Mooij, *Science* **290**, 773-777 (2000).

[5] A. J. Berkley, H. Xu, R. C. Ramos, M. A. Gubrud, F. W. Strauch, P. R. Johnson, J. R. Anderson, A. J. Dragt, C. J. Lobb, F. C. Wellstood, *Science* **300**, 1548-1550 (2003).

[6] W. G. van der Wiel, *et al.*, *Rev. Mod. Phys.* **75**, 1-22 (2003).

[7] J. Clarke, A. N. Cleland, M. H. Devoret, D. Esteve, J. H. Martinis, *Science* **239**, 992-997 (1988).

[8] R. Hanson, L.P. Kouwenhoven, J.R. Petta, S. Tarucha, and L.M.K. Vandersypen, *Rev. Mod. Phys.* **79**, 1217-1265 (2007).

[9] Y. Nakamura, Y. A. Pashkin, J. S. Tsai, *Nature* **398**, 786 (1999).

[10] D. Vion, A. Aassime, A. Cottet, P. Joyez, H. Pothier, C. Urbina, D. Esteve, and M. H. Devoret, *Science* **296**, 886-889 (2002).

[11] Y. Yu, S. Han, X. Chu, S.-I. Chu, Z. Wang, *Science* **296**, 889-892 (2002).

[12] J. M. Martinis, S. Nam, J. Aumentado, C. Urbina, *Phys. Rev. Lett.* **89**, 117901 (2002).

[13] I. Chiorescu, Y. Nakamura, C. J. P. M. Harmans, J. E. Mooij, *Science* **299**, 1869-1871 (2003).

[14] R.E. Collin *Foundations for microwave engineering* (Wiley-IEEE Press New York, 2001)

[15] Y. Nakamura, Y. A. Pashkin, J. S. Tsai, *Phys. Rev. Lett.* **87**, 246601 (2001).

[16] J. Claudon, F. Balestro, F. W. J. Hekking, O. Buisson, *Phys. Rev. Lett.* **93**, 187003 (2004).

[17] B. L. T. Plourde, T.L. Robertson, P.A. Reichardt, T. Hime, S. Linzen, C.-E. Wu, and John Clarke, *Phys. Rev. B* **72**, 060506(R) (2005).

[18] S. Saito, T. Meno, M. Ueda, H. Tanaka, K. Semba, and H. Takayanagi, *Phys. Rev. Lett.* **96**, 107001 (2006).

[19] A. Izmalkov, M. Grajcar, E. Il'ichev, N. Oukhanski, Th. Wagner, H.-G. Meyer, W. Krech, M. H. S. Amin, A. Maassen van den Brink and A. M. Zagoskin, *Europhys. Lett.* 65, 844-849 (2004).

[20] W. D. Oliver, Y. Yu, J. C. Lee, K. K. Berggren, L. S. Levitov, T. P. Orlando, *Science* 310, 1653-1657 (2005).

[21] M. Sillanpaa, T. Lehtinen, A. Paila, Yu. Makhlin, P. Hakonen, *Phys. Rev. Lett.* 96, 187002 (2006).

[22] D.M. Berns, W.D. Oliver, S.O. Valenzuela, A.V. Shytov, K.K. Berggren, L.S. Levitov, T.P. Orlando, *Phys. Rev. Lett.* 97, 150502 (2006).

[23] C.M. Wilson, T. Duty, F. Persson, M. Sandberg, G. Johansson, and P. Delsing, *Phys. Rev. Lett.* 98, 257003 (2007).

[24] S. O. Valenzuela, W. D. Oliver, D. M. Berns, K. K. Berggren, L. S. Levitov, T. P. Orlando, *Science* 314, 1589-1592 (2006).

[25] A.O. Niskanen, Y. Nakamura, and J.P. Pekola, *Phys. Rev. B* **76**, 174523 (2007).

[26] J.Q. You, Yu-xi Liu, and Franco Nori, *Phys. Rev. Lett.* 100, 047001 (2008).

[27] I. Chiorescu, P. Bertet, K. Semba, Y. Nakamura, C.J.P.M. Harmans, and J.E. Mooij, *Nature* **431**, 159 (2004).

[28] A. Wallraff, D. I. Schuster, A. Blais, L. Frunzio, R.-S. Huang, J. Majer, S. Kumar, S. M. Girvin and R. J. Schoelkopf, *Nature* **431**, 162 (2004).

[29] J. Johansson, S. Saito, T. Meno, H. Nakano, M. Ueda, H. Tanaka, K. Semba, and H. Takayanagi, *Phys. Rev. Lett.* **96**, 127006 (2006).

[30] Y. Makhlin, G. Schön, A. Shnirman, *Rev. Mod. Phys.* **73**, 357 (2001).

[31] J. E. Mooij, The Road to Quantum Computing, Science **307**, 1210 (2005)

[32] T. Hime, P.A. Reichart, B.L.T. Plourde, T.L. Robertson, C.-E. Wu, A.V. Ustinov, and J. Clarke, *Science* **314** 1427 (2006)

[33] S.H.W. van der Ploeg, A. Izmalkov, A. Maassen van den Brink, U. Hübner, M. Grajcar, E. Il'ichev, H.-G. Meyer, and A.M. Zagoskin, *Phys. Rev. Lett.* **98**, 057004 (2007).

[34] A.O. Niskanen, K. Harrabi, F. Yoshihara, Y. Nakamura, S. Lloyd, and J.S. Tsai, *Science* **316**, 723 (2007).

[35] M.A. Sillanpaa, J.I. Park, and R.W. Simmonds, *Nature* **449**, 438 (2007).

[36] J. Majer, J.M. Chow, J.M. Gambetta, J. Koch, B.R. Johnson, J.A. Schreier, L. Frunzio, D.I. Schuster, A.A. Houck, A. Wallraff, A. Blais, M.H. Devoret, S.M. Girvin, and R.J. Schoelkopf *Nature* **449**, 443 (2007).

[37] Y. A. Pashkin, T. Yamamoto, O. Astafiev, Y. Nakamura, D. V. Averin, and J. S. Tsai, *Nature* **421**, 823 (2003).

[38] T. Yamamoto, Yu. A. Pashkin, O. Astafiev, Y. Nakamura, J. S. Tsai, *Nature* **425**, 941 (2003).

[39] R. McDermott, R. W. Simmonds, M. Steffen, K. B. Cooper, K. Cicak, K. D. Osborn, S. Oh, D. P. Pappas, J. M. Martinis, *Science* **307**, 1299 (2005).

[40] J.H. Plantenberg, P.C. de Groot, C.J.P.M. Harmans, and J.E. Mooij, *Nature* **447**, 836 (2007).

[41] M. Steffen, A. Ansmann, R.C. Bialczak, N. Katz, E. Lucero, R. McDermott, M. Neeley, E.M. Weig, A.N. Cleland, and J. M. Martinis, *Science* **313**, 1423 (2006).

[42] I. Siddiqi, R. Vijay, F. Pierre, C.M. Wilson, M. Metcalfe, C. Rigetti, L. Frunzio, and M.H. Devoret, *Phys. Rev. Lett.* **93**, 207002 (2004)

[43] N. Katz, M. Ansmann, R.C. Bialczak, E. Lucero, R. McDermott, M. Neeley, M. Steffen, E.M. Weig, A.N. Cleland, J.M. Martinis, A.N. Korotkov *et al.*, *Science* **312**, 1498 (2006)

[44] A. Lupascu, S. Saito, T. Picot, P.C. de Groot, C.J.P.M. Harmans, J.E. Mooij, *Nature Physics* **3**, 119 (2007)

[45] J. E. Mooij, T. P. Orlando, L. S. Levitov, L. Tian, C. H. van der Wal, S. Lloyd, *Science* **285**, 1036-1039 (1999).

[46] T. P. Orlando, J. E. Mooij, L. Tian, C. H. van der Wal, L. S. Levitov, S. Lloyd, and J. J. Mazo, *Phys. Rev. B* **60**, 15398-15413 (1999).

[47] H. Nakamura, *Nonadiabatic Transition* (London, England: World Scientific, 2001).

[48] M. Mark, T. Kraemer, P. Waldburger, J. Herbig, C.Chin, H.-C. Nägerl, and R. Grimm *Phys. Rev. Lett.* **99**, 113201 (2007).

[49] O. Astafiev, K. Inomata, A.O. Niskanen, T. Yamamoto, Yu. A. Pashkin, Y. Nakamura, and J.S. Tsai, *Nature* **449**, 588 (2007).

[50] M.S. Rudner *et al.*, arXiv:0805.1555.

[51] M. Mark, F. Ferlaino, S. Knoop, J.G. Danzl, T. Kraemer, C.Chin, H.-C. Nägerl, and R. Grimm, *Phys. Rev. A* **76**, 042514 (2007).

[52] F. Lang, P.V.D. Straten, B. Brandstätter, G. Thalhammer, K. Winkler, P.S. Julienne, R. Grimm, and J. Hecker Denschlag, *Nature Physics* **4**, 223-226 (2008).

[53] S. Ashab, J.R. Johansson, A.M. Zagoskin, and Franco Nori, *Phys. Rev. A* **75**, 063414 (2007).

Quantum Phase Tomography of a Strongly Driven Qubit

M. S. Rudner,[1] A. V. Shytov,[2] L. S. Levitov,[1,3] D. M. Berns,[1] W. D. Oliver,[4] S. O. Valenzuela,[5] and T. P. Orlando[6]
[1]*Department of Physics, Massachusetts Institute of Technology, Cambridge MA 02139*
[2]*Department of Physics, University of Utah, Salt Lake City, UT 84112*
[3]*Kavli Institute for Theoretical Physics, University of California, Santa Barbara, CA 93106*
[4]*MIT Lincoln Laboratory, 244 Wood Street, Lexington, MA 02420*
[5]*MIT Francis Bitter Magnet Laboratory, Cambridge, MA 02139*
[6]*Department of Electrical Engineering and Computer Science,*
Massachusetts Institute of Technology, Cambridge, MA 02139

The interference between repeated Landau-Zener transitions in a qubit swept through an avoided level crossing results in Stückelberg oscillations in qubit magnetization. The resulting oscillatory patterns are a hallmark of the coherent strongly-driven regime in qubits, quantum dots and other two-level systems. The two-dimensional Fourier transforms of these patterns are found to exhibit a family of one-dimensional curves in Fourier space, in agreement with recent observations in a superconducting qubit. We interpret these images in terms of time evolution of the quantum phase of qubit state and show that they can be used to probe dephasing mechanisms in the qubit.

PACS numbers: 03.67.Lx,03.65.Yz,85.25.Cp,85.25.Dq

Superconducting Josephson devices recently emerged as a platform for exploring coherent quantum dynamics in solid state systems [1]. Due to their macroscopic dimensions, these devices feature strong coupling to RF fields [2, 3, 4], and can be used to study new quantum phenomena associated with strong driving such as Rabi oscillations in the multiphoton regime [5, 6], Landau-Zener-Stückelberg-type (LZS) interference [7, 8, 9], Bloch oscillations [10], and qubit-photon dressed states [11].

In the LZS regime [7, 8, 9], the qubit undergoes repeated Landau-Zener (LZ) transitions at a level crossing, with adiabatic evolution between crossings [12]. Interference between subsequent LZ transitions results in an oscillatory dependence of qubit magnetization in the final state on the detuning from the level crossing and the driving amplitude [7, 13]. The LZS effect is related to earlier observations of photon-assisted transport in quantum dots [14, 15] and in superconducting systems [16, 17], which exhibit multiphoton sidebands with oscillatory dependence on RF field amplitude. Although the observed oscillations washed out more quickly at high RF power in those devices than in the qubits [7, 8, 9], in all cases the oscillations originated from the LZS interference effect.

A new regime of strong driving was reported in a recent work [18], in which a qubit was driven through a manifold of several states spanning a wide energy range up to 120 GHz. The observed LZS interference indicated that even such strong driving was not detrimental for coherence. The change in qubit magnetization induced by the driving pulse exhibited complex checkerboard-like patterns in the two-dimensional phase space parameterized by the DC magnetic flux and RF driving amplitude. These patterns displayed a multiscale character, with multiphoton resonance lines on the finest scale and LZS interference fringes on a larger scale, and additional complexity due to resonance and interference effects involving several pairs of energy levels during each pulse.

In an attempt to better understand the observed patterns, the authors of Ref. [18] employed a two-dimensional Fourier transform (FT). Unexpectedly, the FT revealed a highly ordered structure of *one-dimensional arcs* joined together to form lemon-shaped ovals in Fourier space, in contrast to the familiar Bragg peaks in the Fourier images of periodic patterns. Most surprisingly, these arcs were found to connect the high and low wavenumber regions, which are associated with the multiphoton resonances and LZS interference fringes.

In this article we explain the lemon-shaped structures observed in [18], first using a quasiclassical phase argument and then fully microscopically. We analyze the FT of the transition rate (see Fig.1), which can be measured using short excitation pulses [9]. Then we consider the FT of qubit magnetization produced by long pulses.

Our analysis reveals a relation between the lemon-shaped structures and the coherent dynamics of the qubit. In fact, because the Fourier transform inverts the energy variable and maps it onto the time variable (scaled by $\hbar$), we find that the lemon arcs can be interpreted as an image of the time dependence of the quantum phase of the qubit (see Eq.(2) below). This relation, as we shall discuss, can be exploited to probe fundamental aspects of qubit dynamics such as decoherence and dephasing, and to measure the decoherence times T_2 and T_2^*.

The intensity of each point on the curve in Fourier space arises from a particular ray-like section of the LZS pattern (see Fig.1), with the section direction in one-to-one correspondence with the time interval beween level crossings. The section-by-section mapping to Fourier space is reminiscent of tomographic imaging, and realizes a "tomogram" of the time evolution of the qubit phase.

Employing the FT to image quantum phase is familiar from the work on the mesoscopic Aharonov-Bohm ef-

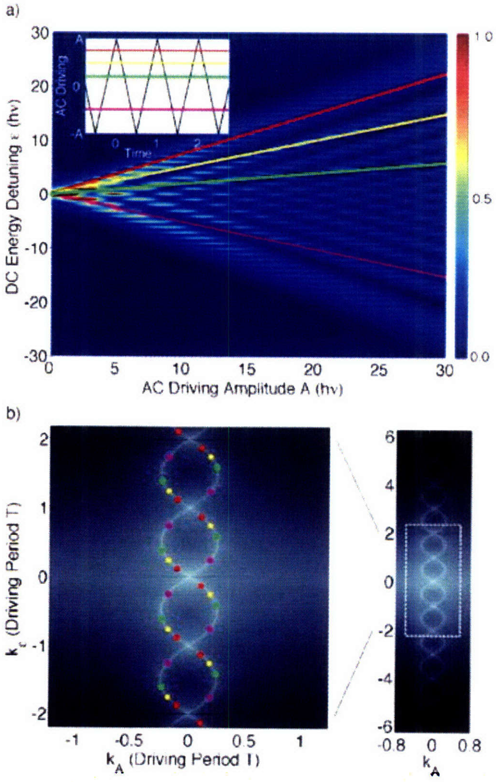

FIG. 1: Tomographic imaging of qubit phase evolution. The pattern of LZS oscillations in (a) the transition rate (12) and (b) its Fourier transform, which exhibits a family of parabolic arcs (8) forming lemon-shaped ovals. Along each arc, k_ε and k_A represent the time separation $t_2 - t_1$ and phase gain ϕ^g_{12}, Eq.(5), between subsequent level crossings, respectively. The Fourier intensity at each such point is mapped from the region near a ray $\varepsilon/A = u$ in the (A, ε) plane, where the parameters A, ε all yield the same time interval and phase gain between level crossings. Four of these rays and the corresponding points in Fourier space are shown in matching colors. A Sawtooth-like driving signal (inset) was used, with the decoherence rate $\Gamma_2 = \frac{1}{4}\omega$ in (12).

fect [20, 21], which used the dependence of conductance on magnetic field. In our approach, however, the *time dependence* of the phase is reconstructed using a two-dimensional FT where the axis associated with the detuning from qubit level crossing plays the role of time.

We also note that in recent work [22, 23, 24] a tomographic reconstruction of the Wigner function on the Bloch sphere was performed. The procedure used in Refs.[22, 23, 24], which employs controlled rotations of the qubit state following its Rabi oscillations, is different from that used in the present work. Our image of qubit time evolution is obtained in Fourier space. Also, because of the nature of the LZS effect, it only provides information about the relative phase of the qubit $|0\rangle$ and $|1\rangle$ states, rather than the entire Bloch vector.

To emphasize aspects common to different experiments that have used harmonic [7, 8, 9, 11, 18], sawtooth-like [10], and bi-harmonic [19] RF driving, we consider a generic periodic driving of the qubit:

$$\mathcal{H} = -\frac{\hbar}{2}\begin{pmatrix} h(t) & \Delta \\ \Delta & -h(t) \end{pmatrix}, \quad h(t) = \varepsilon - Ag(t), \qquad (1)$$

where $h(t)$ is the energy detuning from an avoided crossing, periodically modulated by the driving field $g(t) = g(t+T)$ with amplitude A and zero mean, $\oint g(t)dt = 0$. For simplicity here we focus on the case when $g(t)$ has one maximum and one minimum per period.

Away from the level crossing, the qubit evolves adiabatically as a superposition of the states $|0\rangle$ and $|1\rangle$. The LZS interference can be expressed [7] through the relative phase of the states $|0\rangle$ and $|1\rangle$ gained between subsequent passages through a level crossing:

$$\phi(A,\varepsilon) = \int_{t_1}^{t_2} h(t)dt = \varepsilon(t_2 - t_1) - A\int_{t_1}^{t_2} g(t)dt. \qquad (2)$$

The times $t_{1,2}$ of level crossing are the solutions to

$$Ag(t) = \varepsilon \qquad (g_{\min} < \varepsilon/A < g_{\max}), \qquad (3)$$

represented graphically in the inset of Fig.1a by the intersections between lines of fixed detuning and the driving signal. Quasiclassically, the LZS contrast can be modeled by a sum of functions $\cos(\phi(A,\varepsilon))$, one per each choice of $t_{1,2}$ in (2). We consider a position-dependent wavevector

$$(k_A, k_\varepsilon) = \pm(\nabla_A\phi(A,\varepsilon), \nabla_\varepsilon\phi(A,\varepsilon)), \qquad (4)$$

where $\pm$ accounts for the contributions of $e^{\pm i\phi(A,\varepsilon)}$. Evaluating the derivatives in (4) and, noting that the net contributions of $\nabla_\varepsilon t_{1,2}$ and $\nabla_A t_{1,2}$ vanish due to (3), gives

$$(k_A, k_\varepsilon) = \pm(-\phi^g_{12}, t_2 - t_1), \quad \phi^g_{12} = \int_{t_1}^{t_2} g(t)dt. \qquad (5)$$

Crucially, Eq.(5) defines *a curve* parameterized by a single variable $u = \varepsilon/A$, which is the only parameter upon which the times $t_{1,2}$ found in Eq.(3) depend.

We illustrate this mapping by an example of sawtooth driving (Fig.1 inset) with $g(t)$ linear between the points

$$g(nT) = -g((n \pm \tfrac{1}{2})T) = 1. \qquad (6)$$

In Fig.1, the points in Fourier space arising from different ε/A sections are denoted by dots with colors matching those of the corresponding rays $\varepsilon/A = u$ in the (A, ε) plane and of the constant detuning lines in the inset. The k_ε and k_A coordinates of those points correspond to the time separation (Fig.1a inset) and the phase gain, Eq.(5),

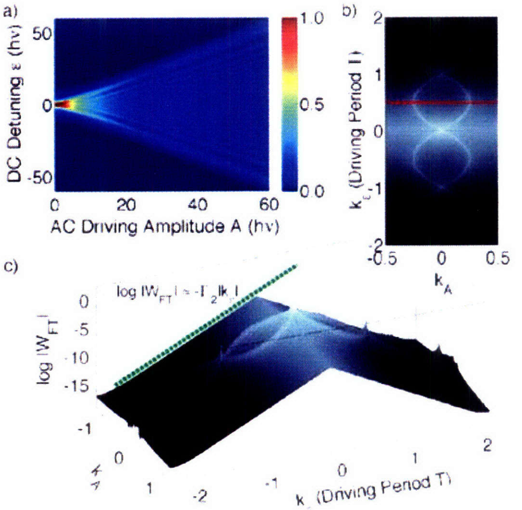

FIG. 2: Transition rate (12) and its FT for sawtooth-like driving for $\Gamma_2 = \omega$, four times larger than in Fig.1. A 3D projection plot of Fourier intensity is shown to illustrate the exponential decay $W_{FT}(k_A, k_\varepsilon) \propto e^{-\Gamma_2 k_\varepsilon}$.

between subsequent level crossings. In this way, the curves (5) reproduce the time evolution of qubit phase.

As shown in Fig.1, each ray maps to a family of points (5). The reason for this multiplicity is that, besides the sign ± in Eq. (5), Eq.(3) has multiple solutions $t_1' = t_1 + n_1 T$ and $t_2' = t_2 + n_2 T$ for each ε and A, where T is the period of driving and $n_{1,2}$ are arbitrary integers. Because $\oint g(t)dt = 0$, all such solutions yield the same phase gain ϕ_{12}^g and the same value of k_A. However, the corresponding values of k_ε are displaced by $(n_2 - n_1)T$, generating the periodic family of arcs shown in Fig.1b.

Another class of solutions to Eq.(3) describes subsequent passages through the level crossing *in the same direction*: $t_2 = t_1 + nT$. In this case t_1 is unconstrained and, because zero phase is gained over a single driving period, we obtain a discrete set of points $(k_A, k_\varepsilon) = (0, nT)$ irrespective of ε, A. As displayed most clearly in Fig.2c, the FT intensity indeed exhibits peaks at $k_\varepsilon = nT$. The peak positions $k_\varepsilon = nT$ agree with the spacing $\hbar\omega$ between multiphoton resonances in the (A, ε) plane.

To find the form of the curves in Fig.1b, we solve Eq.(3) for the case of sawtooth driving, Eq.(6). Without loss of generality we select $-T/2 < t_1 < 0 < t_2 < T/2$ and find

$$t_2 = -t_1 = \tau/2, \quad \tau \equiv T(A - \varepsilon)/2A. \tag{7}$$

Evaluating the phase $\phi_{12}^g = \int_{t_1}^{t_2} g(t)dt = \frac{1}{4}(1 - \varepsilon^2/A^2)T$, we obtain parabolic arcs in Fourier space:

$$(k_A, k_\varepsilon) = \pm\left(-(1 - \tau/T)\tau, \tau + nT\right), \tag{8}$$

$0 < \tau < T$, where the term nT was added to k_ε to account for the multiple solutions to Eq.(3) discussed above.

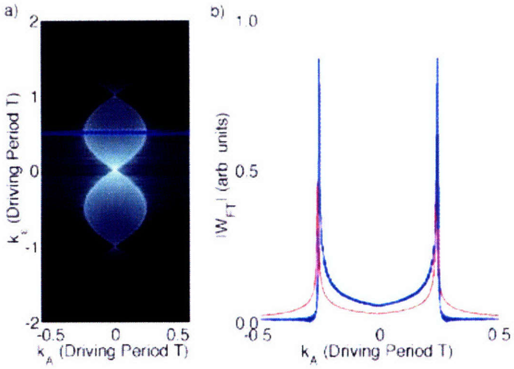

FIG. 3: Test of the result (15) for the Fourier intensity distribution in the lemon. a) FT of the transition rate in Fig.2 after the image was doubled by extending W to negative A as $W(-A, \varepsilon) = W(A, \varepsilon)$. b) Intensity in a mid-lemon section (blue line) compared with a similar section through a lemon in FT of the undoubled image in Fig.2 (red line).

Similarly, in the case of harmonic driving, the solutions of Eq.(3) are $t_2 = -t_1 = \frac{1}{\omega}\arccos(\varepsilon/A)$, which gives the phase $\phi_{12}^g = \int_{t_1}^{t_2} \cos(\omega t)dt = (2/\omega)\sqrt{1 - \varepsilon^2/A^2}$. Substituting these results into Eq.(5) we obtain the sinusoids

$$\omega k_A/2 = \pm \sin(\omega k_\varepsilon/2) \tag{9}$$

which were observed in Ref. [18].

Now we turn to a microscopic analysis of qubit dynamics based on the Hamiltonian (1) to which we add classical noise to model decoherence: $\tilde{h}(t) = h(t) + \delta\varepsilon(t)$. The transitions between qubit states $|0\rangle$ and $|1\rangle$ can be analyzed most easily in a rotating frame where

$$\mathcal{H} = -\frac{\hbar}{2}\begin{pmatrix} 0 & \Delta(t) \\ \Delta^*(t) & 0 \end{pmatrix}, \quad \Delta(t) = \Delta e^{-i\tilde{\phi}(t)}, \tag{10}$$

with $\tilde{\phi}(t) = \int_0^t \tilde{h}(t')dt'$. Perturbation theory in Δ yields the rate of transitions between the states $|0\rangle$ and $|1\rangle$:

$$W = \lim_{\delta t \Gamma_2 \gg 1} \frac{\Delta^2}{4\delta t} \iint_t^{t+\delta t} \langle e^{-i\tilde{\phi}(t_1)} e^{i\tilde{\phi}(t_2)} \rangle_{\delta\varepsilon} dt_1 dt_2, \tag{11}$$

where $\Gamma_2 = \frac{1}{T_2}$ is the decoherence rate. We average over $\delta\varepsilon(t)$ using the white noise model: $\langle e^{i\delta\phi(t_2) - i\delta\phi(t_1)} \rangle_{\delta\varepsilon} = e^{-\Gamma_2 |t_1 - t_2|}$, where $\delta\phi(t) = \int_0^t \delta\varepsilon(t')dt'$.

To find the rate W in closed form, we use the Fourier series $e^{i\phi(t)} = e^{i\varepsilon t}\sum_m f_m e^{-im\omega t}$, where the coefficients f_m can be expressed through the error function of complex argument for the case of sawtooth driving, or Bessel functions for the case of harmonic driving [9]. Using the appropriate Fourier series in (11) and performing the integration over t_1 and t_2, we obtain the expression

$$W(\varepsilon, A) = \frac{\Delta^2}{2} \sum_{m=-\infty}^{\infty} \frac{\Gamma_2 |f_m|^2}{(\varepsilon - \omega m)^2 + \Gamma_2^2}. \tag{12}$$

At $\omega \gtrsim 2\pi\Gamma_2$ this expression describes non-overlapping resonances (see Fig.1), while at $\omega \lesssim 2\pi\Gamma_2$ it describes the partially dephased regime of Ref. [9] (see Fig.2).

To evaluate the Fourier transform of the transition rate $W_{FT}(k_A, k_\varepsilon) = \iint_{-\infty}^{\infty} e^{-iAk_A - i\varepsilon k_\varepsilon} W(\varepsilon, A) d\varepsilon dA$, it is convenient to return to expression (11). Because the phase $\phi(t) = \varepsilon t - \int_0^t Ag(t')dt'$ is linear in ε as well as in A, we can easily bring the Fourier transform of (11) to the form

$$a \iint_t^{t+\delta t} \delta(k_\varepsilon + t_1 - t_2)\delta(k_A + \phi_{12}^g)e^{-\Gamma_2|t_1 - t_2|}dt_1 dt_2$$

with $a = \Delta^2(2\pi)^2/4\delta t$ and ϕ_{12}^g defined in (5). This result can be simplified by performing the integration over t_2 with the help of the delta function $\delta(k_\varepsilon + t_1 - t_2)$, giving

$$W_{FT}(k_A, k_\varepsilon) = \tfrac{\pi}{2}\Delta^2\omega e^{-\Gamma_2|k_\varepsilon|} \oint \delta(k_A + \phi_{12}^g)dt_1, \quad (13)$$

where $t_2 = t_1 + k_\varepsilon$. Result (13) illustrates the effect of dephasing on the lemon structure through the prefactor $e^{-\Gamma_2|k_\varepsilon|}$ (see Fig.2c), which arises from the exponential decay in time $e^{-|t_2 - t_1|/T_2}$, and is consistent with the interpretation of k_ε as a time variable.

It is instructive to compare this behavior with the effect of ensemble averaging, modeled by random offsets $\delta\varepsilon$ with a gaussian distribution. Because the phase factors in (11) are linear in ε, the ensemble-averaged FT is

$$\langle W_{FT}(k_A, k_\varepsilon)\rangle_{\rm ens} \propto e^{-\Gamma_2|k_\varepsilon|}e^{-\frac{1}{2}\lambda k_\varepsilon^2}, \quad \lambda = \langle\delta\varepsilon^2\rangle. \quad (14)$$

Through this dependence, instrinsic dephasing and ensemble averaging, i.e. T_2 and T_2^*, can be distinguished.

The lemon boundary obtained from (13) for a generic $g(t)$ agrees with the quasiclassical result (5). Indeed, the range of k_A for which FT intensity is nonzero, at a fixed k_ε, are determined by the extrema of the function ϕ_{12}^g in t_1. Writing $\delta_{t_1}\phi_{12}^g = g(t_2) - g(t_1) = 0$ we recover Eq.(3).

For the case of harmonic driving, $g(t) = \cos\omega t$, we can evaluate (13) by noting that $\phi_{12}^g = (\sin(\omega t_2) - \sin(\omega t_1))/\omega = (2/\omega)\sin(\frac{1}{2}\omega k_\varepsilon)\cos(\omega(t_1 + \frac{1}{2}k_\varepsilon))$. The integral over t_1 in (13) then yields

$$W_{FT}(k_A, k_\varepsilon) = \frac{\Delta^2\omega\, e^{-\Gamma_2|k_\varepsilon|}}{2\sqrt{\frac{4}{\omega^2}\sin^2(\frac{1}{2}\omega k_\varepsilon) - k_A^2}} \quad (15)$$

for $|k_A| < \frac{2}{\omega}|\sin(\frac{1}{2}\omega k_\varepsilon)|$, and zero elsewhere. We see that $W_{FT}(k_A, k_\varepsilon)$ is concentrated inside the region bounded by the sinusoids (9) with square root singularities at the boundary. Similar behavior with a square root singularity in FT intensity is obtained for the sawtooth case, as illustrated in Fig.3. Because Eq.(15) is derived with the FT taken over $-\infty < A < \infty$, the LZS pattern in Fig.2 had to be doubled to obtain the FT in Fig.3.

Finally, lemon structures are also exhibited by the FT of the qubit steady-state population. The lemon arcs with multiple periods, clearly visible in Fig.4, arise because of a nonlinear dependence of saturated population on W, with quadratic nonlinearity giving double period, cubic nonlinearity giving triple period, etc. This multiplicity of periods was also observed in the data [18].

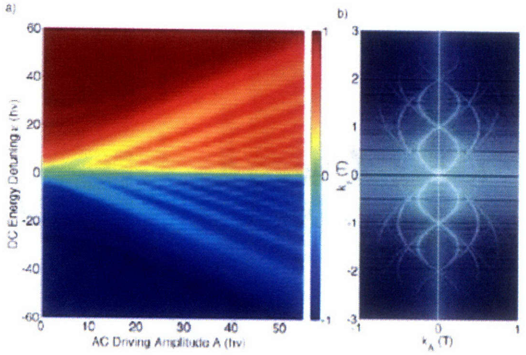

FIG. 4: Qubit magnetization and its FT. Shown is the magnetization of a qubit driven to saturation: $m = (\Gamma_1 - \Gamma_1')/(2W + \Gamma_1 + \Gamma_1')$, $\Gamma_1' = \Gamma_1 e^{-\varepsilon/k_B T}$, where Γ_1 (Γ_1') is the down (up) relaxation rate [9]. Results are shown for sawtooth driving with parameter values: decoherence rate $\Gamma_2 = \frac{1}{2}\omega$, temperature $k_B T = 1.2\hbar\omega$, relaxation rate $\Gamma_1 = 8 \cdot 10^{-5}\omega$, frequency $\nu = 400\,\mathrm{MHz}$, level splitting $\Delta = 12\,\mathrm{MHz}$.

In conclusion, FT-based tomography of two-dimensional LZS patterns is a general technique that offers a way to image the quantum phase evolution of qubits and other quantum systems. In the simplest case of a driving signal with just one maximum and one minimum per period, we predict a chain-like lemon structure in Fourier space which is in perfect agreement with recent observations.

We acknowledge partial support from W. M. Keck Foundation Center for Extreme Quantum Information Theory. The work of M. R. was supported by DOE CSGF, Grant No. DE-FG02-97ER25308. The work at Lincoln Laboratory was sponsored by the US DoD under Air Force Contract No. FA8721-05-C-0002. The views and conclusions contained in this document are those of the authors and should not be interpreted as representing the official policies, either expressly or implied, of the U.S. Government.

---

[1] J. E. Mooij, *Science* **307**, 1210 (2005).

[2] I. Chiorescu, P. Bertet, K. Semba, Y. Nakamura, C. J. P. M. Harmans, J. E. Mooij, Nature 431, 159 (2004).

[3] A. Wallraff, D. I. Schuster, A. Blais, L. Frunzio, R.- S. Huang, J. Majer, S. Kumar, S. M. Girvin, R. J. Schoelkopf, Nature 431, 162 (2004).

[4] D. I. Schuster, A. A. Houck, J. A. Schreier, A. Wallraff, J. M. Gambetta, A. Blais, L. Frunzio, J. Majer, B. Johnson, M. H. Devoret, S. M. Girvin, R. J. Schoelkopf, Nature 445, 515 (2007).

[5] Y. Nakamura, Y. A. Pashkin, J. S. Tsai, *Phys. Rev. Lett.* **87**, 246601 (2001).

[6] S. Saito, T. Meno, M. Ueda, H. Tanaka, K. Semba, H. Takayanagi, *Phys. Rev. Lett.* **96**, 107001 (2006).

[7] W. D. Oliver, Y. Yu, J. C. Lee, K. K. Berggren, L. S. Levitov, T. P. Orlando, *Science* **310**, 1653 (2005).

[8] M. Sillanpää, T. Lehtinen, A. Paila, Yu. Makhlin, P. Hakonen, *Phys. Rev. Lett.* **96**, 187002 (2006).

[9] D. M. Berns, W. D. Oliver, S. O. Valenzuela, A. V. Shytov, K. K. Berggren, L. S. Levitov, T. P. Orlando, *Phys. Rev. Lett.* **97**, 150502 (2006)

[10] N. Boulant, G. Ithier, F. Nguyen, P. Bertet, H. Pothier, D. Vion, C. Urbina, D. Esteve, arXiv:cond-mat/0605061

[11] C. M. Wilson, T. Duty, F. Persson, M. Sandberg, G. Johansson, P. Delsing, Phys. Rev. Lett. 98, 257003 (2007).

[12] A. Izmalkov, M. Grajcar, E. Il'ichev, N. Oukhanski, Th. Wagner, H.-G. Meyer, W. Krech, M. H. S. Amin, A. Maassen van den Brink and A. M. Zagoskin, *Europhys. Lett.* **65**, 844 (2004).

[13] S. Ashhab, J. R. Johansson, A. M. Zagoskin, F. Nori, *Phys. Rev.* A**75**, 063414 (2007)

[14] L. P. Kouwenhoven, S. Jauhar, J. Orenstein, P. L. McEuen, Y. Nagamune, J. Motohisa, and H. Sakaki, *Phys. Rev. Lett.* **73**, 3443 (1994).

[15] W. J. M. Naber, T. Fujisawa, H. W. Liu, and W. G. van der Wiel, Phys. Rev. Lett. 96, 136807 (2006).

[16] P. K. Tien and J. P. Gordon, *Phys. Rev.* **129**, 647 (1963).

[17] Y. Nakamura, J. S. Tsai, *J. Supercond.* **12**, 799 (1999).

[18] D. Berns *et al.*, arXiv:0805.1552

[19] J. Bylander *et al.*, to be published.

[20] R. A. Webb, S. Washburn, C. P. Umbach, R. B. Laibowitz, *Phys. Rev. Lett.* **54**, 2696 (1985).

[21] C. M. Marcus, A. J. Rimberg, R. M. Westervelt, P. F. Hopkins, and A. C. Gossard, *Phys. Rev. Lett.* **69**, 506 (1992).

[22] N. Katz, M. Ansmann, R. C. Bialczak, E. Lucero, R. McDermott, M. Neeley, M. Steffen, E. M. Weig, A. N. Cleland, J. M. Martinis, et al. *Science* 312, 1498 (2006)

[23] M. Steffen, M. Ansmann, R. McDermott, N. Katz, R. C. Bialczak, E. Lucero, M. Neeley, E. M. Weig, A. N. Cleland, J. M. Martinis *Phys. Rev. Lett.* **97**, 050502 (2006).

[24] M. Steffen, M. Ansmann, R. C. Bialczak, N. Katz, E. Lucero, R. McDermott, M. Neeley, E. M. Weig, A. N. Cleland, and J. M. Martinis, *Science* **313**, 1423 (2006).

Bibliography

[1] H. Lo, S. Popescu, and T. Spiller, Introduction to Quantum Computation and Quantum Information, World Scientific, Singapore, 1998.

[2] M. Nielsen and I. Chuang, Quantum Computation and Quantum Information, Cambridge University Press, UK, 2000.

[3] P. Benioff, "The Computer as a Physical System: A Microscopic Quantum Mechanical Hamiltonian Model of Computers as Represented by Turing Machines," *J. Stat. Phys.* **22**, 563 (1980).

[4] R. P. Feynman, "Simulating Physics with Computers," *Int. J. Theor. Phys.* **21**, 467 (1982).

[5] S. Lloyd, "Universal Quantum Simulators," *Science* **273**, 1073 (1996).

[6] S. Somaroo, C. H. Tseng, T. F. Havel, R. Laflamme, and D. G. Cory, "Quantum Simulations on a Quantum Computer," *Phys. Rev. Lett.* **82**, 5381 (1999).

[7] D. Deutsch, "Quantum theory, the Church-Turing principle and the universal quantum computer," *Proc. R. Soc. Lond. A* **400**, 97 (1985).

[8] S. Aaronson, "The Limits of Quantum," *Sci. Am.* **March**, 62 (2008).

[9] P.W. Shor, "Algorithms for Quantum Computation: Discrete Logarithms and Factoring," Proceedings, 35th Annual Symposium on Foundations of Computer Science, IEEE Press, Los Alamitos, California, 1994.

[10] B. Schneier, Applied Cryptography: Protocols, Algorithms, and Source Code in C, Wiley, New York, 1996.

[11] L. M. K. Vandersypen, M. Steffen, G. Breyta, C. S. Yannoni, M. H. Sherwood, and I. L. Chuang, "Experimental realization of Shor's quantum factoring algorithm using nuclear magnetic resonance," *Nature* **414**, 883 (2001).

[12] S. Wiesner, "Conjugate Coding," *Sigact News* **15**, 78 (1983).

[13] C. H. Bennett, F. Bessette, G. Brassard, L. Salvail, and J. Smolin, "Experimental Quantum Cryptography," *J. Cryptology* **5**, 3 (1992).

[14] C. H. Bennett, G. Brassard, C. Crepeau, R. Jozsa, A. Peres, and W. K. Wootters, "Teleporting an Unknown Quantum State via Dual Classical and Einstein-Podolsky-Rosen Channels," *Phys. Rev. Lett.* **70**, 1895 (1993).

[15] D. Bouwmeester, J. Pan, K. Mattle, M. Eibl, H. Weinfurter, and A. Zeilinger, "Experimental quantum teleportation," *Nature* **390**, 575 (1997).

[16] G. Greenstein and A. G. Zajonc, The Quantum Challenge: Modern Research on the Foundations of Quantum Mechanics, Jones and Bartlett, Boston, 2005.

[17] E. Schroedinger, "Discussion of probability relations between separated systems," *Proc. Cambridge Phil. Soc.* **31**, 555 (1935).

[18] A. J. Leggett and A. Garg, "Quantum Mechanics versus Macroscopic Realism: Is the Flux There when Nobody Looks?," *Phys. Rev. Lett.* **54**, 857 (1985).

[19] C. D. Tesche, "Schroedinger's Cat: A Realization in Superconducting Devices," Proc. NY Conf. on Quantum Measurement, Page 36, New York Academy of Sciences, New York, 1986.

[20] C. D. Tesche, "Can a Noninvasive Measurement of Magnetic Flux be Performed with Superconducting Circuits," *Phys. Rev. Lett.* **64**, 2358 (1990).

[21] A. Peres, "Quantum Limitations on Measurement of Magnetic Flux," *Phys. Rev. Lett.* **61**, 2019 (1988).

[22] A. Elby and S. Foster, "Why SQUID experiments can rule out non-invasive measurability," *Phys. Lett. A* **166**, 17 (1992).

[23] J. von Neumann, Mathematical Foundations of Quantum Mechanics, translated by R.T.Beyer, Princeton University Press, Princeton, 1955.

[24] W. H. Zurek, "Pointer basis of quantum apparatus: Into what mixture does the wave packet collapse?," *Phys. Rev. D* **24**, 1516 (1981).

[25] J. P. Paz and W. H. Zurek, "Quantum Limit of Decoherence: Environment Induced Superselection of Energy Eigenstates," *Phys. Rev. Lett.* **26**, 5181 (1999).

[26] J. F. Poyatos, J. I. Cirac, P. Zoller, "Quantum Reservoir Engineering with Laser Cooled Trapped Ions," *Phys. Rev. Lett.* **77**, 4728 (1996).

[27] R. Penrose, "On Gravity's Role in Quantum State Reduction," *Gen. Rel. and Grav.* **28**, 581 (1996).

[28] P. Pearle, "Reduction of the state vector by a nonlinear Schroedinger equation," *Phys. Rev. D* **13**, 857 (1976).

[29] W.H. Zurek, "Decoherence, einselection, and the quantum origins of the classical," *Rev. Mod. Phys.* **75**, 715 (2003).

[30] D. G. Cory, A. F. Fahmy, T. F. Havel, "Ensemble quantum computing by NMR spectroscopy," *Proc. Natl. Acad. Sci.* **94**, 1634 (1997).

[31] D. Loss and D. P. DiVincenzo, "Quantum computation with quantum dots," *Phys. Rev. A* **57**, 120 (1998).

[32] Y. Makhlin, G. Schoen, A. Shnirman, "Quantum-state engineering with Josephson-junction devices," *Rev. Mod. Phys.* **73**, 357 (2001).

[33] B. D. Josephson, "The discovery of tunnelling supercurrents," *Rev. Mod. Phys.* **46**, 251 (1974).

[34] R. F. Voss and R. A. Webb, "Macroscopic Quantum Tunneling in 1-μm Nb Josephson Junctions," *Phys. Rev. Lett.* **47**, 265 (1981).

[35] J. M. Martinis, M. H. Devoret, and J. Clarke, "Energy-Level Quantization in the Zero-Voltage State of a Current-Biased Josephson Junction," *Phys. Rev. Lett.* **55**, 1543 (1985).

[36] R. Rouse, S. Han, and J. E. Lukens, "Observation of Resonant Tunneling between Macroscopically Distinct Quantum Levels," *Phys. Rev. Lett.* **75**, 1614 (1995).

[37] V. Bouchiat, D. Vion, P. Joyez, D. Esteve, and M. Devoret, "Quantum Coherence with a Single Cooper Pair," *Phys. Scr.* **T76**, 165 (1998).

[38] A. Cottet, D. Vion, A. Aassime, P. Joyez, D. Esteve, and M. H. Devoret, "Implementation of a combined charge-phase quantum bit in a superconducting circuit," *Phys. C* **367**, 197 (2002).

[39] J. R. Friedman, V. Patel, W. Chen, S. K. Tolpygo, and J. E. Lukens, "Quantum superposition of distinct macroscopic states," *Nature* **406**, 43 (2000).

[40] J. M. Martinis, S. Nam, J. Aumentado, and C. Urbina, "Rabi Oscillations in a Large Josephson-Junction Qubit," *Phys. Rev. Lett.* **89**, 117901 (2002).

[41] J. E. Mooij, T. P. Orlando, L. S. Levitov, L. Tian, C. H. van der Wal, and S. Lloyd, "Josephson Persistent-Current Qubit," *Science* **285**, 1036 (1999).

[42] T. P. Orlando and K. A. Delin, Foundations of Applied Superconductivity, Addison-Wesley Co., Massachusetts, 1991.

[43] T. P. Orlando, J. E. Mooij, L. Tian, C. H. van der Wal, L. S. Levitov, S. Lloyd, and J. J. Mazo, "Superconducting persistent-current qubit," *Phys. Rev. B* **60**, 15398 (1999).

[44] D. S. Crankshaw, Measurement and On-chip Control of a Niobium Persistent Current Qubit, Doctoral Thesis, Massachusetts Institute of Technology, June 2003.

[45] D. M. Berns and T. P. Orlando, "Implementation Schemes for the Factorized Quantum Lattice-Gas Algorithm for the One Dimensional Diffusion Equation using Persistent-Current Qubits," *Quant. Info. Process.* **4**, 1 (2005).

[46] H. Nakano, H. Tanaka, S. Saito, K. Semba, H. Takayanagi, and M. Ueda, "A theoretical analysis of flux-qubit measurements with a dc-SQUID," arXiv:cond-mat, 0406622v1 (2004).

[47] D. S. Crankshaw, K. Segall, T. P. Orlando, L. S. Levitov, S. Lloyd, S. O. Valenzuela, N. Markovic, M. Tinkham, and K. K. Berggren, "dc measurements of macroscopic quantum levels in a superconducting qubit structure with a time-ordered meter," *Phys. Rev. B* **69**, 144518 (2004).

[48] M. Buettiker, E. Harris, and R. Landauer, "Thermal activation in extremely underdamped Josephson-junction circuits," *Phys. Rev. B* **28**, 1268 (1983).

[49] M. Devoret, J. Martinis, and J. Clarke, "Measurements of Macrocopic Quantum Tunneling out of the Zero-Voltage State of a Current-Biased Josephson Junction," *Phys. Rev. Lett.* **55**, 1908 (1985).

[50] A. Garg, "Escape-field distribution for escape from a metastable potential well subject to a steadily increasing bias field," *Phys. Rev. B* **51** 15592 (1995).

[51] By adding a current source to the SQUID, and accounting for the capacitive part of the current, Kirchoff's current law gives

$$\mathrm{I_b} = \mathrm{I}'_{\mathrm{c,sq}} \sin(\varphi'_{\mathrm{1,sq}}) + \mathrm{C_{sq}}(\frac{\Phi_0}{2\pi})\ddot{\varphi}_{\mathrm{1,sq}}. \tag{C.1}$$

The equation of motion for the SQUID is then just $(\frac{\Phi_0}{2\pi})\mathrm{I_b} - \overbrace{\mathrm{E}'_{\mathrm{j,sq}}}^{\mathrm{k}} \sin(\varphi'_{\mathrm{1,sq}}) = \overbrace{\left(\frac{{\Phi_0}^2}{(2\pi)^2}\right)}^{\mathrm{M_{sq}}} \mathrm{C_{sq}}\,\ddot{\varphi}_{\mathrm{1,sq}}$, giving a natural frequency when there is no bias current of $\omega_{\mathrm{sq}} \equiv \sqrt{\frac{\mathrm{k}}{\mathrm{M_{sq}}}} = \sqrt{\frac{2\pi \mathrm{I}'_{\mathrm{c,sq}}}{\Phi_0 \mathrm{C_{sq}}}}$, and from $\mathrm{F} = -\nabla \mathrm{U}$, $\mathrm{U} = -(\frac{\Phi_0}{2\pi})\mathrm{I_b}\varphi_{\mathrm{1,sq}} - \mathrm{E}'_{\mathrm{j,sq}} \cos(\varphi_{\mathrm{1,sq}})$ Note that I have assumed a linear approximation for sine when finding ω_{sq}.

[52] S. Li, Y. Yu, Y. Zhang, W. Qiu, and S. Han, "Quantitative Study of Macroscopic Quantum Tunneling in a dc SQUID: A System with Two Degrees of Freedom," *Phys. Rev. Lett.* **89**, 98301 (2002).

[53] D. Nakada, Fabrication and Measurement of a Niobium Persistent Current Qubit, Doctoral Thesis, Massachusetts Institute of Technology, June 2004.

[54] W. Oliver, Private Communciation, February 2004.

[55] I. I. Rabi, "Space Quantization in a Gyrating Magnetic Field," *Phys. Rev.* **51**, 652(1937).

[56] Y. Nakamura, Y. Pashkin, and J. Tsai, "Coherent control of macroscopic quantum states in a single-Cooper-pair box," *Nature* **398**, 786 (1999).

[57] Y. Nakamura, Y. Pashkin, and J. Tsai, "Rabi Oscillations in a Josephson-Junction Charge Two-Level System," *Phys. Rev. Lett.* **87**, 246601 (2001).

[58] D. Vion, A. Aassime, A. Cottet, P. Joyez, H. Pothier, C. Urbina, D. Esteve, and M. H. Devoret, "Manipulating the Quantum State of an Electrical Circuit," *Science* **296**, 886 (2002).

[59] I. Chiorescu, Y. Nakamura, C. J. P. M. Harmans, and J. E. Mooij, "Coherent Quantum Dynamics of a Superconducting Flux Qubit," *Science* **299**, 1869 (2003).

[60] B. L. T. Plourde, T. L. Robertson, P. A. Reichardt, T. Hime, S. Linzen, C. E. Wu, and J. Clarke, "Flux Qubits and Readout Device with Two Independent Flux Lines," *Phys. Rev. B* **72**, 060506(R) (2005).

[61] S. Saito, T. Meno, M. Ueda, H. Tanaka, K. Semba, and H. Takayanagi, "Parametric control of a superconducting flux qubit," *Phys. Rev. Lett.* **96**, 107001 (2006).

[62] J. Claudon, F. Balestro, F. W. J. Hekking, and O. Buisson, "Coherent Oscillations in a Superconducting Multilevel Quantum System," *Phys. Rev. Lett.* **93**, 187003 (2004).

[63] A. Shytov, D. Ivanov, M. Feigel'man, "Landau-Zener interferometry for qubits," *Eur. Phys. J. B* **36**, 263 (2003).

[64] A. Izmalkov, M. Grajcar, E. Il'ichev, N. Oukhanski, T. Wagner, H. Meyer, W. Krech, M. Amin, A. Maassen van den Brink, and A. Zagoskin, "Observation of macroscopic Landau-Zener transitions in a superconducting device," *Europhys. Lett.* **65**, 844 (2004).

[65] E. C. G. Stueckelberg, "Theorie der un elastischen Stösse zwischen Atomen," *Helv. Phys. Acta* **5**, 369 (1932).

[66] W. D. Oliver, Y. Yu, J. C. Lee, K. K. Berggren, L. S. Levitov, and T. P. Orlando, "Mach-Zehnder Interferometry in a Strongly Driven Superconducting Qubit," *Science* 310, 1653 (2005).

[67] M. Sillanpää, T. Lehtinen, A. Paila, Y. Makhlin, and P. Hakonen, "Continuous-Time Monitoring of Landau-Zener Interference in a Cooper-Pair Box," *Phys. Rev. Lett.* **96**, 187002 (2006).

[68] C. Wilson, T. Duty, F. Persson, M. Sandberg, G. Johansson, and P. Delsing, "Coherent Times of Dressed States of a Superconducting Qubit under Extreme Driving," *Phys. Rev. Lett.* 98, 257003 (2007).

[69] W. Oliver, Private Communication, July 2005.

[70] A. J. Leggett, S. Chakravarty, A. T. Dorsey, M. P. A. Fisher, A. Garg, and W. Zwerger, "Dynamics of the dissipative two-state system," *Rev. Mod. Phys.* 59, 1 (1987).

[71] C. van der Wal, Quantum Superpositions of Persistent Josephson Currents, Doctoral Thesis, Technical University of Delft, September 2001.

[72] C. Slichter, Principles of Magnetic Resonance, Harper and Row, New York, 1963.

[73] J. M. Martinis, K. B. Cooper, R. McDermott, M. Steffen, M. Ansmann, K. D. Osborn, K. Cicak, S. Oh, D. P. Pappas, R. W. Simmonds, and C. C. Yu "Decoherence in Josephson Qubits from Dielectric Loss," *Phys. Rev. Lett.* 95, 210503 (2005).

[74] R. C. Bialczak, R. McDermott, M. Ansmann, M. Hofheinz, N. Katz, E. Lucero, M. Neeley, A. D. O'Connell, H. Wang, A. N. Cleland, and J. M. Martinis, "1=f Flux Noise in Josephson Phase Qubits," *Phys. Rev. Lett.* 99, 187006 (2007).

[75] D. M. Berns, W. D. Oliver, S. 0. Valenzuela, A. V. Shytov, K. K. Berggren, L. S. Levitov, and T. P. Orlando, "Coherent Quasiclassical Dynamics of a Persistent Current Qubit," *Phys. Rev. Lett.* 97, 150502 (2006).

[76] L. S. Levitov, Private Communcation, January 2006.

[77] W. D. Oliver, Private Communcation, April 2006.

[78] J. Sakurai, Modern Quantum Mechanics, Addison-Wesley, New York, 1994.

[79] It is emphasized that the crossover between high and low frequencies in this case occurs at $\nu T_2 \sim 1$ rather than at $\omega T_2 \sim 1$. This can be inferred from the expression Im $\cot(\pi(\epsilon - i\Gamma_2)/\omega)$, Eq.(3.20), which describes multiphoton resonances broadening. At large Γ_2 this gives $1 + 2e^{-2\pi\Gamma_2/\omega}\cos(2\pi\epsilon/\omega) + O(e^{-4\pi\Gamma_2/\omega})$. The cosine modulation is exponentially suppressed at $\nu \leq \Gamma_2$, whereby transitions are no longer due to a single photon mode.

[80] G. K. White, Experimental Techniques in Low-Temperature Physics, Oxford University Press, Oxford, 1979.

[81] C. Cohen-Tannoudji, "Manipulating atoms with photons," *Rev. Mod. Phys.* **70**, 707 (1998).

[82] I. Marzoli, J. Cirac, R. Blatt, and P. Zoller, “Laser cooling of trapped three-level ions: Designing two-level systems for sideband cooling,” *Phys. Rev. A* **49**, 2771 (1994).

[83] S. O. Valenzuela, W. D. Oliver, D. M. Berns, K. K. Berggren, L. S. Levitov, and T. P. Orlando, “Microwave-Induced Cooling of a Superconducting Qubit,” *Science* 314, 1589 (2006).

[84] Y. Nakamura, C. D. Chen, and J. S. Tsai, “Spectroscopy of Energy-Level Splitting between Two Macroscopic Quantum States of Charge Coherently Superposed by Josephson Coupling,” *Phys. Rev. Lett.* **79**, 2328 (1997).

[85] C. H. van der Wal, A. C. J. ter Haar, F. K. Wilhelm, R. N. Schouten, C. J. P. M. Harmans, T. P. Orlando, S. Lloyd, J. E. Mooij, “Quantum Superposition of Macroscopic Persistent-Current States,” *Science* **290**, 773 (2000).

[86] D. M. Berns, M. S. Rudner, S. O. Valenzuela, K. K. Berggren, W. D. Oliver, L. S. Levitov, and T. P. Orlando, “Amplitude Spectroscopy of a Solid-State Artificial Atom,” Submitted for publication (2008), arXiv:0805.1552.

[87] O. Astafiev, K. Inomata, A. Niskanen, T. Yamamoto, Yu Pashkin, Y. Nakamura, and J. Tsai, “Single Artificial-atom Lasing,” *Nature* **449**, 588 (2007).

[88] M. S. Rudner, Private Communcation, November 2007.

[89] M. S. Rudner, A. V. Shytov, L. S. Levitov, D. M. Berns, W. D. Oliver, S. O. Valenzuela, and T. P. Orlando, “Quantum Phase Tomography of a Strongly Driven Qubit,” Submitted for publication (2008), arXiv:0805.1555.

[90] M. S. Rudner, Private Communcation, January 2008.

[91] J. Q. You, Y. Liu, and F. Nori, “Simultaneous Cooling of an Artificial Atom and Its Neighboring Quantum System,” *Phys. Rev. Lett.* **100**, 047001 (2008).

[92] F. Bloch and A. Siegert, “Magnetic Resonance for Nonrotating Fields,” *Phys. Rev.* **57**, 522 (1940).

[93] M. Grifoni and P. Hänggi, "Driven quantum tunneling," *Physics Reports* **304**, 229 (1998).

[94] C. Cohen-Tannoudji, B. Diu, and F. Laloe, Quantum Mechanics Vol.2, Wiley, 1977.